





# Development of an isopluvial atlas for Egypt using statistical and GIS-based methods

Eman Ahmed Hassan El-Sayed

Water Resources Research Institute, National Water Research Center, Egypt

## Abstract

Rainfall across various climatic zones of Egypt, including arid coastal and semi-arid inland regions, exhibits significant temporal and spatial variability. Precise estimation of effective rainfall depths is essential for design engineers, hydrologists, and consultants involved in the construction of hydraulic structures such as dams, lakes, culverts, and diversions. Moreover, rainfall depth plays a crucial role in the design of urban drainage systems, small-scale irrigation projects, and broader water resource management initiatives. To address this need, an atlas of isopluvial maps for Egypt was developed using statistical methodologies and Geographic Information System (GIS) tools. This study employed short-duration rainfall data from various climatic zones of Egypt to create an empirical formula for estimating short-duration rainfall depths. Maximum annual daily rainfall data from 54 stations were analyzed to estimate short-duration rainfall values. The analytical process used Gamma distributions to determine maximum rainfall depths for various return periods and durations. The derived empirical formula and daily rainfall data were then incorporated into a GIS framework for spatial interpolation and the generation of isopluvial maps. The resulting atlas provides isopluvial maps for return periods ranging from 2 to 200 years and durations from 5 minutes to 24 hours. These maps serve as a valuable resource for decision-makers and design engineers, providing reliable rainfall estimates for specific locations or regions across Egypt. Additionally, the methodology presented in this study offers practical guidance for understanding and modeling the temporal and spatial distribution of rainfall in diverse climatic regions; its potential for improving the design of hydraulic structures is highlighted. Further validation of the atlas using independent datasets is recommended.

## Keywords

Isopluvial maps, maximum daily rainfall, short-duration rainfall, return period, frequency analysis, climate change.

Submitted 5 February 2025, revised 24 April 2025, accepted 9 June 2025

DOI: 10.26491/mhwm/206070

## 1. Introduction

Egypt faces significant challenges due to limited water resources, necessitating efficient use of both natural and non-conventional water sources (Gado et al. 2023). Effective management of floodwaters requires constructing hydraulic structures such as dams, reservoirs, channels, and culverts. Additionally, meteorological data is necessary to anticipate and mitigate flood-related risks. Precise knowledge of extreme rainfall events, including their magnitude and duration, is essential for ensuring the safety of lives, property, and infrastructure (Parvez et al. 2019; Kawara, Elsebaie 2022). Consequently, accurate estimates of maximum runoff are essential for planning and constructing such hydraulic systems (Das et al. 2022). However, the availability of reliable rainfall data in Egypt is hindered by several challenges, including missing data, short record lengths, and inconsistent spatial distribution of rainfall stations. These limitations underscore the importance of developing robust methodologies to estimate rainfall intensities and durations accurately.

In recent years, Egypt has undertaken numerous infrastructure development projects, such as roadways, monorails, railways, bridges, and urban drainage systems in new cities. Before initiating such activities, comprehensive meteorological and hydrological investigations were required to design flood protection

systems (Division of Hydrometeorology 2007). Rainfall patterns, including their frequency, intensity, and spatial distribution, are increasingly influenced by climate change, which has been identified as a major factor in the increased frequency of heavy rainfall events and shifting patterns (Das et al. 2022). Notably, Egypt has already experienced increased frequency of extreme rainfall events and altered seasonal distributions (Nashwan et al. 2019; Roushdi 2022), highlighting the urgent need for updated methodologies to address evolving climatic conditions. Specifically, observed changes in Egypt's rainfall patterns include increased extreme rainfall events and altered seasonal distributions, which have significant implications for water resource management and infrastructure planning. These changes highlight the urgent need for updated methodologies to address evolving climatic conditions (Nashwan et al. 2019; Roushdi 2022).

In arid and semi-arid areas, significant changes in the properties of rainfall from one time to another can be noted. Therefore, understanding the dynamics of rainfall processes, including total rainfall, intensity over specific periods, and year-to-year variability, is essential. Reliable estimates of rainfall depths require comprehensive analyses of long-term historical rainfall data (Parvez et al. 2019). The availability of extensive rainfall records is crucial for conducting frequency analyses to derive accurate rainfall depth estimates (Al-Amri, Subyani 2017; Matos 2018). In Egypt, obtaining long-term, continuous rainfall records can be challenging because of issues such as the limited number of long-operating stations and gaps in existing datasets. These challenges are particularly pronounced for short-duration rainfall data, which is critical for designing hydraulic structures and urban drainage systems. The scarcity of recording rain gauges capable of capturing high-resolution temporal rainfall information, especially in remote or ungauged areas, exacerbates this issue. Additionally, inconsistencies in data collection practices, such as variations in measurement techniques and equipment, further contribute to the limitations of historical rainfall data.

Intensity–duration–frequency (IDF) curves and isopluvial maps are widely used in meteorology, hydrology, and water resource engineering for design, planning, operation, and management purposes (Subyani, Al-Amri 2015; Şen 2019). For example, IDF curves have already been developed for the Sinai Peninsula, a distinct climatic region in Egypt (El-Sayed 2011; Fathy et al. 2014). However, these Sinai-specific curves may not accurately represent rainfall characteristics across the diverse climatic zones of the entire country. The development of new IDF curves for Egypt is not only justified but necessary to address the limitations of outdated data, insufficient spatial and temporal resolution, and the impacts of climate change. These updated curves provide a valuable resource for modern infrastructure planning and water resource management, ensuring that designs are both safe and sustainable in the face of evolving climatic challenges.

The scarcity of short-duration rainfall data in many parts of Egypt exacerbates the challenge of accurately estimating rainfall intensities for critical infrastructure design. This scarcity is often attributed to the limited number of recording rain gauges capable of capturing high-resolution temporal rainfall information. Using reliable rainfall data is strongly recommended for the effective and secure design of

flood protection projects (Ewea et al. 2017). Furthermore, analyzing trends and variability in annual maximum daily rainfall series and understanding their impacts on total rainfall are critical areas of study (Ghenim, Megnounif 2016).

Since climate change has gained international attention from scientists, the intense study of rainfall frequency relationships, including the creation of isopluvial maps, has become an important tool for understanding broader climatic trends (Bonnin et al. 2011; The Rainfall Atlas of Hawai'i 2011; Schroeder 2013).

The objective of this study is to develop an empirical formula and a comprehensive atlas of isopluvial maps for Egypt, using statistical methodologies and GIS tools. Specifically, the study aims to:

1. Estimate short-duration rainfall depths based on daily rainfall records.
2. Generate isopluvial maps for various durations and return periods.
3. Investigate the potential influence of climate change on the derived rainfall estimates and their implications for future infrastructure design.

The expected contributions include providing engineers and policymakers with reliable tools for designing hydraulic structures, urban drainage systems, and flood protection measures. These outputs will enhance the accuracy of rainfall predictions and support adaptive planning in response to evolving climatic conditions. The findings of this study are expected to offer significant benefits to engineers, policymakers, and other stakeholders involved in water resource management and infrastructure planning. By providing accurate rainfall estimates for specific durations and return periods, the study supports the design of resilient hydraulic structures, urban drainage systems, and flood mitigation strategies (Rana et al. 2023). Additionally, the isopluvial maps serve as a valuable resource for identifying high-risk areas and optimizing resource allocation for infrastructure projects (Carvalho et al. 2022). This study offers a novel, nationwide assessment of short-duration rainfall depths and isopluvial mapping for Egypt, building upon existing regional studies such as the IDF curves developed for the Sinai Peninsula. Unlike previous studies that focused on specific regions, this research provides a comprehensive framework applicable to Egypt's diverse climatic zones, incorporating updated methodologies and considerations for climate change impacts.

## **2. Data and methods**

### **2.1. Study area**

Egypt spans diverse climate zones that exhibit significant variability in rainfall patterns, both temporally and spatially. A recent high-resolution climatic classification study identified distinct zones using image clustering techniques applied to meteorological data. These climatic zones reflect differences in rainfall magnitude, frequency, and seasonal variability across the country (Hamed et al. 2022).

1. Mediterranean Coastal Zone: This region experiences relatively higher rainfall compared to the rest of Egypt, with precipitation concentrated during the winter months from the influence of Mediterranean cyclones.



2. Nile Valley and Delta Zone: Characterized by moderate rainfall, this zone benefits from proximity to the Nile River and exhibits more uniform rainfall distribution compared to desert regions.
3. Western Desert Zone: This arid region receives minimal rainfall, with sporadic and highly variable precipitation events driven by rare convective storms.
4. Eastern Desert and Red Sea Coast Zone: This zone experiences localized but intense rainfall events, often associated with tropical systems or Red Sea troughs.
5. Sinai Highlands Zone: Includes mountainous parts of the Sinai Peninsula that occasionally receive convective or orographic rainfall, mostly in spring and autumn.

Understanding these climatic differences is critical for effective water resource management and infrastructure planning. This study focuses on rainfall data collected from 54 meteorological stations distributed across Egypt, ensuring comprehensive coverage of the country's varied climatic conditions. The locations of these stations are shown in Figure 1, highlighting their strategic placement within each climatic zone to capture regional rainfall variability.

## **2.2. Data collection**

Egypt is monitored by an extensive network of rainfall recording stations with more than 100 stations nationwide. Daily rainfall data from 54 meteorological stations were used in this study, with observation periods ranging from 19 to 118 years. These 54 stations were chosen because they provide a representative sample of Egypt's diverse climatic zones, including coastal, desert, and semi-arid regions. Stations with incomplete records or significant data gaps were excluded to ensure data quality.

Rainfall measurements were recorded hourly or daily, depending on the station. Table 1 details the range of available records and the geographic coordinates of these stations. The rainfall data obtained from the Egyptian Meteorological Authority (EMA) stations are recorded on a daily basis for all 54 stations, while the data obtained from the Water Resources Research Institute (WRRI) are recorded on an hourly basis (only three WRRI stations were selected).

Most stations (41 out of 54) have data spanning over 40 years, with 10 stations exceeding 75 years of records. Conversely, 13 stations have records shorter than 40 years, and only two have data for less than 19 years. The data were purchased from the Egyptian Meteorological Authority (EMA), ensuring access to high-quality, officially recorded rainfall measurements.

Additionally, short-duration rainfall data from various climatic zones in Egypt were collected and analyzed to estimate maximum rainfall depths for different durations. Rainfall storm data for durations of up to 24 hours were obtained from three specific stations: Saint Katherine, Marsa Matrouh, and Shalateen. These stations were selected because they represent distinct climatic zones: coastal (Marsa Matrouh), mountainous (Saint Katherine), and desert (Shalateen), ensuring the generalizability of the results across diverse regions. Furthermore, these stations are equipped with hourly monitoring provided by the Water Resources Research Institute (WRRI), which is critical for capturing high-resolution temporal rainfall data. The limited density of hourly recording stations in Egypt, combined with challenges such as insufficient

monitoring infrastructure in remote areas and inconsistent recording practices, made it difficult to expand the analysis to a larger network. Additional stations were considered but excluded due to insufficient storm event data or inconsistent recording practices.

These rainfall events occurred during the period from 2015 to 2024, ensuring a robust dataset for analysis. The availability of hourly data allowed for precise estimation of short-duration rainfall depths, which is critical for constructing accurate empirical formulas and IDF curves.

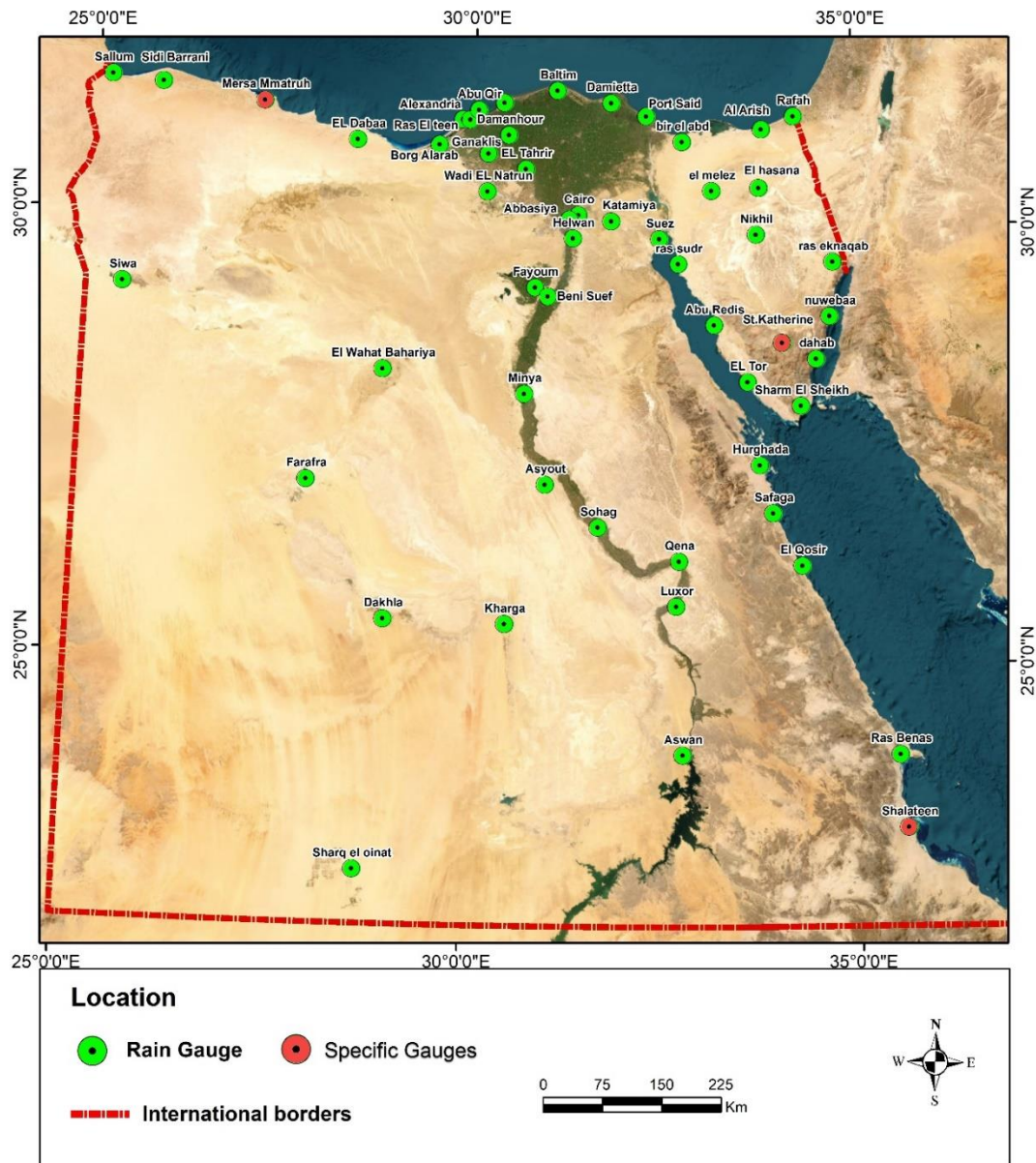


Fig. 1. Location of rain gauge stations.



Table 1. Years of record and locations of rain gauge stations.

No.	Station Name	Coordinates		Observation period	No. of years
		Latitude (DMS)	Longitude (DMS)		
1	Sallum	31°32'00 "N	25°11'00"E	1975:2018	44
2	sidi Barrani	31°38'00"N	25°28'00"E	1975:2018	44
3	Marsa Matrouh	31°20'00"N	27°13'00"E	1968:2018	51
4	EL Dabaa	31°38'00"N	25°28'00"E	1968:2018	51
5	Ras EL Teen	31°12'00"N	29°51'00"E	1968:2022	55
6	Alexandria	29°57'00"N	31°12'00"E	1968:2022	55
7	Rosetta	31°24'00"N	30°24'00"E	1973:2022	50
8	Baltim	31°33'00"N	31°06'00"E	1992:2017	26
9	Damietta	31°25'00"N	31°49'00"E	1968:2017	50
10	Port Said	31°16'00"N	32°17'00"E	1887:2017	118
11	Katamiya	30°04'00"N	31°50'00"E	1973:2020	40
12	Damanhour	31°02'00"N	30°28'00"E	1984:2005	22
13	Ganakleas	30°49'00"N	30°12'00"E	1968:2022	55
14	EL Tahrir	30°39'00"N	30°42'00"E	1968:2022	55
15	Wadi EL Natrun	30°23'00"N	30°12'00"E	1968:2022	55
16	Sohag	26°34'00"N	31°42'00"E	1968:2020	52
17	Qena	26°11'00"N	32°44'00"E	1935:2018	84
18	Luxor	25°40'00"N	32°42'00"E	1939:2018	59
19	Aswan	23°58'00"N	32°47'00"E	1935:2018	82
20	Siwa	29°12'00"N	25°29'00"E	1968:2018	51
21	El Wahat Bahariya	28°20'00"N	28°54'00"E	1969:2014	46
22	Farafra	27°03'00"N	27°58'00"E	2004:2018	15
23	Dakhla	25°29'00"N	29°00'00"E	1968:2018	51
24	Kharga	25°27'00"N	30°32'00"E	1969:2018	50
25	ELArish	31°16'00"N	33°45'00"E	1908:2022	83
26	Rafah	31°16'00"N	34°14'00"E	1990:2013	24
27	Nikhil	29°55'00"N	33°44'00"E	1907:2017	69
28	Abu Redis	28°53'00"N	33°11'00"E	1976:2021	37
29	EL Tor	28°14'00"N	33°37'00"E	1920:2014	65
30	Cairo	30°08'00"N	31°24'00"E	1974:2020	47
31	Abbasiya	30°05'00"N	31°17'00"E	1976:2020	43
32	Helwan	29°52'00"N	31°20'00"E	1908:2020	82
33	Fayoum	29°18'00"N	30°51'00"E	1929:2018	75
34	Beni Suef	29°12'00"N	31°01'00"E	1948:2020	59
35	Minya	28°05'00"N	30°44'00"E	1936:2020	69
36	Asyout	27°03'00"N	31°01'00"E	1924:2018	95
37	Suez	29°52'00"N	32°28'00"E	1887:2020	110
38	Hurghada	27°17'00"N	33°46'00"E	1933:2018	86
39	El Qosir	26°08'00"N	34°18'00"E	1927:2018	92
40	Ras Benas	23°58'00"N	35°30'00"E	1966:2018	53
41	bir el abd	30°58'34.6"N	32°45'32.8"E	1996:2020	23
42	el hasana	30°27'03.1"N	33°46'14.7"E	1938:2017	49
43	nuwebaa	28°58'50.0"N	34°41'00.0"E	1992:2019	28
44	dahab	28°29'43.3"N	34°30'06.8"E	1999:2017	19
45	ras eknaqab	29°35'59.4"N	34°43'57.9"E	1982:2021	40
46	ras sudr	29°34'55.1"N	32°42'50.3"E	1976:2022	47
47	saint Kathrine	28°40'48.1"N	34°03'52.0"E	1934:2022	47
48	el melez	30°25'04.3"N	33°08'56.0"E	1982:2022	41
49	Sharm El Sheikh	27°57'36.0"N	34°18'00.0"E	1982:2015	34
50	Safaga	26°44'00.0"N	33°56'00.0"E	1994:2018	25
51	Sharq el oinat	22°34'34.0"N	28°42'14.0"E	2001:2018	18
52	Abu Qir	30°03'34.0"N	31°18'47.0"E	1973:2022	50
53	Shalateen	35°35'16.0"N	23°07'58.0"E	2000:2018	19
54	Borg El Arab	29°33'10.0"N	30°54'20.0"E	1994:2018	25

### 2.3. Methods

Rain storms recorded from three gauges distributed across Egypt were collected for analysis. Two methods were applied to determine the ratios (generalized WRRI ratios) of storm depths at various durations, ranging from 10 minutes to 18 hours, relative to the 24-hour depth. The first method relies on recorded rainfall depths, while the second method employs frequency analysis. Frequency analysis was used, along with direct recording, to address specific limitations of relying solely on recorded depths. Recorded rainfall data may not adequately capture extreme rainfall intensities due to the limited number of storm events observed over time. Frequency analysis helps overcome these limitations by statistically modeling rainfall patterns and providing estimates for return periods that extend beyond the observed record. This ensures a more robust representation of rainfall intensities, particularly for rare but high-impact events, which are critical for infrastructure design and flood risk management.

Initially, daily rainfall data were used to compile the maximum annual daily rainfall series. These maximum values were then converted into shorter durations (5, 10, 20, 30 minutes, and 1, 2, 3, 6, 12, 18 hours) using the generalized WRRI ratios. These durations are standard for hydrological analysis in Egypt and align with international practices for IDF curve development. Subsequently, the derived series were subjected to statistical analysis to estimate rainfall values corresponding to return periods of 2, 5, 10, 20, 25, 50, 100, and 200 years. These return periods align with standard infrastructure design requirements in Egypt, ensuring the practical applicability of the findings for engineering projects such as drainage systems, flood protection measures, and hydraulic structures.

The methodology for creating the isopluvial maps comprised five steps (Trypaluk 2024):

1. Data Preparation: Maximum daily rainfall records were collected and converted into short durations (e.g., 5, 10, 20, 30 minutes, and up to 24 hours) using generalized WRRI ratios.
2. Frequency Analysis: Various statistical distributions, including gamma, Gumbel, and log-normal, were tested. The gamma distribution was identified as the best fit based on goodness-of-fit metrics (Awadallah, Younan 2012).
3. Rainfall Depth Estimation: Rainfall values for durations from 5 minutes to 24 hours and return periods of 2 to 200 years were estimated.
4. GIS-Based Mapping: Using GIS tools and the inverse-distance-weighted (IDW) interpolation method, isopluvial maps were generated for different durations and return periods (Muhammad 2016).
5. Validation: The empirical formula and isopluvial maps were validated against observed rainfall data and previous studies to ensure accuracy (Fathy et al. 2014; El-Sayed 2017).

By integrating these steps, the study presents a comprehensive methodology for analyzing rainfall variability and providing valuable input for hydrological and engineering applications.



### 3. Results and discussion

#### 3.1. Reduction formula

The Indian Meteorological Department (IMD) recommended an empirical reduction formula to estimate short-duration rainfall intensities from annual maximum rainfall data. This approach is especially useful in regions where sub-daily rainfall data are scarce or unavailable, because it allows engineers and hydrologists to derive short-duration rainfall estimates using more widely available daily rainfall records (Rasel, Islam 2015; Jalee, Farawn 2017). In Saudi Arabia, proposed ratios for 1-day rainfall are as follows: 0.37, 0.40, 0.46, 0.53, 0.61, 0.66, 0.70, 0.76, 0.80, and 0.87 for durations of 10, 15, 30, 60, 120, 180, 240, 360, 480, and 720 minutes, respectively (AlHassoun 2011; Kawara, Elsebaie 2022). Similarly, for the Sinai Peninsula, the proposed ratios for 1-day rainfall are 0.5, 0.57, 0.68, 0.70, 0.72, and 0.82 for durations of 0.5, 1, 2, 6, 12, and 18 hours, respectively (Awadallah, Younan 2012). Additionally, for Sinai, the WRRI-proposed ratios for 1-day rainfall are 0.18, 0.3, 0.36, 0.46, 0.58, 0.72, 0.77, 0.85, and 0.92 for durations of 5, 10, 20, 30, 60, 120, 360, 720, and 1080 minutes, respectively (El-Sayed 2017). The ratios from Saudi Arabia and the Sinai Peninsula were chosen because they represent arid and semi-arid regions with climatic conditions similar to those in Egypt. These regions also rely on sparse but reliable rainfall data, making their methodologies comparable. However, recent rainfall data were employed to develop a generalized equation for estimating short-duration rainfall from daily rainfall records.

The reduction formula was derived using high-resolution, short-duration rainfall data collected from three key stations equipped with advanced monitoring capabilities: Saint Katherine, Marsa Matrouh, and Shalateen. These stations record rainfall depths at a high temporal resolution (5 minutes), ensuring precise and reliable estimates of maximum rainfall depths for durations ranging from 10 minutes to 24 hours. To derive the reduction formula, maximum rainfall depths for each storm were calculated at different durations and accordingly, the corresponding maximum annual rainfall depth. Frequency analyses were performed, and the ratio of storm depths for each duration was computed relative to the 24-hour rainfall depth for each return period. Table 2 illustrates the ratios developed using two distinct methods, while Figure 2 displays the average ratios for durations up to two hours. A logarithmic trendline was applied because it provided the best fit based on statistical metrics such as  $R^2$  and mean absolute error (MAE). The corresponding fitting equation was derived, providing a predictive tool for estimating short-duration rainfall depths.

Table 2. Average depth ratios with respect to 24 hr. depth at different durations.

Ratio	Duration (min)					
	10	15	30	60	120	1440
First method	0.30	0.38	0.50	0.59	0.70	1.00
Second method	0.24	0.30	0.42	0.54	0.60	1.00
Average	0.27	0.34	0.46	0.57	0.65	1.00

The Generalized Water Resources Research Institute (GWRI) developed an empirical reduction formula to estimate short-duration rainfall depths for durations up to two hours. The formula is:

$$R_t = R * [0.1457 \ln(t) - 0.0492]$$

where:  $R_t$  is the estimated rainfall depth in mm at  $t$  duration;  $R$  is the daily rainfall depth in mm;  $t$  is the storm duration in minutes for which the rainfall depth is estimated.

This formula provides a practical tool for converting daily rainfall data into precise short-duration estimates, facilitating its application in hydrological modeling and engineering designs. Validation demonstrated its reliability in capturing extreme rainfall events critical for infrastructure projects. Validation was performed using  $R^2$ . The results showed high accuracy, with  $R^2$  values exceeding 0.95 for most stations. The method's ability to address gaps in conventional estimation methods makes it particularly valuable for adaptive planning.

Furthermore, a comparison between the ratios derived from data and frequency analysis (Table 2) and those estimated using the GWRI formula (Table 3) reveals strong agreement. For most durations, the differences between the two methods are minimal, underscoring the reliability and robustness of the empirical formula. This consistency highlights the formula's effectiveness in providing accurate and reliable estimates of short-duration rainfall depths across diverse climatic zones in Egypt.

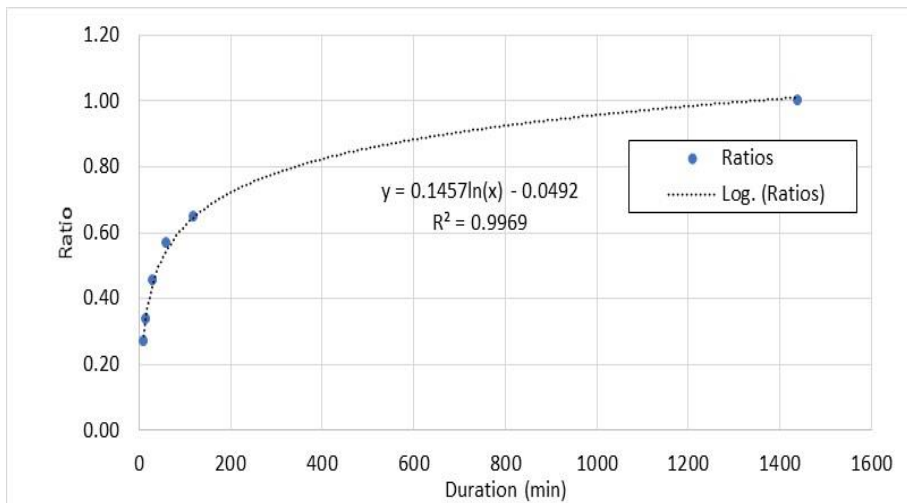


Fig. 2. Average depth ratios with respect to 24 h depth at different durations.

The rainfall depths estimated using the GWRI formula have been compared with the WRI ratios for Sinai (El-Sayed 2017), as shown in Table 3. The comparison reveals that the developed GWRI ratios closely align with the WRI ratios, demonstrating a fairly good agreement between the two methods. This consistency highlights the reliability of the GWRI formula for estimating short-duration rainfall depths. Also, the new formula improves accuracy by incorporating recent rainfall data, making it more adaptable to current climatic conditions in Egypt.



Table 3. Comparison between the calculated GWRI ratios and WRI ratios.

Ratio	Storm Duration (min)									
	5	10	20	30	60	120	360	720	1080	1440
GWRI formula	0.18	0.29	0.35	0.45	0.55	0.65	0.81	0.91	0.97	1.00
WRI ratios	0.18	0.30	0.36	0.46	0.58	0.72	0.77	0.85	0.92	1.00

### 3.2. Short duration estimation

The one-day annual maximum rainfall series was extracted from all available stations, using rainfall data from 54 stations to estimate short-duration rainfall. Daily rainfall records from various stations spanning the entire area of Egypt were converted into shorter durations using the GWRI ratio.

Short durations of 5, 10, 20, 30, 60, 120, 360, 720, and 1080 minutes were generated for all years of available records. These durations are standard for hydrological analysis in Egypt and align with international practices for IDF curve development. As an example, Table 4 presents the tabulated short-duration rainfall data for the Abu-Redis station. Abu-Redis was chosen as an example because it represents a typical station with moderate rainfall variability, making it suitable for illustrating the methodology. Similarly, short-duration rainfall data were tabulated for the remaining 53 stations, providing a comprehensive dataset for analysis across Egypt.

### 3.3. Frequency analysis

The availability of data is essential for frequency analysis. The objective of frequency analysis is to relate the magnitude of extreme events to their frequency of occurrence by applying different probability distributions (Al-Amri, Subyani 2017; Gado et al. 2023). Several theoretical distribution functions have been used worldwide, such as Type I extreme value (Gumbel), general extreme value (GEV), Weibull, gamma, normal, log-normal, Pearson type III and log-Pearson type III distributions (Al-Aboodi et al. 2019; Shamkhi et al. 2022). Previous studies in Egypt and similar arid and semi-arid regions approached rainfall frequency analysis using a variety of probability distributions, often selected based on the availability of data and the specific climatic conditions of the region. In Egypt, previous research has commonly employed distributions such as the Gumbel, log-normal, and Pearson type III to model extreme rainfall events. These distributions were chosen for their ability to capture the variability and extremes observed in historical rainfall records (Trypaluk 2024).

In this study, the available data are sufficient at almost all stations to perform frequency analysis. Multiple probability distribution functions were applied to estimate maximum rainfall values for different return periods using Hyfran Plus v2.1 (El Adlouni, Bobée 2015; Almheiri et al. 2024) and Flood Frequency Analysis (Freq) software v2.0 (Hamed, Rao 2019). These programs offer a suite of powerful, adaptable, and user-friendly mathematical tools for statistically analyzing extreme events. They support various probability distributions and enable users to compare fitting results across multiple statistical distributions within the same dataset. Additionally, the Freq software employs standard goodness-of-fit tests, such as the chi-square test and the Kolmogorov-Smirnov test, to assist in selecting the best-fit distribution.

Table 4. Short duration rainfall series for Abu-Redis station.

Year	Rainfall (mm)	Duration (min)									
		5	10	20	30	60	120	360	720	1080	1440
1976	4.0	0.7	1.2	1.4	1.8	2.3	2.9	3.1	3.4	3.7	4.0
1977	7.1	1.3	2.1	2.6	3.3	4.1	5.1	5.5	6.0	6.5	7.1
1978	2.5	0.5	0.8	0.9	1.2	1.5	1.8	1.9	2.1	2.3	2.5
1979	11.2	2.0	3.4	4.0	5.2	6.5	8.1	8.6	9.5	10.3	11.2
1980	23.7	4.3	7.1	8.5	10.9	13.7	17.1	18.2	20.1	21.8	23.7
1981	0.4	0.1	0.1	0.1	0.2	0.2	0.3	0.3	0.3	0.4	0.4
1982	19.7	3.5	5.9	7.1	9.1	11.4	14.2	15.2	16.7	18.1	19.7
1983	3.6	0.6	1.1	1.3	1.7	2.1	2.6	2.8	3.1	3.3	3.6
1984	4.5	0.8	1.4	1.6	2.1	2.6	3.2	3.5	3.8	4.1	4.5
1985	15.7	2.8	4.7	5.7	7.2	9.1	11.3	12.1	13.3	14.4	15.7
1986	1.9	0.3	0.6	0.7	0.9	1.1	1.4	1.5	1.6	1.7	1.9
1987	4.3	0.8	1.3	1.5	2.0	2.5	3.1	3.3	3.7	4.0	4.3
1988	10.3	1.9	3.1	3.7	4.7	6.0	7.4	7.9	8.8	9.5	10.3
1989	1.2	0.2	0.4	0.4	0.6	0.7	0.9	0.9	1.0	1.1	1.2
1990	44.6	8.0	13.4	16.1	20.5	25.9	32.1	34.3	37.9	41.0	44.6
2000	5.2	0.9	1.6	1.9	2.4	3.0	3.7	4.0	4.4	4.8	5.2
2001	10.0	1.8	3.0	3.6	4.6	5.8	7.2	7.7	8.5	9.2	10.0
2002	2.1	0.4	0.6	0.8	1.0	1.2	1.5	1.6	1.8	1.9	2.1
2003	2.0	0.4	0.6	0.7	0.9	1.2	1.4	1.5	1.7	1.8	2.0
2004	0.7	0.1	0.2	0.3	0.3	0.4	0.5	0.5	0.6	0.6	0.7
2005	2.6	0.5	0.8	0.9	1.2	1.5	1.9	2.0	2.2	2.4	2.6
2006	3.6	0.6	1.1	1.3	1.7	2.1	2.6	2.8	3.1	3.3	3.6
2007	1.7	0.3	0.5	0.6	0.8	1.0	1.2	1.3	1.4	1.6	1.7
2008	2.4	0.4	0.7	0.9	1.1	1.4	1.7	1.8	2.0	2.2	2.4
2009	16.4	3.0	4.9	5.9	7.5	9.5	11.8	12.6	13.9	15.1	16.4
2010	6.6	1.2	2.0	2.4	3.0	3.8	4.8	5.1	5.6	6.1	6.6
2011	0.5	0.1	0.2	0.2	0.2	0.3	0.4	0.4	0.4	0.5	0.5
2012	2.2	0.4	0.7	0.8	1.0	1.3	1.6	1.7	1.9	2.0	2.2
2013	5.8	1.0	1.7	2.1	2.7	3.4	4.2	4.5	4.9	5.3	5.8
2014	5.6	1.0	1.7	2.0	2.6	3.2	4.0	4.3	4.8	5.2	5.6
2015	6.7	1.2	2.0	2.4	3.1	3.9	4.8	5.2	5.7	6.2	6.7
2016	3.0	0.5	0.9	1.1	1.4	1.7	2.2	2.3	2.6	2.8	3.0
2017	0.9	0.2	0.3	0.3	0.4	0.5	0.6	0.7	0.8	0.8	0.9
2018	3.2	0.6	1.0	1.2	1.5	1.9	2.3	2.5	2.7	2.9	3.2
2019	17.8	3.2	5.3	6.4	8.2	10.3	12.8	13.7	15.1	16.4	17.8
2020	5.3	1.0	1.6	1.9	2.4	3.1	3.8	4.1	4.5	4.9	5.3
2021	17.0	3.1	5.1	6.1	7.8	9.9	12.2	13.1	14.5	15.6	17.0

Table 5. Frequency results of rainfall depth (mm) at El-Hasana station.

Return Period (year)	Duration (min)									
	5	10	20	30	60	120	360	720	1080	1440
2	1.4	2.3	2.8	3.5	4.5	5.5	5.9	6.5	7.1	7.7
5	2.6	4.4	5.3	6.7	8.5	10.5	11.2	12.4	13.4	14.6
10	3.5	5.8	7.0	8.9	11.3	14.0	14.9	16.5	17.8	19.4
20	4.3	7.2	8.7	11.1	14.0	17.4	18.6	20.5	22.2	24.1
25	4.6	7.7	9.2	11.8	14.8	18.4	19.7	21.8	23.5	25.6
50	5.4	9.1	10.9	13.9	17.5	21.8	23.3	25.7	27.8	30.2
100	6.3	10.5	12.5	16.0	20.2	25.1	26.8	29.6	32.0	34.8
200	7.1	11.8	14.2	18.1	22.9	28.4	30.4	33.5	36.3	39.4

The probability distributions were analyzed to identify the distribution that best fits the annual rainfall data series. For all 54 stations, the gamma distribution provided the best fit. The gamma distribution was selected based on its statistically validated superiority over other distributions, its adaptability to regional

variations, and its consistent performance across all stations. These considerations ensure that the chosen model provides accurate and reliable rainfall estimates for engineering and hydrological applications across Egypt. Consequently, this distribution was used to estimate rainfall values for durations ranging from 5 minutes to 1440 minutes (24 hours) and for return periods of 2, 10, 25, 50, 100, and 200 years. They provide a robust framework for addressing both current and future challenges posed by rainfall variability and climate change, ensuring that hydraulic structures and urban systems are resilient and sustainable. Table 5 illustrates the results of the frequency analysis for the El-Hasana station as an example. Similar analyses were conducted for the rainfall series from the remaining stations, ensuring a comprehensive understanding of rainfall patterns across Egypt.

### 3.4. IDF curves

The rainfall depths obtained from the frequency analysis were used to calculate rainfall intensity for various return periods (2, 5, 10, 20, 25, 50, 100, and 200 years) and durations ranging from 10 minutes to 1440 minutes (Table 4). Rainfall IDF curves, which illustrate the relationship between rainfall intensity, duration, and frequency, were developed for specific rainfall stations. The curves were derived directly from the frequency analysis results without additional adjustments. A total of seven sets of IDF curves were constructed for selected locations. Figure 3 shows the IDF curves for the Saint Katherine station as an example. Importantly, although the IDF curve formulation is consistent across the analyzed stations, the specific intensity values vary significantly due to spatial variation in rainfall depths.

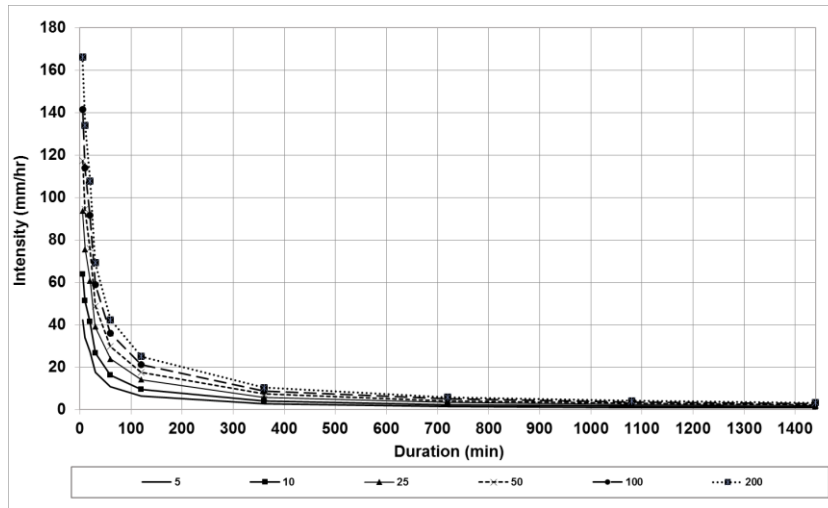


Fig. 3. Maximum rainfall intensities for different time intervals and return periods at Saint Katherine station.

Significant spatial variations in rainfall intensities were observed across Egypt's diverse climatic zones. These curves are essential tools for hydrological and hydraulic design, providing critical insights into the expected rainfall intensities over various durations and frequencies for engineering and water resource planning purposes. Previous IDF curves for Egypt, such as those developed for the Sinai Peninsula (Fathy et al. 2014), were based on limited datasets and did not account for recent climate trends. The IDF curves developed in this study incorporate updated rainfall data through 2024 and are based on advanced statistical techniques,

making them more accurate and reflective of current climatic conditions. These new IDF curves generally show higher rainfall intensities, particularly for shorter durations and higher return periods, compared to the older curves for the Sinai Peninsula, likely reflecting the impact of more recent and extensive data.

### **3.5. Isopluvial maps**

Various short durations, up to 24 hours and return periods up to 200 years, were used to create isopluvial maps. These maps were generated using the Spatial Analyst tool of Arc-GIS. A raster surface is interpolated from points using the spatial analyst's inverse distance-weighted (IDW) approach. The IDW interpolation method is straightforward and easy to implement. It is based on the principle that objects adjacent to one another are more similar than those farther apart. Also, it assigns weights to sample points, such that the influence of one point on another declines with distance from the new point being estimated. A review of comparative studies of more than 70 spatial interpolation methods for 53 comparative studies in environmental sciences concluded that IDW, ordinary kriging (OK), and ordinary co-kriging (OCK) are the most frequently used methods (Muhammad 2016).

Isopluvial maps were developed for short durations of 5, 10, 15, 30, 60, 120, 360, 720, 1080, and 1440 minutes for various return periods; 2, 5, 10, 20, 25, 50, 100, and 200 years. These maps were generated using the IDW interpolation method. The accuracy of the IDW-generated maps was evaluated using rainfall data from independent stations not included in the interpolation process. Cross-validation techniques were applied by withholding data from specific stations, interpolating rainfall values for those locations, and comparing the interpolated results with the observed rainfall data. Further, the results were qualitatively validated by comparing the interpolated maps with observed rainfall patterns at selected stations, ensuring alignment with real-world observations. While IDW is straightforward and effective for evenly distributed data, it may over-smooth rainfall estimates in areas with sparse or unevenly distributed stations, such as Egypt's desert regions. This sensitivity to station density highlights a potential limitation of IDW in capturing local extreme rainfall events, particularly in regions with complex terrain. However, these evaluations confirmed that the IDW method provided reliable estimates of rainfall intensity across Egypt. The resulting maps were demonstrated both with and without filling the contour, as illustrated in Figures 3 through 6. The spatial resolution of the generated maps is  $1 \times 1$  km, ensuring sufficient detail to capture local variations in rainfall intensity. This resolution aligns with standard practices for hydrological applications and ensures that the maps are suitable for engineering design and water resource management.

These maps highlight spatial variations in rainfall intensity across Egypt, offering essential tools for infrastructure planning. Figures 4-7 illustrate sample maps, which are valuable for identifying high-risk areas and optimizing the design of flood protection measures and hydraulic systems. These maps can be integrated into current engineering practices by providing precise rainfall intensity estimates at specific locations, aiding in the calibration of hydrological models and the design of drainage infrastructure tailored to local conditions.



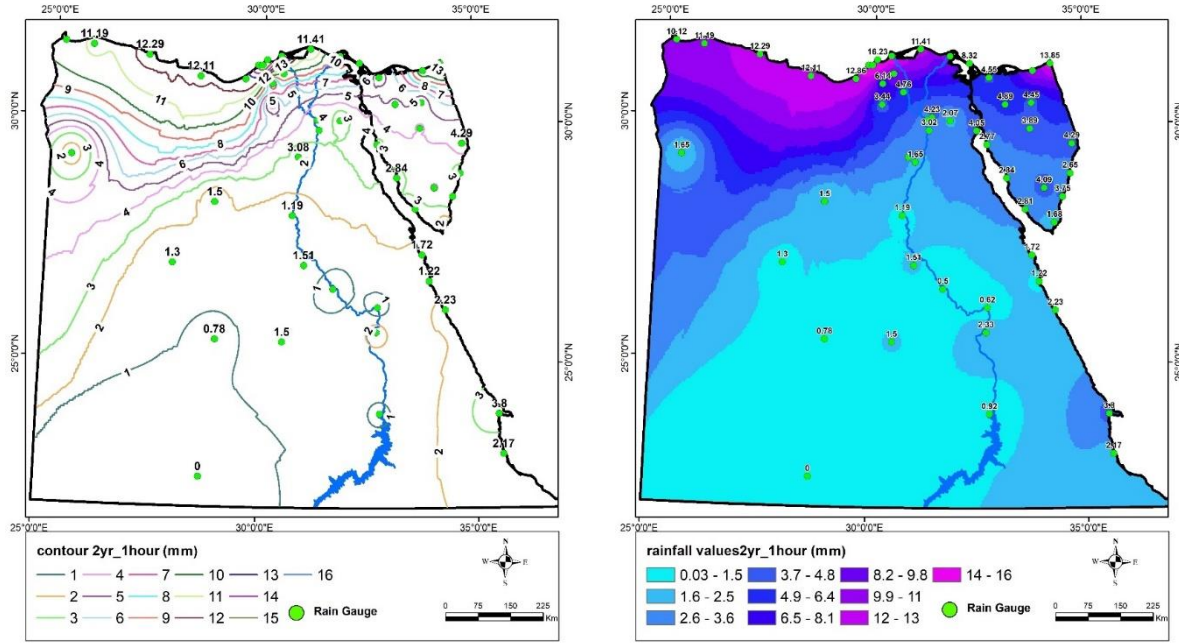


Fig. 4. 1-hour isopluvial maps for a 2-year return period.

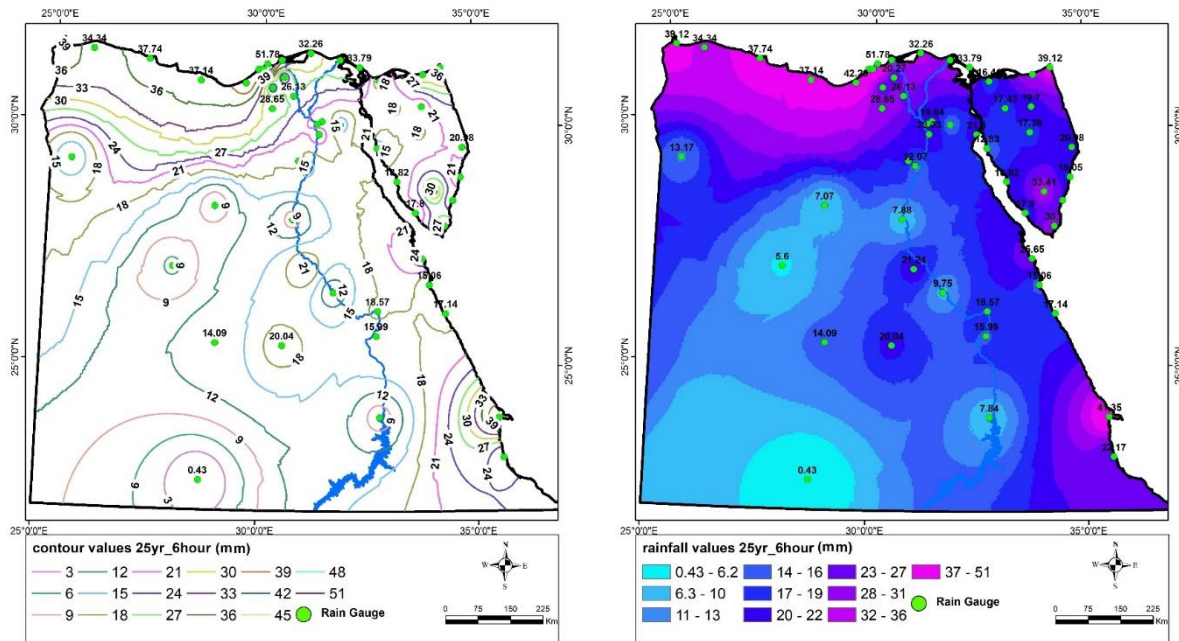


Fig. 5. 6-hour isopluvial maps for a 25-year return period.

For instance, urban planners can use these maps to design stormwater management systems capable of withstanding extreme weather events. To quantify the uncertainty associated with the isopluvial maps, confidence intervals were calculated for the interpolated rainfall values at a 95% confidence level, providing a range within which true values are expected to fall with a specified level of confidence. These intervals ensure the reliability of the maps for practical applications. Sensitivity analyses were performed by comparing the IDW interpolation method with alternative techniques, such as kriging and spline interpolation. The results demonstrated that IDW outperformed the other methods in accurately capturing spatial rainfall patterns for this dataset. However, the analyses also highlighted the importance of

considering alternative methods in future studies, particularly for regions with complex terrain or limited station coverage.

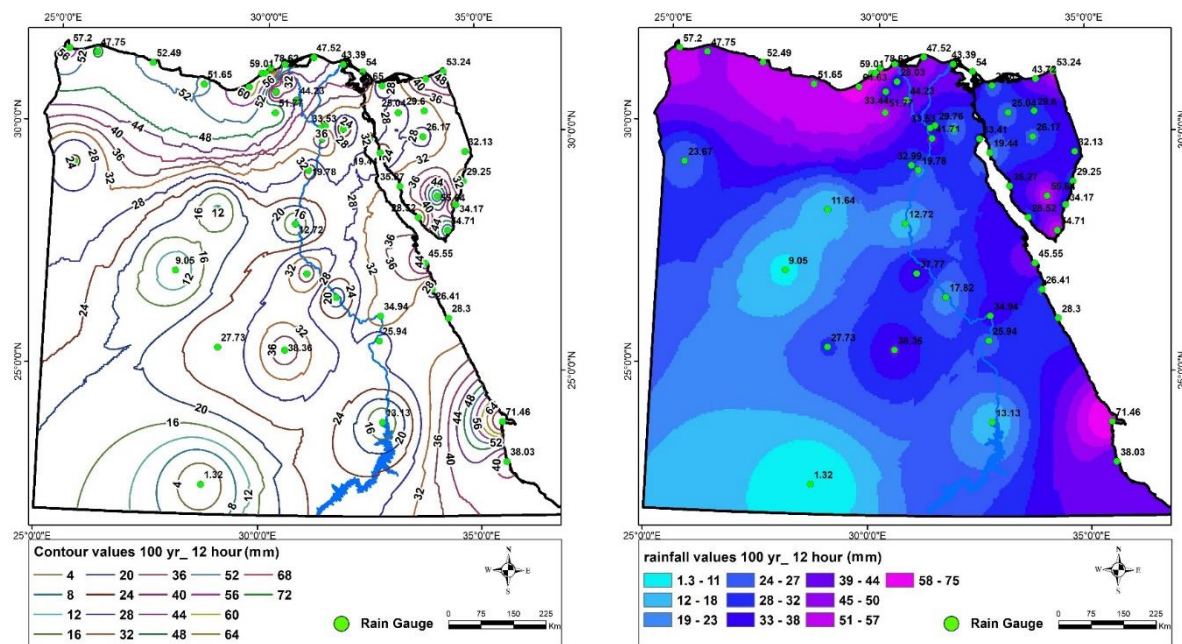


Fig. 6. 12-hour isopluvial maps for a 100-year return period.

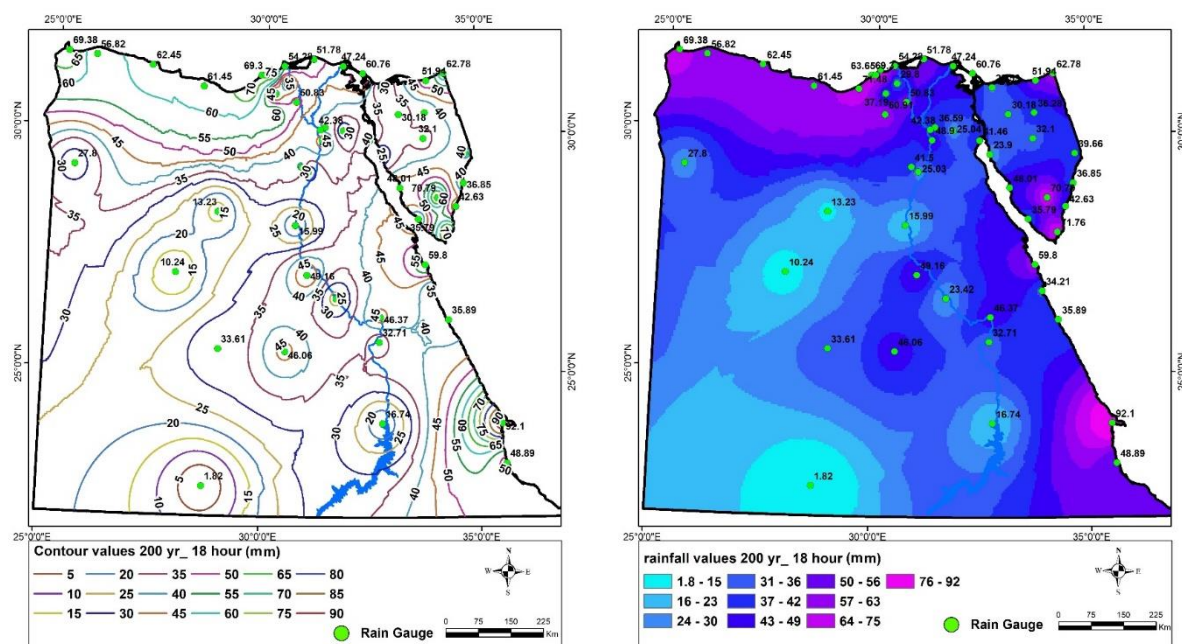


Fig. 7. 18-hour isopluvial maps for a 200-year return period.

### 3.6. Climate change implications

The analysis conducted in this study revealed an increasing frequency of extreme rainfall events, consistent with global trends associated with climate change. These findings align with observations from previous studies that have documented shifts in rainfall patterns driven by rising global temperatures and changing atmospheric dynamics (Zittis et al. 2022). Specifically, the results indicate a notable increase in the

intensity and variability of short-duration rainfall events across various regions of Egypt, particularly in coastal and mountainous areas (Nashwan et al. 2019; Roushdi 2022).

To quantify these changes, recent rainfall data (2000-2024) were compared with historical records (1968-2000). The analysis shows a statistically significant upward trend in extreme rainfall intensities, with an average increase of 15-20% in maximum daily rainfall depths across the studied regions. The statistical significance of these trends was confirmed using the Mann-Kendall test, yielding p-values less than 0.05 for most of the stations analyzed. These observed trends are supported by regional climate models, such as the Coordinated Regional Climate Downscaling Experiment (CORDEX) for Africa. Specifically, CORDEX projections under RCP4.5 and RCP8.5 scenarios indicate a 10-30% increase in extreme rainfall intensities by the end of the century, particularly in coastal and western regions of Egypt. These results highlight the need to revise existing design standards for hydraulic structures and adopt proactive strategies to address evolving climatic conditions. Incorporating satellite-based observations could further enhance adaptability by enabling real-time monitoring and extending coverage to remote areas.

Furthermore, the spatial distribution of rainfall estimates in this study aligns with the high-resolution climatic zonation of Egypt developed by Hamed et al. (2022), which provides a reliable benchmark for validating the isopluvial maps. Comparing the interpolated rainfall depths with the observed data analyzed by Nashwan et al. (2019) further validates the accuracy of the IDW-generated maps. This study highlights the critical importance of continuous data updates and adaptive planning to enhance resilience against evolving climate challenges (Kourtis, Tsihrintzis 2022).

#### **4. Conclusions and recommendations**

This research introduces a comprehensive framework for rainfall estimation and infrastructure planning in Egypt. The analysis highlights an increasing frequency of heavy rainfall events and noticeable shifts in rainfall patterns, largely driven by climate change. This emphasizes the need to reassess the safety of existing hydraulic structures and incorporate updated rainfall analyses into the design of new structures. The methodologies outlined in this study provide practical guidelines for developing temporal and spatial distributions of rainfall, significantly contributing to improved water resource management and infrastructure planning.

The findings reveal that certain regions in Egypt are particularly vulnerable to these changes. Coastal areas, such as the northern coast, and mountainous regions, like Saint Katherine, are experiencing statistically significant increases in short-duration rainfall intensity and variability. These regions, along with arid zones like the Red Sea coast, face heightened risks of flash floods and severe water runoff events, threatening critical infrastructure such as urban drainage systems, roads, bridges, and flood protection measures. Ungauged locations lacking sufficient monitoring infrastructure are particularly vulnerable, as they rely heavily on accurate rainfall estimates for effective planning and design.

The proposed empirical formula, based on recent and extensive rainfall data, is more accurate than previously used reduction ratios. This improvement in accuracy is attributed to the incorporation of

updated records from 54 stations across Egypt, capturing a broader range of climatic variability and recent trends influenced by climate change. The formula facilitates precise runoff and discharge estimations, which are essential for designing hydraulic structures and supporting flood forecasting, particularly in ungauged locations. The alignment between the calculated GWRRI ratios and the WRRI ratios highlights the reliability of the new formula. For instance, at durations exceeding 120 minutes, the GWRRI formula provides more conservative and realistic estimates than the WRRI ratios, reducing overestimation or underestimation of rainfall depths. These refinements ensure that the new formula better reflects current climatic conditions and variability across Egypt. The formula was also tested against observed rainfall data from independent stations, confirming its reliability and robustness. This quantitative validation underscores its superiority over older methods, making it a practical tool for hydrological analysis and infrastructure design. These results facilitate precise runoff and discharge estimations, which are essential for designing hydraulic structures. They also provide critical meteorological support insights for flood forecasting, especially in ungauged areas. Furthermore, this research serves as a valuable resource for decision-makers, designers, engineers, and planners involved in water resource management and infrastructure development, offering actionable insights to address evolving climatic challenges.

The key contributions of the study include:

- Development of a validated empirical formula for estimating short-duration rainfall depths, offering a practical tool for hydrological analysis.
- Creation of isopluvial maps for critical durations and return periods, supporting infrastructure design and planning.
- Identification of climate-driven changes in rainfall patterns, including a statistically significant increase in short-duration rainfall intensity and variability, particularly in coastal and mountainous regions.

Despite these advancements, certain limitations must be acknowledged. The dataset is constrained by the availability and quality of rainfall records, particularly in remote and ungauged areas. Moreover, the empirical formula and isopluvial maps are based on historical data and may not fully capture future changes in rainfall patterns due to climate change. Uncertainties in interpolation methods, such as IDW, and the assumption of stationarity in frequency analysis also introduce potential biases.

Based on these findings, it is recommended that decision-makers prioritize the updating of design storm standards for urban drainage and small-scale hydraulic structures, particularly in coastal and mountainous areas identified as high-risk. Engineers should use the developed empirical formula for more accurate short-duration rainfall estimation in ungauged basins. Furthermore, investment in expanding the ground-based monitoring network and integrating satellite rainfall data is crucial for improving real-time monitoring and future climate change impact assessments.

## References

Al-Aboodi A.H., Hassan A.A., Ibrahim H.T., 2019, Rainfall intensity probability for design of drainage system in Basrah City, south of Iraq, *ARPJ Journal of Engineering and Applied Sciences*, 14 (5), 954-961.



- Al-Amri N.S., Subyani A.M., 2017, Generation of rainfall Intensity Duration Frequency (IDF) curves for ungauged sites in Arid Region, *Earth Systems and Environment*, 1, DOI: 10.1007/s41748-017-0008-8.
- AlHassoun S.A., 2011, Developing an empirical formulae to estimate rainfall intensity in Riyadh region, *Journal of King Saud University – Engineering Sciences*, 23 (2), 81-88, DOI: 10.1016/j.jksues.2011.03.003.
- Almheiri K.B., Rustum R., Wright G., Adeloye A.J., 2024, The necessity of updating IDF curves for the Sharjah Emirate, UAE: A comparative analysis of 2020 IDF values in light of recent urban flooding, *Water*, 16 (18), DOI: 10.3390/w16182621.
- Awadallah A.G., Younan N.S., 2012, Conservative design rainfall distribution for application in arid regions with sparse data, *Journal of Arid Environments*, 79, 6675, DOI: 10.1016/j.jaridenv.2011.11.032.
- Bonnin G.M., Martin D., Lin B., Parzybok T., Yekta M., Riley D., 2011, Precipitation-frequency atlas of the United States, NOAA Atlas 14, Volume 1, Version 5.0, available online at [https://hdsc.nws.noaa.gov/hdsc/pfds/pfds\\_map\\_cont.html](https://hdsc.nws.noaa.gov/hdsc/pfds/pfds_map_cont.html) (09.06.2025).
- Carvalho R. de C.F., Moreira T.R., de Souza K.B., Costa G.A., Zanetti S.S., Barbarosa K.V., Filho C.B.C., Miranda M.R., Filho P.A.G., dos Santos A.R., Ramalho A.H.C., Ferreira E.S.A., Araujo E.F., das Neves F.P., de Lima J.F.V., Moreau J.S., Belan L.L., Aguiar M.O., Gorsani R.G., da Silva Gandine S.M., dos Santos A.R., 2022, GIS-based Approach applied to study of seasonal rainfall influence over flood vulnerability, *Water* 14 (22), DOI: 10.3390/w14223731.
- Das A.K., Srivastava P., Yadav B.P., 2022, Isopluvial analysis and Intensity Duration Frequency (IDF) curves for different cities in India, *Mausam*, 73 (4), 887-898, DOI: 10.54302/mausam.v73i4.3530.
- Division of Hydrometeorology, 2007, Atlas of Statewise Generalised Isopluvial (Return Period) Maps of the Southern Peninsula (part-1), Office of the Director General of Meteorology, India Meteorological Department.
- El Adlouni S., Bobée B., 2015, Hydrological Frequency Analysis using HYFRAN-PLUS Software (Version-V2.1), available online at <https://wrpllc.com/books/HyfranPlus/hyfranplusdescrip.html> (data access 09.06.2025).
- El-Sayed E.A.H., 2011, Generation of rainfall Intensity Duration Frequency curves for ungauged sites, *Nile Basin Water Science and Engineering Journal*, 4 (1), 112-124.
- El-Sayed E.A.H., 2017, Development of empirical formula to estimate short duration rainfall, *Nile Water Sciences and Engineering Journal*, 10 (1), 20-28.
- Ewea H.A., Elfeki A.M., Al-Amri N.S., 2017, Development of intensity-duration-frequency curves for the Kingdom of Saudi Arabia, *Geomatics, Natural Hazards and Risk*, 8 (2), 570-584, DOI: 10.1080/19475705.2016.1250113.
- Fathy I., Negm A.M., El-Fiky M., Nassar M., 2014, Intensity Duration Frequency curves for Sinai Peninsula, Egypt, *IMPACT: International Journal of Research in Engineering and Technology*, 2 (6), 105-112.
- Gado T.A., Shalaby B.A., Guo Y., Rashwan I.M.H., 2023, Assessment of satellite-based precipitation estimates over Egypt, *Journal of Hydrologic Engineering*, 29 (1), DOI: 10.1061/JHYEFF.HEENG-6051.
- Ghenim A.N., Megnounif A., 2016, Variability and trend of annual maximum daily rainfall in Northern Algeria, *International Journal of Geophysics*, 2016 (1), DOI: 10.1155/2016/6820397.
- Hamed K., Rao A.R. (eds.), 2019, *Flood Frequency Analysis*, CRC Press, 376 pp., DOI: 10.1201/9780429128813.
- Hamed M.M., Nashwan M.S., Shahid S., 2022, Climatic zonation of Egypt based on high-resolution dataset using image clustering technique, *Progress in Earth Planetary Science*, 35, DOI: 10.1186/s40645-022-00494-3.
- Jalee L.A., Farawn M.A., 2013, Developing rainfall Intensity-Duration-Frequency relationship for Basrah City, 5 (1), 105-112, DOI: 10.30572/2018/KJE/511235.
- Kawara A.Q., Elsebaie I.H., 2022, Development of rainfall intensity, duration and frequency relationship on a daily and sub-daily basis (Case Study: Yalamlam Area, Saudi Arabia), *Water*, 14 (6), DOI: 10.3390/w14060897.
- Kourtis I.M., Tsihrantzis V.A., 2022, Update of intensity-duration-frequency (IDF) curves under climate change: a review, *Water Supply*, 22 (5), 4951-4974, DOI: 10.2166/ws.2022.152.
- Matos J.E., 2018, Generic method for merging satellite and historical ground station data to design rainfall Intensity Duration Frequency (IDF) curves in recordless sub-saharian countries, *Open Journal of Modern Hydrology*, 8 (4), DOI: 10.4236/ojmh.2018.84008.
- Muhammad A., 2016, An evaluation of spatial interpolation methods for estimating rainfall and air temperature in Egypt, *The Arabian Journal of Geographical Information Systems*, 9 (2) 1-51.

- Nashwan M.S., Shahid S., Wang X., 2019, Assessment of satellite-based precipitation measurement products over the hot desert climate of Egypt, *Remote Sensing*, 11 (5), DOI: 10.3390/rs11050555.
- Parvez M.B., Thankachan A., Inayathulla M., 2019, Isopluvial maps of daily maximum precipitation for different frequency for upper cauvery Karnataka, *Praxis Science and Technology Journal*, 8 (10), 20-38, 2019.
- Rana V.K., Linh N.T.T., Ditthakit P., Elkhachy I., Nguyen T.T., Nguyen N.-M., 2023, Mapping and analysing framework for extreme precipitation – induced flooding, *Earth Science Informatics*, 16, 4213-4234, DOI: 10.1007/s12145-023-01137-x.
- Rasel M., Islam M., 2015, Generation of rainfall Intensity-Duration-Frequency relationship for North-Western region in Bangladesh, *IOSR Journal of Environmental Science, Toxicology and Food Technology*, 9 (9), 41-47, DOI: 10.9790/2402-09914147.
- Roushdi M., 2022, Spatio-temporal assessment of satellite estimates and gauge-based rainfall products in northern part of Egypt, *Climate*, 10 (9), DOI: 10.3390/cli10090134.
- Schroeder J.F., 2013, Surface representations of rainfall at small extents: A study of rainfall mapping based on volunteered geographic information in Kona, Hawaii, A Thesis presented to the Faculty of the USC Graduate School University of Southern California.
- Şen Z., 2-19, Annual daily maximum rainfall-based IDF curve derivation methodology, *Earth Systems and Environment*, 3 (3), 463-469, DOI: 10.1007/s41748-019-00124-x.
- Shamkhi M.S., Azeez M.K., Obeid Z.H., 2022, Deriving rainfall intensity-duration-frequency (IDF) curves and testing the best distribution using EasyFit software 5.5 for Kut city, Iraq, *Open Engineering*, 12 (1), 834-843.
- Subyani A.M., Al-Amri N.S., 2015, IDF curves and daily rainfall generation for Al-Madinah city, western Saudi Arabia, *Arabian Journal of Geosciences*, 8 (12), 11107-11119, DOI: 10.1007/s12517-015-1999-9.
- The Rainfall Atlas of Hawai'i, 2011, Geography Department – University of Hawai'i at Mānoa, available online at <https://www.hawaii.edu/climate-data-portal/hawaii-climate-atlases/> (data access 09.06.2025).
- Trypaluk C., Unruh D., St. Laurent M., Jordan A., Mantripragada R.S.S., Pavlovic S., Fall G., Salas F., 2024, Precipitation-Frequency Atlas of the United States, Volume 12 Version 2.0: Interior Northwest Idaho, Montana, Wyoming.
- Zittis G., Almazroui M., Alpert P., Ciais P., Cramer W., Dahdal Y., Fnais M., Francis D., Hadjinicolaou P., Howari F., Jrrar A., Kaskaoutis D.G., Kulmala M., Lazoglou G., Mihalopoulos N., Lin X., Rudich Y., Sciare J., Stenchikov G., Xoplaki E., Lelieveld J., 2022, Climate change and weather extremes in the Eastern Mediterranean and Middle East, *Reviews of Geophysics*, 60 (3), DOI: 10.1029/2021RG000762.

# Hydrological modeling with SWAT: A case study of Shahpur catchment

Muhammad Husnain Shabir<sup>ID</sup>, Abdul Shakoor

Abasyn University Islamabad, Pakistan

Imran Hafeez<sup>ID</sup>

NUST, Pakistan

## Abstract

In this study, the hydrology of Shahpur catchment is modeled to calculate the hydrological discharge of Shahpur Dam and to establish the water balance component using the Soil and Water Assessment Tool (SWAT). Shahpur catchment is located on the Nandana River basin in Pakistan, about 45 km from Islamabad and 8 km north of Fateh Jang. The Arc SWAT 2012 version 10.5.24, which was created for Arc Map 10.5, was used to delineate the study area and its sub-components, combine the data layers, and edit the model database and SWAT CUP SUFI2 algorithm for calibration and validation. Calibration from 2000-2004 and validation from 2006-2010 employed historic daily flow data and climatic data collected from the Shahpur Dam site office and Pakistan Meteorological Department (PMD) Islamabad. Based on literature reviews, 11 parameters with stronger influence on runoff were chosen. Nash-Sutcliffe efficiency (NSE), percent bias (PBIAS), and root-mean-square/standard deviation ratio (RSR) were used as statistical indicators. Results indicated satisfactory agreement between measured and simulated discharge values at yearly and monthly scales, demonstrating robust performance during both calibration ( $R^2 = 0.95$ ) and validation ( $R^2 = 0.82$ ) periods. The findings support the applicability of the model for effective watershed management in Shahpur based on favorable indicators and comparative outcomes.

## Keywords

Hydrological Modeling, Shahpur Dam, Watershed Management, SWAT Model, SWAT CUP SUFI2.

Submitted 14 April 2025, revised 18 June 2025, accepted 12 July 2025

DOI: 10.26491/mhwm/208181

## 1. Introduction

Water is a key aspect for economic development, including agricultural and industrial expansion, particularly in the context of rapidly growing population and urbanization. Under changing land use and climate, sustainable water resource management and optimal allocation of water resources across multiple water uses are key difficulties that many civilizations are either facing or will confront in the next decades (Stehr et al. 2008). To address water management challenges, we must investigate and evaluate the many aspects of hydrologic processes occurring within the study area. Because all of these activities occur within separate micro-watersheds, the studies must be done on a watershed basis. For understanding the complicated hydrological response of a watershed and its direct relationship to climate, geography, geology, and land use, advanced mathematical models have been constructed. Water flows not just over the surface of land, but also underneath it in the unsaturated zone and even deeper in the saturated zone (Singh, Woolhiser 2002). Simulating these processes through a watershed model is essential for addressing a variety of water resource, environmental, and social issues. SWAT model predictions have been deemed computationally efficient by researchers (Neitsch et al. 2005). The tool has shown dependability in numerous regions throughout the world. Khan et al. (2014) used the SWAT model on a large scale to

examine hydrological processes in a mountainous environment of the Upper Indus River Basin, as well as in other Asian locations (Supit, Ohgushi 2012; Nasrin et al. 2013).

Beroho et al. (2025) investigated the 9th April watershed in northern Morocco, a semi-arid region with limited hydrometeorological data. They integrated SWAT with projected land use-land cover (LULC) and climate scenarios to model future hydrological responses and sediment transport. Fadil et al. (2011) employed it in several African locations. Schuol et al. (2008) and Ashagre (2009) also used it in simulations. Kamuju (2019) studied the St. Joseph River watershed in the United States. SWAT is a GIS-based watershed- or river basin-scale model that can represent both geographic diversity and physical processes within smaller modeling units known as hydrologic response units (HRUs) for the long-term planning and management of river surface water resources. Its predictions have been declared computationally effective by researchers (Neitsch et al. 2009). It has been proven to be reliable in a majority of places globally.

## **2. Materials and methods**

### **2.1. Study area**

We selected the Shahpur Dam as a study site to perform hydrological modeling by using SWAT and GIS analysis. The dam site is located at 33°37'0", 73°41'0"E in Fateh Jang Tehsil near the Kala Chitta Range in the Attock District, about 45 km from Islamabad and 8 km north of Fateh Jang, as shown in Figure 1. The dam was commissioned by the Small Dams Organization, Government of Punjab, in 1982 and was completed in 1986 at a cost of PKR 36.5 million. The main dam is a concrete gravity type with 0.6 m thick stone masonry skin and a centrally located spillway. There is an ungated ogee spillway in the middle of the dam for passing flood discharges. The capacity of the spillway is 1008 m<sup>3</sup>/s. This discharge is based on 230 mm rainfall, which is the maximum probable in 24 hours with a 1000-year return period. The width of the spillway is 85 m, which could easily handle a discharge of 460 m<sup>3</sup>/sec with a head of 3 m above the crest. A flip-type stilling basin was installed to dissipate the energy of falling water from the spillway. The reservoir of Shahpur Dam has a gross storage capacity of 14,320 acre-feet (17.7×10<sup>6</sup>m<sup>3</sup>), of which 4,079 acre-feet (5.0×10<sup>6</sup>m<sup>3</sup>) is dead storage capacity and the rest is live usable storage (Cheema, Bandaragoda 1997; Ghumman et al. 2019).

### **2.2. Creation of database**

#### **2.2.1. Time-based datasets**

SWAT requires climate data to supply moisture and energy inputs that govern the water balance and establish the key results of the various components of the hydrological cycle. Hydrological modeling requires long-term meteorological datasets of precipitation, temperature, wind speed, solar radiation, and relative humidity. The minimal essential inputs for the SWAT model are precipitation and temperature, whereas the remaining factors are optional. The model's weather-generating feature allows it to create



data based on these inputs (Ghoraba 2015). Weather data (daily maximum and minimum temperature, relative humidity, and wind speed) of the study area is obtained from PMD Islamabad.

The Shahpur Dam site office, located in Fateh Jhang, provided daily precipitation data. Historic daily flow data were provided for the years 2000-2004 for calibration and 2006-2010 for flow simulation validation. The monthly inflow to Shahpur Dam was measured at a station located near the dam.

### 2.2.2. Spatial datasets

Topography, land use-land cover, and soil composition are spatial datasets that characterize every land system and are essential for the hydrological model (Arnold et al. 1998). The input element of the SWAT model involves components of the land system that consist of DEM, land use, and soil (Ghoraba 2015). The DEM is downloaded from the Earth Explorer of the United States Geological Survey (USGS). Then, using the extract-by-mask feature, the study region is isolated from the large DEM file shown in Figure 2. For delineation, an SRTM DEM with resolution  $30\text{ m} \times 30\text{ m}$  was used. The automatic watershed delineation feature was applied to define the watershed. Landsat 8 satellite imagery was used to create a land use map through supervised classification, employing ERDAS IMAGINE 2012, as shown in Figure 3 (Beroho et al. 2023). The water cycle is affected by changes in land use and vegetation; the impact depends on the species' morphology and plant cover density. Four main classes have been defined. The most important groups are urban (4.84%), water (2.71%), barren (57.63%), and agricultural land (34.82%). The original land use classes were replaced with SWAT classes and specified using a lookup table. These conversions are presented in Table 1. For this research, two types of soil shown in Table 1 were found in SWAT by using a soil map, which was downloaded from FAO maps. The study area was clipped by the clip feature in Arc GIS, also shown in Figure 4 (Malik et al. 2022).

Table 1. Conversion of LULC to SWAT classes and soil classification.

Sr. No.	LULC classes	Area [%]	Sr. No.	SWAT soil class	Description	Area [%]
1	Built Up	4.84	1	I-X-c-3512	Gelic Regosols	15.3489
2	Water	2.71	2	Rc40-2b-3843	Haplic Chernozems	84.6511
3	Barren	57.63				
4	Vegetation	34.82				

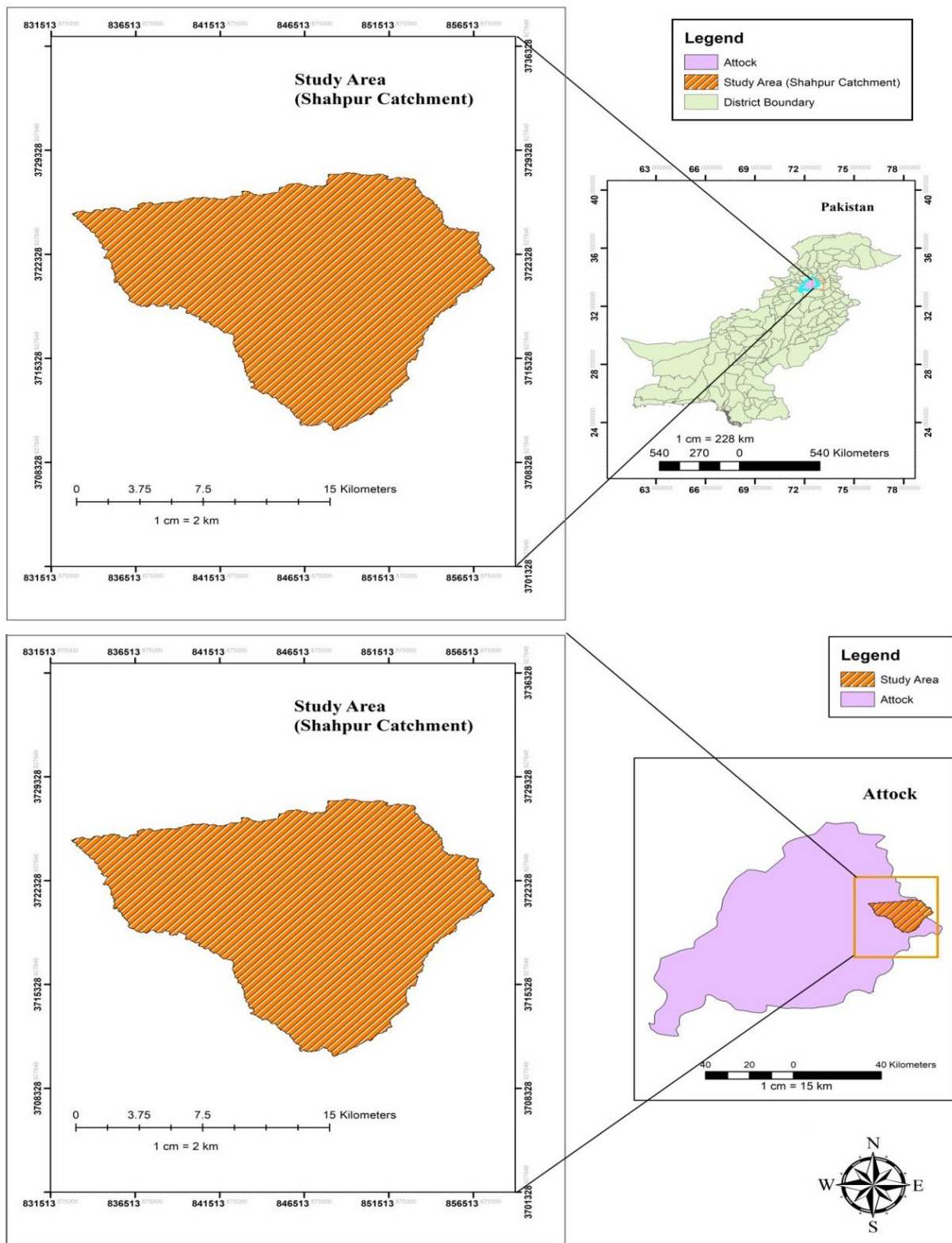


Fig. 1. Study area location on maps of Pakistan and the Attock District.

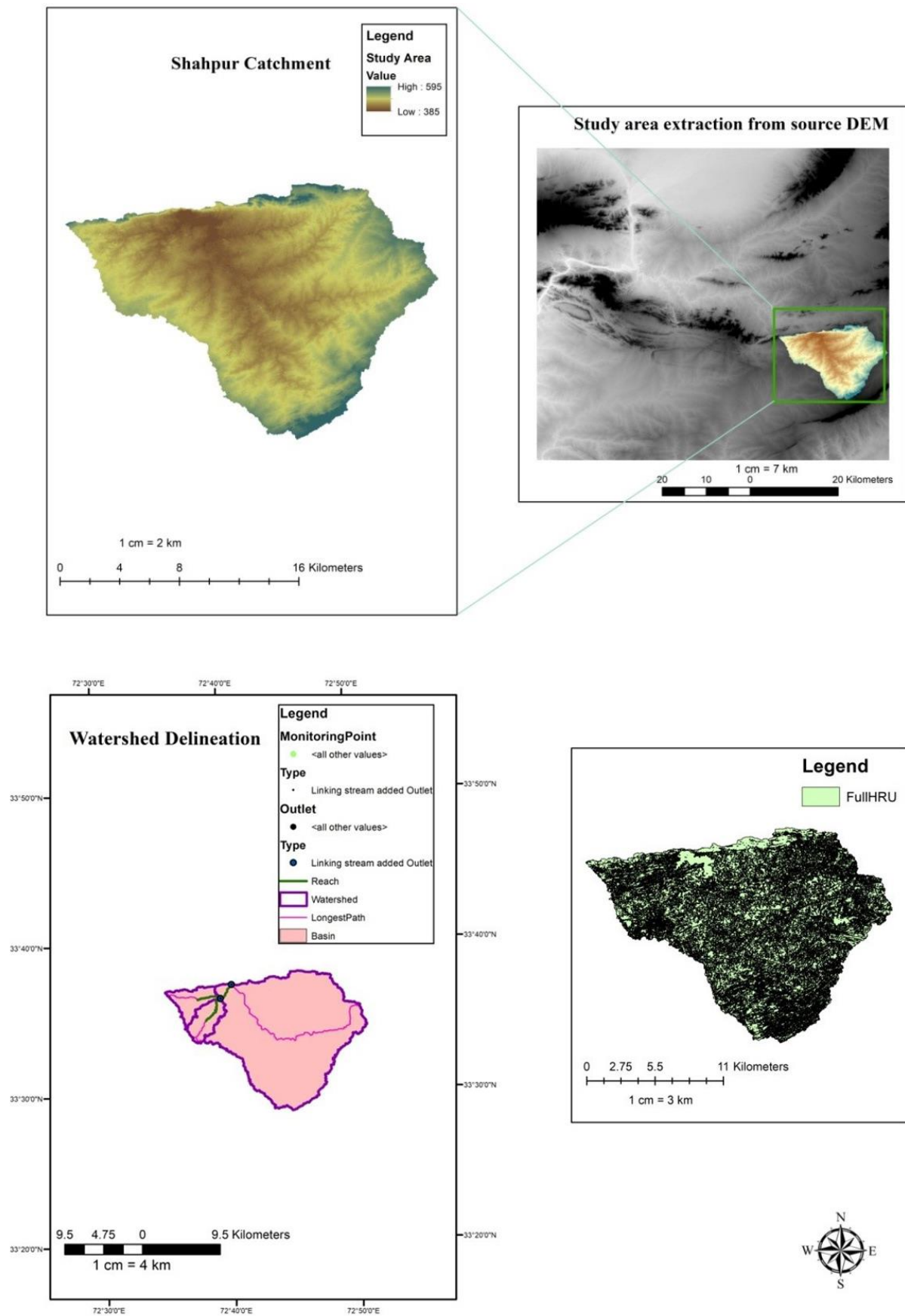


Fig. 2. Study area extraction and watershed delineation.

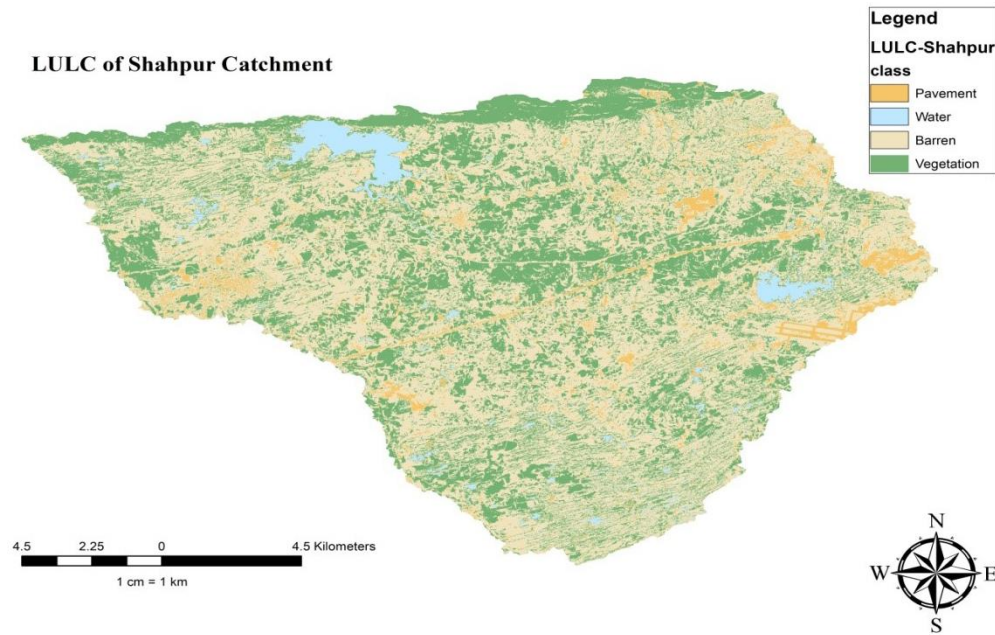


Fig. 3. Land use-land cover of Shahpur Catchment. LULC Mapping: LULC classes were mapped to SWAT land cover and soil classes using standard lookup tables, derived from FAO soil maps and Landsat 8 imagery, ensuring accurate representation of the catchment's spatial characteristics.

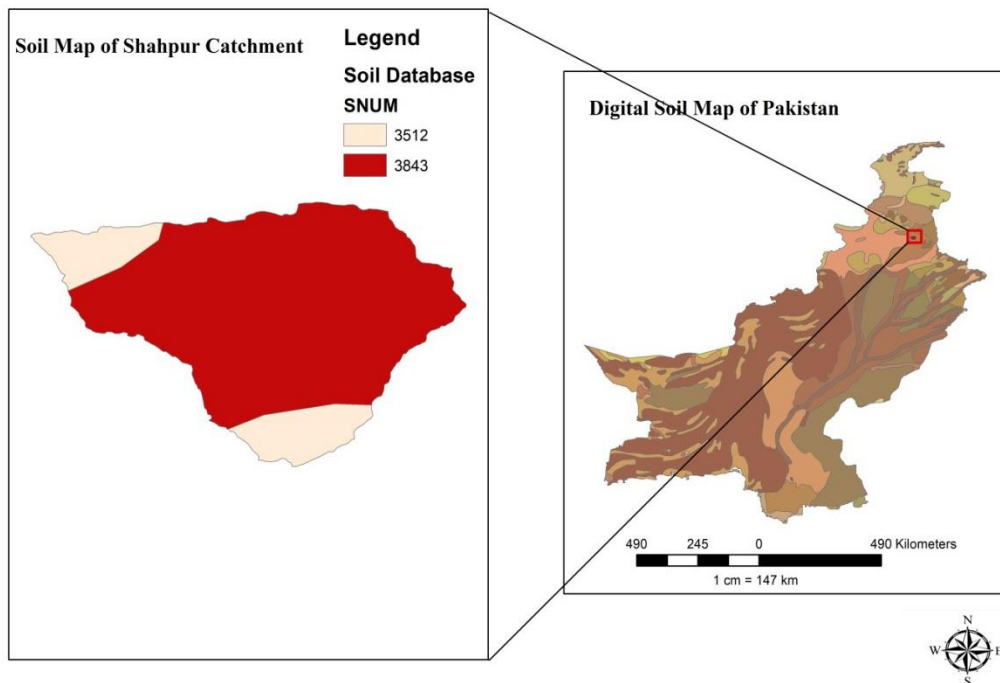


Fig. 4. Soil map of Shahpur Catchment. Mapping was performed using FAO soil maps and SWAT lookup tables.

### 2.3. Model simulation

The Shahpur Dam watershed hydrologic modeling was performed using Arc SWAT 2012 version 10.5.24, which was created for Arc Map 10.5. The model is ready for simulation once data files have been prepared, and all model inputs have been finalized. The simulation spans four years, from 2000 to 2004, which coincides with the availability of climatic data.



## 2.4. Model efficiency

Model calibration and validation are important steps in the simulation, applied to evaluate parameter estimation outcomes. There are several approaches for assessing and evaluating the model's efficiency. The coefficient of determination ( $R^2$ ), root-mean-square error ( $RMSE$ ), standard deviation ratio ( $RSR$ ), Nash–Sutcliffe efficiency index ( $NSE$ ), and percent bias ( $PBIAS$ ) were used for calibration and validation (Moriassi et al. 2007; Fadil et al. 2011).

### 2.4.1. Coefficient of determination ( $R^2$ )

By following a best fit line, it is an excellent approach to indicate the consistency between observed and simulated data. Higher values indicate less error variance, and values greater than 0.50 are regarded as acceptable. It ranges from zero to 1.0 (Santhi et al. 2001; Van Liew et al. 2007).

$$R^2 = \frac{[\sum_{i=1}^n (Q_{m,j} - \bar{Q}_m)(Q_{s,j} - \bar{Q}_s)]^2}{\sum_{i=1}^n (Q_{m,j} - \bar{Q}_m)^2 \sum_{i=1}^n (Q_{s,j} - \bar{Q}_s)^2} \quad (1)$$

Where  $Q_{s,j}$  is the discharge flow's simulated value,  $Q_{m,j}$  is the discharge flow's measured value, and  $Q_m$  is the mean of the measured discharge flow;  $n$  is the length of the measured discharge, and  $Q_s$  is the mean of the simulated discharge flow.

### 2.4.2. Nash–Sutcliffe efficiency ( $NSE$ )

$NSE$  is a normalized statistical approach for predicting the relative level of noise vs data.

$$NSE = 1 - \left[ \frac{\sum_{i=1}^n (Y_i^{obs} - Y_i^{sim})^2}{\sum_{i=1}^n (Y_i^{obs} - Y_i^{mean})^2} \right] \quad (2)$$

Where  $Y^{sim}_i$  is the  $i$ th simulation, and  $Y^{obs}_i$  is the  $i$ th observation (stream flow), the mean of the actual data,  $Y^{mean}_i$  is the simulated value, and  $n$  is the sum of all observations (Nash, Sutcliffe 1970).

### 2.4.3. Percent bias ( $PBIAS$ )

$PBIAS$  calculates the average tendency of simulated values to be greater or lower than observed values. The statistic ranges from  $-10$  to  $+10$ .  $PBIAS$  has an optimum value of 0.0, with low-magnitude values indicating accurate model simulation. Positive values indicate model underestimation bias, whereas negative values suggest model overestimation bias (Gupta et al. 1999).

$$PBIAS = \left[ \frac{\sum_{i=1}^n (Y_i^{obs} - Y_i^{sim}) \times 100}{\sum_{i=1}^n (Y_i^{obs})} \right] \quad (3)$$

#### 2.4.4. *RMSE-RSR*

An *RSR* range of 0 to 0.5 indicates good performance for both the calibration and validation periods. The lower the value of *RSR*, the smaller the *RMSE* as normalized by the standard deviation of the data, indicating the precision of the model simulation (Singh et al. 2005).

$$RSR = \frac{\sqrt{\sum_{i=1}^n (Y_i^{obs} - Y_i^{sim})^2}}{\sqrt{\sum_{i=1}^n (Y_i^{obs} - Y_i^{mean})^2}} \quad (4)$$

### 3. Results

#### 3.1. Parameter sensitivity analysis

After running the SWAT model, the model parameters must be calibrated and analyzed for sensitivity. Based on a literature review, 11 factors with stronger influence on runoff were chosen, supported by Arnold et al. (2012) and Abbaspour (2007). The (SUFI2) algorithm was used to determine the parameters in this project. To achieve the best match between the model's output and the observed flow data, the model is repeatedly simulated by adjusting the evapotranspiration calculation technique and the values of hydrological parameters that were selected by the model.

#### 3.2. Model calibration and validation results

The SWAT-CUP tool is one of the best tools for calibrating the SWAT model, and it is appropriate for assisting decision-makers in conceptualizing sustainable watershed management, allowing decision-makers to better calibrate the model (Mengistu et al. 2019). The simulated and actual surface runoff were compared for calibration. Only the fundamental scale and range of values generated by the model were verified using monitoring data. The exact value of calibrated hydrological parameters was utilized for validation after obtaining acceptable runoff data. Following that, the model's performance with calibrated parameters was evaluated to recreate the hydrological functioning of the watershed over a period that was not employed in the calibration phase. The observed flow data obtained from the Shahpur Dam site office, recorded at a gauging station downstream from the Shahpur Dam on the Nandana River, were used for flow calibration and validation. The available data were compared to the projected results to determine the effectiveness of the SWAT simulation. The calibration was performed on a monthly and an annual basis using outflow data from 2000 to 2004; the parameters were then validated between 2006 and 2010. To reduce the gap between the simulated and actual values, 11 model parameters (Table 2) were adjusted (Arnold et al. 2012).

All sub-watersheds received a 2% increase in CN2, a 0.3% increase in ALPHA BF, a 0.1% increase in GW DELAY, a 0.5% increase in GWQMN, a 0.3% increase in SLSUBBSN, a 0.4% increase in SURLAG, a 3% increase in OVN, and a 0.35% increase in ESCO. SOL-AWC and CH N2, the starting parameters, were multiplied by 1.2 and 0.3, respectively (Abbaspour 2007). The calibration of the model for various water balance components produced satisfactory agreement (Gasirabo et al. 2023).

Table 2. Parameter descriptions.

Parameter	Definition	Modification method	Initial range	Optimal parameter value
CN2	Initial SCS runoff curve number for moisture condition	r	35-98	96.24
ALPHA_BF	Base flow alpha factor	v	0-1	0.52
GW_DELAY	Ground water delay(days)	v	0-500	31
GWQMN	Threshold depth of water in the shallow aquifer required for return flow to occur	v	0-5000	900
SOL_AWC	Available water capacity of the soil layer	r	0-1	15
SLSUBBSN	Average slope length	r	10-150	50
SURLAG	Surface runoff lag coefficient(days)	r	0.05-24	3.93
OV_N	Manning's "n" value for overland flow	r	0.01-1	5.98
ESCO	Soil evaporation compensation factor	r	0-1	0.72
EPCO	Plant uptake compensation factor	r	0-1	0.18
CH_N2	Manning coefficient for main channel	r	-0.01-0.3	0.035

### 3.3. Graphical comparison of calibration and validation results

Predicted and actual yearly flows over the calibration period are compared in Figure 5. The average flow for the simulated period was 11.89 m<sup>3</sup>/s, whereas the average actual flow over the same time was about 13.00 m<sup>3</sup>/s. Maximum flow was in 2003; minimum flow was in 2000. Depending on the meteorological information obtained from the PMD, the simulation results demonstrate a good fit with peak and low-flow periods. According to Figure 6, the flow results for the validation period indicate good agreement between observed and model-simulated data. The simulation's average annual flow was 24.45 m<sup>3</sup>/s, whereas the average measured flow over the same period was 26.16 m<sup>3</sup>/s, a close match. The findings indicate that the model can be successfully applied to forecast annual average river flow levels. The  $R^2$  statistics for calibration and validation, indicating the reliability of the findings, are displayed in Figures 7 and 8, where  $R^2$  is 0.99 and 0.96, respectively, demonstrating that the model findings for both periods are excellent. The model's annual stream flow data indicated a *PBIAS* of 1.8 for the calibration period and 0.51 for the validation period. These numbers show that the model overestimated stream flow during the validation period while simulating stream flow with a less precise model during the calibration phase. *RSR* was 0.52 for the calibration period and 0.29 for the validation period, according to the data. Table 5 and 6 provide summaries of the statistical analysis of simulated and actual yearly stream flow data. Based on *NSE*, the model results for calibration (0.91) and for validation (0.86) are both satisfactory. Monthly flow model results are also depicted in Figures 9, 10, 11, and 12 with  $R^2$  values that are quite acceptable. The modeled monthly stream flow data indicated a *PBIAS* of 0.34 for the calibration period and 0.08 for the

validation period. These numbers show that the model overestimated stream flow during the validation period while simulating stream flow with a less precise model during the calibration phase. *RSR* was 0.23 for the calibration period and 0.31 for the validation period, according to the data. Table 3 and 4 provide summaries of the statistical analysis of simulated and actual monthly stream flow data. According to the *NSE* approach, the model results of 0.89 for calibration and 0.58 for validation are both satisfactory. The simulation underestimates the peak flow values experienced in January, May, and September. The location of the peaks was generally well-simulated for both the calibration and validation periods. If additional precipitation and temperature datasets from meteorological observatories with specific coverage of the research region were available, the model results might be enhanced significantly and achieve outstanding accuracy. Numerous studies have shown the SWAT model's under-prediction of peak flows (Fadil et al. 2011; Ghoraba 2015).

Table 3. Statistical analysis of simulated and actual monthly stream flow for calibration.

Calibration (2000-2004)	Observed	Simulated
Mean	1.16	0.92
$R^2$	0.95	
<i>NSE</i>	0.89	
<i>PBIAS</i>	0.34	
<i>RSR</i>	0.23	

Table 4. Statistical analysis of simulated and actual monthly stream flow for validation.

(2006-2010)	Observed	Simulated
Mean	3.58	1.90
$R^2$	0.82	
<i>NSE</i>	0.58	
<i>PBIAS</i>	0.08	
<i>RSR</i>	0.31	

Table 5. Statistical analysis of simulated and actual annual stream flow for calibration.

Calibration (2000-2004)	Observed	Simulated
Mean	13	11.89
$R^2$	0.99	
<i>NSE</i>	0.91	
<i>PBIAS</i>	1.8	
<i>RSR</i>	0.52	

Table 6. Statistical analysis of simulated and actual annual stream flow for validation.

(2006-2010)	Observed	Simulated
Mean	26.16	24.45
$R^2$	0.96	
<i>NSE</i>	0.86	
<i>PBIAS</i>	0.51	
<i>RSR</i>	0.29	

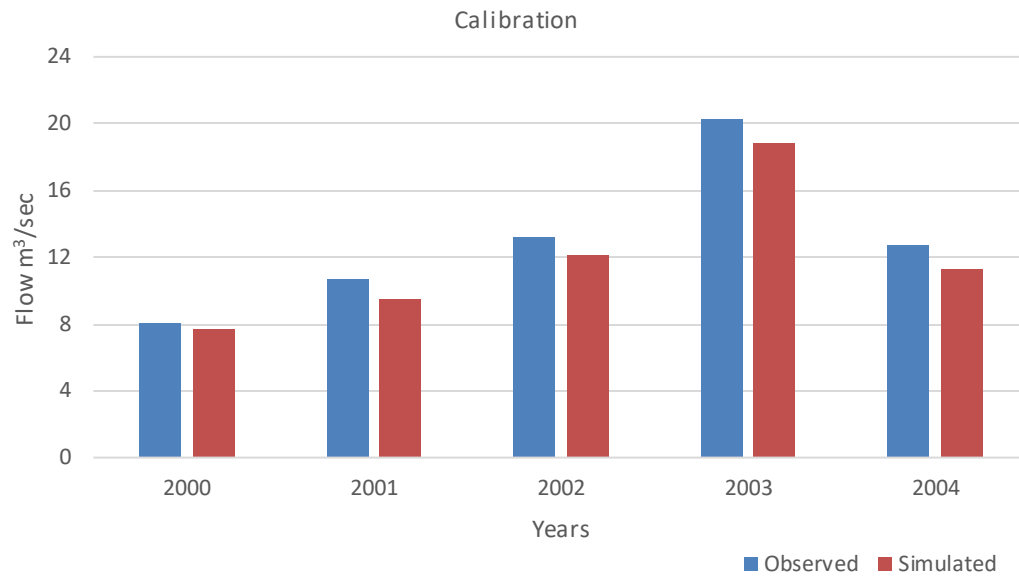


Fig. 5. Observed and predicted annual stream flow during the calibration period (2000-2004).

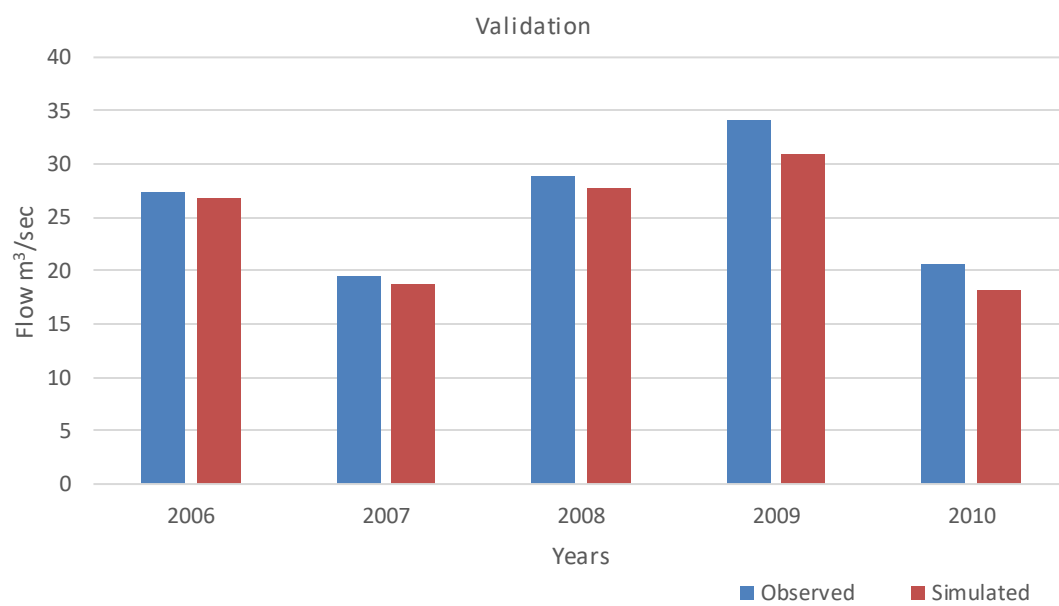


Fig. 6. Observed and simulated annual stream flow during the validation period (2006-2010).



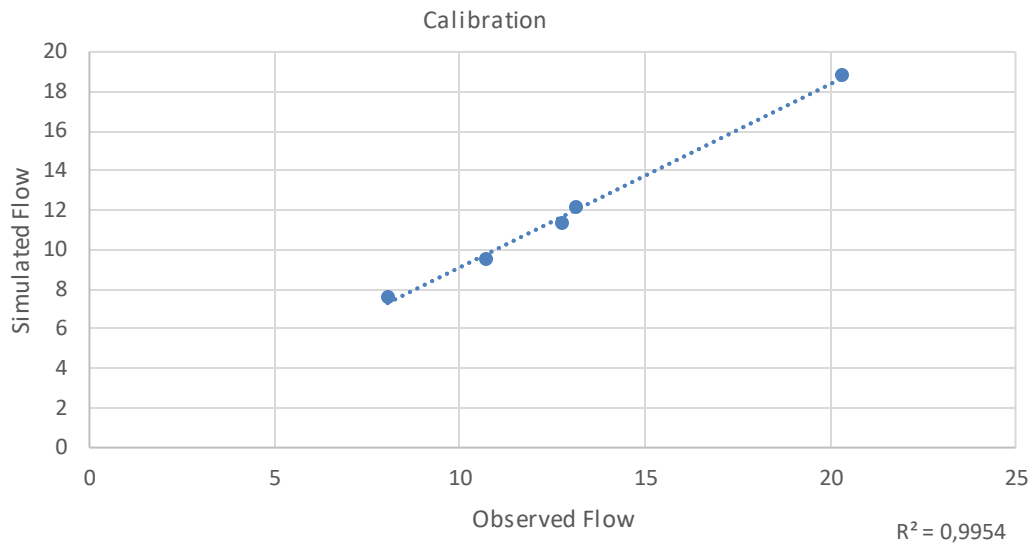


Fig. 7. Annual value of  $R^2$  for the calibration period (2000-2004).

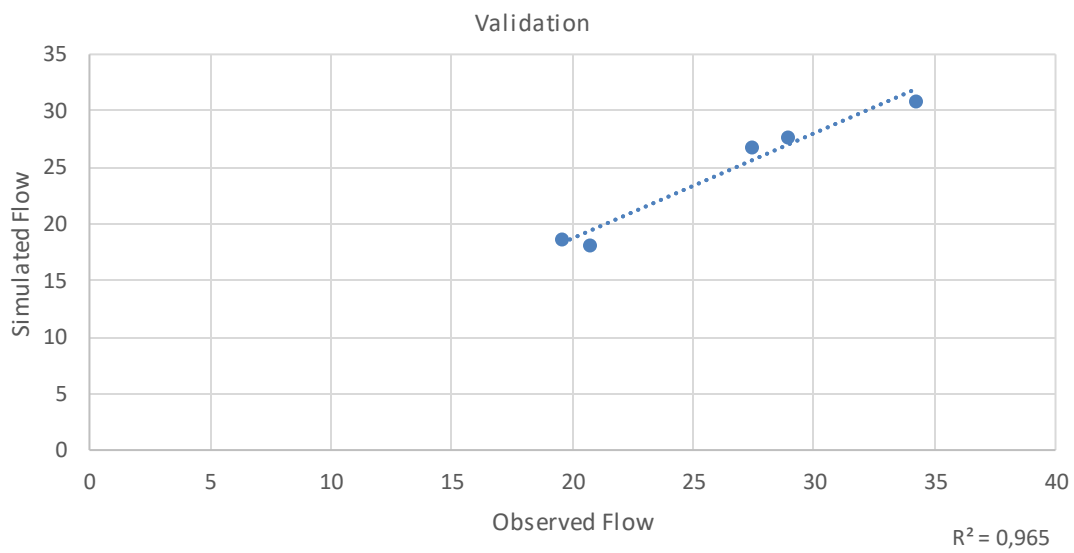


Fig. 8. Annual value of  $R^2$  for the validation period (2006-2010).

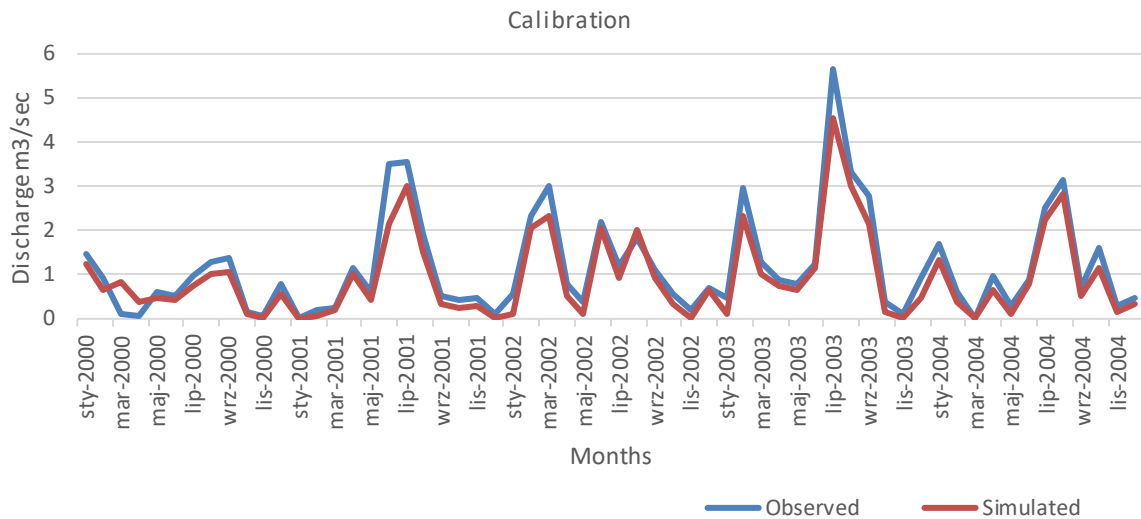


Fig. 9. Monthly flow model results for the calibration period (2000-2004).

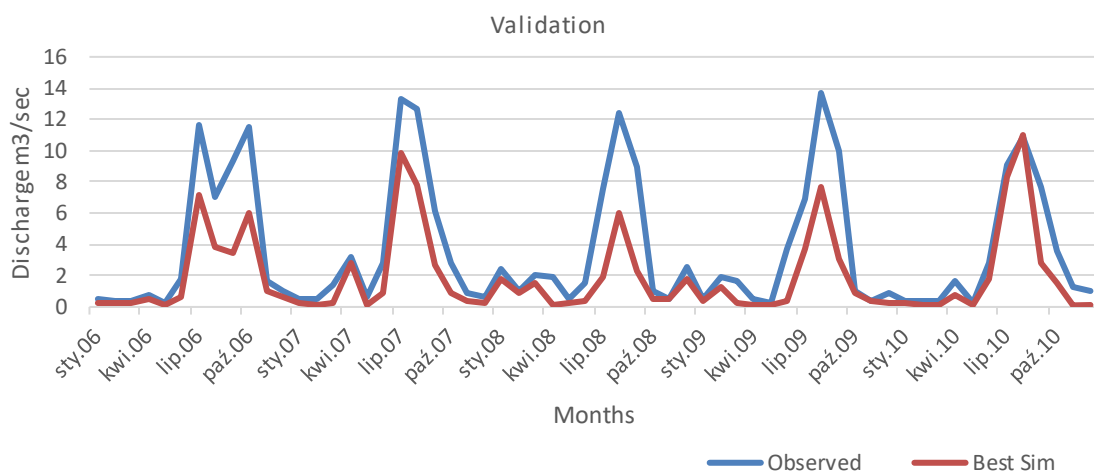


Fig. 10. Monthly flow model results for the validation period (2006-2010).

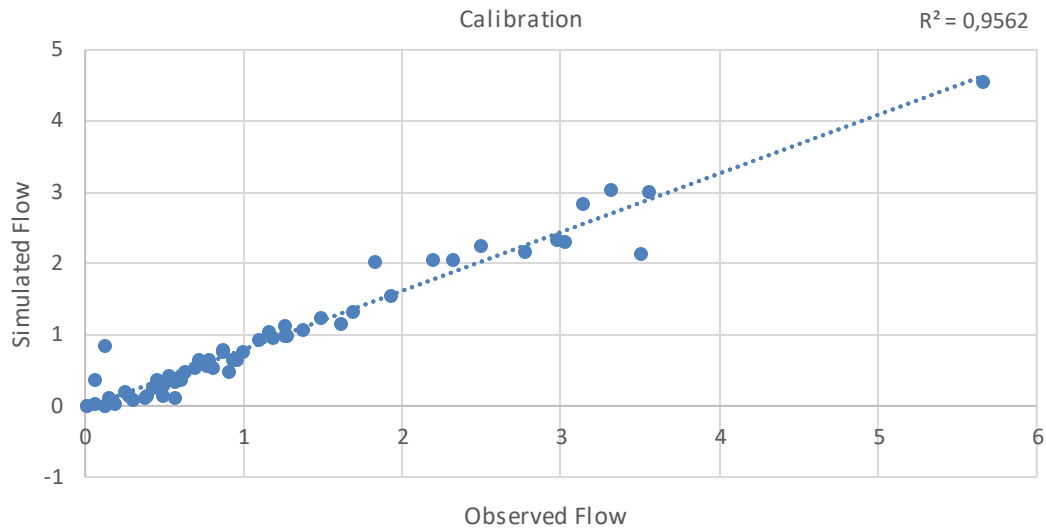


Fig. 11. Monthly value of  $R^2$  for the calibration period (2000-2004).

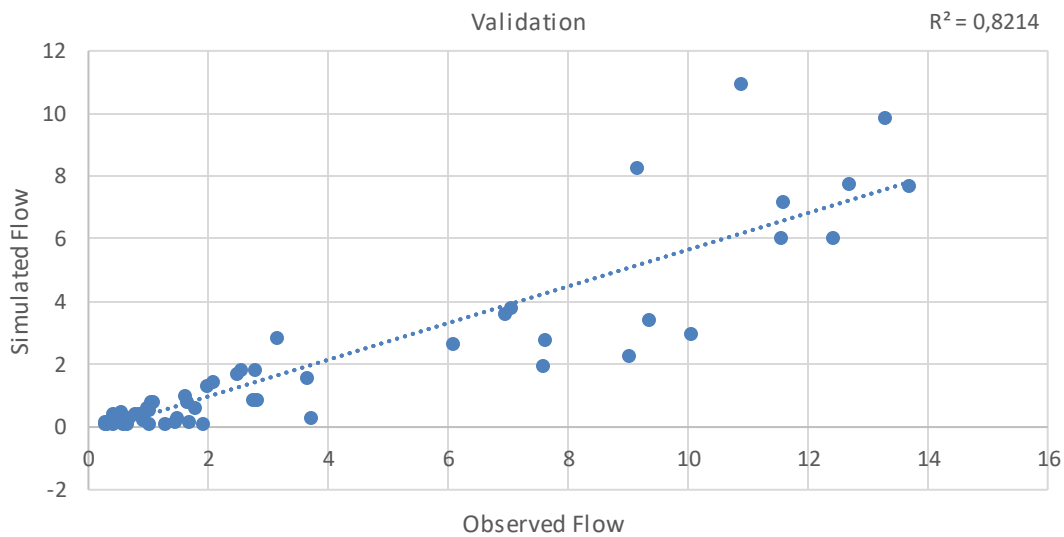


Fig. 12. Monthly value of  $R^2$  for the validation period (2006-2010).

### 3.4. Water balance components

In addition to annual and monthly flow, the SWAT model assessed additional essential water balance components. According to (Sathian, Shyamala 2009), the most essential aspects of a basin's water balance are precipitation, surface runoff, lateral flow, base flow, and evapotranspiration (Arnold et al. 1998).

Except for precipitation, all of these variables require prediction to be quantified because their measurement is difficult. The average annual basin values for various water balance components throughout the model's simulations of the calibration and validation periods are presented in Table 7, computed as a proportion of the annual rainfall average in Figure 13. Among these aspects, actual evapotranspiration ( $ET$ ) generated the most water loss from the watershed. A high evapotranspiration

rate expected might be ascribed to the type of plant cover and high temperature associated with the location. For the calibration period, the average annual evapotranspiration is 0.31, and for the validation period, the value is 0.30. The quantity of stream flow leaving the watershed's outflow during the time step is known as total water yield (*WYLD*). The majority of the rainfall received by the basin is lost as stream flow, as can be observed. On the other hand, for the calibration period, the ratio of the simulated average annual surface runoff to the average annual precipitation is 0.41 and 0.32 for the validation period. The lateral flow (Lat Q) was significantly impacted by the terrain slope. As the slope rises, the lateral flow, calculated as a proportion of annual rainfall average, is 1% for the calibration period and 13% for the validation period. Therefore, lateral flow is a crucial factor in river flow on sloping terrain. It has little effect on shallowly sloped ground. Deep aquifer recharging is substantial in all situations, with average percentages of 16% and 7% of total rainfall for both simulated periods. The water from the shallow aquifer that returns to the reach during the time step is known as groundwater contribution to stream flow (GWQ), and it varies greatly among streams. For both the calibration and validation periods, the average annual contribution of groundwater relative to precipitation is 11% and 18%, respectively.

Table 7. Average annual water balance components.

Months	Rain [mm]	Snow fall [mm]	SURF Q [mm]	LAT Q [mm]	Water Yield [mm]	ET [mm]	Sed. Yield [mm]	PET [mm]
1	22.48	0	10.36	0.03	12.11	1.74	6.3	20.87
2	37.52	0	21.66	0.03	26.21	4.66	14.7	30.16
3	22.72	0	11.18	0.04	17.47	6.15	6.78	61.2
4	21.92	0	6.22	0.04	11.32	11.68	3.43	91.67
5	15.36	0	4.27	0.04	7.06	9.96	2.33	172.67
6	42.24	0	16.65	0.04	17.08	20.66	10.03	162.62
7	83.6	0	40	0.04	40.52	30	25.36	125.4
8	71.34	0	31.87	0.05	36.33	26.66	20	105.67
9	36.94	0	15.67	0.05	25.07	13.61	10.1	97.44
10	18.24	0	9.46	0.05	16.03	4.03	5.91	76.75
11	6.7	0	2.11	0.05	5.57	1.99	1.13	38.28
12	17.84	0	9.04	0.04	11.86	1.73	5.54	20.18
0	396.9	0	178.49	0.5	226.63	132.87	111.61	1002.91

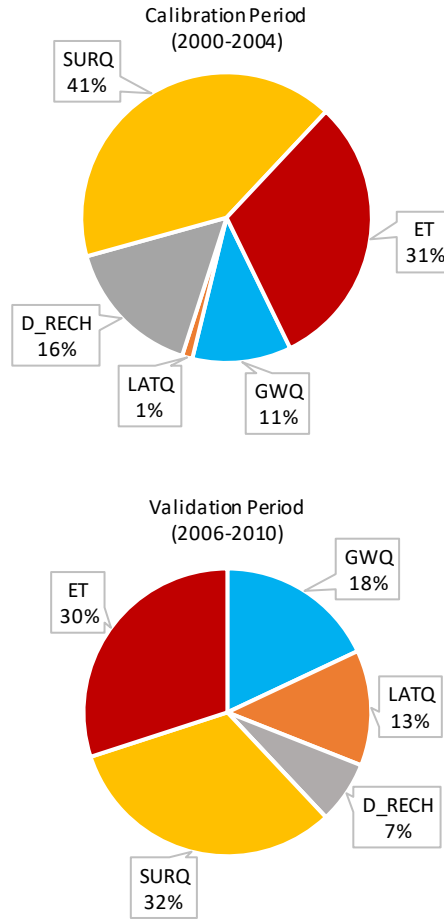


Fig. 13. Average annual water balance as a relative percentage to precipitation.

#### 4. Conclusion and recommendations

The current study attempted to simulate the influence of climatic change, LULC, soil, and topographic conditions on the Shahpur catchment using Arc SWAT 2012 and the input of long-term meteorological data, satellite data, soil data, and DEM images. The Shahpur catchment's hydrologic model was calibrated and certified using the SWAT-CUP SUFI-2 program to improve the output so that it matches the reported discharge at the gauging station located near the Shahpur Dam site office (Brighenti et al. 2019). The observed flow data obtained from the Shahpur Dam site office, recorded by a gauging station downstream from the Shahpur Dam on the Nandana River, were used for flow calibration and validation. The SWAT model's effectiveness and capability were determined by the hydrological study in this research project. The model's efficiency was assessed using accurate calibration from 2000 to 2004 and validation from 2006 to 2010. The calibrated model can be used to investigate the effects of rising temperatures, land use change, and other management-relevant scenarios on streamflow and soil erosion proactively. To evaluate the effectiveness of the model,  $R^2$ , Nash-Sutcliffe efficiency ( $NSE$ ), percent bias ( $PBIAS$ ) and  $RMSE$  factors were evaluated for both annual and monthly flows. On an annual basis, manual calibration was conducted first, followed by automatic calibration. On a monthly basis, the model's calibration and validation generated satisfactory simulation results.



The validation  $R^2$  value for monthly stream flow was 0.82%, while the calibration  $R^2$  value was 0.95%, demonstrating the symmetric regression of the model. The  $NSE$ , which measures how well the model fit the observed data, was 0.58 for validation and 0.89 for calibration. The  $PBIAS$  parameter indicates underestimation, with calibration and validation results of 34 and 8%, respectively. The  $PBIAS$  parameter displays the difference between the simulated and observed amounts, with a value of 0 ideal. Positive values indicate underestimation, whereas negative values represent overestimation. The validation  $RMSE$  value was 0.31%, while the calibration  $R^2$  value was 0.23%, for monthly stream flow. The model's yearly stream flow data indicated a  $PBIAS$  of 1.8 for the calibration period and 0.51 for the validation period. These numbers show that the model underestimated stream flow during the validation period while simulating the stream flow with precision during the validation phase.  $RSR$  was 0.52 for the calibration period and 0.29 for the validation period, according to the data. The average flow for the simulated period was 11.89 m<sup>3</sup>/s, while the average real flow was approximately 13.00 m<sup>3</sup>/s. The flow reached its peak in 2003, with the lowest flow occurring in 2000. The validation period flow result shows good correlations between observed and model-simulated data. The average yearly flow in the simulation was 24.45 m<sup>3</sup>/s, while the average observed flow over the same period was roughly 26.16 m<sup>3</sup>/s, suggesting a striking match. The calibration of the model for various water balance components produced satisfactory agreement. The findings of this research suggest that precise water consumption data are required to produce a more accurate representation of water production and the availability of deep aquifer recharge resources with a reduced uncertainty range. Natural year-to-year variability owing to climate, as well as water abstraction and consumption, is included in the stated uncertainty. These results show that the model can correctly anticipate average annual and monthly stream flow levels. It was concluded from the results that if more reliable precipitation and temperature data sets from climatic observatories with good specific coverage of the research region were available, the model results might be greatly improved, with exceptional precision. The hydrological modeling of the Shahpur catchment using the SWAT model revealed important insights but also highlighted several gaps. Limitations in meteorological data restricted the model's accuracy, suggesting the need for a more comprehensive dataset that includes additional climatic parameters. Additionally, the study primarily focused on surface water without integrating groundwater interactions. Finally, the absence of climate change scenarios indicates a critical area for future research to support effective water resource management. The SWAT model operates on several assumptions about hydrological processes that may not hold true in all contexts. These assumptions could limit the applicability of the model results to other similar catchments. Future research should prioritize enhanced data collection by establishing more meteorological stations to improve model accuracy and real-time monitoring. Integrating advanced remote sensing technologies would provide timely data on land use and vegetation changes. A comprehensive approach using coupled surface and groundwater models is recommended to better understand the hydrological cycle. Previous studies in hydrological modeling have often focused on general applications of the SWAT model in various regions, but many have lacked comprehensive calibration and validation specific to localized settings like the Shahpur

catchment. This research provides a hydrological model tailored for the Shahpur catchment, facilitating improved water resource management in a rapidly urbanizing region. The successful calibration and validation of the SWAT model enhance predictive capabilities for streamflow under varying climatic and land use scenarios. Moreover, the findings underscore the importance of localized data integration, which can inform future watershed management strategies and contribute to sustainable development in water-scarce areas. By addressing specific challenges related to water resource allocation, this study contributes valuable insights for policy-making and environmental planning. We propose that this model be employed for Shahpur watershed management based on its robust performance and comparative outcomes.

Most existing studies focus on large river basins, leaving a contextual and methodological gap in applying and validating SWAT in semi-arid regions with limited historical data. This study addresses these gaps by successful calibration and validation of the SWAT model using available data from 2000-2010 for the Shahpur catchment. The results show strong model performance and highlight the model's potential for effective watershed management. The study is limited by the unavailability of recent meteorological and discharge data, as well as the exclusion of dynamic land use and climate change scenarios. Despite these limitations, the study contributes significantly by establishing a baseline framework for future hydrological modeling in similar environments. We recommend that future research should incorporate high-resolution, more detailed climate and land use datasets, investigate groundwater–surface water interactions, and apply scenario-based modeling to assess the long-term impacts of climate variability and land use change on watershed hydrology.

## Abbreviations

CUP	Calibration and Uncertainty Programs
D_RECH	Deep Recharge
DEM	Digital Elevation Model
ET	Evapotranspiration
GWQ	Groundwater Contribution to Streamflow
LATQ	Lateral Flow
NSE	Nash–Sutcliffe Efficiency
PBIAS	Percent Bias
PET	Potential Evapotranspiration
PMD	Pakistan Meteorological Department
RMSE	Root Mean Square Error
RSR	Ratio of RMSE to the standard deviation
SUFI	Uncertainty in Sequential Uncertainty Fitting
SURQ	Surface Runoff
SWAT	Soil and Water Assessment Tool

## References

- Abbaspour K.C., 2007, User Manual for SWAT-CUP, SWAT Calibration and Uncertainty Analysis Programs, Swiss Federal Institute of Aquatic Science and Technology, Eawag, Duebendorf, Switzerland.
- Arnold J.G., Srinivasan R., Muttiah R.S., Williams J.R., 1998, Large area hydrologic modeling and assessment Part I: Model development, *Journal of the American Water Resources Association*, 34 (1), 73-89, DOI: 10.1111/j.1752-1688.1998.tb05961.x.
- Arnold J.G., Moriasi D.N., Gassman P.W., Abbaspour K.C., White M.J., Srinivasan R., Santhi C., Harmel R.D., van Griensven A., Van Liew M.W., Kannan N., Jha M.K., 2012, SWAT: Model use, calibration, and validation, *Transactions of the ASABE*, 55 (4), 1491-1508.
- Ashagre B., 2009, SWAT to identify watershed management options: Anjeni watershed, Blue Nile Basin, Ethiopia, A Thesis Presented to the Faculty of the Graduate School of Cornell University.
- Beroho M., Aboumaria K., El Hamdouni Y., Ouallali A., Jauffer L., Kader S., Hughes P.D., Spalevic V., Kuriqi A., Mrabet R., Kebede F., Briak H., 2025, A novel SWAT-based framework to integrate climate and LULC scenarios for predicting hydrology and sediment dynamics in the watersheds of Mediterranean ecosystems, *Journal of Environmental Management*, 388, DOI: 10.1016/j.jenvman.2025.125446.
- Beroho M., Briak H., Cherif E.K., Boulahfa I., Ouallali A., Mrabet R., Kebede F., Bernardino A., Aboumaria K., 2023, Future scenarios of Land Use/Land Cover (LULC) based on a CA-Markov Simulation Model: Case of a Mediterranean watershed in Morocco, *Remote Sensing*, 15 (4), DOI: 10.3390/rs15041162.
- Brighenti T.M., Bonumá N.B., Grison F., de Almeida Mota A., Kobiyama M., Chaffe P.L.B., 2019, Two calibration methods for modeling streamflow and suspended sediment with the SWAT model, *Ecological Engineering*, 127, 103-113, DOI: 10.1016/j.ecoleng.2018.11.007.
- Cheema M.A., Bandaragoda D.J., 1997, Baseline survey for farmers organizations of Mirwal and Shahpur small dams, Punjab, Pakistan, IWMI Pakistan Report R-038/IIMI Pakistan Report R-038.
- Fadil A., Rhinane H., Kaoukaya A., Kharchaf Y., Bachir O.A., 2011, Hydrologic modeling of the Bouregreg watershed (Morocco) using GIS and SWAT model, *Journal of Geographic Information System*, 3 (4), DOI: 10.4236/jgis.2011.34024.
- Gasirabo A., Xi C., Kurban A., Liu T., Baligira H.R., Umuhoza J., Umugwaneza A., Edovia U.D., 2023, SWAT model calibration for hydrological modeling using concurrent methods, a case of the Nile Nyabarongo River Basin in Rwanda, *Frontiers in Water*, 5, DOI: 10.3389/frwa.2023.1268593.
- Ghoraba S.M., 2015, Hydrological modeling of the Simly Dam watershed (Pakistan) using GIS and SWAT model, *Alexandria Engineering Journal*, 54 (3), 583-594, DOI: 10.1016/j.aej.2015.05.018.
- Ghumman A.R., Ghazaw Y., Abdel-Maguid R.H., Zafar A., 2019, Investigating parameters of geomorphic direct runoff hydrograph models, *Water Resources and the Regime of Water Bodies*, 46 (1), 19-28, DOI: 10.1134/S0097807819010068.
- Gupta H.V., Sorooshian S., Yapo P.O., 1999, Status of automatic calibration for hydrologic models: Comparison with multilevel expert calibration, *Journal of Hydrologic Engineering*, 4 (2), 135-143, DOI: 10.1061/(ASCE)1084-0699(1999)4:2(135)
- Kamuju N., 2019, Prediction of surface runoff changes with LandUse-LandCover impact using remote sensing data and GIS based ARCSWAT model of Indrayani Watershed, Maharashtra, India, *International Journal of Scientific Research in Computer Science, Engineering and Information Technology*, 5 (6), DOI: 10.32628/CSEIT19564.
- Khan A.D., Arnold J.G., Di Luzio M., Ghoraba S., 2014, Hydrological modeling of upper Indus Basin and assessment of deltaic ecology, *International Journal of Modern Engineering Research*, 4 (1), 73-85.
- Malik M.A., Dar A.Q., Jain M.K., 2022, Modelling streamflow using the SWAT model and multi-site calibration utilizing SUFI-2 of SWAT-CUP model for high altitude catchments, NW Himalaya's, *Modeling Earth Systems and Environment*, 8 (1), 1203-1213, DOI: 10.1007/s40808-021-01145-0.
- Mengistu A.G., van Rensburg L.D., Woyessa Y.E., 2019, Techniques for calibration and validation of SWAT model in data scarce arid and semi-arid catchments in South Africa, *Journal of Hydrology: Regional Studies*, 25, DOI: 10.1016/j.ejrh.2019.100621.

- Moriasi D.N., Arnold J.G., Van Liew M.W., Bingner R.L., Harmel R.D., Veith T.L., 2007, Model evaluation guidelines for systematic quantification of accuracy in watershed simulations, *Transactions of the ASABE*, 50 (3), 885-900.
- Nash J.E., Sutcliffe J.V., 1970, River flow forecasting through conceptual models part I – A discussion of principles, *Journal of Hydrology*, 10 (3), 282-290, DOI: 10.1016/0022-1694(70)90255-6.
- Nasrin Z., Gholamabbas S., Ebrahim H., 2013, Hydrological and sediment transport modeling in maroon dam catchment using soil and water assessment tool (SWAT), *International Journal of Agronomy and Plant Production*, 4 (10), 2791-2795.
- Neitsch S.L., Arnold J.G., Kiniry J.R., Williams J.R., 2005, Soil and Water Assessment Tool Theoretical Documentation. Version 2005, USDA-ARS Grassland, Soil and Water Research Laboratory, Agricultural Research Service, Texas, USA.
- Neitsch S.L., Arnold J.G., Kiniry J.R., Williams J.R., 2009, Soil and Water Assessment Tool Theoretical Documentation. Version 2009, USDA-ARS Grassland, Soil and Water Research Laboratory, Agricultural Research Service, Texas, USA.
- Santhi C., Arnold J.G., Williams J.R., Dugas W.A., Srinivasan R., Hauck L.M., 2001, Validation of the SWAT model on a large river basin with point and nonpoint sources, *Journal of the American Water Resources Association*, 37 (5), 1169-1188, DOI: 10.1111/j.1752-1688.2001.tb03630.x.
- Sathian K.K., Shyamala P., 2009, Application of GIS integrated SWAT model for basin level water balance, *Indian Journal of Soil Conservation*, 37, 100-105.
- Schulz J., Abbaspour K.C., Yang H., Srinivasan R., Zehnder A.J.B., 2008, Modeling blue and green water availability in Africa, *Water Resources Research*, 44 (7), DOI: 10.1029/2007WR006609.
- Singh J., Knapp H.V., Arnold J.G., Demissie M., 2005, Hydrological modeling of the Iroquois river watershed using HSPF and SWAT, *Journal of the American Water Resources Association*, 41 (2), 343-360, DOI: 10.1111/j.1752-1688.2005.tb03740.x.
- Singh V.P., Woolhiser D.A., 2002, Mathematical modeling of watershed hydrology, *Journal of Hydrologic Engineering*, 7 (4), 270-292, DOI: 10.1061/(ASCE)1084-0699(2002)7:4(270).
- Stehr A., Debels P., Romero F., Alcayaga H., 2008, Hydrological modelling with SWAT under conditions of limited data availability: evaluation of results from a Chilean case study, *Hydrological Sciences Journal*, 53 (3), 588-601, DOI: 10.1623/hysj.53.3.588.
- Supit C., Ohgushi K., 2012, Dam construction impacts on stream flow and nutrient transport in Kase River Basin, *International Journal of Civil and Environmental Engineering*, 12 (3), 1-5.
- Van Liew M.W., Veith T.L., Bosch D.D., Arnold J.G., 2007, Suitability of SWAT for the conservation effects assessment project: comparison on USDA agricultural research service watersheds, *Journal of Hydrologic Engineering*, 12 (2), 173-189, DOI: 10.1061/(ASCE)1084-0699(2007)12:2(173).

# A winter flash flood in Skenderaj, Kosovo: heavy rainfall analysis and early warning perspectives

Vlado Spiridonov, Ivica Milevski, Boro Jakimovski

Ss Cyril and Methodius University Skopje, North Macedonia

Lavdim Osmanaj, Venera Hajdari Llapashtica

University of Prishtina

## Abstract

Flash floods pose a significant risk to infrastructure in Kosovo, particularly in urban and riverine areas. This research focuses on an intense river flood event that took place on January 19, 2023, in the Skenderaj catchment. The study's main goal was to establish a flash flood early warning system by combining sophisticated atmospheric modeling, hydrological evaluation, and rainfall hazard analysis. The ARW model with 2-km resolution effectively captured rainfall intensity and local flood occurrences, particularly around Skenderaj and Istog, whereas the 4-km NMM model better represented wider spatial precipitation patterns. Hydrological results demonstrated that precipitation strongly dictated river discharge and runoff dynamics, with the highest flows recorded in northern Albania. To validate and enhance forecast accuracy for flash flood warnings, datasets from the Global Flood Awareness System (GloFAS), the European Flood Awareness System (EFAS), and ERA5 reanalysis were incorporated. These resources provided essential information on antecedent conditions, such as soil moisture and snowmelt, which substantially influenced runoff and flood magnitude. The ECMWF Copernicus framework also contributed by supplying 24-hour river discharge forecasts for Kosovo's basins, aiding in timely and spatially detailed flood alerts. The Novel Thunderstorm Alert System (NOTHAS) was updated to integrate crucial hydrological variables – including surface and convective runoff, snow water equivalent, soil moisture, and slope – thereby enhancing the precision of flood warnings. This improved system enabled effective classification of flood risk zones, thus identifying areas vulnerable to flash floods and landslides. The study highlights the crucial role of high-resolution weather modeling, hydrological insights, and integrated early warning systems in enhancing flash flood prediction and mitigation efforts.

## Keywords

Flash floods, early warning system, hydrological modeling, atmospheric simulations, flood risk assessment, Kosovo.

Submitted 27 May 2025, revised 15 July 2025, accepted 23 July 2025

DOI: 10.26491/mhwm/208584

## 1. Introduction

Ongoing shifts in global climate patterns have intensified the occurrence and severity of extreme weather phenomena, notably intense storms and flash floods. Such events pose escalating risks to populations, infrastructure, and economies, especially in regions characterized by complex terrain and limited hydrological infrastructure. In Kosovo and the broader Balkan Peninsula, the frequency and intensity of convective storms during the warmer months have increased, often triggering extreme precipitation and subsequent flash flood events. The rapid development of these hydrometeorological hazards necessitates advancements in accurate forecasting models, robust early warning systems (EWS), and comprehensive flood risk management frameworks (Archer et al. 2006; Borga et al. 2007).

Numerical weather prediction (NWP) tools, including the Weather Research and Forecasting (WRF) model, have become pivotal in simulating convective processes and forecasting heavy rainfall episodes.



However, flash flood prediction remains challenging due to the complex coupling between atmospheric dynamics and hydrological responses. The accuracy of WRF-based forecasts is strongly influenced by model setup parameters such as initial and boundary conditions, spatial resolution, and microphysical parameterizations, particularly for local convection (Lee, Hong 2006; Skamarock et al. 2008; Spiridonov et al. 2020, 2023). To improve flood forecasting methodology, it is essential to integrate meteorological forecasts with hydrological models that convert precipitation into surface runoff and streamflow. Coupled meteorological-hydrological-hydraulic modeling frameworks have shown promise in generating timely and skillful flash flood predictions (Varlas et al. 2023). Furthermore, efforts to optimize microphysics schemes within WRF enhance rainfall estimations in basins lacking dense observational networks .

Effective flash flood early warning systems rely on continuous monitoring through ground stations, remote sensing platforms, and hydrological networks. Unfortunately, in Kosovo and similar regions, real-time observational data are often sparse or incomplete, hindering accurate flood detection and early warnings (Cluckie, Han 2000; Thielen et al. 2009; Hapuarachchi et al. 2011). Integration of satellite precipitation products, such as GPM-IMERG, with radar and hydrological data has improved early warning system capabilities (Giannaros et al. 2022). Large-scale forecasting and early warning systems such as the Global Flood Awareness System (GLOFAS) (Alfieri et al. 2013), the European Flood Awareness System (EFAS) (Thielen et al. 2009), and reanalysis datasets like ERA5 (Hersbach et al. 2020) provide valuable inputs for flood risk assessment and decision-making. In addition to hydrometeorological forecasting, geospatial techniques play a crucial role in flood hazard mapping and vulnerability assessment. Advances in Geographic Information Systems (GIS) and machine learning methods have enhanced spatial flood risk analyses, supporting improved urban planning and land-use policies. The increasing vulnerability to flooding due to climate change is exacerbated by anthropogenic activities such as uncontrolled urban growth, deforestation, and modifications of natural waterways, which reduce landscape permeability and increase flood exposure (Kane, Shogren 2000; Dobler et al. 2012; Didovets et al. 2019; Moragoda, Cohen 2020). Previous research by Osmanaj et al. (2025) focused on evaluating the performance of the WRF non-hydrostatic model in simulating the severe flash flood event that occurred on June 24, 2023, at Peja in northeastern Kosovo, during which more than 54 mm of rainfall was recorded within two hours.

This study analyzes a winter flash flood event that struck the small catchment of Skenderaj on January 19, 2023 (see Agaj et al. 2024; Osmanaj et al. 2025). The main objective is to develop a flash flood early warning system by integrating high-resolution atmospheric modeling using the WRF model, hydrological simulations, and hydrometeorological hazard assessments. This integrated approach aims to enhance the accuracy of flash flood forecasting methodologies and improve operational early warning capabilities in data-scarce regions. By combining meteorological modeling, hydrological analysis, and geospatial risk assessment, this research aims to contribute to the development of more accurate flash flood forecasting methodologies and improved early warning capabilities.

The structure of this paper is as follows: Section 2 presents the observational analysis of the event, Section 3 details the numerical modeling approach, Section 4 discusses the simulation results with validation

against observations, and Section 5 concludes with recommendations for enhancing flood risk management strategies.

## **2. Motivation**

Flooding has become an increasingly frequent and devastating phenomenon across Kosovo and the broader Balkan region, particularly during spring and summer. In 2023 alone, Kosovo experienced two major flood events, in January and June, causing extensive damage to cities such as Skenderaj, Mitrovica, Peja, and Podujeva. These floods resulted in significant economic losses, infrastructure damage, and human casualties, underscoring the urgent need for improved flood management and mitigation strategies.

The increasing frequency and severity of floods are linked to climate change, which has disrupted hydrological patterns and intensified extreme weather events. Rising global temperatures contribute to unpredictable rainfall distributions, leading to both prolonged droughts and extreme precipitation. The 2019-2021 Climate Change Strategy Action Plan for Kosovo acknowledges these risks, yet flood management remains hindered by inadequate infrastructure, incomplete flood risk mapping, and insufficient early warning systems.

Additionally, human factors such as poor urban planning, riverbed degradation, and inadequate stormwater infrastructure have exacerbated flood risks. Unregulated construction, deforestation, and the concretization of river channels have reduced the land's natural ability to absorb excess water, increasing the likelihood of urban and riverine flooding.

Given these challenges, there is a pressing need for comprehensive flood risk assessment, improved early warning systems, and climate adaptation strategies. Strengthening institutional coordination, investing in resilient infrastructure, and integrating hydrometeorological data into urban planning are critical steps toward mitigating future flood impacts and enhancing community resilience. Recent extreme rainfall events have demonstrated the inadequacy of current flood forecasting and warning systems in Kosovo. The flood event on January 19, 2023, led to river overflows, while the June 24, 2023, urban flood in Peja highlighted the vulnerability of city infrastructure. The need for an integrated, real-time flash flood early warning system is crucial for mitigating future risks.

## **3. Methods**

The main objectives of this research are:

1. To evaluate the most suitable model configuration for accurately simulating the atmospheric behavior and physical processes associated with torrential rainfall over Kosovo.
2. To develop an algorithm for an integrated hydrometeorological hazard module for early flash-flooding warning



Fig. 1. Domain configuration of the WRF-NMM (Non-hydrostatic Mesoscale Model) single-model setup over southeastern Europe, illustrating nested grid spacings of 4 km, 3 km, 2 km, and 1 km. The central blue rectangle highlights the location of Kosovo within the model domain.

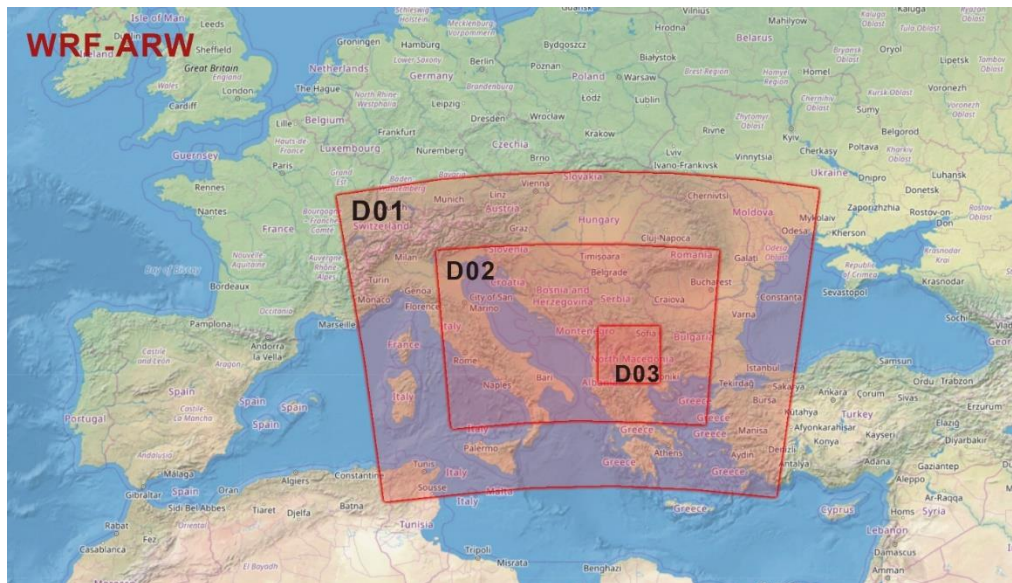


Fig. 2. WRF-ARW (ARW) triple-nested model domain configuration: the outermost domain (D1) covers central Europe with an 18 km grid resolution, the intermediate domain (D2) captures southeastern Europe at 6 km resolution, and the innermost domain (D3) focuses on Kosovo with a 2 km grid.

To address these objectives, a series of high-resolution simulations was performed using the Weather Research and Forecasting (WRF) model. The procedure included sensitivity testing of physical schemes and resolutions, using both ARW and NMM dynamic cores (Janjic 2003; Kain et al. 2006; Lee, Hong

2006; Han, Hong 2018). Hourly warnings and rainfall outputs were compared with historical observations and flash-flood guidance thresholds (Spiridonov et al. 2021; Liu et al. 2018).

### **3.1. Meteorological model framework**

The WRF model was selected for its robust treatment of atmospheric processes and flexibility in spatial and physical configurations. It supports both single- and nested-domain simulations and includes a wide range of physics options, such as the Thompson microphysics scheme (Thompson et al. 2008; Thompson, Eidhammer 2014), Yonsei University PBL (Hong 2010), Monin-Obukhov surface layer physics (Janjic 1996), RRTM longwave radiation (Mlawer et al. 1997), and Dudhia shortwave radiation (Dudhia 1989). The ARW core (Skamarock et al. 2008) was applied in a triple-nested configuration ( $18 \times 6 \times 2$  km) optimized for resolving convective-scale dynamics over Kosovo. The NMM core (Janjic 2003) was tested in single-domain setups with horizontal resolutions of 1 km, 2 km, 3 km, and 4 km (Fig. 1), echoing strategies used in regional storm-scale studies (Xue, Martin 2006; Schwartz et al. 2015).

The ARW nested run shown in Figure 2 was configured with time steps of 30, 10, and 3.3 seconds across the three domains, while NMM runs used shorter steps (down to 2 seconds) to maintain numerical stability. The experiments explored variations in microphysics (e.g., WSM6, Ferrier), cumulus schemes (e.g., Shin, Hong 2015), and vertical levels (32 layers), consistent with prior optimization studies (Misenis, Zhang 2010; Chawla et al. 2018; Chinta et al. 2021). All simulations were initialized with GDAS/FNL  $0.25^\circ$  global datasets, updated every 6 hours (Bernadet et al. 2000; Elmore et al. 2002; Kain et al. 2006). A spin-up period of 18 hours preceded each run to allow model stabilization before the targeted flood event onset (Jankov et al. 2007; Liu et al. 2021). Table 1 summarizes the domain configurations, model cores, physical parameterizations, and initialization data used in each of the eight experimental setups.

Table 1. Model setup and key parameters used in numerical experiments.

Parameter	Exp	1	2	3	4	5	6	7	8
<b>Type of experiment</b>		Simulation Triple-nested run	Simulation Single domain	Simulation Single domain	Simulation Single domain	Simulation Single domain	Simulation Single domain	Simulation Single domain	Simulation Single domain
<b>Model dynamics</b>		ARW Skamarock et al. (2008)	NMM Janjic (2003)	NMM	NMM	NMM	NMM	NMM	NMM
<b>Model microphysics</b>		28 Thompson, Eidhammer (2014)	8 Thompson et al. (2008)	8	3 Ferrier (1994)	8 Thompson et al. (2008)	8	6 WSM6 Hong, Lim (2006)	8
<b>PBL-scheme</b>		1 Yonsei Univ. YSU Hong (2010)	1	1	1	2 Mellor-Yamada Janjic (2001)	1	1	1
<b>Surface physics-schemes</b>		1 Monin-Obukhov Janjic (1996)	1	1	1	2 Monin-Obukhov (Janjic Eta) Janjic (1996)	2	1	1
<b>Cumulus parameterization</b>		14 Shin, Hong (2015); Han et al. (2016) 14,14,0	0	0 Explicit treatment of convection	0	0	0	0	0
<b>Long-wave radiation</b>		1 RRTM Scheme Mlawer et al. (1997)	1	1	1	1	1	1	1
<b>Short-wave radiation</b>		1 Dudhia (1989)	1	1	1	1	1	1	1
<b>Hor. Grid res.</b>		18×6×2km	4-km	4 km (larger domain)	3 km	2-km	2-km (larger domain)	1 km	1 km (larger domain)
<b>Ver. Grid. Res.</b>		32	32	32	32	32	32	32	32
<b>Time step (dt)</b>		30×10×3.3 s	8 s	8 s	6 s	4 s	4 s	2 s	2 s
<b>Sim. Lead time</b>		60 h	60 h	60 h	60 h	60 h	60 h	60 h	60 h
<b>Total grid points e_we e_sn e_vert</b>		113,190,15181 , 124, 136 44,44,44	100 150 44	250 300 44	100 150 44	100 150 44	200 250 44	100 150 44	200 250 44
<b>Initial data and LBC</b>		GDAS FNL	GDAS FNL	GDAS FNL	GDAS FNL	GDAS FNL	GDAS FNL	GDAS FNL	GDAS FNL

### 3.2. Design of an integrated hydrometeorological module for a flash-flood warning system

A robust river flood forecasting methodology has been developed by integrating meteorological, hydrological, and topographic parameters, enabling accurate prediction of flood risk during extreme weather events in Kosovo. This approach incorporates accumulated rainfall (mm/24 h), storm surface runoff (kg/m<sup>2</sup>), river discharge (m<sup>3</sup>/s), soil moisture (kg/m<sup>2</sup>), snowmelt equivalent (kg/m<sup>2</sup>), and terrain slope-surface roughness (m), each weighted according to expert judgment and regional statistical analysis. These parameters are normalized and combined into a composite flood risk index using a weighted scoring function that reflects their individual contributions to flood generation.

An integrated approach is applied by combining ECMWF high-resolution forecast river discharge or ERA5 reanalysis discharge data with WRF-ARW model outputs to enhance the accuracy of flood risk predictions for Kosovo. This approach avoids the use of separate rainfall-runoff models, relying instead on discharge data from ECMWF and meteorological fields from WRF to predict flood risk levels. ERA5 provides river discharge data at a 0.25° resolution, while ECMWF high-resolution forecasts offer more detailed discharge estimates at finer spatial resolution (e.g., 0.1°). These datasets are essential for assessing river flow conditions across the Kosovo domain. To ensure consistency, ERA5 discharge data (typically provided at 24-hour intervals) is resampled to match the 3-km spatial resolution and forecast intervals (e.g., hourly or every 3 hours) of WRF-ARW model outputs. This is accomplished through interpolation techniques such as bilinear or cubic spline interpolation to ensure spatial and temporal alignment.

WRF-ARW outputs include key meteorological fields necessary for flood risk estimation. The integrated system combines these fields with river discharge observations to calculate a multivariate cumulative distribution function (CDF), used for classifying flood risk based on historical reference values and critical thresholds. Among the variables, river discharge is especially important for identifying areas where flow is likely to exceed channel capacity, signaling heightened flood risk and triggering alerts within the flash flood early warning system.

### 3.2.1. Multivariate CDF for flood risk assessment

The multivariate cumulative distribution function (CDF) is used to compute the composite flood risk score. Let  $X = (AR, RO, Q, SM, SME, SL)$  represent the vector of the key hydrometeorological parameters, and  $T = (T_{AR}, T_{RO}, T_Q, T_{SM}, T_{SME}, T_{SL})$  represent their corresponding thresholds. The cumulative distribution function  $F_{FloodRisk}$  for the flood risk, considering the parameters and their thresholds, is expressed as:

$$F_{FloodRisk}(x_{AR}, x_{RO}, x_Q, x_{SM}, x_{SME}, x_{SL}) = P(AR \leq x_{AR}, RO \leq x_{RO}, Q \leq x_Q, SM \leq x_{SM}, SME \leq x_{SME}, SL \leq x_{SL}) \quad (1)$$

To capture the influence of the thresholds and the weighted contributions of each parameter, the CDF can be expanded by incorporating the normalized values of the parameters and their weights. The weight for each parameter is calculated as:



$$\omega_i = \frac{f_i(x_i, T_i)}{\max(f_i(x_i, T_i))} \quad (2)$$

where:  $\omega_i$  represents the normalized weight for parameter  $i$ ;  $f_i(x_i, T_i)$  is the probability density function (PDF) or cumulative distribution of parameter  $i$  based on its threshold  $T_i$ ;  $\max(f_i(x_i, T_i))$  normalizes the weight to ensure it sums up appropriately.

The final multivariate CDF for the flood risk is:

$$F_{FloodRisk}(x_{AR}, x_{RO}, x_Q, x_{SM}, x_{SME}, x_{SL}) = \prod_{i=1}^6 \left( \frac{f_i(x_i, T_i)}{\max(f_i(x_i, T_i))} \right)^{\omega_i} \quad (3)$$

where: the product is taken over all five parameters (AR, RO, Q, SM, SME, SL);  $f_i(x_i, T_i)$  is the distribution function corresponding to the parameter  $i$ ;  $\omega_i$  is the weight applied to each parameter.

The Composite Flood Risk Score (*CRI*) is then derived from the CDF, which quantifies the overall flood risk. It is calculated using:

$$CRI = \sum_{i=1}^6 \omega_i \cdot f_i(x_i, T_i) \quad (4)$$

Here: *CRI* is the Composite Risk Index, representing the total flood risk;  $\omega_i$  is the weight assigned to each parameter;  $f_i(x_i, T_i)$  is the cumulative distribution function for each parameter.

The *CRI* is then categorized into three risk levels that correspond to different flood severity levels:

- Low Risk:  $CRI \leq 0.3$  – Minimal risk of flooding.
- Medium Risk:  $0.3 < CRI \leq 0.6$  – Potential for localized to significant flooding.
- High Risk:  $CRI > 0.6$  – Severe to catastrophic flooding expected.

The *CRI* is continuously updated using real-time data from the WRF model and local hydrological observations, allowing for timely flood alerts when the *CRI* exceeds thresholds for higher-risk categories.

These alerts are disseminated to relevant authorities and the public via the integrated geo-hazard alert system, providing a comprehensive flood forecasting tool.

Model outputs, including 24-hour accumulated precipitation, surface runoff, river discharge, soil moisture, and snowmelt (snow water equivalent), are processed to generate flood hazard maps at 12-hour intervals.

These maps categorize flood risk into three zones: low (yellow), moderate (orange), and high (red).

Additionally, population impact is assessed, ranging from low (<1K) to high (>10K). For instance, Skenderaj was identified as a high-risk area on both January 18 and 19, 2023, with a moderate population impact (1K – 10K affected individuals).

Geographic Information System (GIS)-based analysis was used to overlay model outputs with terrain characteristics, soil types, and land use. This integrative approach identified areas prone to flash floods, landslides, and severe soil erosion. The performance of the hydrological model was validated by

comparing simulated flood extents and discharge rates with historical flood records and field observations, ensuring its reliability in predicting extreme events.

## 4. Results

### 4.1. Simulation of rainfall patterns

The interpretation of results begins with analyzing total precipitation amounts over 24, 48, and 60 hours, obtained from the ARW triple-nested run (Fig. 3).

The simulation with the 2-km nested run provides a more realistic depiction of accumulated precipitation over Kosovo. Based on rainfall patterns, the highest precipitation amounts occurred between January 19 at 00 UTC and January 20 at 00 UTC, primarily in the northwestern regions of Kosovo. The total 60-hour accumulation in Istog, the westernmost location, exceeded 130 mm, while in Skenderaj, where flooding was recorded, the total reached 44.1 mm.

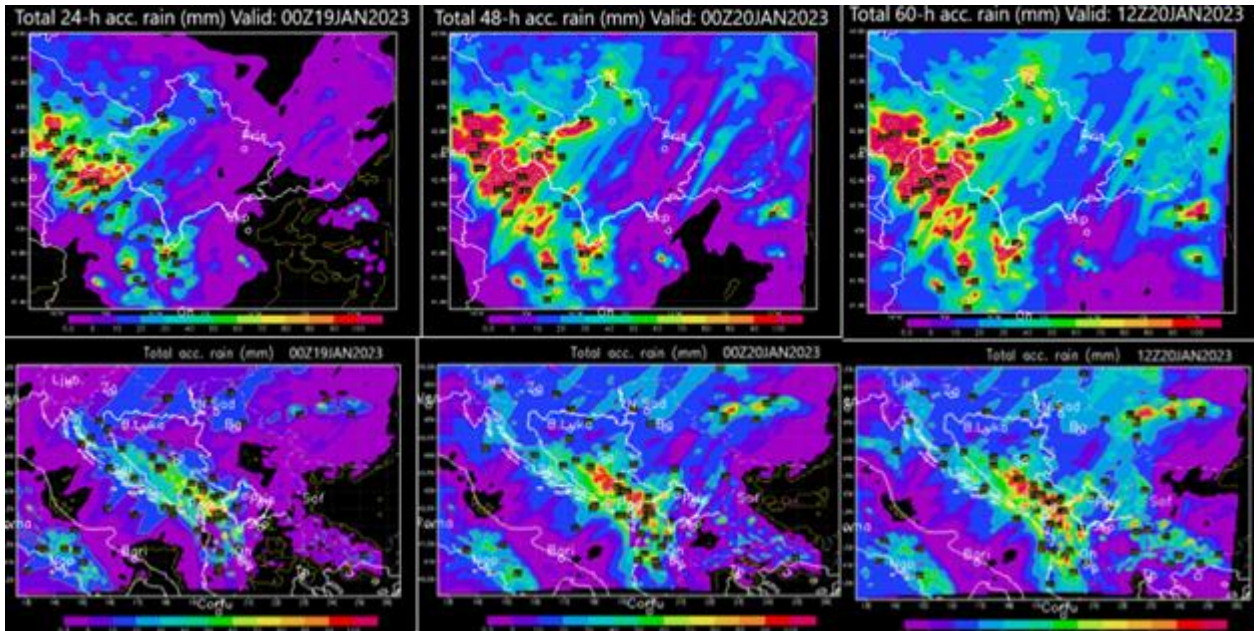


Fig. 3. ARW forecast of total accumulated precipitation (mm) over 24, 48, and 60 hours, with the 2-km run shown in the upper panels and the 6-km run in the lower panels.

The 6-km run captured the spatial distribution of precipitation reasonably well, but underestimated the accumulated amounts, with 55.4 mm for Istog and 33.6 mm for Skenderaj. The relative rainfall intensities for both nested runs can be assessed using the time series of hourly rainfall (mm) (Fig. 4a-b). The ARW 2-km nested run (Fig. 4a) indicates two peaks of intense hourly precipitation: one on January 18 from 05-06 UTC in Istog (white curve) and another during the intense rainfall period on January 19 from 10-11 UTC. For Skenderaj, two smaller peaks are observed on January 18, from 07-08 UTC, with intensities of 6.4 mm/h and 5 mm/h, and another from 08-09 UTC, both with relative intensities of 4 mm/h. The 6-km run shown in Figure 4b, covering a larger area, captured the timing of the peaks in Istog and Skenderaj but underestimated the hourly precipitation amounts.

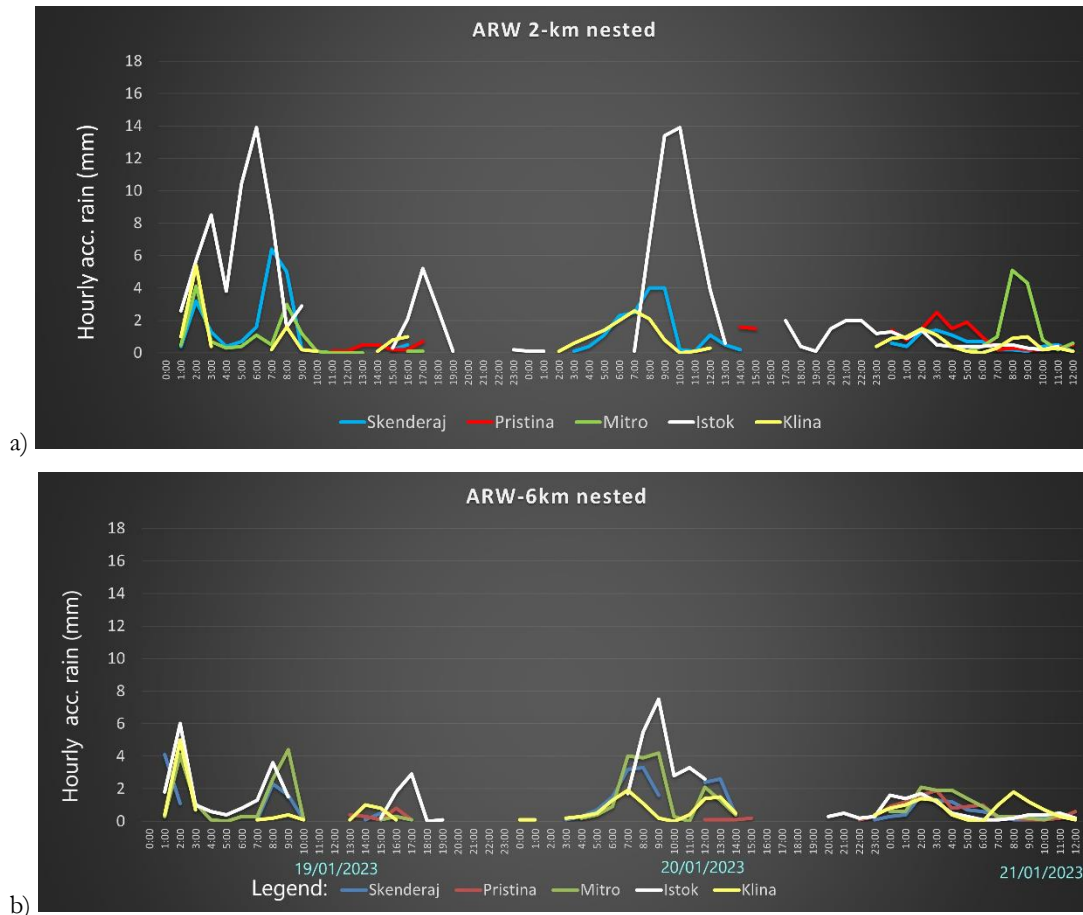


Fig. 4. Time series of relative rainfall intensities during the simulation period using (a) the ARW 2-km (upper chart) and (b) the ARW 6-km (lower chart) run.

In the NMM model simulations, in addition to total precipitation, snowfall amounts are also included. Among all numerical experiments, starting with the 1-km, 2-km, and 4-km grid resolutions for smaller and larger areas, and the 3-km resolution for a uniform area, the experiment with the 4-km resolution provided the most realistic results. The integration domain covers a larger area of Southeast Europe, including various geographical regions such as the Adriatic, Ionian, and Aegean Seas, parts of the Alps, the Dinarides, and the mountainous complexes of western Macedonia, as well as the complex topography and landscapes of the area. For this reason, the model maps of accumulated precipitation and relative intensities are presented in Appendix A, allowing readers to become more familiar with the rainfall patterns and time series. Here, we focus on interpreting the results for the NMM 4-km integration, with a time step of 8 seconds and explicit treatment of convective processes. The simulation over a larger area with a 4 km horizontal resolution shows widespread rainfall over the central Balkans and the southern part of the Apennine Peninsula. It is evident that in some areas of Herzegovina and Montenegro, the total precipitation amounts exceed 100 mm over the 60 hours, while the model shows around 200 mm in northern Albania. Based on the model results, no significant precipitation amounts were observed in Kosovo during the first 24 hours of the simulation, except for the extreme western mountainous region. However, in the next 24-48 hours, the total precipitation amount increases significantly. The largest

simulated 60-hour total is in Pristina (around 59.2 mm), while in Skenderaj, it is 42.2 mm, which is very similar to the ARW 2-km run. It is important to note that the NMM 4-km model calculated maximum hourly precipitation for Skenderaj as 17.1 mm, during the period when the flood occurred. In contrast, the ARW 2-km nested run underestimated the maximum hourly precipitation about 2-fold. The difference is that the two peaks correspond to the location of Istog. Additionally, the total 60-hour accumulated precipitation was 2.5 times higher than that obtained using the NMM 4-km model. The ARW model uses the Thompson, Eidhammer (2014) microphysics scheme, the Yonsei Univ. (YSU) PBL scheme for parameterization of the atmospheric boundary layer (Hong 2010), and a scale- and aerosol-aware convective parameterization scheme (Shin, Hong 2015; Han et al. 2016) for the 18 and 6-km grid. The 2-km run was performed with explicit treatment of convection, avoiding parameterization. On the other hand, the NMM 4-km run utilizes the Thompson microphysics scheme without convection parameterization. It is evident that the ARW model better reproduced the spatial distribution of total precipitation amounts, while the NMM model more accurately detected the relative precipitation intensities. As for the snowfall shown over the accumulated 24, 48, and 60 hours, it is evident that during the first 24 hours, snowfall occurs over the Alps, central parts of the Apennine Peninsula, and the Dinarides. In the next 24 hours, snow accumulates over the northwestern parts of Kosovo, western Macedonia, and toward Greece. With the passage of the cold front, a larger portion of the central Balkans experienced increased snow accumulation.

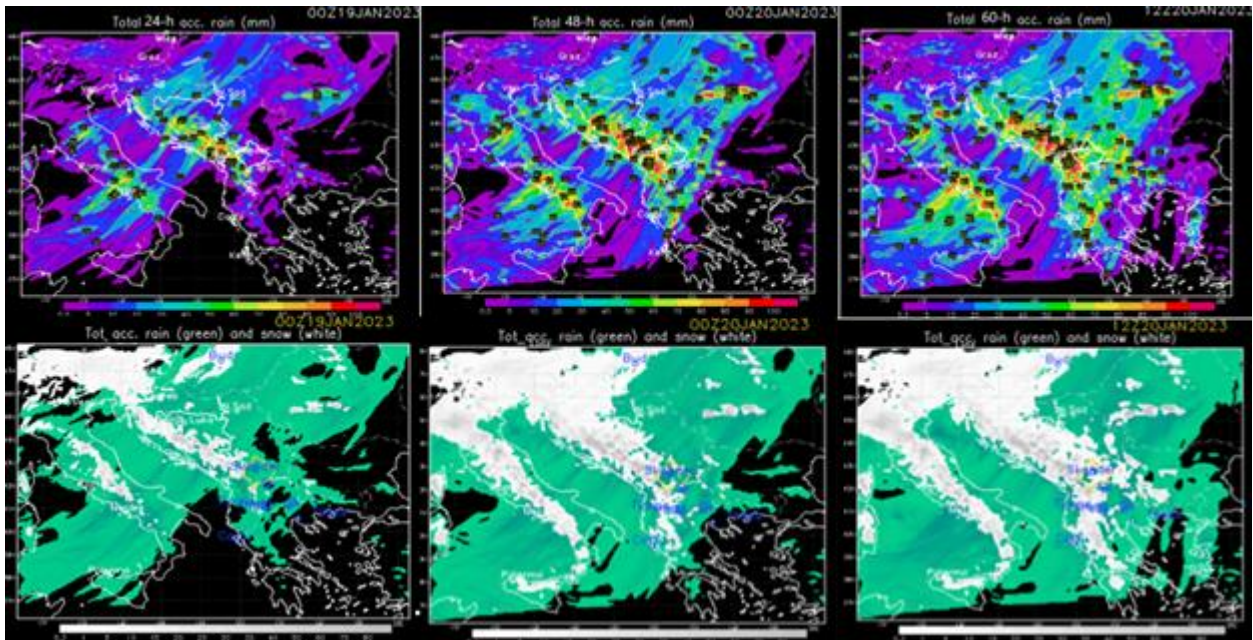


Fig. 5. NMM forecast of total accumulated rain (upper) and snow (lower) in mm for southeastern Europe, with 24, 48, and 60 hours lead time. The model was initialized on January 18, 2023, at 00 UTC.



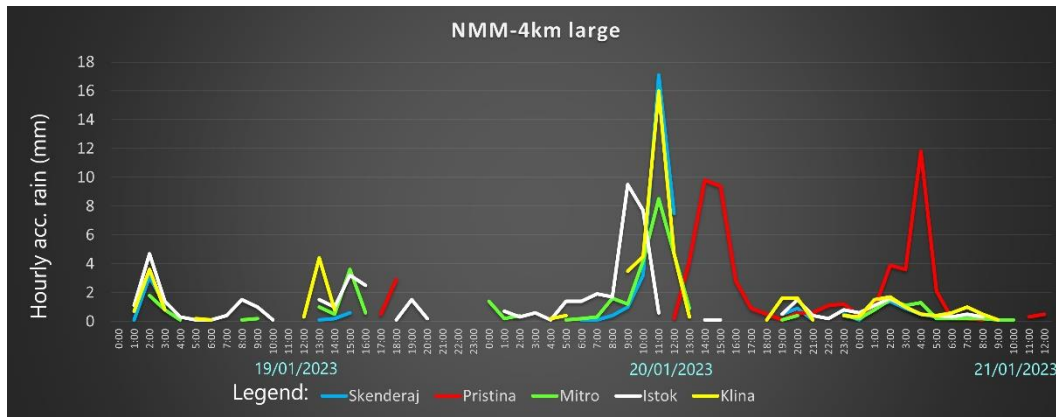


Fig. 6. Time series of rainfall intensities at five locations during the simulation period using the NMM 4-km run.

#### 4.2. Prototype evaluation of a multi-source hydrometeorological flood early warning system

To demonstrate the capabilities of the newly developed early warning methodology, a prototype hydrometeorological flood alert system was applied to a significant precipitation event that affected Kosovo on January 18-19, 2023. This system integrates high-resolution numerical weather prediction outputs with key hydrological and geomorphological parameters to assess flood potential with improved spatial and temporal accuracy.

The geo-hazard mapping framework was designed to evaluate flood susceptibility based on cumulative impacts from both prolonged stratiform and short-duration convective rainfall. The Novel Thunderstorm Alert System (NOTHAS) (Spiridonov et al. 2021, 2022, 2023) was used to forecast convective activity and issue corresponding alerts. Numerical experiments revealed that NOTHAS, running at a 4 km spatial resolution with a 36-hour lead time, effectively identified zones of significant instability. As shown in Figure 7, a Level 3 flood alert was issued across much of Kosovo during the peak rainfall period on January 19, capturing the critical timing and spatial extent of the event. In parallel, alternative model configurations also detected areas of potential localized flooding, although some underestimations were noted – particularly in simulations using the NMM model with smaller domain coverage. These results emphasize the importance of domain configuration and model selection in operational forecasting. To enhance the precision of flood risk evaluation, additional analysis was conducted using a flood risk potential mapping (FRPM) algorithm. This tool integrates WRF-ARW model outputs with geospatial data including terrain slope, digital elevation models (DEMs), drainage density, river proximity, land use characteristics, soil types, and dynamic hydrological indicators such as river discharge, runoff, and snow water equivalent. By combining these multiple data sources, the FRPM algorithm generates spatially resolved flood risk maps, as illustrated in Figure 8, offering a robust foundation for early warning and impact assessment. Together, these prototype results illustrate the utility of a coupled meteorological and hydrological alert system, supporting real-time flood preparedness and mitigation planning.

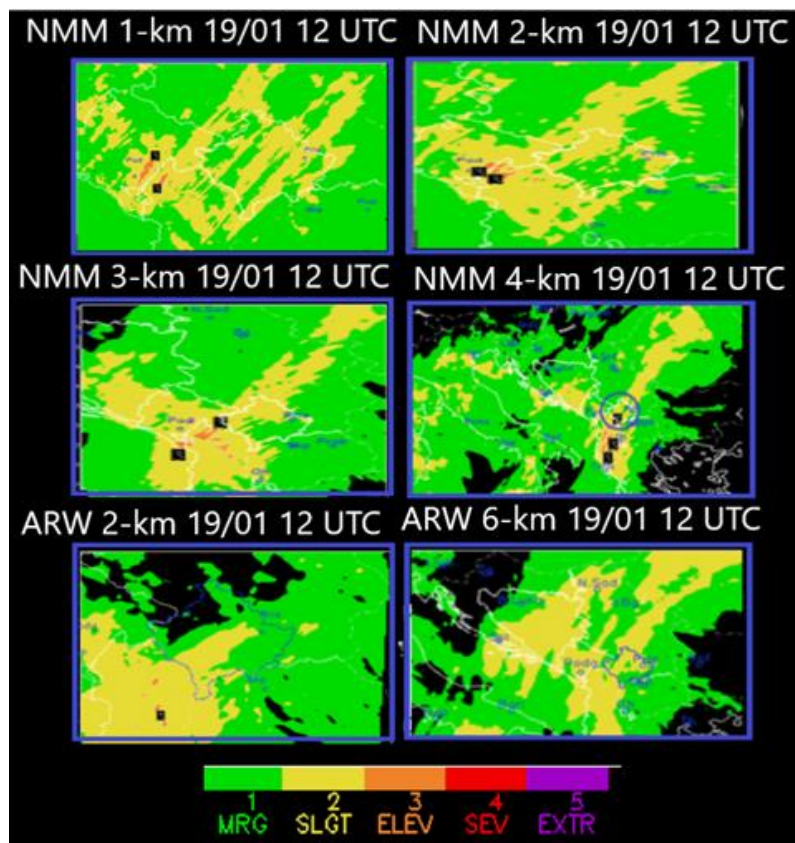


Fig. 7. NOTHAS severe weather alert with different model configurations. Valid: 19 January 2023, 12 UTC.

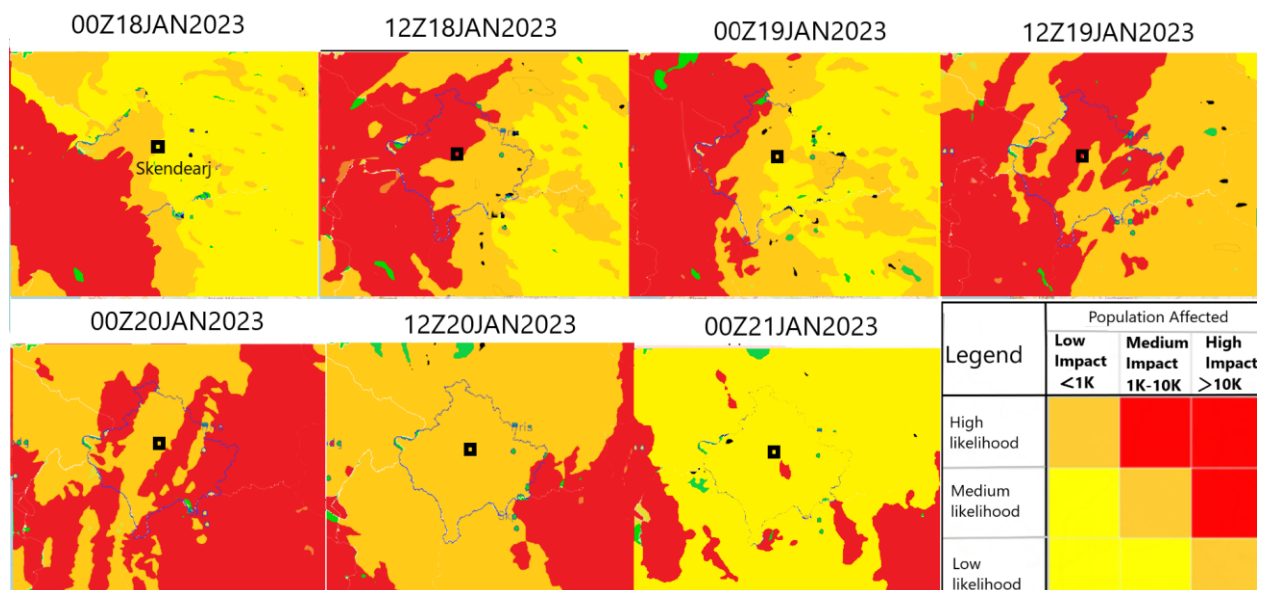


Fig. 8. Flood potential risk mapping and impact assessment of Kosovo, based on the WRF-ARW model. Valid: 00Z18JAN2023 00:00 UTC at 12-hour intervals.

### 4.3. Comparative analysis and verification

To assess the reliability of the flood forecasting system, a comparative analysis was performed between the numerical simulations and the European Flood Awareness System (EFAS) platform outputs. The results showed strong agreement with the observed precipitation fields (Fig. 9a), providing a solid foundation for integrating additional parameters influencing flood dynamics. The ARW nested run at 2 km resolution

produced more detailed rainfall patterns, capturing areas of maximum precipitation. Although the EFAS flood alert system primarily represents 24-hour observed precipitation, the spatial distribution of rainfall was accurately depicted in other simulations, despite some underestimation of total precipitation, particularly in the NMM 4-km run. Combined daily GPCP satellite-gauge data for Kosovo and ERA5 hourly time-series data were used for verification of simulated precipitation and temporal intensities (Fig. 9b). The EFAS system, particularly for January 19 and 20, 2023 (Fig. 9b), highlighted Skenderaj as a high-risk area between downstream regions along the White Drin and Ibar Rivers. This zone was identified as having a high probability of exceeding the 5-year maximum precipitation threshold, providing valuable insights into flood formation and propagation.

A comparison of the newly developed flood risk system with the EFAS impact assessment revealed a strong correlation between the two, particularly for high-risk areas from January 18 to 20, 2023 (Fig. 9c). The initial results were promising, demonstrating agreement in flood risk identification. However, further model sensitivity studies are necessary to refine geomorphological factor assessments and tests across different geographical regions and flash-flood scenarios, enhancing the robustness and predictive accuracy of the flood risk system.



Fig. 9a. Observed precipitation (mm). European Flood Awareness System (EFAS). Valid: 19-21 Jan 2023, 00:00 UTC.

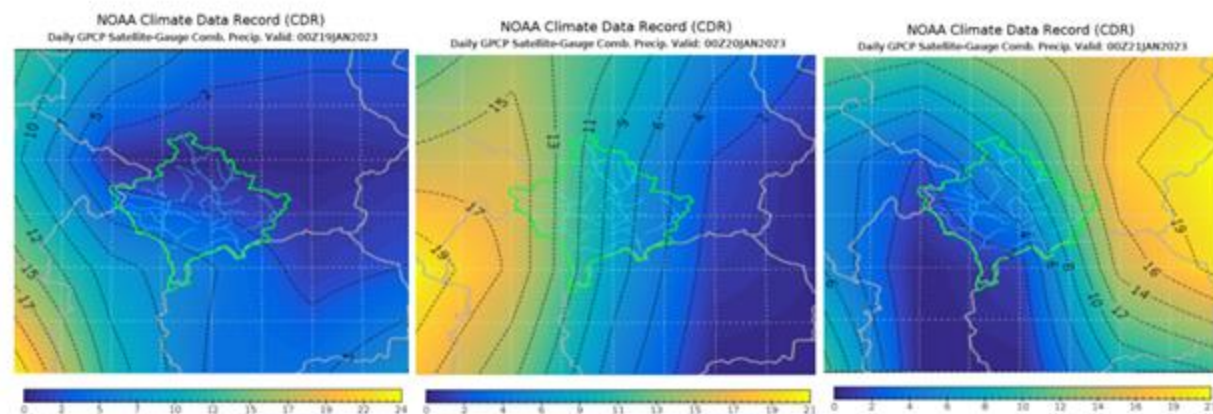


Fig. 9b. Daily GPCP Satellite-Gauge Comb. Precipitation from NOAA. European Flood Awareness System (EFAS). Valid: 19-21 Jan 2023, 00:00 UTC.



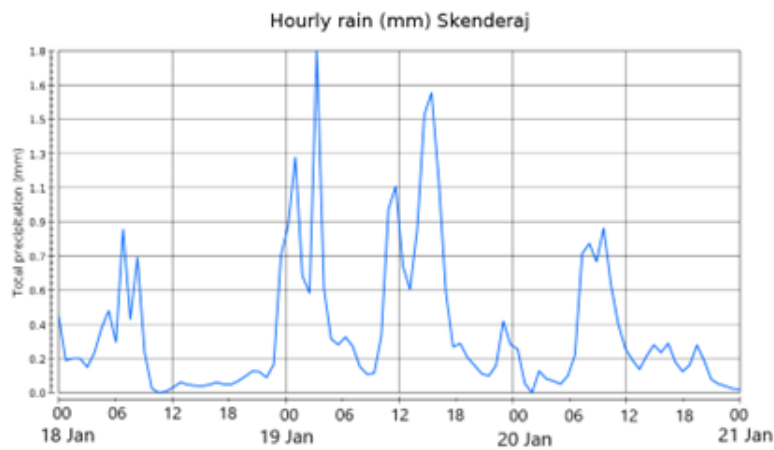


Fig. 9c. ERA5 hourly time-series data on single levels from 18/01/2023 00:00 to 21/01/2023 00:00. European Flood Awareness System (EFAS). Valid: 19-21 Jan 2023, 00:00 UTC.

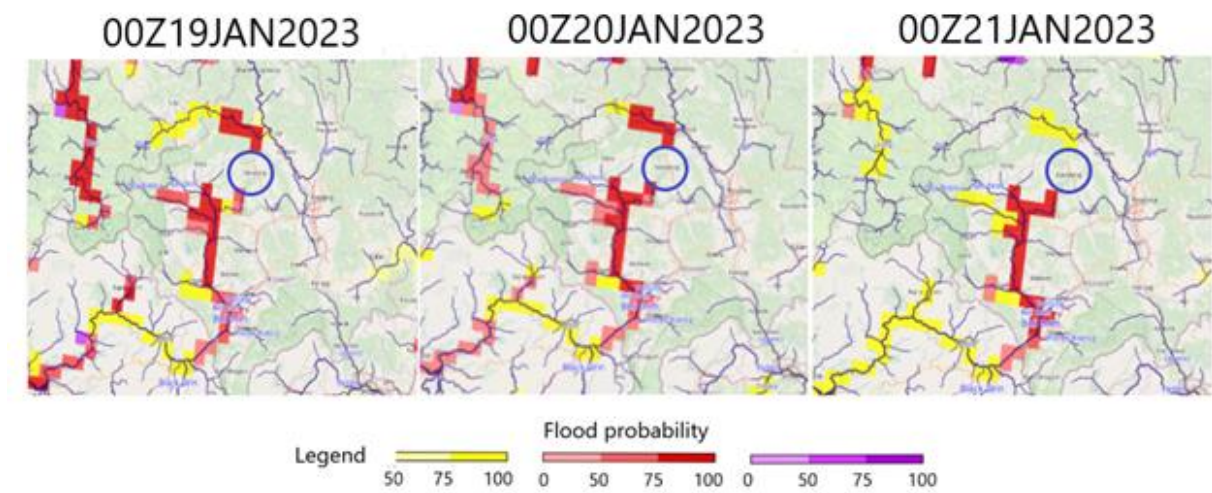


Fig. 9d. Flood probability and threshold level exceedance ongoing. European Flood Awareness System (EFAS). Valid: 19-21 Jan 2023, 00:00 UTC.

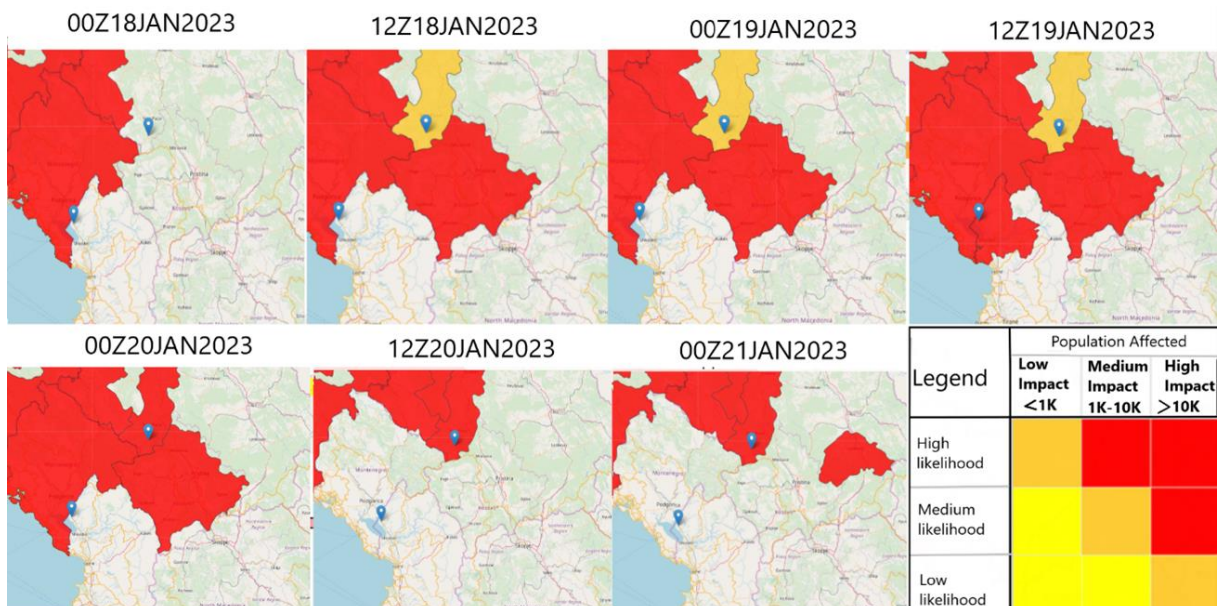


Fig. 9e. Rapid impact assessment. Layers show the main catchments and major rivers in the central domain of Kosovo. European Flood Awareness System (EFAS). Valid: 19-21 Jan 2023, 00:00 UTC.

Regarding flood risk probabilities, the EFAS system, particularly for January 19 and 20, 2023 (Fig. 9d), indicates that the Skenderaj watershed is positioned between high-risk areas downstream along the White Drin River and the lower reaches of the Ibar River. This region exhibits a high probability of exceeding the 5-year maximum total precipitation threshold (red), as derived from the combined ensemble model outputs. In addition to meteorological factors that contributed to flood initiation, this detail may provide further insights into the formation and propagation of flooding in the Skenderaj region. A comparison between the newly developed flood risk mapping system, based on ARW and NMM model outputs and a diagnostic algorithm that incorporates both meteorological and hydro-geological parameters, reveals a strong correlation with the EFAS impact assessment for the same analysis period (Fig. 9e). The initial results are highly encouraging, demonstrating a clear agreement in high-risk areas from January 18, 2023, 12 UTC to January 20, 2023, 00 UTC.

However, to obtain more reliable results, further model sensitivity studies are necessary, incorporating a more detailed assessment of geomorphological factors and testing across different geographical regions and flash-flooding case studies. These steps will enhance the robustness and predictive accuracy of the flood risk assessment system.

## 5. Conclusions

This study provides a comprehensive assessment of the January 2023 extreme rainfall event in Kosovo, with a focus on enhancing early warning capabilities through the integration of meteorological and hydrological modeling. High-resolution simulations using the 2-km WRF-ARW model more accurately captured the spatial and temporal dynamics of precipitation – particularly over localities such as Skenderaj and Istog – compared to coarser simulations, which tended to underestimate peak rainfall intensities and their timing.

The 4-km WRF-NMM model contributed to a broader understanding of precipitation distribution across southeastern Europe, but lacked the spatial precision needed for effective flash flood detection at the small catchment scale. Differences in model performance were linked to domain resolution, microphysical parameterizations, and representation of convective processes. A series of numerical experiments was conducted to examine model sensitivity to various configurations, including the model core used (ARW vs. NMM), initialization method (nested versus single-domain deterministic runs), scalability of atmospheric processes (in terms of spatial and temporal resolution), and the selection of microphysical and convective schemes. These experiments helped identify key drivers of simulation accuracy, especially in small, flood-prone catchments.

Hydrological analyses revealed elevated surface runoff, increased soil saturation, and peak river discharge across critical areas, reflecting the strong coupling between atmospheric forcing and catchment response.

Particularly in the Skenderaj watershed, hydrological indicators suggested heightened flash flood potential, even in the absence of major river channels. This emphasizes the importance of refined diagnostic tools for flash flood detection in small basins.

A key contribution of this study is the development of a probabilistic flash flood forecasting methodology based on a cumulative distribution function (CDF) that integrates key hydrological variables – such as river discharge, runoff, drainage density, terrain slope, and soil moisture – with meteorological output from the WRF-ARW model. By calibrating threshold values that represent the combined atmospheric and hydrological drivers of flash floods, the framework enables impact-based flood categorization tailored to local-scale dynamics, with effectiveness demonstrated in the Skenderaj basin. The incorporation of NOTHAS and GIS-based geo-hazard mapping further improved the spatial localization of high-risk zones. Comparative validation against EFAS forecasts confirmed the reliability of the simulations, demonstrating consistency in both the intensity and spatial extent of the event.

Unlike traditional flood forecasting methods that often rely on deterministic hydrological modeling or river stage thresholds, the proposed CDF-based system offers a more adaptive and probabilistic approach that accounts for multiple interacting drivers of flash floods. This approach is particularly valuable for data-scarce, small catchments where real-time measurements are limited and forecast uncertainty is high.

This research introduces a novel approach for coupling meteorological simulations with hydrology-based alert algorithms. It highlights the value of integrated risk metrics grounded in hydrometeorological principles, particularly for early warning in small and vulnerable catchments. However, further case studies and numerical experiments are essential to test robustness across diverse events and hydrological settings before this methodology can be considered for operational use by water management and crisis response agencies in Kosovo. The findings represent a promising step toward localized, data-driven flood forecasting systems, with strong potential for real-time implementation in disaster risk reduction frameworks.

## **Acknowledgments**

We express our sincere appreciation to the Hydrometeorological Institute of Kosovo for their generous provision of precipitation data and daily rainfall distribution for the case study event. Our gratitude extends to the Faculty of Computer Science and Engineering (FINKI) for the invaluable access granted to advanced computing facilities, essential for running our model effectively.

Special recognition is reserved for the editor and the anonymous reviewers, whose dedication and time invested in providing insightful reviews and constructive recommendations significantly enriched the quality of our work.

## **References**

- Agaj T., Jaskula J., Bytyqi V., Agaj S., 2024, Understanding flood in Kosovo: Spatial patterns, urban influences and implications for resilience in Lumbardhi i Pejës and Klina catchments, *International Journal of Disaster Risk Reduction*, 113, DOI: 10.1016/j.ijdr.2024.104830.
- Alfieri L., Burek P., Dutra E., Krzeminski B., Muraro D., Thielen J., Pappenberger F., 2013, GloFAS – global ensemble streamflow forecastin and flood early warning, *Hydrology and Earth System Sciences*, 17 (3), 1161-1175, DOI: 10.5194/hess-17-1161-2013.
- Archer D.R., Leesch F., Harwood K., 2006, Learning from the extreme River Tyne flood in January 2005, *Water Environment Journal*, 21 (2), 133-141, DOI: 10.1111/j.1747-6593.2006.00058.x.
- Bernardet L.R., Grasso L.D., Nachamkin J.E., Finley C.A., Cotton W.R., 2000, Simulating convective events using a high-resolution mesoscale model, *Journal of Geophysical Research: Atmospheres*, 105 (D11), 14963-14982, DOI: 10.1029/2000JD900100.
- Borga M., Boscolo P., Zanon F., Sangati M., 2007, Hydrometeorological analysis of the 29 August 2003 flash flood in the Eastern Italian Alps, *Journal of Hydrometeorology*, 8 (5), 1049-1067, DOI: 10.1175/JHM593.1.
- Chawla I., Osuri K.K., Mujumdar P.P., Niyogi D., 2018, *Hydrology and Earth System Sciences*, 22 (2), 1095-1117, DOI: 10.5194/hess-22-1095-2018.
- Chinta S., Sai J.Y., Balaji C., 2021, Assessment of WRF model parameter sensitivity for high-intensity precipitation events during the Indian summer monsoon, *Earth and Space Science*, 8 (6), DOI: 10.1029/2020EA001471.
- Cluckie I.D., Han D., 2000, Fluvial flood forecasting, *Water and Environmental Management*, 14 (4), 270-276, DOI: 10.1111/j.1747-6593.2000.tb00260.x.
- Didovets I., Krysanova V., Bürger G., Snizhko S., Balabukh V., Bronstert A., 2019, Climate change impact on regional floods in the Carpathian region, *Journal of Hydrology: Regional Studies*, 22, DOI: 10.1016/j.ejrh.2019.01.002.
- Dobler C., Bürger G., Stötter J., 2012, Assessment of climate change impacts on flood hazard potential in the Alpine Lech watershed, *Journal of Hydrology*, 460-461, 29-39, DOI: 10.1016/j.jhydrol.2012.06.027.
- Dudhia J., 1989, Numerical study of convection observed during the Winter Monsoon Experiment using a mesoscale two-dimensional model, *Journal of the Atmospheric Sciences*, 46 (20), 3077-3107, DOI: 10.1175/1520-0469(1989)046<3077:NSOCOD>2.0.CO;2.
- Elmore K.L., Stensrud D.J., Crawford K.C., 2002, Ensemble cloud model applications to forecasting thunderstorms, *Journal of Applied Meteorology*, 41, 363-383, DOI: 10.1175/1520-0450(2002)041<0363:ECMATF>2.0.CO;2.
- Ferrier B.S., 1994, A double-moment multiple-phase four-class bulk ice scheme. Part I: Description, *Journal of Atmospheric Sciences*, 51 (2), 249-280, DOI: 10.1175/1520-0469(1994)051<0249:ADMMPF>2.0.CO;2.
- Giannaros C., Dafis S., Stefanidis S., Giannaros T.M., Koletsis I., Oikonomou C., 2022, Hydrometeorological analysis of a flash flood event in an ungauged Mediterranean watershed under an operational forecasting and monitoring context, *Meteorological Applications*, 29 (4), DOI: 10.1002/met.2079.
- Han J.-Y., Hong S.-Y., 2018, Precipitation forecast experiments using the Weather Research and Forecasting (WRF) model at gray-zone resolutions, *Weather and Forecasting*, 33, 1605-1616, DOI: 10.1175/WAF-D-18-0026.1.
- Han J.-Y., Hong S.-Y., Sunny Lim K.-S., Han J., 2016, Sensitivity of a cumulus parameterization scheme to precipitation production representation and its impact on a heavy rain event over Korea, *Monthly Weather Review*, 144 (6), 2125-2135, DOI: 10.1175/MWR-D-15-0255.1.
- Hapuarachchi H.A.P., Wang Q.J., Pagano T., 2011, A review of advances in flash flood forecasting, *Hydrological Processes*, 25 (18), 2771-2784, DOI: 10.1002/hyp.8040.
- Hersbach H., Bell B., Berrisford P., Hirahara S., Horányi A., Muñoz Sabater J., Nicolas, Peubey C., Radu R., Schepers D., Simmons A., Soci C., Abdalla S., Abellan X., Balsamo G., Bechtold P., Biavati G., Bidlot J., Bonavita M., De Chiara G., Dahlgren P., Dee D., Diamantakis M., Dragani R., Flemming J., Forbes R., Fuentes M., Geer A., Haimberger L., Healy S., Hogan R.J., Hólm E., Janisková M., Keeley S., Laloyaux P., Lopez P., Lupu C., Radnoti G., de Rosnay P., Rozum I., Vamborg F., Villaume S., Thépaut J.-N., 2020, The ERA5 global reanalysis, *Quarterly Journal of the Royal Meteorological Society*, 146 (730), 1999-2049, DOI: 10.1002/qj.3803.

- Hong S.-Y., 2010, A new stable boundary-layer mixing scheme and its impact on the simulated East Asian summer monsoon, *Quarterly Journal of the Royal Meteorological Society*, 136 (651), 1481-1496, DOI: 10.1002/qj.665.
- Hong S.Y., Lim J.-O.J., 2006, The WRF single-moment 6-class microphysics 515 scheme (WSM6), *Asia-Pacific Journal of Atmospheric Sciences*, 42 (2), 129-151.
- Janjic Z.I., 1996, The surface layer in the NCEP Eta Model, preprints, 11<sup>th</sup> Conference on Numerical Weather Prediction, Norfolk, VA, American Meteorological Society, 354-355.
- Janjic Z.I., 2001, Nonsingular Implementation of the Mellor-Yamada Level 2.5 Scheme in the NCEP Meso model, National Centres for Environmental Prediction (NCEP), Office Note #437, available online at [https://repository.library.noaa.gov/view/noaa/11409/noaa\\_11409\\_DS1.pdf](https://repository.library.noaa.gov/view/noaa/11409/noaa_11409_DS1.pdf) (data access 06.08.2025).
- Janjic Z.I., 2003, A nonhydrostatic model based on a new approach, *Meteorology and Atmospheric Physics*, 82, 271-285, DOI: 10.1007/s00703-001-0587-6.
- Jankov I., Gallus W.A. Jr., Segal M., Koch S.E., 2007, Influence of initial conditions on the WRF-ARW model QPF response to physical parameterization changes, *Weather and Forecasting*, 22 (3), 501-519, DOI: 10.1175/WAF998.1.
- Kain J.S., Weiss S.J., Levit J.J., Baldwin M.E., Bright D.R., 2006, Examination of convection-allowing configurations of the WRF-NMM model for the prediction of severe convective weather: The SPC/NSSL Spring Program 2004, *Weather and Forecasting*, 21 (2), 167-181, DOI: 10.1175/WAF906.1.
- Kane S., Shogren J.F., 2000, Linking adaptation and mitigation in climate change policy, *Climatic Change*, 45, 75-102, DOI: 10.1023/A:1005688900676.
- Lee J.W., Hong S.Y., 2006, A numerical simulation study of orographic effects for a heavy rainfall event over Korea using the WRF model, *Atmosphere*, 16 (4), 319-332.
- Liu C., Guo L., Ye L., Zhang S., Zhao Y., Song T., 2018, A review of advances in China's flash flood early-warning system, *Natural Hazards*, 92, 619-634, DOI: 10.1007/s11069-018-3173-7.
- Liu Y., Chen Y., Chen O., Wang J., Zhuo L., Rico-Ramirez M.A., Han D., 2021, To develop a progressive multimetric configuration optimisation method for WRF simulations of extreme rainfall events over Egypt, *Journal of Hydrology*, 598, DOI: 10.1016/j.jhydrol.2021.126237.
- Mlawer E.J., Taubman S.J., Brown P.D., Iacono M.J., Clough S.A., 1997, Radiative transfer for inhomogeneous atmospheres: RRTM, a validated correlated-k model for the longwave, *Journal of Geophysical Research*, 102 (D14), 16663-16682, DOI: 10.1029/97JD00237.
- Misenis C., Zhang Y., 2010, An examination of the sensitivity of WRF/Chem predictions to physical parameterizations, horizontal grid spacing, and nesting options, *Atmospheric Research*, 97 (3), 315-334, DOI: 10.1016/j.atmosres.2010.04.005.
- Moragoda N., Cohen S., 2020, Climate-induced trends in global riverine water discharge and suspended sediment dynamics in the 21st century, *Global and Planetary Change*, 191, DOI: 10.1016/j.gloplacha.2020.103199.
- Osmanaj L., Spiridonov I., Jakimovski B., Spiridonov V., 2025, Assessment of the WRF model in reproducing a flash-flood heavy rainfall event over Kosovo, *Acta Geophysica*, 73, 917-932, DOI: 10.1007/s11600-024-01365-9.
- Schwartz C., Romine G.S., Sobash R.A., Fossell K.R., Weisman M.L., 2015, NCAR's experimental real-time convection-allowing ensemble prediction system, *Weather and Forecasting*, 30 (6), 1645-1654, DOI: 10.1175/WAF-D-15-0103.1.
- Shin H.H., Hong S.-Y., 2015, Representation of the subgrid-scale turbulent transport in convective boundary layers at gray-zone resolutions, *Monthly Weather Review*, 143 (1), 250-271, DOI: 10.1175/MWR-D-14-00116.1.
- Skamarock W.C., Klemp J.B., Dudhia J., Gill D.O., Barker D.M., Duda M.G., Huang X.-Y., Wang W., Powers J.G., 2008, A Description of the Advanced Research WRF Version 3, NCAR Technical Note, NCAR/TN-475+STR.
- Spiridonov V., Baez J., Telenta B., Jakomovski B., 2020, Prediction of extreme convective rainfall intensities using a free-running 3-D sub-km-scale cloud model initialized from WRF km-scale NWP forecasts, *Journal of Atmospheric and Solar-Terrestrial Physics*, 209, DOI: 10.1016/j.jastp.2020.105401.
- Spiridonov V., Curic M., Grcic M., Jakimovski B., 2022, Ensemble cloud model application in simulating the catastrophic heavy rainfall event, *Journal of Atmospheric Science Research*, 5 (4), 35-49, DOI: 10.30564/jasr.v5i4.5081.

- Spiridonov V., Curic M., Sladic N., Jakimovski B., 2021, Novel Thunderstorm Alert System (NOTHAS), *Asia-Pacific Journal of Atmospheric Sciences*, 57, 479-498, DOI: 10.1007/s13143-020-00210-5.
- Spiridonov V., Grcić M., Sladić N., Ćurić M., Jakimovski B., 2023, The capability of NOTHAS in the prediction of extreme weather events across different climatic areas, *Acta Geophysica*, 71, 3007-3024, DOI: 10.1007/s11600-023-01122-4.
- Thielen J., Bartholmes J., Ramos M.-H., de Roo A., 2009, The European Flood Alert System – Part 1: Concept and development, *Hydrology and Earth System Sciences*, 13 (2) 125-140, DOI: 10.5194/hess-13-125-2009.
- Thompson G., Eidhammer T., 2014, A Study of aerosol impacts on clouds and precipitation development in a large winter cyclone, *Journal of the Atmospheric Sciences*, 71 (10), 3636-3658, DOI: 10.1175/JAS-D-13-0305.1.
- Thompson G., Field P.R., Rasmussen R.M., Hall W.D., 2008, Explicit forecasts of winter precipitation using an improved bulk microphysics scheme. Part II: Implementation of a new snow parameterization, *Monthly Weather Review*, 136 (12), 5095-5115, DOI: 10.1175/2008MWR2387.1.
- Varlas G., Papaioannou G., Papadopoulos A., Markogianni V., Vardakas L., Dimitriou E., 2023, Flash flood forecasting using integrated meteorological-hydrological-hydraulic modeling: Application in a Mediterranean river, *Environmental Sciences Proceedings*, 26 (1), DOI: 10.3390/environsciproc2023026035.
- Xue M., Martin W.J., 2006, A high-resolution modeling study of the 24 May 2002 Dryline Case during IHOP. Part I: Numerical simulation and general evolution of the dryline and convection, *Monthly Weather Review*, 134 (1), 149-171, DOI: 10.1175/MWR3071.1.

# Estimation of the energy potential of solar radiation and comparison with normative data for Ukraine

Ihor Redko<sup></sup>, Oleksandr I. Redko<sup></sup>, Andriy Redko<sup></sup>, Nina Bakumenko<sup></sup>, Adam Ujm<sup></sup>,  
Vadym Zadiranov<sup></sup>

<sup>1</sup> Ukrainian State University of Railway Transport, Ukraine

<sup>2</sup> O.M. Beketov National University of Urban Economy in Kharkiv, Ukraine

<sup>3</sup> Sumy National Agrarian University, Ukraine

<sup>4</sup> V.N. Karazin Kharkiv National University, Ukraine

<sup>5</sup> University of Applied Sciences in Nysa, Poland

## Abstract

This article presents the results of an analysis of the long-term variability of average monthly and annual solar radiation in Ukraine from 2011 to 2020. The measurement data are compared with earlier periods and the standard period of 1961-1990. The statistical characteristics of changes in solar radiation are determined. The characteristics of solar radiation are compared with normative data of the National Standard of Ukraine (DSTU-NBV.1.1.-27:2010). In recent years, the annual amounts of direct radiation have increased by 18-23%. The total annual radiation in 2020 was 6% greater than in 1961-1990. Hourly and daily direct and scattered radiation were analyzed with empirical dependencies and engineering calculations. The efficiency of using the sustainable potential of solar energy depends on the climatic characteristics of the specific area or region. Inconsistencies in regulations can therefore create a problem where the best places for energy production lack public interest, infrastructure, and cost-effective consumption. Depending on the regional climatic conditions of Ukraine, the solar energy potential varies from 1400 MJ/m<sup>2</sup> in the western regions to 1950 MJ/m<sup>2</sup> in the eastern ones. An important characteristic of solar energy resources is the duration of sunshine. For Kyiv, the average monthly duration varies from 180 h in March to 120 h in November. The possible annual duration of sunshine varies accordingly from 4452 h (2011) to 4481 h (2020). The maximum values were observed in June (331 h) and August (334 h).

## Keywords

Solar radiation, long-term change of total solar radiation, solar energy potential, climatic standard.

Submitted 12 July 2024, revised 11 June 2025, accepted 4 August 2025

DOI: 10.26491/mhwm/208954

## 1. Introduction

Solar radiation is characterized by high availability, stability, and thus is the least risky renewable energy source (RES) from an economic perspective (Mierzwiak et al. 2022; Liu et al. 2023; Kapica et al. 2024). Variability and uncertainty are the most difficult parameters to account for when evaluating the solar radiation potential. Variability is determined by processes associated with changes in the state of the atmosphere and the radiation balance of the Earth's surface. Uncertainty indicates the difficulty of forecasting when using various models of behavior of the object under study. There is a limit to the maximum production of electricity (heat), which changes over time and is difficult to predict (uncertainty). As power generation from RES penetrates further into the global energy system, it is necessary to provide accurate forecasts of solar energy potential to avoid the consequences of changing the parameters of the energy system and to ensure appropriate control.



Rational volume-planning, plasticity, and color scheme of facades make it possible to make maximum use of solar radiation to increase the comfort of the indoor environment. Sun protection of insulated facades prevents temperature deformation of the surface structure and stabilizes the temperature regime of the premises (Ujma 2014; Sadooghi, Kherani 2019). Climatological characteristics are used when performing energy calculations and drawing up energy passports and audits, as well as when designing heating and ventilation systems.

The climate of Ukraine has changed significantly in recent years (Lipinskyi et al. 2003; Murtazinova 2009; Voloshina, Kuryshina 2010; Rybchenko, Savchuk 2015; Lopushanska, Iwanow 2022). Existing standards (DSTU-NBV.1.1.-27:2010) need clarification for the development of engineering and architectural solutions for the energy efficiency of buildings. The DSTU-NBV.1.1.-27:2010 introduced climatic zoning of the territory of Ukraine. But the climate has changed in the past ten years, requiring that climate data in the standard documents be clarified.

In recent years in Ukraine, the duration of sunlight, as well as direct, scattered, and total solar radiation, have changed. However, a significant increase in the duration of sunlight and direct solar radiation in combination with a simultaneous decrease in diffuse radiation did not contribute to the growth of total radiation (Rybchenko, Savchuk 2013).

When designing installations that use solar energy, it is necessary to account for the spatio-temporal change in the distribution of solar radiation, which depends on astronomical and meteorological factors, i.e., the geographical latitude and the height of the sun, as well as the transparency of the atmosphere. Weather conditions in Ukraine depend on the large-scale circulation of the atmosphere over the northern hemisphere and regional features. The eastern regions of Ukraine are located on the axis of the extratropical maximum (Zubkovich 2013). This axis passes through Ukraine from the southwest to the northeast. One of the signs of modern climatic changes is a noticeable weakening of wind speed over Ukraine, which causes changes in synoptic characteristics. A predominance of significant baric gradients was observed over eastern Ukraine. A comparative analysis of the variability of average daily air temperature and daily precipitation in the winter season in Kyiv, in relation to the change in global temperature in the 20<sup>th</sup> century, is provided in Murtazinova (2009). That study analyzed data for 1910-2002, showing an increase in the variability of the average daily temperature in December and a sharp decrease in the inter-day variability in January and February.

Solar radiation varies depending not only on geographical latitude, but also on regional climatic conditions. Thus, in Precarpathia and the Ukrainian Carpathians, the solar energy potential (SEP) is 1400-1500 MJ/m<sup>2</sup>. In the summer, in the north of Ukraine, SEP is 1550-1800 MJ/m<sup>2</sup>, and in the eastern and central regions SEP is 1850-950 MJ/m<sup>2</sup>, increasing in the southern regions to 2000-2150 MJ/m<sup>2</sup> (Dmytrenko, Barandich 2007). When designing solar power plants, comprehensive indicators of the potential of solar energy are required (Dmytrenko, Barandich 2007; Rybchenko, Savchuk 2015), which are not measured widely enough in Ukraine. Therefore, it is necessary to develop methods for designing engineering systems and developing architectural solutions.

Analytical expressions for calculating specific solar heat fluxes for clear sky conditions depending on geographic latitude, inclination, time angle, and angle of inclination of the solar collector plane are given in Ozarkiv et al. (2007). The values of hourly direct and scattered radiation for the conditions of the city of Lviv (50° north latitude) are given. In Halchak et al. (2019), the results of modeling the parameters of the direct flow of solar radiation under a clear sky, accounting for the transparency of the atmosphere, are indicated. Average monthly values of the hourly change in the intensity of direct solar flux are used in the calculations.

Rybchenko and Savchuk (2015) and Dmytrenko and Barandich (2007) show the results of zoning based on a set of indicators of solar energy potential, duration of sunshine, and cloudiness. Average monthly values of solar radiation are determined using the NASA SSF database obtained from satellites. At the same time, data for the past five-year period are necessary to estimate the potential of solar energy (Madesh, Sandhu 2015). The NASA SSF database contains data for the period of 1983-2005.

Measurements are made at more than 1,000 weather stations in various places around the world. Calculations are performed for a grid of  $2.5 \times 2.5$  degrees of the earth's surface, thus the results are less accurate than those measured at weather stations. Methods of computer modeling and calculation of solar inflows were developed by Sergeychuk (2011) for non-standard solutions of enclosed structures using a point calculation device. The formation of the regime of solar heat gain from both direct solar rays and diffuse radiation in a building of complex geometry is also considered.

A large number of relevant computer programs have been created. The Atmospheric Radiation model was used to develop the DSTU-NBV.1.1.-27:2010. To use these computer packages, builders and designers must be highly qualified. Therefore, calculation engineering methods are being developed for practical application.

Statistical characteristics give an idea of the time structure of the series. The temporal structure of solar radiation ranges for Ukrainian cities has been little studied. Statistical characteristics of solar radiation are given in Pivovarova (1988). Interannual variability has been studied more than temporal and diurnal variability. In Kuznietsov and Lysenko (2017), it is shown that power change as a random process can be considered nearly stationary. The mathematical expectation of the magnitude of the jumps (change in power) is close to zero, and their distribution has signs of symmetry. The models use ratios recommended by the European Solar Radiation Catalog (ESRA). The numerical results are compared with the actinometric data of the Boryspil and Kovel stations. Noticeable differences are due to local daily and seasonal features of the state of the real atmosphere. Methods by which the energy exposure of the surface is estimated according to the parameters of solar flux, the intensity of which is calculated relative to the solar constant using approximate empirical estimates of the atmospheric transparency coefficient, are given in Mysak et al. (2014).

The purpose of this study is to analyze the patterns of multi-year distribution of actual solar radiation flows from 2011 to 2020, as well as to compare them with data from earlier periods and normative data.

## 2. Materials and methods

### 2.1. Study area

The solar radiation fields of Poland and Ukraine, as illustrated in Figure 1, are the subject of analysis. The geographical coordinates of Ukraine span from the westernmost point at 48°25'09"N, 22°08'14"E to the easternmost at 49°15'38"N, 40°13'41"E, the northernmost point at 52°22'45"N, 33°11'21"E, and the southernmost at 44°23'14"N, 33°44'17"E. The territory of Poland extends approximately from 49°00'N to 54°50'N and from 14°07'E to 24°08'E. The analysis focuses on solar radiation data over the period 2011-2020.

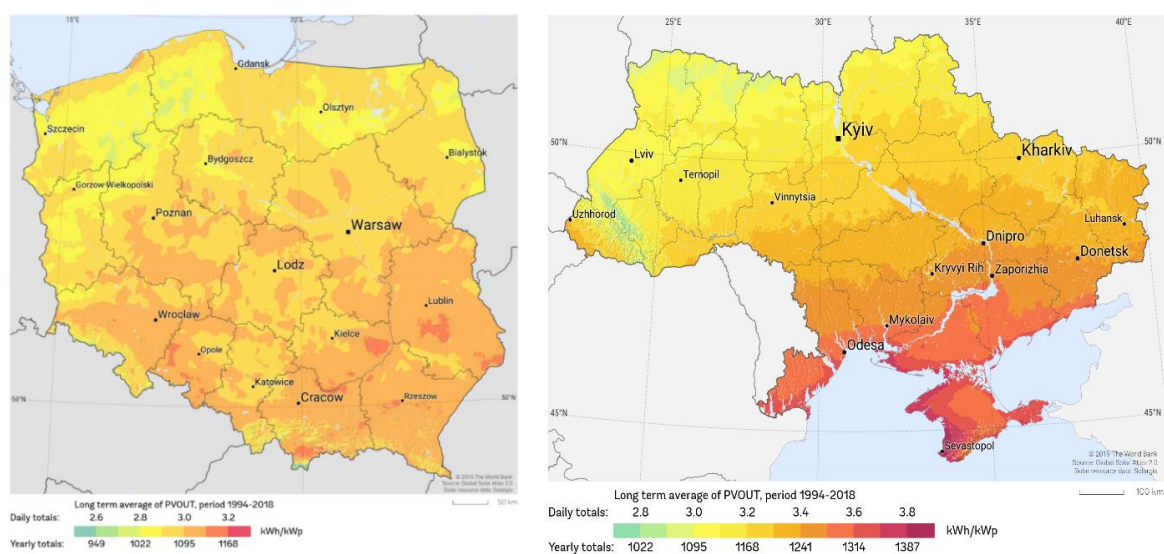


Fig. 1. The study area (Solar Resource Map, Global Solar Atlas-Poland (Solargis)).

Temporal changes in solar radiation for two Ukrainian cities – Kyiv (50°27' N, 30°31' E) and Odesa (46°29' N, 30°43' E). According to DSTU-NBV.1.1.-27:2010, the territory of Ukraine is divided into three regions for architectural and construction purposes: Polyssia and Forest Steppe (northwest), Steppe (southeast), and the Ukrainian Carpathians. The climatic characteristics of these regions differ significantly. The methodology for calculating the average monthly sums of direct and scattered solar radiation for different latitudes (44-50°N) and tabular data under conditions of clear sky and medium cloudiness are given. When calculating hourly energy illuminance from direct and scattered radiation, tabular data are for clear sky conditions. At cloudiness values of 10 points, tabular data are given for January and July; at other cloudiness values, data interpolation is required.

### 2.2. Data description

The study is based on observational data of monthly and annual averages of direct, diffuse, reflected, and global solar radiation on both horizontal and perpendicular surfaces under clear sky and average cloudiness conditions for the period 2011-2020 (a total of 120 months). The dataset contained gaps (April, June, and July 2020), which were filled using arithmetic mean values from the corresponding time series. Additionally, data on sunshine duration (monthly and annual averages) and the potential annual number of

clear days were used. The primary data source was the Borys Sreznevskyi Central Geophysical Observatory (Kyiv, Ukraine). Measurement data are presented for two meteorological stations (Table 1).

Table 1. Details of the meteorological stations.

Station name	Latitude	Longitude	Average annual temperature	Altitude
Kyiv (Boryspil, airport)	50°27'16.9"N	30°31'25.7"E	+9°C	184 m
Odesa (airport)	46°28'39"N	30°43'57.4"E	+11.3°C	57 m

To forecast the time series, its statistical characteristics were determined and compared with the normative values provided in the DSTU-NBV.1.1.-27:2010. Observation data from the Boryspil (Kyiv) meteorological station were compared with data from other cities (Katowice and Częstochowa, Poland) located at latitudes close to that of Kyiv (approximately 50°N). The main method used to identify trend and cyclical components in the time series was statistical, implemented using the STATISTICA software package (<https://www.statistica.com/en/software/tibco-data-science/-/tibco-statistica>).

### 2.3. Model performance

Statistical calculations were performed using the following equations:

- mathematical expectation:

$$M(x) = \sum_1^h x_i p_i \quad (1)$$

- 1<sup>st</sup> quartile  $Q_1$ , 2<sup>nd</sup> quartile (median)  $Q_2$ , 3<sup>rd</sup> quartile  $Q_3$ :

$$Q_1 = x_1 + h_i \frac{\frac{1}{4}n - \sum_{i=1}^{j-1} f_i}{f_j}; \dots Q_2 = \frac{h+1}{2}; \dots Q_3 = x_i + h_i \frac{\frac{3}{4}n - \sum_{i=1}^{j-1} f_i}{f_j} \quad (2)$$

- 2<sup>nd</sup> central moment (dispersion):

$$D = \frac{1}{n} \sum_i f_i (x_i - \bar{x})^2 \quad (3)$$

- mode:

$$M_0 = x_{i-1} + h_{M_0} \frac{f_i - f_{i-1}}{(f_i - f_{i-1}) + (f_i - f_{i+1})} \quad (4)$$

- coefficient asymmetry:

$$A_s = \frac{M_3}{G^3} \quad (5)$$

- kurtosis coefficient:

$$A_K = \frac{M_4}{G^4} - 3 \quad (6)$$

The calculations were made using the R 4.03 software for statistical data analysis (<https://www.r-project.org/>), free software with wide capability for various methods of data processing (Dalgaard 2008).

The monthly data were used to calculate hourly values of solar radiation according to the following methodology:

Incoming total solar radiation during the day is determined by the relation (Kalogirou 2014):

$$H_0 = \frac{3600h_s G_{sc}}{\pi} \left[ 1 + 0.33 \frac{360N}{365} \right] \times \left( \cos L \cdot \cos \delta \cdot \sin h_{ss} + \left( \frac{\pi h_{ss}}{180} \right) \sin L \cdot \sin \delta \right) \quad (7)$$

where:  $G_{sc}$  is the solar constant;  $G_{sc} = 1330 \text{ W/m}^2$ ;  $N$  is the day of the year;  $L$  is the geographical latitude;  $\delta$  is the declination of the sun;  $h_{ss}$  is the height of the sun;  $h_s$  is the length of the solar day.

$$h_s = \frac{2}{15} \cos^{-1}[-\tan L \cdot \tan \delta] \cos^{-1}[-\tan L \cdot \tan \delta]$$

$$\delta = 23.45 \cdot \sin \left[ \frac{360}{365} (N + 284) \right]$$

$$h_{ss} = \cos^{-1}[-\tan L \cdot \tan \delta]$$

The temporal arrivals of solar radiation are determined by the relation (Collares-Perera, Rabl 1979):

$$r = \frac{i}{H_0} = \frac{\pi}{24} [\alpha + \beta \cosh] \cdot \frac{(\cosh - \cosh_{ss})}{\sinh_{ss} - \frac{2\pi h_{ss}}{360} \cosh_{ss}} \quad (8)$$

where:  $\alpha = 0.409 + 0.5016 \sin(h_{ss} - 60)$ ;  $\beta = 0.6609 - 0.4767 \sin(h_{ss} - 60)$ .

### 3. Main results and their discussion

Figure 2 shows the long-term change in total solar radiation for the conditions of Kyiv (Boryspil station) (Fig. 2a) and Odesa (Fig. 2b).

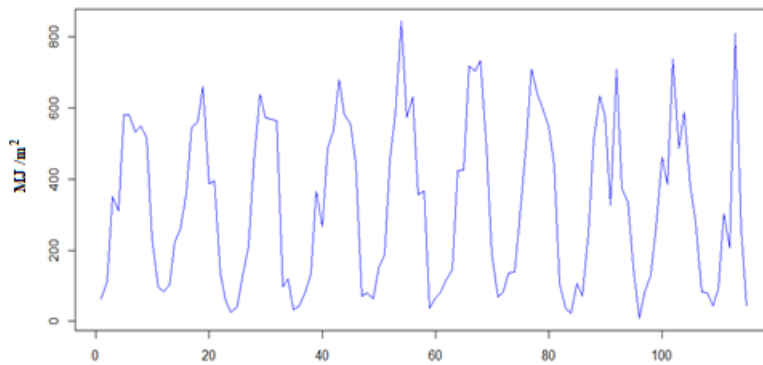


Fig. 2a. Solar radiation on a perpendicular surface (I) by month from January 2011 to December 2020.

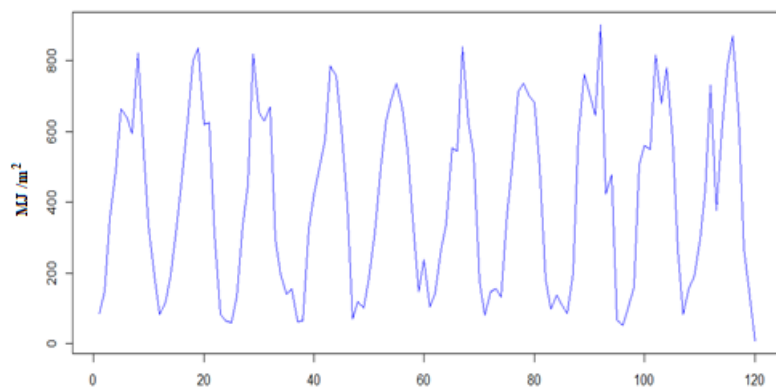


Fig. 2b. Solar radiation on a perpendicular surface (I) by month from January 2011 to December 2020.

Table 2 shows data from the State Standard of Ukraine 2010 for Kyiv, compared with data from other weather stations located near 50°N.

Table 2. Total solar radiation according to data from weather stations close to 50°N by month (horizontal surface, average cloudiness).

Weather station/The source, period	I	II	III	IV	V	VI	VII	VIII	IX	X	XI	XII
Boryspil, Kyiv, [1], 50°27'N, 30°31'E (1961-1980), $\Delta_1$ , % The amount of radiation/the percentage of deviation of this value from the standard value, $\frac{\text{MJ}}{\text{m}^2}$ /%	107/25	161/13	304/12	405/10	604/7	650/10	649/10	517/4	384/13	220/16	89/10	66/12
Boryspil, Kyiv, (1961-1980). State Standards, $\Delta_2$ , %	96/13	141/0	266/2	417/8	591/5	622/5	611/4	511/3	362/7	210/10	81/1	55/7
Boryspil, Central Geophysical Observatory (2011-2020), $\Delta_3$ , %	82/3	149/5	300/11	449/17	587/4	660/12	605/3	600/21	417/23	226/19	81/0	61/3
Boryspil, (1961-2005), State Standard 2010	85	142	270	385	565	590	588	495	338	190	81	59
Kharkiv, 49°58'N, 36°15'E, State Standard	77	149	281	401	578	606	609	526	364	202	84	59

Weather station/The source, period	I	II	III	IV	V	VI	VII	VIII	IX	X	XI	XII
Częstochowa [PN ISO] 50°49'N, 19°06'E (1971-1991)	85	135	239	396	526	491	562	436	309	199	105	81
Katowice [PN ISO] 50°14'N, 19°02'E (1971-1991)	95	127	233	373	570	511	577	454	337	200	109	85

Note:  $\Delta_1$ ,  $\Delta_2$ ,  $\Delta_3$  are deviations from DSTU-NBV.1.1.-27:2010.

The data of Standard 2010 differ by 21-23% from the data measured from 2011 to 2020. When the longitude changes from 19° to 36°E, the values of solar radiation differ slightly (Table 3), while under the influence of regional conditions (e.g., in Katowice, under the influence of mountain conditions, or in Kharkiv, influenced by steppe conditions), they can differ significantly. Temporal differences in measurements were observed over the period of 1961 to 2020. Thus, in the last decade, in the summer months, there was an increase in the values of total solar radiation up to 700-900 MJ/m<sup>2</sup>.

Using the values of actinometric measurements from 2011 to 2020, the average monthly values were calculated, along with standard deviation, coefficient of variation, asymmetry coefficient, kurtosis coefficient, and amplitude (Table 3).

Table 3. Statistical characteristics of average monthly amounts of total solar radiation for the period of 2011-2022.

Station, characteristics	Months of the year											
	I	II	III	IV	V	VI	VII	VIII	IX	X	XI	XII
Arithmetic average, MJ/m <sup>2</sup>	Weather station in BORYSPIL, Kyiv											
	80.00	129.6	263.00	415.00	528.70	640.56	569.44	587.11	440.90	247.00	71.00	54.3
Standard deviation, MJ/m <sup>2</sup>	29.23	40.34	69.47	84.55	127.29	103.61	114.69	101.42	180.51	112.34	37.87	28.3
The coefficient of variation	0.365	0.311	0.264	0.203	0.240	0.161	0.201	0.172	0.409	0.454	0.533	0.52
Asymmetry coefficient	0.37	0.96	-0.09	-0.54	-0.35	0.73	-0.76	-0.35	0.18	0.26	0.91	-0.2
Kurtosis coefficient	-0.98	0.62	-1.29	-1.38	-1.28	-1.06	-0.45	-0.56	0.09	-1.39	-0.28	-1.7
Amplitude (max/min) MJ/m <sup>2</sup>	97/58	197/109	318/225	502/339	662/501	759/516	703/473	919/514	740/203	354/125	113/56	85/41
Arithmetic average MJ/m <sup>2</sup>	ODESA weather station											
	108.7	153.9	341.6	502.4	617.2	676.2	722.9	739.6	531.6	293.1	111.4	116
Standard deviation, MJ/m <sup>2</sup>	38.94	63.64	84.66	106.79	131.08	90.5	86.92	101.35	105.15	96.19	43.04	65.7
The coefficient of variation, %	0.358	0.413	0.247	0.212	0.212	0.133	0.120	0.137	0.197	0.328	0.386	0.56
Asymmetry coefficient	0.68	0.72	0.33	0.64	-0.19	0.14	-0.01	0.29	-1.04	0.38	0.6	0.12
Kurtosis coefficient	-0.57	-0.04	-0.54	-0.2	-1.05	-1.46	-1.66	-1.62	-0.07	-1.05	-1.21	-0.9
Amplitude (max/min) MJ/m <sup>2</sup>	123/74	209/127	417/255	673/444	760/516	789/640	772/638	730/595	491/363	326/203	161/80	133/44



Figure 3 shows the annual course of the standard deviation for the conditions of the meteorological stations in Kyiv and Odesa. There is a seasonal change in the amount of total solar radiation. At the same time, in the northern regions of Ukraine, the changes are 100-180 MJ/m<sup>2</sup>. The variability of solar radiation is shown in Figure 4.

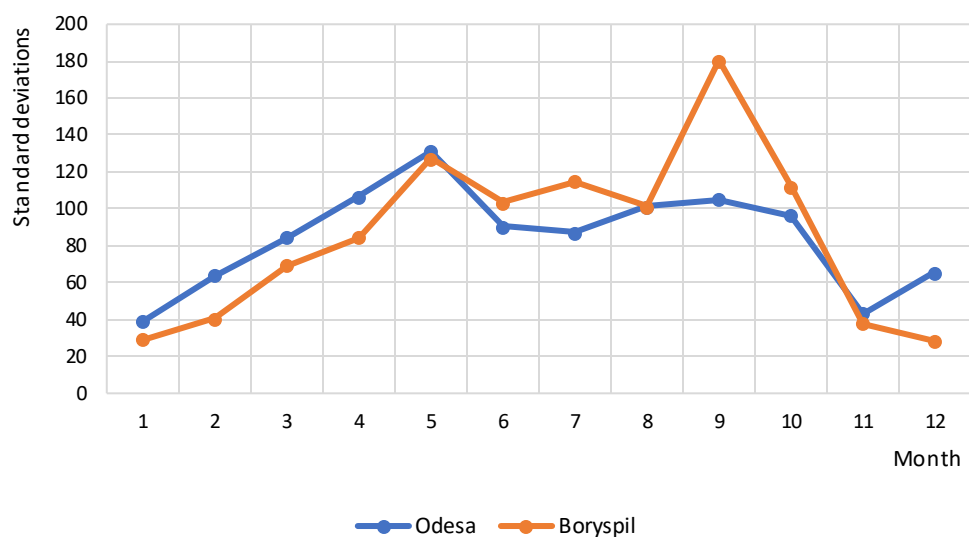


Fig. 3. Annual course of the standard deviations.

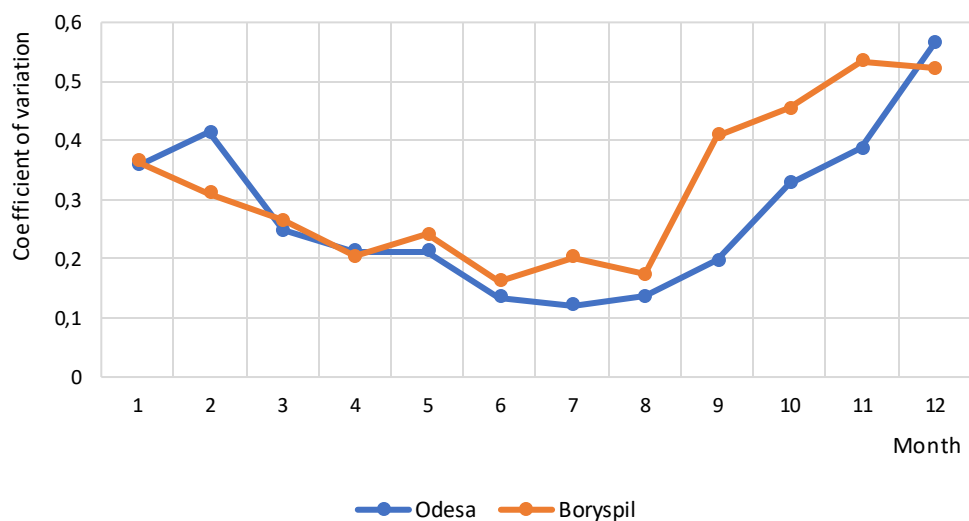


Fig. 4. Annual course of the coefficient of variation.

The change in the relative standard deviation is more significant in the autumn-winter months, reaching 30-34%. This ratio is typical for both northern and southern regions of the country. For Kyiv, the coefficient of variation is 20-34% and the amplitude is 919/514 MJ/m<sup>2</sup>. For Odesa, they are 12-30% and 789/640 MJ/m<sup>2</sup>, respectively.

The change in the asymmetry coefficient is shown in Figure 5.

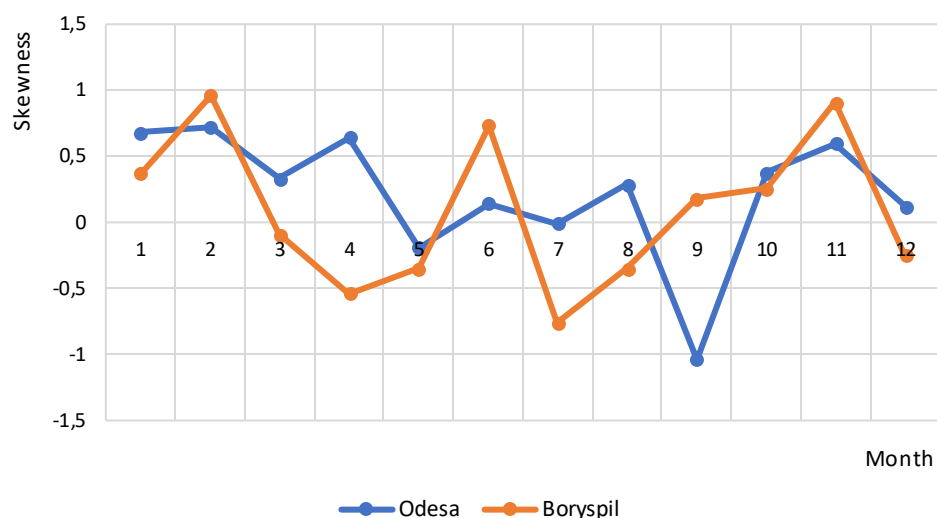


Fig. 5. Annual course of the asymmetry coefficient.

For Odesa, values fluctuate from  $-1.1$  to  $0.75$ . For the northern territories, a period with negative asymmetry is observed from March to May. From August to December, the asymmetry is positive and reaches maximum values of  $(-1)$ ,  $1$ .

Figure 6 shows the values of the kurtosis coefficient.

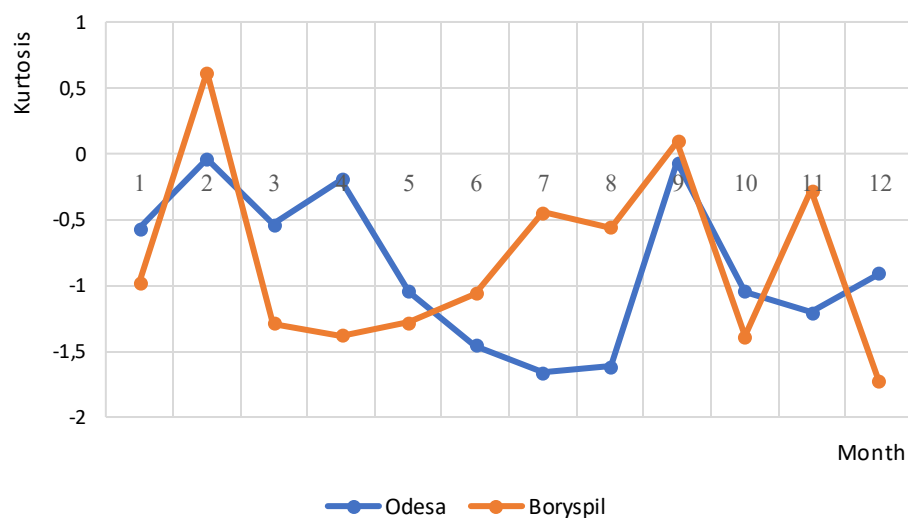


Fig. 6. Annual course of the kurtosis coefficient.

In the distribution of total solar radiation, there is a negative kurtosis ( $E$ ) during the year for the southern regions of Ukraine, with a maximum  $E$  of  $-1.75$ . For Kyiv, from March to November, kurtosis is negative with maximum values of  $1.4$ - $1.75$ . In February, kurtosis is positive ( $E = 0.6$ ), indicating sharp peaks in the distribution curves.

Figure 7 shows a comparison of average monthly and average daily values for the Central Geophysical Observatory and the State Standard of Ukraine. An increase in radiation has been observed during the last decade.

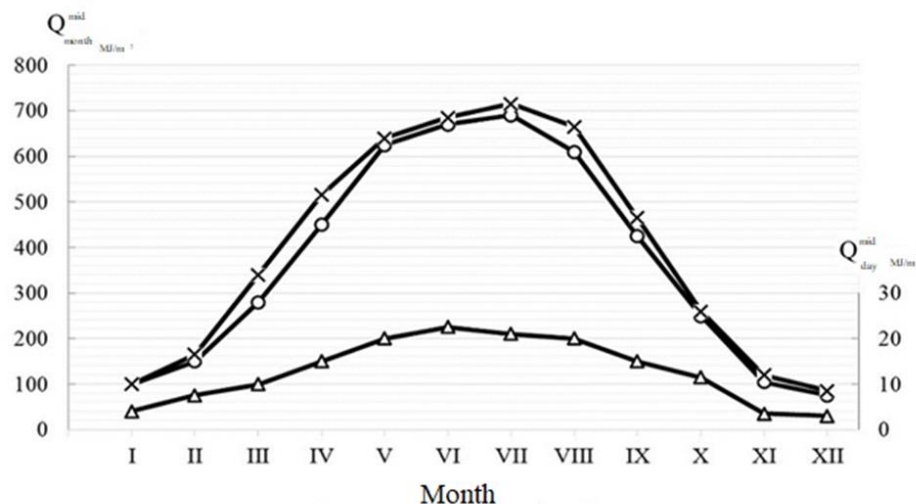


Fig. 7. Average monthly and average daily values of solar radiation. —○— State standard of Ukraine; —x— Central Geophysical Observatory ; —△— day.

Table 4 compares data from the State Standard of Ukraine with climatic data from different periods. The data of the State Standard of Ukraine (8-11%) coincides with the data from the early periods.

Table 4. Comparison of total solar radiation according to DSTU-NBV.1.1.-27:2010 with climatic data of different periods (for Odesa conditions with medium cloudiness).

Months	[12]	$\Delta$ [%]	Central Geophysical Observatory	$\Delta$ [%]	[10]
I	101	-11	101	-4	114
II	157	-2	164	+2	160
III	214	-4	345	+13	306
IV	454	-2	515	+11	465
V	627	0	648	+3	631
VI	667	-4	692	0	698
VII	690	-3	709	0	712
VIII	608	-2	653	+5	623
IX	431	-5	458	0	452
X	261	-7	257	-9	282
XI	109	-8	113	-4	118
XII	75	-16	89	0	89

An increase in average monthly values has been observed in recent years. Average daily values in every month of the year are shown in Figure 7. Using calculation dependencies, average daily values for any day of the year can be determined. Using these daily averages, hourly values can be determined.

Knowing the radiation input data, the average monthly and hourly values can be determined: Collares-Perera and Rabl (1979), Page et al. (2001), Zekai (2008), Duffie and Beckman (2013), Walker (2013), Kalogirou (2014), Mysak et al. (2014).

For Kyiv at noon on July 15, we determine:

$$r = \frac{\pi}{24} [0.8344 + 0.2566 \cdot \cos(-7.5^\circ)] \times \frac{(\cos(-7.5^\circ) - \cos 118^\circ)}{\sin 118^\circ - \left(\frac{2\pi \cdot 118^\circ}{360}\right) \cos 118^\circ} = 0.112.$$

The incidence of total solar radiation at noon on July 15 for Kyiv is:

$$i = r \cdot H_0 = 0.112 \cdot 7078 = W/m^2 \quad W/m^2 \text{ according to the Standard of Ukraine (862 W/m}^2\text{)}.$$

For example, for Kyiv ( $L = 50^\circ$ ), the daily incidence of radiation on July 15 is:

$$\delta = 23.45 \sin \left[ \frac{360}{365} (N + 284) \right] = 23.45 \sin \left[ \frac{360}{365} (106 + 284) \right] = 21.2^\circ$$

$$h_{ss} = \cos^{-1} [-\tan(50^\circ) \cdot \tan(21.2^\circ)] = 118^\circ$$

$$h_s = \frac{2}{15} \cos^{-1} [-\tan(50^\circ) \cdot \tan(21.2^\circ)] = 15.7 \text{ hours}$$

$$H_0 = \frac{3600 \cdot 15.7 \cdot 1300}{\pi} \left[ 1 + 0.33 \frac{360 \cdot 196}{365} \right] \times \left( \cos 50^\circ \cdot \cos 21.2^\circ \cdot \sin 118^\circ + \left( \frac{\pi \cdot 118}{180} \right) \sin 50^\circ \cdot \sin 21.2^\circ \right) \\ = 25,48 MJ / (m^2 \cdot day)$$

$$\text{or } (= 7078 W \cdot h / (m^2 \cdot day)).$$

According to the Standard 2010 data, the total daily solar radiation on June 15 for Kyiv under a clear sky is  $Q = 7544 \text{ W} \cdot h / (m^2 \cdot day)$  ( $\Delta = 6\%$ ).

An important characteristic of solar energy resources is the duration of sunshine. According to data from Dmytrenko and Barandich (2007), effective use of solar energy is ensured when the duration of sunshine (average monthly values) is  $>200$  h. According to the data from the Boris Sreznevskiy Central Geophysical Observatory, the actual annual duration of sunshine for 2011-2020 at Kyiv (Boryspil) varies from 2222 hours (2011) to 2184 hours (2020). The possible annual duration of sunshine varies from 4452 hours (2011) to 4481 hours (2020), respectively. The average monthly value of the actual duration of sunshine varies from 203 hours (March 2011) to 135 hours (November 2011). The maximum values are 302 hours in May and 305 hours in June. In 2020, the actual monthly average values vary from 180 hours in March to 120 hours in November. Maximum values are observed in June (331 hours) and August (334 hours). In the southern regions of Ukraine, the actual annual duration of sunshine for 2011-2020 at Odesa varies from 2387 hours (2011) to 2709 hours (2020). The possible duration of sunshine varies from 4717 hours (2011) to 4242 hours (2020), respectively. Average monthly values of the actual duration of sunshine vary from 180 hours (March 2011) to 169 hours (November 2011). The maximum values are observed in July (333 hours in 2011) and August (371 hours in 2011). In 2020, the actual monthly average values ranged from 217 hours (March 2020) to 168 hours (November 2020), respectively. The maximum values were observed in July (379 hours in 2020) and August (380 hours in 2020).

The criterion for the expediency of using solar energy is that the annual number of clear and semi-clear days is  $>200$  (with  $>244$  days, the potential is assessed as high). The State Standard of Ukraine does not specify the number of clear days.

#### 4. Conclusions


The results of analyzing the multi-year series of solar radiation for 2011-2020 indicate an increase in the average monthly and annual solar radiation in both the southern and northern regions of the country in the last years of the decade. Comparing data from the DSTU-NBV.1.1.-27:2010 with actual measurement data, the data from the state standard of Ukraine differ from the data of the last decade by 18-23% and require clarification. To determine daily and hourly solar radiation, empirical dependences are presented that are simple and convenient for use in engineering calculations and assessments of solar energy resources.

#### References

- Collares-Perera M., Rabl A., 1979, The average distribution of solar radiation-correlations between diffuse and hemispherical and between daily and hourly insolation values, *Solar Energy*, 22 (2), 155-164, DOI: 10.1016/0038-092X(79)90100-2.
- Dalgaard P., 2008, *Introductory Statistics with R*, NY: Springer New York, 365 pp.
- Dmytrenko L.V., Barandich S.L., 2007, Assessment of solar power climatic resources in Ukraine, (in Ukrainian), *Naukovi pratsi UkrNDHMI – Scientific papers the UkrSRHI*, 256, 121-129, available online at <http://dspace.nbuv.gov.ua/handle/123456789/51525> (data access 04.08.2025).
- DSTU-NBV.1.1.-27:2010, *Budivel'na klimatologia*, Minregionbud Ukraini, K.: 2011, 124 pp. (National Standard of Ukraine: Building Climatology Ministry of Regional Construction of Ukraine).
- Duffie J.A., Beckman W.A., 2013, *Solar engineering of thermal processes*, 4<sup>th</sup> edition, John Wiley and Sons, Inc., Hoboken, New Jersey, 910 pp.
- Global Solar Atlas, World Bank Group, Energy Sector Management Assistance Program (ESMAP) and Solargis, available online at <https://globalsolaratlas.info> (data access 04.08.2025).
- Liu H.-Y., Skandalos N., Braslina L., Kapsalis V., Karamanis D., 2023, Integration solar energy and nature-based solutions for climate-neutral urban environments, *Solar*, 3 (3), 382-415, DOI: 10.3390/solar3030022.
- Halchak V.P., Boyarchuk V., Syrotyuk V., Syrotyuk S., 2019, Parameters of direct solar energy flux in clear sky taken into account of atmosphere transparency, *Scientific and Applied Journal Vidnovluvana energetika*, 2 (57), DOI: 10.36296/1819-8058.2019.2(57).22-31.
- Kalogirou S.A., 2014, *Solar Energy Engineering Processes and Systems*. Academic Press, Oxford:, 819 pp., DOI: 10.1016/B978-0-12-374501-9.X0001-5.
- Kapica J., Jurasz J., Canales F.A., Bloomfield H., Guezgouz M., De Felice M., Kobus Z., 2024, The potential impact of climate change on European renewable energy droughts, *Renewable and Sustainable Energy Reviews*, 189 (Part A), DOI: 10.1016/j.rser.2023.114011.
- Kuznietsov M., Lysenko O., 2017, Statistical analysis of energy indices of solar radiation (Based on the data of Tokmak Sola Power Station), (in Russian), *Problemele Energeticii Regionale*, 2 (34), 140-148, DOI: 10.5281/zenodo.1189379.
- Lipinskyi V.M., Diachuk V.A., Babichenko V.M., 2003, *Climate of Ukraine*, (in Ukrainian), Raevsky Publ. House, Kiev, 343 pp.
- Lopushanska M.P., Iwanow E.A., 2022, Climate factors and their role in the solar energy development in the Lviv region, (in Ukrainian), *Environmental Science*, 6 (45), 54-59, DOI: 10.32846/2306-9716/2022.eco.6-45.9.
- Madesh A., Sandhu K.S., 2015, Hybrid wind/photovoltaic energy system developments: Critical review and findings, *Renewable and Sustainable Energy Reviews*, 52, DOI: 10.1016/j.rser.2015.08.008.

- Mierzwiak M., Kroszczyński K., Araszkiewicz A., 2022, On solar radiation prediction for the East-Central European region, *Energies*, 15 (9), DOI: 10.3390/en15093153.
- Murtazinova V.F., 2009, Synoptic processes that determine the modern climate of Ukraine, (in Ukrainian), [in:] *Physical Geography and Geomorphology*, 57, 18-22, available online at <http://eprints.library.odetu.edu.ua>.
- Mysak Y.S., Woznyak O.T., Datsko O.S., Shapoval S.P., 2014, *Solar Energy: Theory and Practice: Monograph*, Publishing House of Lviv Polytechnic, 340 pp.
- Ozarkiv I.M., Ferenc O.B., Kobrynowych M.S., 2007, Features of calculation of geliodrying chamber for wood drying there are fluidizers wood, (in Ukrainian), *Scientific Bulletin of National Forest technology University of Ukraine*, 17 (1), 91-96, available online at [https://nv.nltu.edu.ua/Archive/2007/17\\_1/index.htm](https://nv.nltu.edu.ua/Archive/2007/17_1/index.htm) (data access 04.08.2025).
- Page J.K., Albuissou M., Wald L., 2001, The European Solar Radiation Atlas: a valuable digital tool, *Solar Energy*, 71 (1), 81-83, DOI: 10.1016/S0038-092X(00)00157-2.
- Pivovarova Z.I., 1988, *Radiation characteristics of the climate of the USSR*, (in Russian), L.: Gidrometeoizdat, 291 pp.
- Rybchenko L., Savchuk S., 2013, Radiation state under the condition of intense droughts 2001-2010 yrs. in Ukraine, (in Ukrainian) *Ukrainian Geographical Journal*, 1, 5-11, DOI: 10.15407/ugz2013.01.005.
- Rybchenko L.S., Savchuk S.V., 2015, Potential of helioenergetical and climatic resources of solar radiation in Ukraine, (in Ukrainian), *Ukrainian Geographical Journal*, 4, 16-23, DOI: 10.15407/ugz2015.04.
- Sadooghi P., Kherani N.P., 2019, Influence of slat angle and low-emissive partitioning radiant energy veils on the thermal performance of multilayered windows for dynamic facades, *Renewable Energy*, 143, 142-148, DOI: 10.1016/j.renene.2019.04.121.
- Sergeychuk O.V., 2011, Geometric computerized model «Atmospheric Radiation» for an Energy Efficient Building, (in Russian), *Energy Efficiency in Architecture and Construction*, KNUCA, Kiev, 1, 22-28. Available online at <https://repository.knuba.edu.ua/bitstreams/88373fe9-9f89-4fcc-a2d3-df65bbb81e6a/download> (data access 04.08.2025).
- Ujma A., 2012, Wpływ lokalizacji budynku mieszkalnego na jego parametry energetyczne, *Budownictwo o Zoptimalizowanym Potencjale Energetycznym*, 2 (10), 104-110.
- Ujma A., 2014, Parametry budynku energooszczędnego w warunkach klimatu Jury Krakowsko-Częstochowskiej, *Budownictwo o Zoptimalizowanym Potencjale Energetycznym*, 1(13), 138-147.
- Voloshina O.V., Kuryshina V.Yu., 2010, Space-temporal distribution of total solar radiation in south-west part of the Ukraine, (in Ukrainian), *Ukrainian Hydrometeorological Journal*, 6, 84-92.
- Walker A., 2013, *Solar Energy Technologies and the Project Delivery Process for Building*, John Wiley and Sons. Inc., 298 pp.
- Zekai Z., 2008, *Solar Energy Fundamentals and Modeling Techniques: Atmosphere, Environment, Climate Change and Renewable Energy*, Springer-Verlag, London, 276 pp., DOI: 10.1007/978-1-84800-134-3.
- Zubkovich S.A., 2013, Problem of typification of synoptic processes over the eastern regions of Ukraine, (in Russian), *East European Journal of Advanced Technologies: Ecology*, 3/11 (63), 26-29, available online at <https://journals.urau.ua/eejet/article/view/14591/12365> (data access 04.08.2025).

# Trends and prediction of extreme precipitation indices in three cities of Burkina Faso using non-parametric statistics and the Holt-Winters smoothing method

Joseph Yaméogo 

Ziniaré University Center/Joseph Ki-Zerbo University, Burkina Faso

## Abstract

Climate extremes have become increasingly important in recent years, leading to renewed scientific interest. However, few studies have focused on precipitation extremes in cities in Burkina Faso, a Sahelian country in West Africa. The aim of this study is to analyze trends and to project future extreme precipitation indices in three cities in Burkina Faso. To this end, precipitation data, recorded daily, were collected from the National Meteorological Agency of Burkina Faso (NMABF) over the period 1991-2020. The stations selected were Boromo for the small town of Boromo, Saria for the medium-sized town of Koudougou, and Bobo-Dioulasso for the town of Bobo-Dioulasso. The precipitation data were used to calculate the extreme precipitation indices described by ETCCDMI (Expert Team for Climate Change Detection Monitoring and Indices) using Rclimdex. Descriptive statistics, the Mann-Kendall test, and trends from innovative models were used to analyze the extreme precipitation indices; the Holt-Winters additive model was used to analyze future projections. The study showed considerable variability and a monotonic increasing trend in extreme precipitation indices over the period 1991-2020. However, for the city of Koudougou, the trend was a non-monotonic increase. The forecast based on the Holt-Winters additive model shows considerable variability in the extreme precipitation indices, with an upward trend over the period 2020-2030. On the other hand, in the city of Koudougou, indices of precipitation duration will decrease, indicating that the city will be affected most by the frequency and intensity of extreme precipitation.

## Keywords

Innovative graphical trend; additive Holt-Winters model; extreme precipitation indices, Burkina Faso.

Submitted 18 May 2025, revised 25 July 2025, accepted 6 August 2025

DOI: 10.26491/mhwm/209088

## 1. Introduction

Fluctuations in temperature and precipitation are widely recognized as relevant indicators of global climate change and variability (IPCC 2021). Anthropogenic activities that increase greenhouse gases cause temperature increases and regional changes in mean climate, resulting in climate extremes in various parts of the world (IPCC 2023). In West Africa, several studies, including in Nigeria (Gbode et al. 2019), Mauritania, Guinea, Côte d'Ivoire, Senegal, Mali, and Niger (Barry et al. 2018), have observed these changes. Sylla et al. (2015) add that the increase in the intensity of very wet events, particularly in the pre- and early monsoonal periods, will be more marked over the Sahel and under Representative Concentration Pathway (RCP) 8.5 than in the Gulf of Guinea under RCP 4.5. Urban areas will also be affected by climate extremes in West Africa (Herslund et al. 2015), which is a major concern.

African cities are experiencing an unprecedented increase in the rate of urbanization. Between 1990 and 2022, 500 million people are expected to move to urban centers in Africa (OECD 2022). By 2050, Africa's urban population is expected to reach 1.06 billion (Ezeh et al. 2020). This demographic growth will increase the impact of climate extremes on urban populations. Extreme precipitation caused flooding in Dar es Salaam on 22 December 2011, resulting in 20 deaths, extensive damage, and loss of livelihoods



(Giugni et al. 2015). The same happened in Lagos, Nigeria (Doan et al. 2023) and Dakar, Senegal (Diémé et al. 2025). In Burkina Faso, the situation is no better than in other West African countries. The country is experiencing an increase in precipitation and extreme temperature indices in the north, Boucle du Mouhoun, and southwest regions (Rouamba et al. 2023; Yaméogo, Rouamba 2023a; Yanogo, Yaméogo 2023; Yaméogo 2024; Yaméogo, Sawadogo 2024; Yaméogo 2025), with dramatic consequences for the population (Yaméogo, Rouamba 2023b). In this context, (Gimeno et al. 2022) note that the increase in urban populations associated with climate change makes societies increasingly vulnerable to extreme precipitation.

A few studies have examined extreme precipitation trends and projections. For example, the work of Rouamba et al. (2023) in the municipality of Boromo, in the south of Burkina Faso (Sougué et al. 2023), and in ten cities in Burkina Faso addressed the issue of trends and forecasts of climatic extremes in recent years. Several statistical methods, especially approaches based on the classical theory of extremes (peak-on-threshold) and linear regression models, have been used by various authors to understand the spatiotemporal trends in climate extremes (Béventaoré, Barro 2022; Rouamba et al. 2023). Parametric regression models have also been used to predict future extreme events using CMIP6 data (Koala et al. 2023). These studies do not account for trends and seasonality of the time series of climate extremes, which can bias trends and forecasts of precipitation extremes.

Several other advanced forecasting methods are reported in the literature, including the Holt-Winters smoothing method, which accounts for trend and seasonality (Nurhamidah et al. 2020). This method has advantages, such as reducing the weight of historical data, and simplicity. Therefore, it has been used in several studies in the field of climatology (Gundalia, Dholakia 2012; Gowri et al. 2022; Bhagat, Ramaswamy 2023). This prediction method can make valuable contributions to understanding future trends and impacts of climate change (Pala, Şevgin 2024). The method thus forms the basis of statistical modeling for climate prediction in the region. The general objective of this study is to analyze the evolution of extreme precipitation indices and their projection from 2020 to 2030 using non-parametric smoothing and Holt-Winters methods in three cities in Burkina Faso. The secondary objectives of this study are to:

- analyze the variability of extreme precipitation indices over the period 1991-2020;
- analyze the trends in extreme precipitation indices over the period 1991-2020;
- determine the projection of extreme precipitation indices for the period 2020-2030.

## **2. Materials and methods**

### **2.1. Study area**

The study areas are in Burkina Faso, West Africa (Fig. 1). Three cities are considered in the study: Bobo-Dioulasso, in the urban commune of the Houet province in the Hauts Bassins region. These cities vary in physical characteristics. The soils of Koudougou, Burkina Faso, are varied. They include leached tropical ferruginous soils, often poor in organic matter and nutrients, and lithosols on cuirass, better suited to

grazing. Hydromorphic soils are also found along watercourses, which are favorable to certain crops. The area is affected by soil degradation, with a widening of the Sahel and a decline in vegetation. The soils in Boromo, Burkina Faso, are diverse and include cuirass, hydromorphic, and tropical ferruginous soils. These soils have various properties influenced by their origin and environment. Some are suitable for agriculture, while others are susceptible to erosion. The soils of Bobo-Dioulasso, Burkina Faso, are mainly characterized by ferrallitic soils, tropical ferruginous soils, and eutrophic brown soils. These soils result from weathering of Birrimian rocks and vary according to relief and topography. In human terms, the study towns have different populations. Bobo-Dioulasso is the second-largest city in Burkina Faso, covering an area of 1,805 km<sup>2</sup>. Its population is >900,000. Koudougou is a medium-sized town, Burkina Faso's third-largest city. Its population has been particularly dynamic in recent decades. Its urban population has more than quadrupled over the past few decades, from 36,838 in 1975 to 88,184 in 2006 and 160,239 in 2019 (Sirven 1987; INSD 2011). Boromo is one of the country's smaller towns. Its urban population is estimated at 20,193 (INSD 2011). Unlike other towns, Boromo is facing an influx of people fleeing terrorism in the north of the country. This situation makes the small town of Boromo vulnerable and exacerbates social problems (Yaméogo et al. 2022).

These three towns were selected based on three criteria: the availability of rainfall data over a given period, the degree of missing data over a given period, and the size of the population potentially affected by extreme rainfall. The populations of these towns have increased considerably as a result of the security crisis in the northern, eastern, and Boucle du Mouhoun areas.

The topography varies throughout the region. The towns studied have altitudes ranging from 232 to 314 to >478 m (Fig. 2).

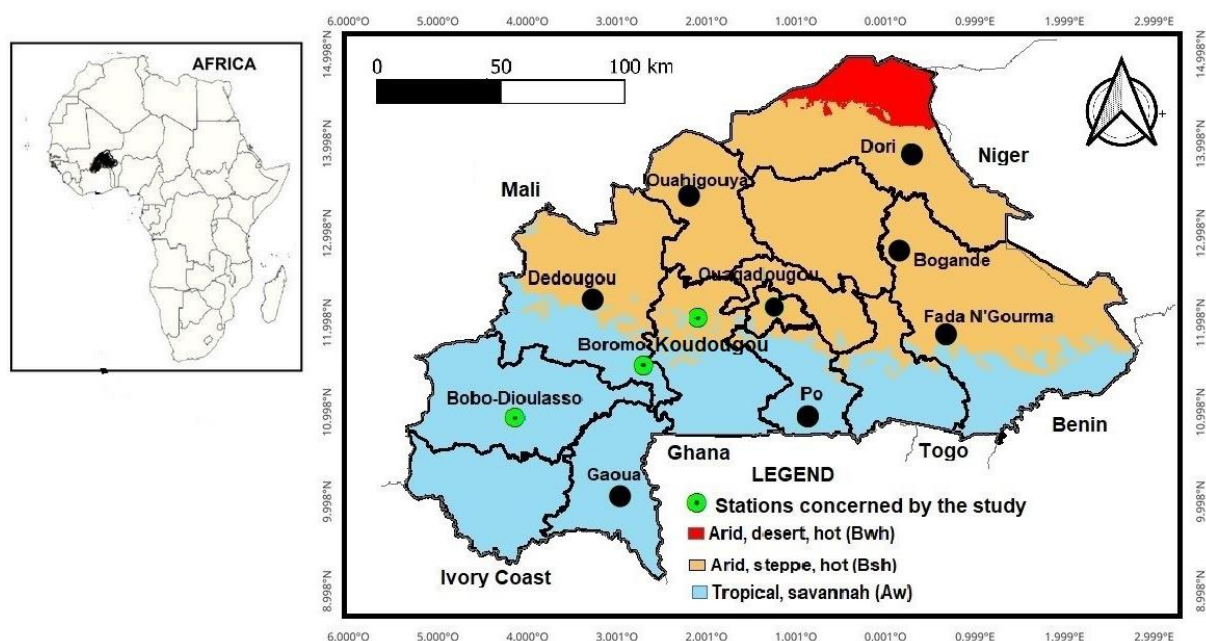


Fig. 1. Geographical location of study towns and stations.

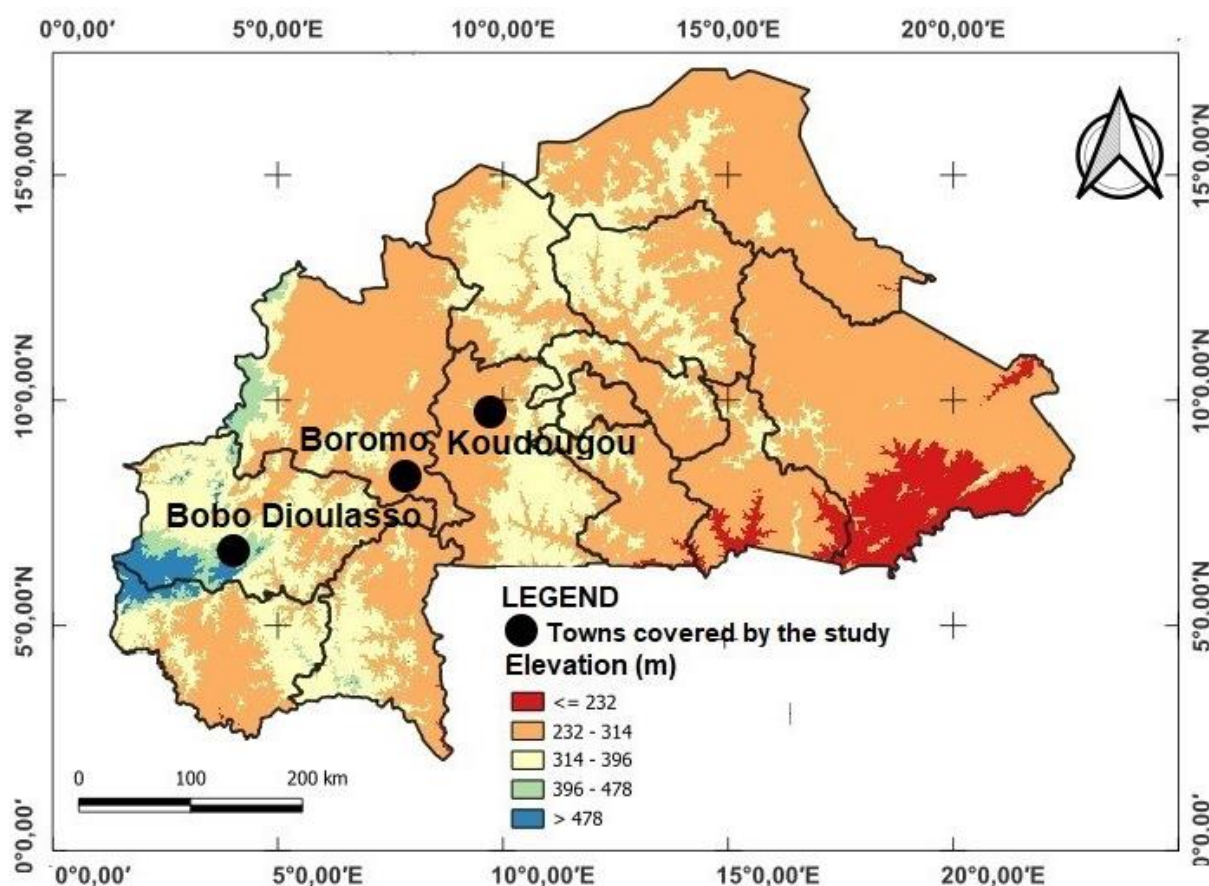


Fig. 2. The topography of Burkina Faso.

## 2.2. Data and methods

Daily precipitation data were obtained from the National Meteorological Agency of Burkina Faso for 1991-2020 (Table 1). One station was selected for each of the three towns. The Saria station represents the town of Koudougou, the Boromo station the city of Boromo, and the Bobo-Dioulasso station the city of Bobo-Dioulasso.

Table 1. Characteristics of the selected stations

Station names	Type of station selected	Type of domain climate	Period selected	Latitude (N)	Longitude (E)
Bobo-Dioulasso	Synoptic station	Sudanian	1991-2020	11.1667	-4.3167
Boromo	Synoptic station	Sudano-sahelian	1991-2020	11.75	-2.9333
Saria	Climatological station	Sudano-sahelian	1991-2018	12.2667	-2.15

Daily precipitation data were fed into Rclimindex, which produced extreme precipitation indices for the period 1991-2020, representing precipitation intensity, precipitation frequency, and precipitation duration. RclimDex provides a user-friendly graphical interface for calculating the 27 basic indices recommended by the CCI/CLIVAR Expert Team on Climate Change Detection, Monitoring and Indices (ETCCDMI) (Karl et al. 1999; Zhang, Yang 2004). In the present study, 10 indices were selected (Table 2).

Table 2. Extreme precipitation indices used in the study. Source: Lourdes et al. (2021).

Index classification	Index	Description	Unit
Intensity indices precipitation	Rx1day	Maximum precipitation over 1 day	mm
	Rx5day	Maximum consecutive precipitation over 5 days	mm
	SDII	Annual total precipitation divided by the number of wet day	mm/day
	prcptot	Total precipitation in wet days $\geq 1$ mm	mm
Frequency indices precipitation	R99ptot	Number of days with precipitation $\geq 99$ th percentile	day
	R95ptot	Number of days with precipitation $\geq 95$ th percentile	day
	R10mm	Number of days precipitation $\geq 10$ mm	day
	R20mm	Number of days precipitation $\geq 20$ mm	day
Duration indices precipitation	CDD	Maximum number of consecutive days with precipitation $< 1$ mm	day
	CWD	Maximum number of consecutive days with precipitation $\geq 1$ mm	day

The data projections for the 10-year period (2020-2030) were based on the extreme precipitation indices extracted from the daily data using Rclimdex. The temporal data for the extreme precipitation indices were processed in XLSTAT 2019 using the Holt-Winters method.

### 2.2.1. Mann-Kendall Test

It is a non-parametric test and there is no requirement that the data must be normally distributed (Oufrih et al. 2023). In this test,  $H_0$  is the null hypothesis, which states that the data come from a population whose observations are independent of each other and are uniformly distributed, and the alternative to  $H_0$ , which states that the data have a monotone tendency (Aditya et al. 2021). These test values  $(X_j - X_k)$  where  $j > k$  and the test statistic  $S$  is calculated by applying the formula (Shah, Kiran 2021):

$$S = \sum_{k=1}^{n-1} \sum_{j=k+1}^n \text{sgn}(X_j - X_k) \quad (1)$$

With,  $X_j$  and  $X_k$  are the annual values for years  $j$  and  $k$ ,  $j > k$ , respectively.

The  $\text{sgn}$  function is calculated as follows:

$$\text{sgn}(X_j - X_k) = \begin{cases} 1 & \text{if } X_j - X_k > 0 \\ 0 & \text{if } X_j - X_k = 0 \\ -1 & \text{if } X_j - X_k < 0 \end{cases} \quad (2)$$

The test statistic,  $\tau$ , can be calculated as follows:

$$\tau = \frac{S}{\sqrt{\frac{n-1}{3}}} \quad (3)$$

In order to statistically quantify the significance of the trend, it is necessary to calculate the probability associated with  $S$  and the sample size  $n$ . The formula to calculate the variance  $S$  is as follows:

$$Var(S) = \frac{1}{18} \left[ n(n-1)(2n+5) - \sum_{i=1}^m (t_i - 1)(2t_i + 5) \right] \quad (4)$$

Where  $q$  is defined as the number of linked groups and  $t_p$  is defined as the number of data items in the  $p^{\text{th}}$  group. The values of  $S$  and  $Var(S)$  are used for the calculation of the test statistic  $Z$ , which is:

$$Z = \begin{cases} \frac{s-1}{\sqrt{Var(s)}}, & \text{if } s > 0 \\ 0 & \text{if } s = 0 \\ \frac{s+1}{\sqrt{Var(s)}}, & \text{if } s < 0 \end{cases} \quad (5)$$

The null hypothesis  $h_0$  (no trend) is rejected if the significance level or p-value is  $>5\%$ .

### 2.2.2. Innovative trend analysis method (ITAM)

This technique, introduced by Şen (2017), or referred to as new trend analysis (Sezen, Partal 2020), is non-parametric and its use does not require a normal distribution of observations (Şen et al. 2019; Mallick et al. 2021). It is a very useful tool for detecting trends in precipitation time series data (Pastagia, Mehta 2022; Patel, Mehta 2023). In addition, the ITAM is more sensitive in determining the trend than the Mann-Kendall (MK) test (Mohorji et al. 2017; Sanusi, Abdy 2021; Kessabi et al. 2024). In ITAM, the data series is divided into two equal parts such that (Dabanlı et al. 2016; Mohorji et al. 2017; Şen et al. 2019; Marak et al. 2020; Kougbegbede 2024; Muthiah et al. 2024).

Mathematically, the procedure of the method is translated as follows (Güçlü 2020):

- Any data consisting of  $n$  data,  $a_1, a_2, \dots, a_n$  is separated into two equal series  $\{b_{1, n/2}\}$  and  $\{b_{2, n/2}\}$ , such as:

$$\{b_{1, n/2}\} = \{a_1, a_2, \dots, a_{n/2}\} \quad (6)$$

and

$$\{b_{2, n/2}\} = \{a_{n/2+1}, a_{n/2+2}, \dots, a_n\} \quad (7)$$

- Each series with the same number of elements is then listed in ascending order. The series is named as follows:  $\{S_1\}$ , et  $\{S_2\}$ , with:

$$\{S_1\} = \{\min(b_{1, n/2}), \dots, b_j, \dots, \max(b_{1, n/2})\} \quad (1 < j < n/2) \quad (8)$$

and

$$\{S_2\} = \{\min(b_{2, n/2}), \dots, b_j, \dots, \max(b_{2, n/2})\} \quad (1 < j < n/2) \quad (9)$$

The  $\{S_1\}$  data on the horizontal axis are plotted against the values of the following series:  $1, 2, 3, \dots, (n/2) - 1, n/2$ .

The data for  $\{S_2\}$  are on the vertical axis according to the values:  $1, 2, 3, \dots, (n/2) - 1, n/2$ .

According to Mandal et al. (2021), each series is then sorted independently in ascending order. The first half of the series ( $X$ ) is plotted on the X axis and the second half of the series ( $Y$ ) is plotted on the Y axis. The presence of a trend is indicated by a 1:1 (45°) line in the scatterplot. The presence of a trend is indicated by a 1:1 (45°) line in the scatterplot. Coordinates on the 45° line indicate no trend, below it a negative trend, and above it an upward trend (Dabanli et al. 2016; Almazroui et al. 2019; Chowdari et al. 2023; Yaméogo 2025). A detailed interpretation of the ITAM is given in Figure 3 below, based on data from the present study at the Bobo-Dioulasso station.

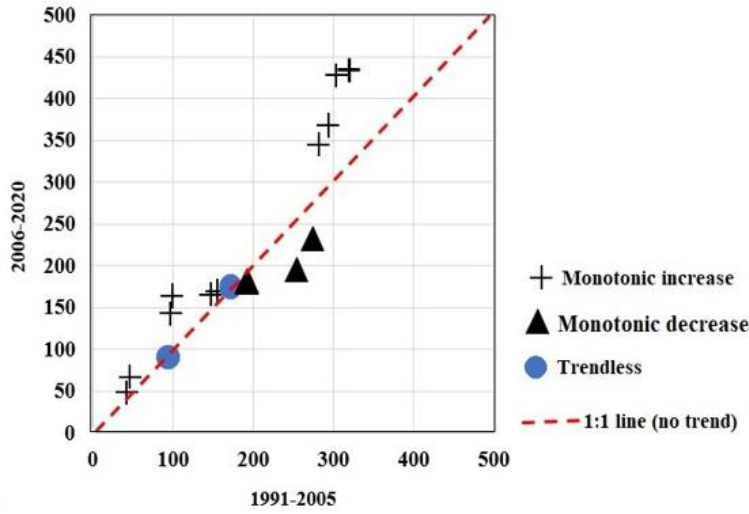


Fig. 3. Different interpretations of ITAM's results.

### 2.2.3. Slope ( $S$ ) of ITAM

The slope trend  $S$  is calculated using the following expression (Şen 2017):

$$S = \frac{2 * (\bar{Y}_2 - \bar{Y}_1)}{n} \quad (10)$$

Where,  $\bar{Y}_1$  and  $\bar{Y}_2$  are the arithmetic means of the first series and the second half of the series of the dependent variable, and  $n$  is the number of data points.

### 2.2.3. The Percentage Bias Method (PBM)

The percentage bias method was used to estimate the percentage change in precipitation in the second half of the time series compared with the first half (Mandal et al. 2021):

$$PMB = 100 - \sum_{i=1}^n \frac{Y_i}{X_i} \times 100 \quad (11)$$

Where  $PBM$  is the percentage bias,  $n$  is the total extent of the sub-series separately,  $X_i$  and  $Y_i$  are the values of the observation data in the first and second sub-series, respectively. Positive and negative  $PBM$  values indicate increasing and decreasing trends, respectively, for the first sub-series.

#### 2.2.4. Holt-Winters exponential smoothing model

The Holt-Winters method, which allows the seasonal model to adapt over time, is one of the best-known forecasting techniques (Lawton 1998). It involves estimating three smoothing parameters associated with level, trend, and seasonal variables (Atoyebi et al. 2023). Designed for trend and seasonal time series, the Holt-Winters method is a commonly used tool for forecasting trade data containing seasonality, changing trends, and seasonal correlation (Gelper et al. 2010). Several studies (Irwan et al. 2023) have also used this method to forecast hydro-climatological data series. The Holt-Winters approaches are modeled in one of two ways: additive or multiplicative (Koehler et al. 2001; Thomasson 2017; Natayu et al. 2022).

#### 2.2.5. Holt-Winters seasonal additive model

The Holt-Winters additive method, which has a linear trend and constant seasonal variation (additive), has a prediction composed of the level ( $L_t$ ), trend ( $b_t$ ), and seasonal variation ( $s_t$ ) (Puah et al. 2016). The additive model incorporates seasonality but with the addition of a trend as follows (Pertiwi 2020; Wiguna et al. 2023):

- Level:

$$L_t = \alpha(Y_t - s_{t-c}) + (1 - \alpha)(L_{t-1} - b_{t-1}) \quad (12)$$

- Trend:

$$b_t = \beta(L_t - L_{t-1}) + (1 - \beta)b_{t-1} \quad (13)$$

- Seasonal:

$$s_t = \gamma(Y_t - L_t) + (1 - \gamma)s_{t-c} \quad (14)$$

The prediction for period  $F_{t+m}$  is:

$$F_{t+m} = L_t + b_{tm} + s_{t-s+m} \quad (15)$$

The smoothing parameters,  $\alpha$ ,  $\beta$ , and  $\gamma$  have values that vary between 0 and 1. In this study, the parameters are fixed at 0.2. This means that the prediction is flexible, i.e. strongly influenced by the most recent observations.

#### 2.2.6. Multiplicative Holt-Winters method (MHW)

The multiplicative model is used if the data show variable seasonal fluctuations, and the different equations are as follows (Pleños 2022; Irwan et al. 2023; Wiguna et al. 2023):

- Level:

$$L_t = \alpha \frac{Y_t}{s_{t-s}} + (1 - \alpha)(L_{t-1} + b_{t-1}) \quad (16)$$



- Trend:

$$b_t = \beta(L_t - L_{t-1}) + (1 - \beta)b_{t-1} \quad (17)$$

- Seasonal:

$$S_t = \gamma \frac{Y_t}{L_t} + (1 - \gamma)S_{t-s} \quad (18)$$

The prediction period  $t$  is :

$$S_t = F_{t+m} = (L_t + b_t m)S_{t-s+m} \quad (19)$$

The smoothing parameters,  $\alpha$ ,  $\beta$ , and  $\gamma$  have values that vary between 0 and 1. In this study, the parameters are fixed at 0.2. This means that the prediction is flexible.

Where,  $Y_t$  – level in the 2<sup>nd</sup> period  $t$ ;  $L_{t-1}$  – level in the 2<sup>nd</sup> period  $t-1$ ;  $b_t$  – trend in the 2<sup>nd</sup> period  $t$ ;  $b_{t-1}$  – trend in the 2<sup>nd</sup> period  $t-1$ ;  $S_t$  – seasonality in the 2<sup>nd</sup> factors;  $Y_t$  – data in the 2<sup>nd</sup> period  $t$ ;  $s$  – seasonal period;  $t$  – seasonal period;  $m$  – predictive time period.

#### 2.2.7. Analysis of the Holt-Winters model performance

Goodness of fit is a critical criterion for assessing the accuracy of a predicted model relative to the true value (Atoyebi et al. 2023). Mean error ( $ME$ ),  $MSE$  (mean squared error),  $RMSE$  (root mean squared error) and  $MAPE$  (mean absolute percentage error), mean absolute deviation ( $MAD$ ), and mean squared deviation ( $MSD$ ) have typically been used to examine model performance (Pinel 2020; Atoyebi et al. 2023). Other valuation parameters are also considered, such as the mean square error ( $MSE$ ), the root mean square error ( $RMSE$ ), and the mean absolute error ( $MAE$ ). However, the use of  $MAD$  and  $MSD$  as indicators of prediction accuracy can be problematic in that they do not facilitate comparisons between different time series or time intervals, and the absolute measures  $MAD$  and  $MSD$  are affected by the size of the time series data (Atoyebi et al. 2023). The statistics  $MAD$  and  $MSE$ , provide no guidance on whether the model is good or not. This makes it impossible to use both measures (Gundalia, Dholakia 2012). Therefore,  $MAPE$  is used in studies as a valid indicator of model performance (Gundalia, Dholakia 2012; Puah et al. 2016).  $MAPE$  is also used in this study.  $MAPE$  consists of dividing the absolute error of each period by the true value of that period and calculating an average percentage of absolute errors (Wiguna et al. 2023). The mathematical formula used to calculate  $MAPE$  is as follows (Wiguna et al. 2023):

$$MAPE = \frac{1}{n} \sum_{t=1}^n \left| \frac{A_t - Y_t}{A_t} \right| \times 100\% \quad (20)$$

With,  $A_t$  – actual data;  $Y_t$  – forecasting data;  $n$  – number of periods. Prediction performance is interpreted using a prediction rating scale (Table 3). A summary of the methods used in the study is presented in Figure 4.

Table 3. Prediction model performance assessment scale (Gowri et al. 2022; Pinel 2020).

<i>MAPE</i>	Scale of interpretation	Significance
<10%	The ability to predict is very good	xxxxx
10-20%	Good ability of the model for prediction	xxxx
20-50%	The predictive ability of the model is feasible	xxx
>50%	Poor ability of the prediction model	x

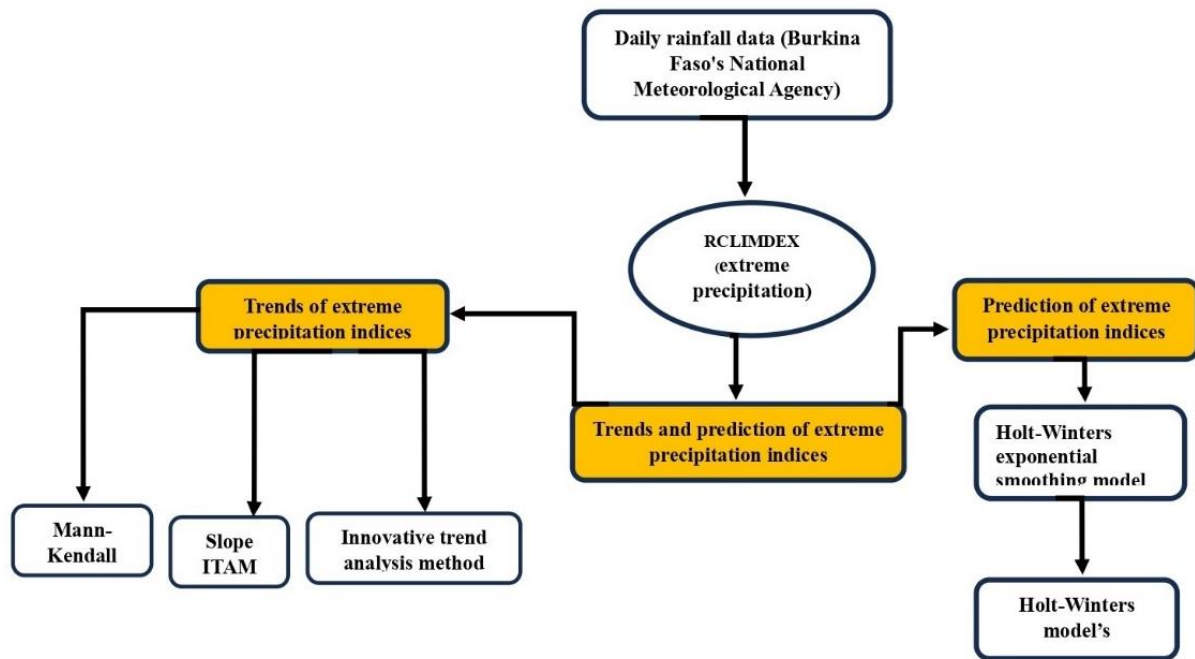


Fig. 4. Data and methods used in the study.

### 3. Results

#### 3.1. Descriptive statistics and test of extreme precipitation indices between 1991 and 2020

Table 4 shows that the extreme precipitation indices are highly variable for the Bobo-Dioulasso and Boromo stations and moderately variable for the Saria station over the period 1991-2020. The variability is particularly high for indices such as:  $r99ptot$ ,  $r95ptot$ ,  $cwd$ ,  $R20mm$ , and  $Rx1day$ . Furthermore, the descriptive statistics show that the maxima and minima are relatively higher at the Bobo-Dioulasso station than at the other stations (Boromo and Koudougou). This difference could be explained by the climatic range of the stations. The Bobo-Dioulasso station is in the Sudanese zone (with precipitation of more than 900 mm per year). On the other hand, the other stations have low annual precipitation, which varies between 600 mm and 900 mm.

#### 3.2. Trends in the indices of extreme precipitation between 1991 and 2020: an analysis using the Mann-Kendall test

The Mann-Kendall test shows that there was no trend in the extreme precipitation indices in the three cities of Burkina Faso over the period 1991-2020 (Table 5). The fact remains that a trend was observed for the frequency index ( $r99ptot$ ) in the Bobo-Dioulasso station.

Table 4. Descriptive statistics for extreme precipitation indices from 1991 to 2020.

Station	Variable	Minimum	Maximum	Mean	Standard deviation	CV
Bobo-Dioulasso	Rx1day	38.1	114	68.9	18.1	26.27
	Rx5day	61.1	208	120.5	33.1	27.47
	sdi	10.2	18.5	14.3	2.1	14.69
	prcptot	675.1	1361.9	1024.7	176.6	17.23
	R10mm	25	45	34.4	5.5	15.99
	R20mm	11	26	18.2	3.8	20.88
	R95ptot	0	568.7	209.1	142.5	68.15
	R99ptot	0	263.7	57.1	74.5	130.47
	cdd	61	106	80.3	11	13.70
	cwd	3	12	5.3	1.9	35.85
	Variable	Minimum	Maximum	Mean	Standard deviation	CV
Boromo	Rx1day	44.2	134	75.7	26	34.35
	Rx5day	64.3	216.5	114.6	31.8	27.75
	SDII	10	17.5	14.3	1.8	12.59
	prcptot	643.1	1128.8	915.8	136.3	14.88
	R10mm	23	38	31.3	3.9	12.46
	R20mm	8	23	16	3.6	22.50
	R95ptot	44.2	434.4	199.9	110	55.03
	R99ptot	0	228	65	75	115.38
	cdd	50	117	82.4	15.4	18.69
	cwd	3	10	5	1.7	34
	Variable	Minimum	Maximum	Mean	Standard deviation	CV
Koudougou	Rx1day	50	127	73.1	19.2	26.27
	Rx5day	64	172	115.6	26.2	22.66
	SDII	10.8	17.7	14.3	1.5	10.49
	prcptot	624.8	1151.6	825.3	111.6	13.52
	R10mm	21	34	27.3	3.6	13.19
	R20mm	1	4	2	1	50
	R95ptot	54	307	174.2	75.7	43.46
	R99ptot	0	198	54.9	58.7	106.92
	cdd	63	133	92.8	18	19.40
	cwd	2	8	4.6	1.5	32.61

Table 5. Trend in extreme precipitation indices using the Mann-Kendall test.

	Index classification	Indices	Kendall's Tau	S	Var(S)	p-value	Trend	Trend direction
Bobo-Dioulasso station	Intensity indices Precipitation	rx1day	0.166	72.000	3140.667	0.205	no	-
		rx5day	0.124	54.000	3140.667	0.344	no	-
		sdii	0.136	59.000	3141.667	0.301	no	-
		prcptot	0.103	45.000	3141.667	0.432	no	-
	Frequency indices Precipitation	r10mm	0.082	35.000	3121.667	0.543	no	-
		r20mm	0.071	30.000	3104	0.603	no	-
		r95ptot	0.058	25.000	3137	0.668	no	-
		r99ptot	0.262	97.000	2648.333	<b>0.049</b>	<b>Yes</b>	<b>increase</b>
	Duration indices Precipitation	cdd	0.058	25.000	3133.667	0.668	no	-
		cwd	0.191	73.000	2881	0.180	no	-
Boromo station	Intensity indices Precipitation	rx1day	-0.018	-8.000	3140.667	0.901	no	-
		rx5day	0.085	37.000	3141.667	0.521	no	-
		sdii	0.154	67.000	3141.667	0.239	no	-
		prcptot	0.071	31.000	3141.667	0.592	no	-
	Frequency indices Precipitation	r10mm	0.093	39.000	3091.667	0.494	no	-
		r20mm	0.165	69.000	3093	0.221	no	-
		r95ptot	0.071	31.000	3141.667	0.592	no	-
		r99ptot	-0.140	-53.000	2732.333	0.320	no	-
	Duration indices Precipitation	cdd	-0.028	-12.000	3134	0.844	no	-
		cwd	0.003	1.000	2708.333	1.000	no	-
Saria station	Intensity indices Precipitation	rx1day	0	0.000	2558	1.000	no	-
		rx5day	-0.130	-49.000	2561	0.343	no	-
		sdii	0.212	80.000	2562	0.119	no	-
		prcptot	-0.074	-28.000	2562	0.594	no	-
	Frequency indices Precipitation	r10mm	-0.125	-46.000	2532.667	0.371	no	-
		r20mm	0.076	25.000	2332.333	0.619	no	-
		r95ptot	0.011	4.000	2562	0.953	no	-
		r99ptot	0.036	12.000	2293.333	0.818	no	-
	Duration indices Precipitation	cdd	-0.051	-19.000	2557	0.722	no	-
		cwd	-0.064	-22.000	2432.667	0.670	no	-

### 3.3. Trends in the indices of extreme precipitation between 1991 and 2020: an analysis using the innovative trend method

The innovative template trends method shows clear trends in the precipitation extremes indices according to the study stations.

#### 3.3.1. Trends in the indices of extreme precipitation in the city of Bobo-Dioulasso

At this station, especially in the city of Bobo-Dioulasso, the precipitation intensity indices are increasing for prptot, rx5day, and sdii; rx1day decreased non-monotonically. For the extreme precipitation frequency indices, the trends are non-monotonic for r20mm, r10mm, and monotonic for r95ptot and r99ptot.

Conversely, the duration indices (cdd and cwd) are non-monotonic. Figure 5 summarises the trends of the extreme precipitation indices for the city of Bobo-Dioulasso over the period 1991-2020.

Figures 5b, 5c, and 5d, which group together precipitation intensity indices, show increases, in contrast to Figure 5a. The same applies to precipitation frequency indices. Figures 5f, 5g, and 5h, (but not 5e), are also increasing over the period 1991-2020. For the precipitation duration index, Figure 5i shows an increasing trend, while Figure 5j shows a non-monotonic increasing trend. The trends in extreme precipitation are increasing overall, and this situation could be explained by the climatic range in which the Bobo-Dioulasso station is located. The station is in the Sudanian zone, with annual precipitation in excess of 900 mm.

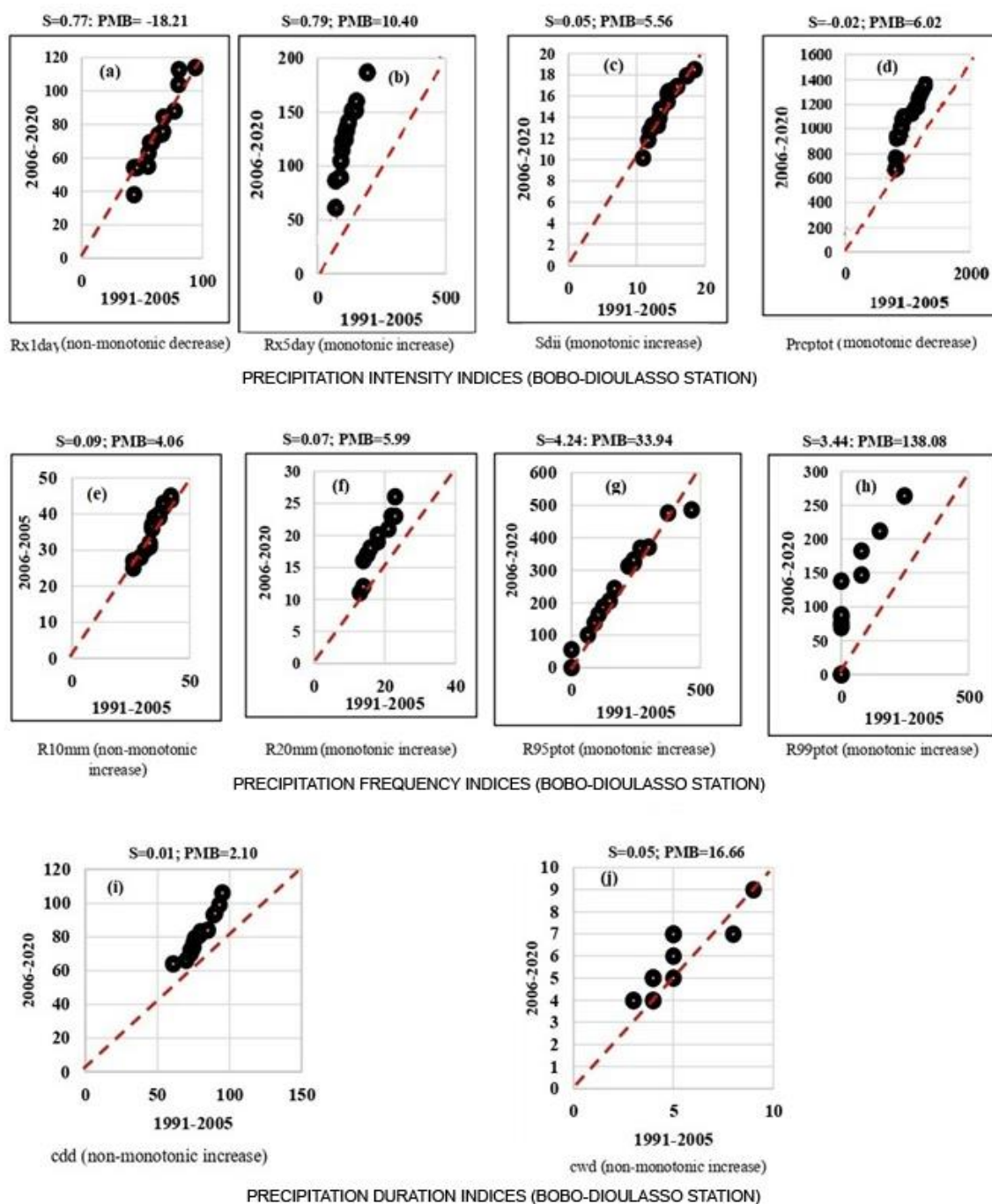


Fig. 5. Template trends of the extreme precipitation indices (station of Bobo-Dioulasso).

### 3.3.2. Trends in the indices of extreme precipitation in the city of Boromo

Figure 6 shows the graphical trends at the Boromo station in the town of Boromo. The precipitation intensity indices (Fig. 6b, 6c, 6d) increase monotonically. The precipitation frequency indices (Fig. 6e, 6f, 6h) are also increasing, with the exception of Figure 6g, which shows a non-monotonically increasing trend. In addition, the trends are non-monotonically decreasing in Figure 6i and non-monotonically increasing in Figure 6j.

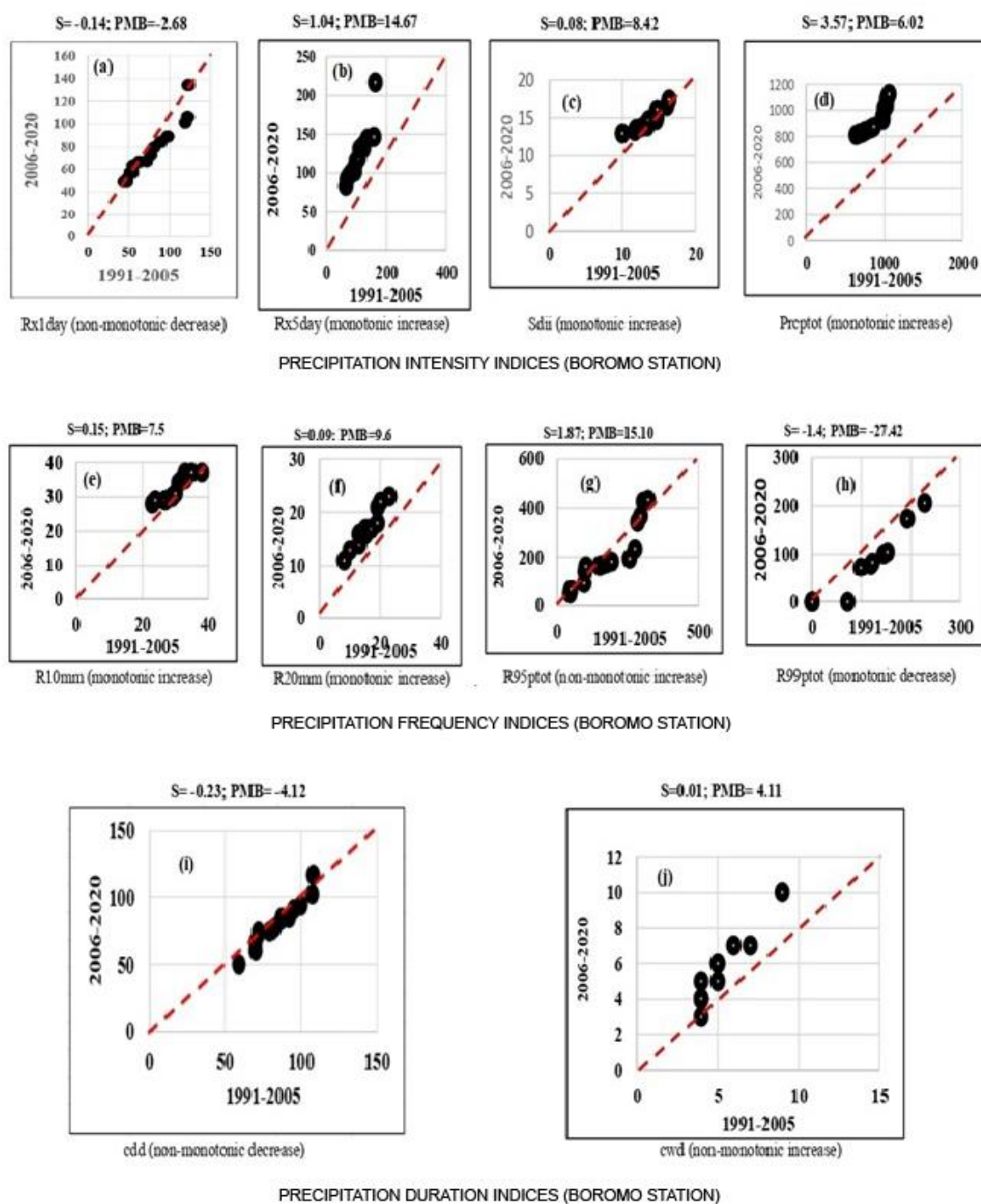


Fig. 6. Template trends of the extreme precipitation indices (Boromo station).

### 3.3.3. Trends in the indices of extreme precipitation in the city of City of Koudougou

The graphical trends of the extreme precipitation indices for the Saria station are more non-monotonic (Fig. 7). Extreme precipitation at the Saria station (city of Koudougou) shows unclear, even decreasing trends for precipitation duration indices, unlike the other two stations studied. This situation could be explained by the station's location in the Sudano-Sahelian region, where precipitation varies between 600 mm and 900 mm per year.

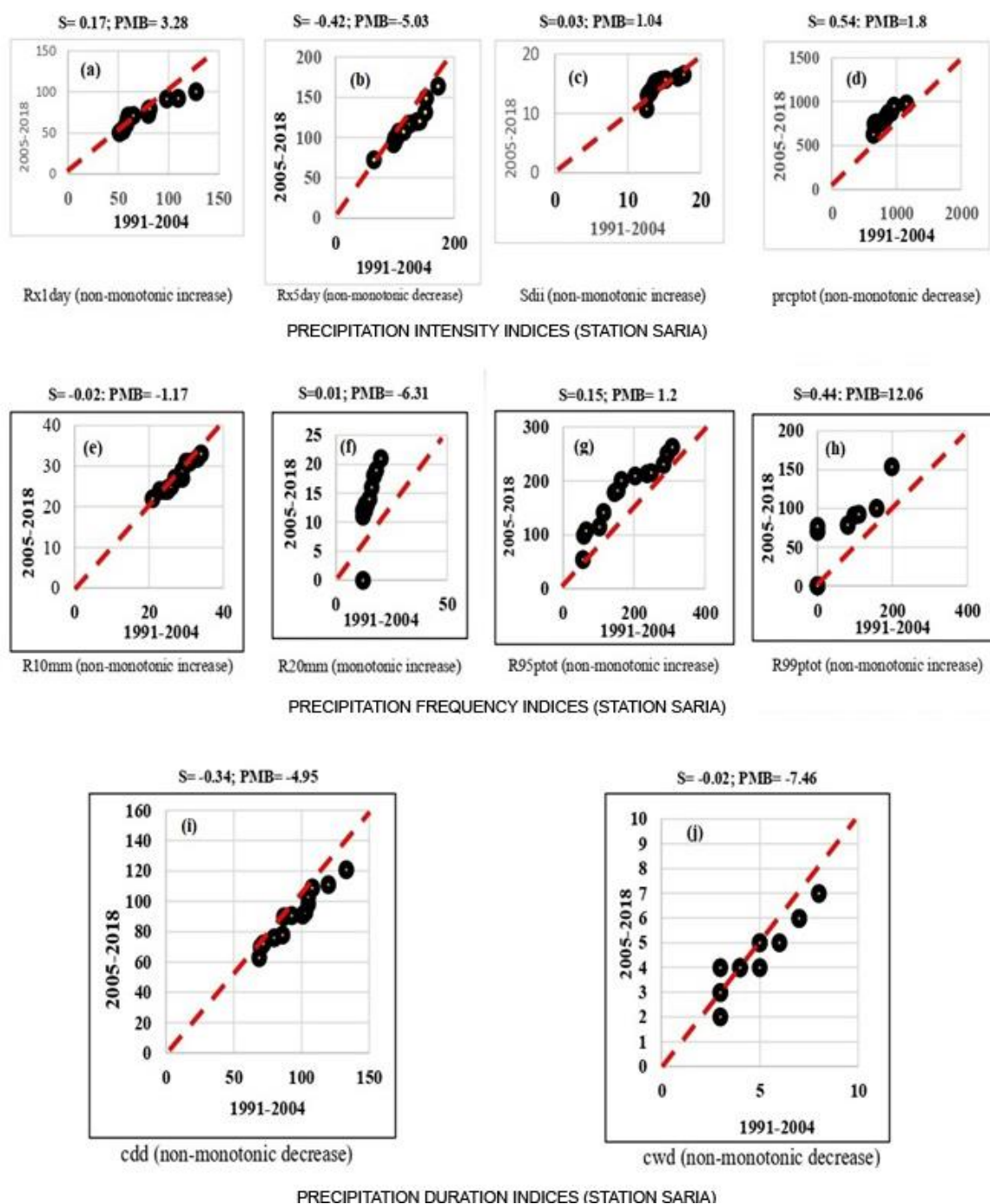


Fig. 7. Template trends of the extreme precipitation indices (station Saria).



### **3.4. Future projections of extreme precipitation indices for cities in Burkina Faso from 2020 to 2030**

It is necessary to assess the performance of the Holt-Winters model to analyze the predicted precipitation indices for the three cities. Two models, additive and multiplicative, were used to assess the accuracy of the models proposed for each station. The prediction period is 10 years, specifically 2020-2030.

#### **3.4.1. The case of the city of Bobo-Dioulasso (Bobo-Dioulasso station)**

Table 6 shows that the additive Holt-Winters model is more accurate than the multiplicative Holt-Winters model based on the MAPE results. Nevertheless, the additive model does not fit  $R95_{ptot}$  and  $R99_{ptot}$  very well, with values of 86.05 and 73.7, respectively, indicating poor predictive ability of the model for these two indices. However, this model is more appropriate for the other extreme precipitation indices. This disparity leads to the use of the Holt-Winters additive model to analyze the future evolution of the extreme indices.

#### **3.4.2. The case of the city of Boromo (Boromo station)**

The performance of the additive and multiplicative models, according to MAPE, shows better accuracy for the additive model compared to the multiplicative model (Table 7). However, as at the Bobo-Dioulasso station, the additive model does not correctly adjust indices such as  $r95_{ptot}$  and  $r99_{ptot}$ .

#### **3.4.3. The case of the city of Koudougou (Saria station)**

As with the two stations above, the extreme precipitation index data applied to the additive and multiplicative models shows that the additive model provides a better fit for the extreme precipitation indices at the Saria station (Table 8).

Table 6. Results of the evaluation of the Holt-Winters additive and multiplicative models for the Bobo-Dioulasso station.

Index	Model parameters			Observation	DDL	SCE	MCE	RMCE	MAPE	MPE	MAE
	$\alpha$	$\beta$	$\gamma$								
rx1day	0.2	0.2	0.2	30	14	8131.8	580.84	24.10	<b>24.27<sup>xxx</sup></b>	-8.124	14.3
rx5day	0.2	0.2	0.2	30	14	41235	2945.36	54.3	<b>37<sup>xxx</sup></b>	-13.686	37.8
sdi	0.2	0.2	0.2	30	14	172.5	12.32	3.5	<b>18<sup>xxxx</sup></b>	-1.628	2.5
r10mm	0.2	0.2	0.2	30	14	1398.7	99.91	10	<b>20.5<sup>xxx</sup></b>	0.409	7.3
r20mm	0.2	0.2	0.2	30	14	586.8	41.91	6.5	<b>30.6<sup>xxx</sup></b>	-4.505	5.1
cdd	0.2	0.2	0.2	30	14	4441.5	317.25	17.8	<b>14.3<sup>xxxx</sup></b>	-1.094	11.8
cwd	0.2	0.2	0.2	30	14	98.073	7	2.65	<b>37.8<sup>xxx</sup></b>	-1.915	1.9
R95ptot	0.2	0.2	0.2	30	14	913811	652722	255.5	86.05 <sup>x</sup>	-10.94	198
R99ptot	0.2	0.2	0.2	30	14	147205	10515	102.5	73.7 <sup>x</sup>	21.68	70.8
prcptot	0.2	0.2	0.2	30	14	1074813	76772	277.07	20.9 <sup>xxx</sup>	-0,590	205.3
Holt-Winters Seasonal Additive Model											
Index	Model parameters			Observation	DDL	SCE	MCE	RMCE	MAPE	MPE	MAE
	$\alpha$	$\beta$	$\gamma$								
rx1day	0.2	0.2	0.2	30	14	8543.4	610.2	24.7	<b>26.2<sup>xxx</sup></b>	-11.2	15.5
rx5day	0.2	0.2	0.2	30	14	45638.6	3259.9	57.1	<b>37.8<sup>xxx</sup></b>	-20.2	36.4
sdi	0.2	0.2	0.2	30	14	171.1	12.2	3.5	<b>18<sup>xxxx</sup></b>	-3.5	2.5
r10mm	0.2	0.2	0.2	30	14	1371.1	97.9	9.9	<b>21.7<sup>xxx</sup></b>	-2.3	7.6
r20mm	0.2	0.2	0.2	30	14	574.2	41	6.4	<b>31<sup>xxx</sup></b>	-8.8	5.1
cdd	0.2	0.2	0.2	30	14	5077.8	362.7	19	<b>16<sup>xxxx</sup></b>	-2.9	13.1
cwd	0.2	0.2	0.2	30	14	113.4	8.1	2.8	<b>39.7<sup>xxx</sup></b>	-13.5	2
r95ptot	0.2	0.2	0.2	30	14	1139410	81386.5	285.3	<b>100.6<sup>x</sup></b>	-43.6	213
R99ptot	0.2	0.2	0.2	30	14	170915.7	12208.3	110.5	<b>83<sup>x</sup></b>	15	71.9
prptot	0.2	0.2	0.2	30	14	1027791	73413.6	270.9	<b>20.9<sup>xxx</sup></b>	-3	203.4
Multiplicative Holt-Winters method											

xxxxx: model is very good

xxx: Good forecasting ability

xxx: Model's forecasting ability is feasible

x: Bad forecasting model ability

Table 7. Results of the evaluation of the Holt-Winters additive and multiplicative models for the Boromo station.

Index	Model parameters			Observations	DDL	SCE	MCE	RMCE	MAPE	MPE	MAE
	$\alpha$	$\beta$	$\gamma$								
rx1day	0.2	0.2	0.2	30	14	31164.6	2226	47.2	<b>48.3<sup>xxx</sup></b>	-9.4	33.9
rx5day	0.2	0.2	0.2	30	14	48533	3466.6	59	<b>37.9<sup>xxx</sup></b>	-7.6	44.3
sdii	0.2	0.2	0.2	30	14	163	11.6	3.4	<b>18.4<sup>xxxx</sup></b>	-1.0	2.7
r10mm	0.2	0.2	0.2	30	14	863.1	61.6	7.9	<b>19.1<sup>xxxx</sup></b>	-2.5	6
r20mm	0.2	0.2	0.2	30	14	475	34	5.8	<b>25.8<sup>xxx</sup></b>	-3.2	4.3
cdd	0.2	0.2	0.2	30	14	8619	615.6	24.8	<b>21.7<sup>xxx</sup></b>	-3.8	16.6
cwd	0.2	0.2	0.2	30	14	118	8.4	2.9	<b>38.9<sup>xxx</sup></b>	-11.2	1.8
r95ptot	0.2	0.2	0.2	30	14	681573	48684	220.6	115.9 <sup>x</sup>	-55.2	162.4
r99ptot	0.2	0.2	0.2	30	14	301900	21564.3	146.8	<b>106.3<sup>x</sup></b>	73.7	111.7
prcptot	0.2	0.2	0.2	30	14	102563	73259.4	270.7	<b>23.4<sup>xxx</sup></b>	-2.2	212.2
Holt-Winters Seasonal Additive Model											
Index	Model parameters			Observations	DDL	SCE	MCE	RMCE	MAPE	MPE	MAE
	$\alpha$	$\beta$	$\gamma$								
rx1day	0.2	0.2	0.2	30	14	33035	2359.6	48.5	53.7 <sup>x</sup>	-27.2	35.6
rx5day	0.2	0.2	0.2	30	14	60375	4312.5	65.7	<b>44.1<sup>xxx</sup></b>	-18.8	49.9
sdii	0.2	0.2	0.2	30	14	189.2	13.5	3.6	<b>20<sup>xxxx</sup></b>	-3.8	2.9
r10mm	0.2	0.2	0.2	30	14	988	70.5	8.4	<b>20.2<sup>xxx</sup></b>	-5.3	6.3
r20mm	0.2	0.2	0.2	30	14	682.5	48.7	6.9	<b>31.2<sup>xxx</sup></b>	-10.3	5.1
cdd	0.2	0.2	0.2	30	14	8916	636.8	25.2	<b>22.3<sup>xxx</sup></b>	-5.8	16.9
cwd	0.2	0.2	0.2	30	14	135.4	9.6	3.1	<b>44.1<sup>xxx</sup></b>	-22.01	1.9
r95ptot	0.2	0.2	0.2	30	14	1815688	129691.9	360.1	211.8 <sup>x</sup>	-177.9	244.5
R99ptot	0.2	0.2	0.2	30	14	167615	11972.4	109.4	64.1 <sup>x</sup>	63.6	77.6
prcptot	0.2	0.2	0.2	30	14	1228361	87740	296.2	<b>25.2<sup>xxx</sup></b>	-6.6	226.3
Multiplicative Holt-Winters method											

xxxxx: model is very good

xxxx: Good forecasting ability

xxx: Model's forecasting ability is feasible

x: Bad forecasting model ability

Table 8. Results of the evaluation of the Holt-Winters additive and multiplicative models for the Boromo station.

Index	Model parameters			Observations	DDL	SCE	MCE	RMC E	MAPE	MPE	MAE
	$\alpha$	$\beta$	$\gamma$								
rx1day	0.2	0.2	0.2	28	12	10161.9	846.8	29.1	<b>27.7<sup>xxx</sup></b>	-1.8	21.4
rx5day	0.2	0.2	0.2	28	12	17430.9	1452.6	38.1	<b>21.7<sup>xxx</sup></b>	-5.6	24.3
sdii	0.2	0.2	0.2	28	12	41.5	3.5	1.9	<b>8.9<sup>xxxxx</sup></b>	2.2	1.3
r10mm	0.2	0.2	0.2	28	12	640.5	53.4	7.3	<b>20.4<sup>xxx</sup></b>	-1.9	5.6
r20mm	0.2	0.2	0.2	28	12	33.3	2.8	1.7	53.8 <sup>x</sup>	-17.3	1.1
cdd	0.2	0.2	0.2	28	12	15067	1255.6	35.4	<b>31<sup>xxx</sup></b>	-2.5	26.5
cwd	0.2	0.2	0.2	28	12	135	11.3	3.4	68.2 <sup>x</sup>	-28.5	2.5
r95ptot	0.2	0.2	0.2	28	12	147144	12262	110.7	<b>43.1<sup>xxx</sup></b>	-5	75.6
r99ptot	0.2	0.2	0.2	28	12	67676.3	5639.7	75.1	71.9 <sup>x</sup>	17.8	53.1
prcptot	0.2	0.2	0.2	28	12	553259	46101	214.7	<b>19.3<sup>xxxx</sup></b>	-0.9	160.2
Holt-Winters Seasonal Additive Model											
Index	Model parameters			Observations	DDL	SCE	MCE	RMC E	MAPE	MPE	MAE
	$\alpha$	$\beta$	$\gamma$								
rx1day	0.2	0.2	0.2	28	12	13309.3	1109.1	33.3	<b>31.3<sup>xxx</sup></b>	-11.5	23.6
rx5day	0.2	0.2	0.2	28	12	18357	1529.7	39.1	<b>22.5<sup>xxx</sup></b>	-9.7	24.7
sdii	0.2	0.2	0.2	28	12	38.2	3.2	1.8	<b>8.6<sup>xxxxx</sup></b>	1.8	1.3
r10mm	0.2	0.2	0.2	28	12	672	56	7.5	<b>20.6<sup>xxx</sup></b>	-4.3	5.6
r20mm	0.2	0.2	0.2	28	12	65.6	5.5	2.3	77.7 <sup>x</sup>	-52.1	1.5
cdd	0.2	0.2	0.2	28	12	14366.2	1197.2	34.6	<b>30.8<sup>xxx</sup></b>	-7.2	26
cwd	0.2	0.2	0.2	28	12	157.4	13.1	3.6	74 <sup>x</sup>	-49.6	2.5
R95ptot	0.2	0.2	0.2	28	12	315065	26255.4	162	62.2 <sup>x</sup>	-38.4	110.7
R99ptot	0.2	0.2	0.2	28	12	75320.3	6276.7	79.2	83 <sup>x</sup>	38	59.4
prcptot	0.2	0.2	0.2	28	12	521007	43417	208.4	<b>19<sup>xxxxx</sup></b>	-3.8	155.5
Multiplicative Holt-Winters method											

xxxxx: model is very good

xxxx: Good forecasting ability

xxx: Model's forecasting ability is feasible

X: Bad forecasting model ability

### 3.5. Projection trajectories between 2020 and 2030 for extreme precipitation indices

Because the additive model is a better fit to the extreme precipitation index data from the study stations, this model is adopted for future predictions for the period 2020-2030. In addition, the fit of the model varies between the study stations. Therefore, the analyses are based on the study stations.

#### 3.5.1. The case of the city of Bobo-Dioulasso (Bobo-Dioulasso station)

The results of the predictions for the 2030 period show that the precipitation intensity indices (rx1day, r5day, sdi, and prcptot) and the precipitation frequency indices (r10mm, r20mm, r95ptot, r99ptot) will increase between 2020 and 2030. The situation is different for the precipitation duration indices, with CDD steadily increasing until 2030 and CWD decreasing over the same period (Fig. 8). In the figure, blue indicates observed precipitation extremes, and red lines indicate the Holt-Winters prediction of precipitation extremes. The dotted green line indicates the trend. The figure shows that the indices rx5day and cwd display downward trends until 2030. On the other hand, the other indices (rx1day, sdi, prcptot, r10mm, r20mm, r95ptot, r99ptot) show increasing trends until 2030. Given this situation, flooding and water-borne diseases are likely to be a problem in the city in the coming years.

#### 3.5.2. The case of the city of Boromo (Boromo station)

At this station, precipitation intensity and duration indices are increasing (Fig. 9). However, the precipitation frequency indices show different trends. R10mm and r99ptot decrease, while r20mm and r95ptot increase from 2020 to 2030.

#### 3.5.3. The case of the city of Koudougou (Saria station)

The precipitation intensity indices show different trends. In fact, rx1day and rx5day are decreasing, while sdi and prcptot increase continuously from 2020 to 2030. The same is true for the precipitation frequency indices, which show a decreasing trend for r10mm, r95ptot, and r99ptot. The only frequency index that increases is r20mm. In addition, the precipitation duration indices increase from 2020 to 2030. The city of Koudougou should suffer less from climatic disasters than the other two cities, in the sense that intensity and frequency are low over the period 2020-2030. However, the increase in precipitation duration will be detrimental to farmers on the outskirts of the city and urban market gardeners. Figure 10 shows the changes in extreme precipitation indices from 2020 to 2030. The figure shows that two forecast trends are also noticeable at the Saria station. In contrast to the other stations, the forecast trends are more negative than positive. The downward trends are represented by Figure 10 (rx1day), (rx5day). Conversely, Figure 10 (sdi), (prcptot), (r20mm), and (cdd) shows upward trends. Thus, the city of Koudougou may be less affected by extreme precipitation than the other two cities of Bobo-Dioulasso and Boromo.

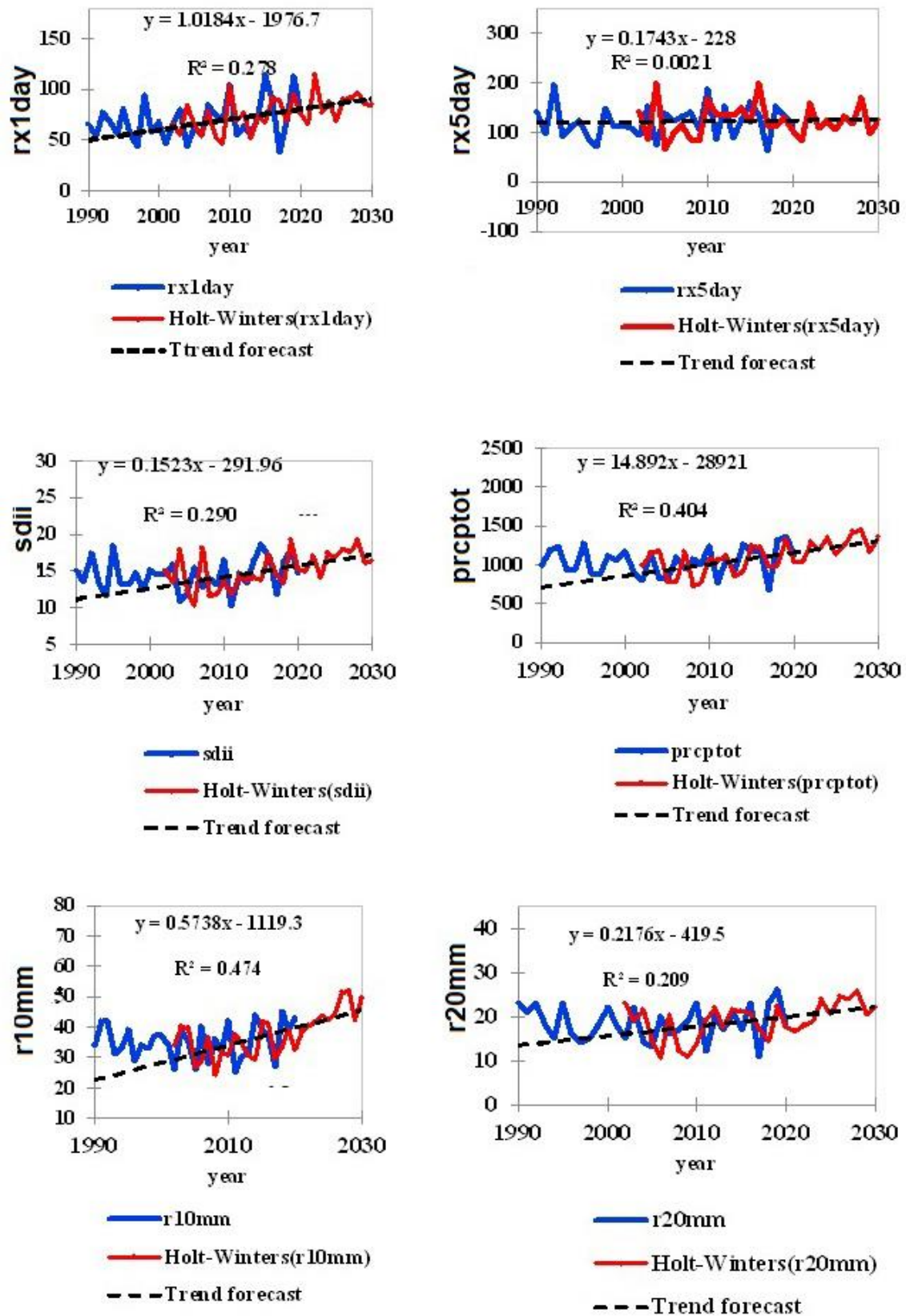


Fig. 8. Predictions of the changes in the indices of extreme precipitation for the station of Bobo-Dioulasso.

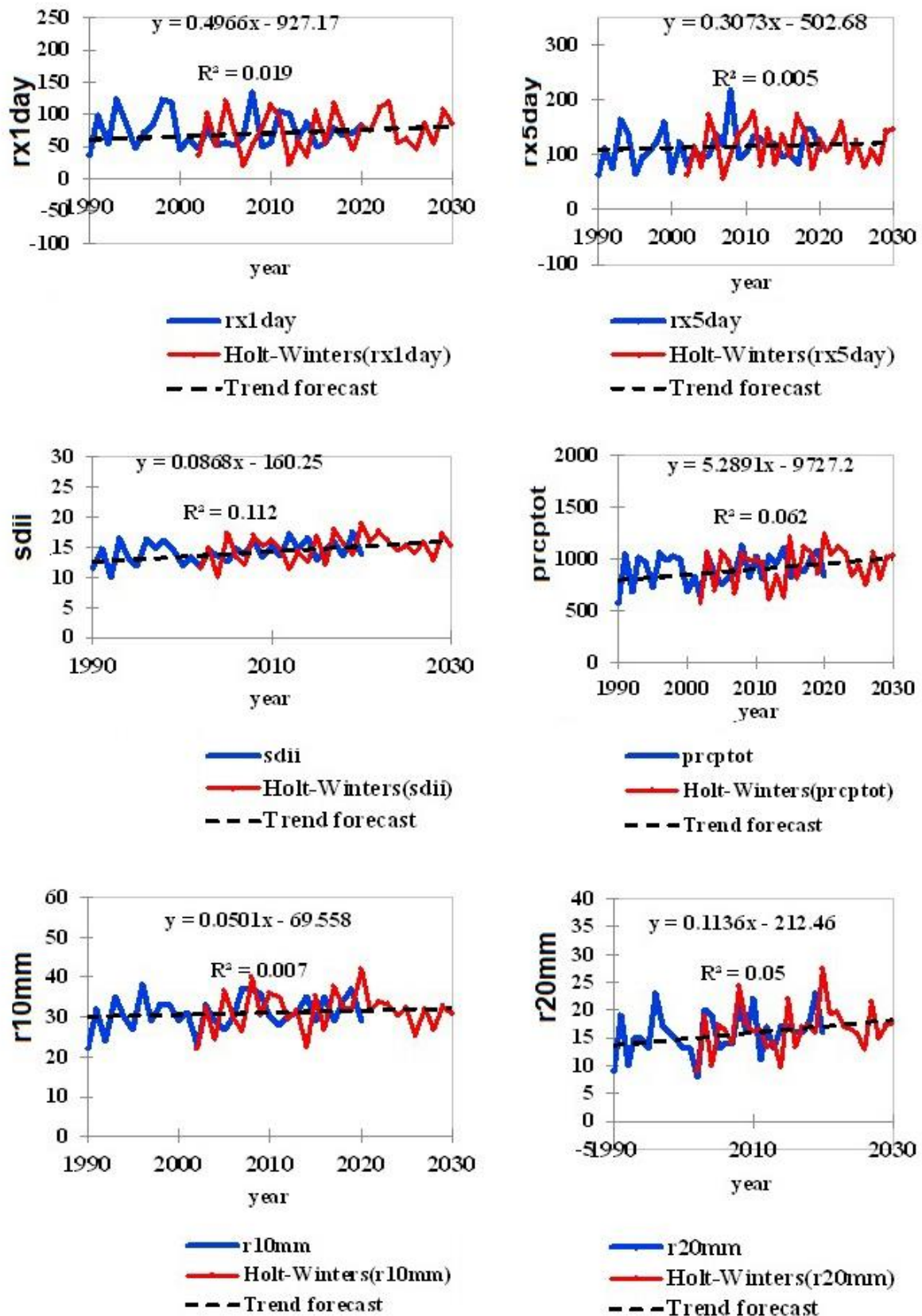


Fig. 9. Predictions of the changes in the indices of extreme precipitation for the station of Boromo.



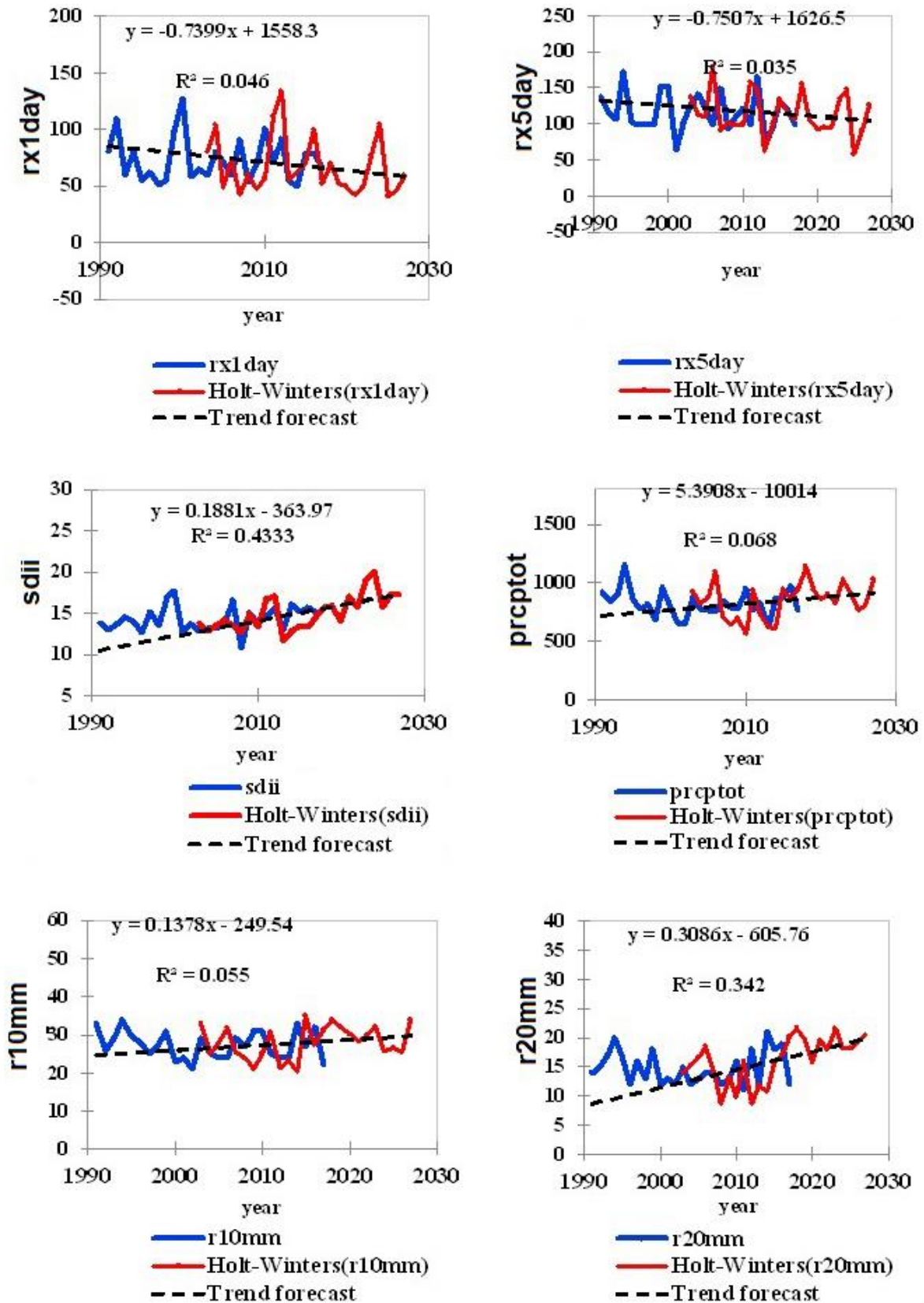


Fig. 10. Predictions of the changes in the indices of extreme precipitation for the station of Saria.

## **4. Discussion**

### **4.1. Analysis of inter-annual variability and trends in extreme precipitation indices in West Africa**

Time series are records of processes that change over time (Ihaka 2005). This study has shown strong variability in extreme precipitation indices at the three study stations. In addition, the extreme precipitation indices showed a continuous increase from 1991 to 2020. The results confirm the work of other authors in Burkina Faso and West Africa (Bigi et al. 2018). Indeed, extreme precipitation indices such as rx1day, rx5day, prcptot, and sdii increased and r95ptot decreased from 1991 to 2021 in the Boucle du Mouhoun region of Burkina Faso (Rouamba et al. 2023). Yanogo and Yaméogo (2023) also note that indices such as prcptot and r95ptot are increasing for the Ouahigouya station in Burkina Faso. These results are confirmed by the study of Tazen et al. (2019) in Burkina Faso, which showed an upward trend in indices such as Rx1day, Rx5day, and r99ptot from 1961 to 2015. This trend has also been observed in other West African countries by various authors. In Niamey, Niger, the same indices (rx1day, rx5day, prcptot) also increased between 1990 and 2020 (Bassirou et al. 2023). Bigi et al. (2018) add that a similar trend was observed in Niamey city (Niger) between 1980 and 2009. This confirms the studies by Konate et al. (2023) in Côte d'Ivoire during 1961-2015. Indeed, the authors note that indices such as prcptot, sdii, rx1day, rx5day, r20mm, r95ptot, and r99ptot increased in Ivorian cities (Gagnoa, Daloa, Yamoussoukro), while cdd and cwd decreased between 1961 and 2015. In other cities (Korhogo, Odienné, Bondoukou, Man, Abidjan, Adiaké, San-Pedro, Tabou, Sassandra), indices such as prcptot, sdii, CDD, CWD, R10mm, and R20mm show significantly negative trends (Konate et al. 2023). The exception is San-Pedro, which shows significantly positive trends for the prcptot, sdii, CDD, and R10mm indices. This situation shows that when the zones are located in the Ivory Coast's Sudanese-type climate, the trends of the indices are negative. On the other hand, when the zones are located in the Baulean-type climate zones, the extreme precipitation indices tend to show positive trends overall. Furthermore, in the Attean climate, the precipitation indices are positive overall. It is therefore clear that the trends vary according to the climatic zone, a situation that is also revealed by the results of the zones studied using the innovative method.

### **4.2. Analysis of the predictions of the extreme precipitation index**

Forecasting precipitation is important for two reasons: it is a major scientific challenge, but it is also crucial for planning and developing agricultural strategies (Graham, Mishra 2017). In the study cities, precipitation intensity and frequency indices are expected to increase between 2020 and 2030 in the large city of Bobo-Dioulasso, the medium-sized city of Koudougou, and the small city of Boromo. However, the city of Koudougou should be less affected than the other two cities, as many extreme indices such as cdd, r95ptot, r99ptot, r10mm, rx1day and rx5day will decrease continuously until 2030. These results are consistent with those for Africa (Abiodun et al. 2017). Indeed, the authors note that coastal cities will experience an increase in extreme precipitation indices, with cities such as Maputo, Logos, and Port Said expected to experience an increase in the intensity and frequency of extreme precipitation between 2081 and 2100. Other authors, such as Biasutti (2013) and Trepekli et al. (2019), note that precipitation is

expected to be concentrated in more intense extreme precipitation events, interspersed with long periods of low precipitation over the West African Sahel. Another study conducted in Africa by Habiyakare et al. (2024) confirms the findings of the previous authors. In fact, according to these authors, West Africa, East Africa, and the eastern part of South Africa show an increasing trend in extreme precipitation, and changes in extreme precipitation indices show a general increase in the occurrence and frequency of extreme precipitation indices in all scenarios by the end of the 21<sup>st</sup> century.

#### **4.3. The sources of uncertainty and limitations of the methods**

Precipitation in Burkina Faso tends to be erratic from month to month and season to season. This makes it difficult to make accurate forecasts. The Holt-Winters exponential smoothing method is therefore used in this study. This method has clear advantages because it accounts for trends and seasonality (Pongdatu, Putra 2018), which corresponds to the characteristics of precipitation in the tropics. This situation has led other authors (Pertiwi 2020) to use this method in the tropics. However, this method has shortcomings that need to be considered. The method is deterministic because for each point in the future, the forecast provides a single value that approximates the future outcome. It does not allow other possibilities to be considered. In addition, exponential smoothing forecasting techniques only consider historical data, which means that they ignore any information that may be generated at the same time (Pardoux, Goldfarb 2013). Pinel (2020) adds that the Holt-Winters method has three major shortcomings: first, there is no guarantee that the method is optimal for a given data series; exponential smoothing methods are sometimes far from optimal. In addition, forecasts are more accurate in the short term (a few years). On the other hand, they cannot provide forecast intervals, i.e. an interval containing the forecast with a given probability. This is because a probabilistic framework has not yet been defined. Thus, the results of the forecasting study are limited. Indeed, if the period considered is intermediate (2020-2030), the forecasts of the Holt-Winters method become less accurate as the time considered is extended. In this study, therefore, the forecast for the first five years (2020-2025) is more accurate than that for the remaining five years (2025-2030). In addition, the data analysis is done with software that only allows models of deterministic precision as mean square error, and the choice of parametric models is limited to 0.2  $\alpha$ ,  $\beta$ , and  $\gamma$ . These constraints do not allow for any flexibility in the accuracy of the forecasts. Nevertheless, our results provide decision-makers with an indication of the evolution of extreme precipitation indices over the period 2020-2030, with greater accuracy between 2020 and 2025, given the short-term option of the forecasting method.

#### **5. Conclusions**

The study analyzed the trends and projected trajectories of extreme precipitation indices in the cities of Burkina Faso. The precipitation intensity and frequency indices are variable, with an upward trend for the cities of Bobo-Dioulasso, Boromo, and Koudougou. Template trends also show a steady increase in precipitation intensity and frequency indices for the cities of Bobo-Dioulasso and Boromo. For the city of Koudougou, a non-monotonic increasing trend is observed for the precipitation intensity and frequency indices. The rain duration indices show a non-monotonic decreasing trend. The Holt-Winters method can

be used to make short-term predictions. This method was used to predict extreme precipitation indices between 2020 and 2030, which are increasing for the intensity and frequency indices in the cities of Bobo-Dioulasso and Boromo. However, the indices have relatively high variability, accompanied by an upward trend over the period 2020-2030. Under these conditions, the authorities in the affected towns should give absolute priority to widening the gutters to allow rainwater to drain away. In addition, the town of Boromo is in a special situation compared to the others, since its population has increased in response to internal migration caused by terrorism in the country. The migrants have settled in flood-prone areas, and the local authorities should encourage them to move away from easily flooded areas.

## References

- Abiodun B.J., Adegoke J., Abatan A.A., Ibe C.A., Egbebiyi T.S., Engelbrecht F., Pinto I., 2017, Potential impacts of climate change on extreme precipitation over four African coastal cities, *Climatic Change*, 143, 399-413, DOI: 10.1007/s10584-017-2001-5.
- Aditya F., Gusmayanti E., Sudrajat J., 2021, Rainfall trend analysis using Mann-Kendall and Sen's slope estimator test in West Kalimantan, *IOP Conference Series: Earth and Environmental Science*, 893 (1), DOI: 10.1088/1755-1315/893/1/012006.
- Almazroui M., Şen Z., Mohorji A.M., Islam M.N., 2019, Impacts of climate change on water engineering structures in arid regions: case studies in Turkey and Saudi Arabia, *Earth Systems and Environment*, 3, 43-57, DOI: 10.1007/s41748-018-0082-6.
- Atoyebi S.B., Olayiwola M.F., Oladapo J.O., Oladapo D.I., 2023, Forecasting Currency in Circulation in Nigeria Using Holt-Winters Exponential Smoothing Method, *South Asian Journal of Social Studies and Economics*, 20 (1), 25-41, DOI: 10.9734/sajsse/2023/v20i1689.
- Barry A.A., Caesar J., Klein Tank A.M.G., Aguilar E., McSweeney C., Cyrille A.M., Nikiema M.P., Narcisse K.B., Sima F., Stafford G., Touray L.M., Ayilari-Naa J.A., Mendes C.L., Touunkara M., Gar-Glahn E.V.S., Coulibaly M.S., Dieh M.F., Mouhaimouni M., Oyegade J.A., Sambou E., Laogbessi E.T., 2018, West Africa climate extremes and climate change indices, *International Journal of Climatology*, 38 (S1), e921-e938, DOI: 10.1002/joc.5420.
- Bassirou H., Masamaéya D.T.G., Sanda I.S., Cheo A.E., Sougue M., Pouye I., 2023, Extreme rainfall and streamflow in Niamey City: Trends and relationship between higher streamflow and rainfall, *International Journal of Water Resources Engineering*, 9 (1), 21-32, DOI: 10.37628/jwre.v9i1.802.
- Béwentaoré S., Barro D., 2022, Space-time trend detection and dependence modeling in extreme event approaches by functional peaks-over-thresholds: Application to precipitation in Burkina Faso, *International Journal of Mathematics and Mathematical Sciences*, 1, DOI: 10.1155/2022/2608270.
- Bhagat S.K., Ramaswamy K., 2023, Precipitation variations in the central Vietnam to forecast using Holt-Winters Seasonal Additive Forecasting method for 1990 to 2019 trend, *IOP Conference Series: Earth and Environmental Science*, 1216 (1), DOI: 10.1088/1755-1315/1216/1/012019.
- Biasutti M., 2013, Forced Sahel rainfall trends in the CMIP5 archive, *Journal of Geophysical Research: Atmospheres*, 118 (4), 1613-1623, DOI: 10.1002/jgrd.50206.
- Bigi V., Pezzoli A., Rosso M., 2018, Past and future precipitation trend analysis for the City of Niamey (Niger): An overview, *Climate*, 6 (3), DOI: 10.3390/cli6030073.
- Chowdari K.K., Deb Barma S., Bhat N., Girisha R., Gouda K.C., Mahesha A., 2023, Trends of seasonal and annual rainfall of semi-arid districts of Karnataka, India: application of innovative trend analysis approach, *Theoretical and Applied Climatology*, 152 (1), 241-264, DOI: 10.1007/s00704-023-04400-9.
- Dabanli İ., Şen Z., Yeleğen M.O., Şişman E., Selek B., Güçlü Y.S., 2016, Trend assessment by the innovative-Şen method, *Water Resources Management*, 30 (14), 5193-5203, DOI: 10.1007/s11269-016-1478-4.

- Diémé L.P.M., Bouvier C., Bodian A., Sidibé A., 2025, Detection of flooding by overflows of the drainage network: Application to the urban area of Dakar (Senegal), *Natural Hazards and Earth System Sciences*, 25, 1095-1112, DOI: 10.5194/egusphere-2023-2458.
- Doan Q.-V., Kobayashi S., Kusaka H., Chen F., He C., Niyogi D., 2023, Tracking urban footprint on extreme precipitation in an African megacity, *Journal of Applied Meteorology and Climatology*, 62 (2), 209-226, DOI: 10.1175/JAMC-D-22-0048.1.
- Ezeh A., Kissling F., Singer P., 2020, Why sub-Saharan Africa might exceed its projected population size by 2100, *The Lancet*, 396 (10258), 1131-1133, DOI: 10.1016/S0140-6736(20)31522-1.
- Gbode I.E., Adeyeri O.E., Menang K.P., Intsiful J.D., Ajayi V.O., Omotosho J.A., Akinsanola A.A., 2019, Observed changes in climate extremes in Nigeria, *Meteorological Applications*, 26 (4), 642-654, DOI: 10.1002/met.1791.
- Gelper S., Fried R., Croux C., 2010, Robust forecasting with exponential and Holt–Winters smoothing, *Journal of forecasting*, 29 (3), 285-300, DOI: 10.1002/for.1125.
- Gimeno L., Sorí R., Vazquez M., Stojanovic M., Algarra I., Eiras-Barca J., Gimeno-Sotelo L., Nieto R., 2022, Extreme precipitation events, *Wiley Interdisciplinary Reviews: Water*, 9 (6), DOI: 10.1002/wat2.1611.
- Giugni M., Simonis I., Buchignani E., Capuano P., De Paola F., Engelbrecht F., Mercogliano P., Topa M.E., 2015, The impacts of climate change on African cities, [in:] *Urban Vulnerability and Climate Change in Africa: A Multidisciplinary Approach*, Springer, 37-75. DOI: 10.1007/978-3-319-03982-4\_2.
- Gowri L., Manjula K.R., Sasireka K., Deepa D., 2022, Assessment of statistical models for rainfall forecasting using machine learning technique, *Journal of Soft Computing in Civil Engineering*, 6(2), 51-67, DOI: 10.22115/SCCE.2022.304260.1363.
- Graham A., Mishra E.P., 2017, Time series analysis model to forecast rainfall for Allahabad region, *Journal of Pharmacognosy and Phytochemistry*, 6 (5), 1418-1421.
- Gundalia M.J., Dholakia M.B., 2012, Prediction of maximum/minimum temperatures using Holt Winters method with Excel spreadsheet for Junagadh region, *International Journal of Engineering Research and Technology*, 1 (6), DOI: 10.17577/IJERTV1IS6301.
- Güçlü Y.S., 2020, Improved visualization for trend analysis by comparing with classical Mann-Kendall test and ITA, *Journal of Hydrology*, 584, DOI: 10.1016/j.jhydrol.2020.124674.
- Habiyakare F., Jiang T., Yahaya I., Ndabagenga D., Kagabo J., Su B., 2024, Spatial variation and trend of extreme precipitation in Africa during 1981-2019 and its projected changes at the end of 21st century, *Journal of Geoscience and Environment Protection*, 12 (3), 192-221, DOI: 10.4236/gep.2024.123012.
- Herslund L., Lund D.H., Jørgensen G., Mguni P., Kombe W.J., Yeshitela K., 2015, Towards climate change resilient cities in Africa—Initiating adaptation in Dar es Salaam and Addis Ababa, [in:] *Urban Vulnerability and Climate Change in Africa: A Multidisciplinary Approach*, Springer, 319-348, DOI: 10.1007/978-3-319-03982-4\_10.
- Ihaka R., 2005, Time Series Analysis, Lecture Notes for 475726, Statistics Department, University of Auckland.
- INSD, 2011, Le Burkina en chiffres, 8, Institut National de la Statistique et de la Démographie.
- IPCC, 2021, Summary for Policymakers, [in:] *Climate Change 2021: The Physical Science Basis. Contribution of Working Group I to the Sixth Assessment Report of the Intergovernmental Panel on Climate Change*, IPCC.
- IPCC, 2023, *Climate Change 2023: Synthesis Report. Contribution of Working Groups I, II and III to the Sixth Assessment Report of the Intergovernmental Panel on Climate Change*, Core Writing Team, H. Lee and J. Romero (eds.), IPCC, Geneva, Switzerland, DOI: 10.59327/IPCC/AR6-9789291691647.
- Irwan I., Abdy M., Karwingsi E., Ahmar A.S., 2023, Rainfall forecasting in Makassar City using triple exponential smoothing method, *ARRUS Journal of Social Sciences and Humanities*, 3 (1), 52-58, DOI: 10.35877/soshum1707.
- Karl T.R., Nicholls N., Anver G., 1999, CLIVAR/GCOS/WMO Workshop on indices and indicators for climate extremes workshop summary, [in:] *Weather and Climate Extremes: Changes, Variations and a Perspective from the Insurance Industry*, T.R. Karl, N. Nicholls, Ghazi A. (eds.), Springer, Dordrecht, 3-7, DOI: 10.1007/978-94-015-9265-9\_2.
- Kessabi R., Hanchane M., Ait Brahim Y., El Khazzan B., Addou R., Belmahi M., 2024, Characterization of annual and seasonal rainfall trend using innovative trend analysis (ITA) and classical methods: the case of Wadi Sebou basin (WSB) Morocco, *Euro-Mediterranean Journal for Environmental Integration*, 10, 555-573, DOI: 10.1007/s41207-024-00507-1.

- Koala S., Nakoulma G., Dipama J.-M., 2023, Évolution des précipitations et de la température à l'Horizon 2050 avec les modèles climatiques CMIP5 dans le bassin versant du Nakambé (Burkina Faso), *International Journal of Progressive Sciences and Technologies*, 37 (2), 110-124, DOI: 10.52155/ijpsat.v37.2.5133.
- Koehler A.B., Snyder R.D., Ord J.K., 2001, Forecasting models and prediction intervals for the multiplicative Holt–Winters method, *International Journal of Forecasting*, 17 (2), 269-286, DOI: 10.1016/S0169-2070(01)00081-4.
- Konate D., Didi S.R., Dje K.B., Diedhiou A., Kouassi K.L., Kamagate B., Paturol J.-E., Coulibaly H.S.J.-P., Kouadio C.A.K., Coulibaly T.J.H., 2023, Observed changes in rainfall and characteristics of extreme events in Côte d'Ivoire (West Africa), *Hydrology*, 10(5), 104, DOI: 10.3390/hydrology10050104.
- Kougbeagbede H., 2024, Detection of annual rainfall trends using innovative trend analysis method in Benin, *International Journal of Global Warming*, 32 (1), 54-64, DOI: 10.1504/IJGW.2024.135361.
- Lawton R., 1998, How should additive Holt–Winters estimates be corrected?, *International Journal of Forecasting*, 14 (3), 393-403, DOI: 10.1016/S0169-2070(98)00040-5.
- Lourdes F.M., Kim Y.K., Choi M., Kim J.-C., Do X.K., Nguyen T.H., Jung K., 2021, Detailed trend analysis of extreme climate indices in the Upper Geum River Basin, *Water*, 13 (22), DOI: 10.3390/w13223171.
- Mallick J., Talukdar S., Alsubih M., Salam R., Ahmed M., Kahla N.B., Shamimuzzaman M., 2021, Analysing the trend of rainfall in Asir region of Saudi Arabia using the family of Mann-Kendall tests, innovative trend analysis, and detrended fluctuation analysis, *Theoretical and Applied Climatology*, 143, 823-841, DOI: 10.1007/s00704-020-03448-1.
- Mandal T., Sarkar A., Das J., Rahman A.T.M.S., Chouhan P., 2021, Comparison of classical Mann-Kendal test and graphical innovative trend analysis for analyzing rainfall changes in India, [in:] *India: Climate Change Impacts, Mitigation and Adaptation in Developing Countries*, Cham: Springer International Publishing, 155-183, DOI: 10.1007/978-3-030-67865-4\_7.
- Marak J.D.K., Sarma A.K., Bhattacharjya R.K., 2020, Innovative trend analysis of spatial and temporal rainfall variations in Umiam and Umtru watersheds in Meghalaya, India, *Theoretical and Applied Climatology*, 142, 1397-1412, DOI: 10.1007/s00704-020-03383-1.
- Mohorji A.M., Şen Z., Almazroui M., 2017, Trend analyses revision and global monthly temperature innovative multi-duration analysis, *Earth Systems and Environment*, 1, DOI: 10.1007/s41748-017-0014-x.
- Muthiah M., Sivarajan S., Madasamy N., Natarajan A., Ayyavoo R., 2024, Analyzing Rainfall trends using statistical methods across Vaippar Basin, Tamil Nadu, India: A comprehensive study, *Sustainability*, 16 (5), DOI: 10.3390/su16051957.
- Natayu A., Clarke Q.J.H., Fikri M., 2022, Benchmark of Holt–Winters and SARIMA methods in predicting Jakarta climate, preprints.
- Nurhamidah N., Nusyirwan N., Faisol A., 2020, Forecasting seasonal time series data using the holt-winters exponential smoothing method of additive models, *Jurnal Matematika Integratif*, 16 (2), 151-157, DOI: 10.24198/jmi.v16.n2.29293.151-157.
- OECD, 2022, *Africa's Urbanisation Dynamics 2022. The Economic Power of Africa's Cities*, West African Studies, OECD/UN ECA/AfDB, OECD Publishing, Paris, DOI: 10.1787/3834ed5b-en.
- Oufrigh O., Elouissi A., Benzater B., 2023, Trend assessment by the Mann-Kendall test and the Innovative Trend Analysis method (North-West Algeria), *GeoScience Engineering*, 69 (2), 186-233, DOI: 10.35180/gse-2023-0099.
- Pala Z., Şevgin F., 2024, Statistical modeling for long-term meteorological forecasting: a case study in Van Lake Basin, *Natural Hazards*, 120, 14101-14116, DOI: 10.1007/s11069-024-06747-2.
- Pardoux C., Goldfarb B., 2013, *Prévision à court terme: méthodes de lissage exponentiel*, Université de Paris Douchien, 52 pp.
- Pastagia J., Mehta D., 2022, Application of innovative trend analysis on rainfall time series over Rajsamand district of Rajasthan state, *Water Supply*, 22 (9), 7189-7196, DOI: 10.2166/ws.2022.276.
- Patel S., Mehta D., 2023, Statistical analysis of climate change over Hanumangarh district, *Journal of Water and Climate Change*, 14 (6), 2029-2041, DOI: 10.2166/wcc.2023.227.
- Pertiwi D.D., 2020, Applied exponential smoothing Holt-Winters method for rainfall forecast in Mataram City, *Journal of Intelligent Computing and Health Informatics*, 1 (2), 46-49, DOI: 10.26714/jichi.v1i2.6330.
- Pinel S., 2020, Ajustement de courbes et séries chronologiques, IUT STID, UE21 M2102, 37 pp.

- Pleños M., 2022, Time series forecasting using holt-winters exponential smoothing: Application to abaca fiber data, *Zeszyty Naukowe SGGW w Warszawie – Problemy Rolnictwa Światowego*, 22 (2), 17-29, DOI: 10.22630/PRS.2022.22.2.6.
- Pongdatu G.A.N., Putra Y.H., 2018, Seasonal time series forecasting using SARIMA and Holt Winter's exponential smoothing, *IOP Conference Series: Materials Science and Engineering*, 407 (1), DOI: 10.1088/1757-899X/407/1/012153.
- Puah Y.J., Huang Y.F., Chua K.C., Lee T.S., 2016, River catchment rainfall series analysis using additive Holt–Winters method, *Journal of Earth System Science*, 125 (2), 269-283, DOI: 10.1007/s12040-016-0661-6.
- Rouamba S., Yaméogo J., Sanou K., Zongo R., Yanogo I.P., 2023, Trends and variability of extreme climate indices in the Boucle du Mouhoun (Burkina Faso), *GEOREVIEW: Scientific Annals of Stefan cel Mare University of Suceava: Geography Series*, 33 (1), 70-84, DOI: 10.4316/GEOREVIEW.2023.01.07.
- Sanusi W., Abdy M., 2021, Innovative trend analysis of annual maximum precipitation in Gowa regency, *Journal of Physics: Conference Series*, 1899 (1), DOI: 10.1088/1742-6596/1899/1/012092.
- Şen Z., 2017, Innovative trend significance test and applications, *Theoretical and Applied Climatology*, 127, 939-947, DOI: 10.1007/s00704-015-1681-x.
- Şen Z., Şişman E., Dabanli I., 2019, Innovative polygon trend analysis (IPTA) and applications, *Journal of Hydrology*, 575, 202-210, DOI: 10.1016/j.jhydrol.2019.05.028.
- Sezen C., Partal T., 2020, Wavelet combined innovative trend analysis for precipitation data in the Euphrates-Tigris basin, Turkey, *Hydrological Sciences Journal*, 65 (11), 1909-1927, DOI: 10.1080/02626667.2020.1784422.
- Shah S.A., Kiran M., 2021, Mann-Kendall test: trend analysis of temperature, rainfall and discharge of Ghotki feeder canal in district Ghotki, Sindh, Pakistan, *Environment & Ecosystem Science*, 5 (2), 137-142, DOI: 10.26480/ees.02.2021.137.142.
- Sirven P., 1987, Démographie et villes au Burkina Faso, *Les Cahiers d'Outre-Mer*, 40 (159), 265-283, available online at [https://www.persee.fr/doc/caoum\\_03735834\\_1987\\_num\\_40\\_159\\_3227](https://www.persee.fr/doc/caoum_03735834_1987_num_40_159_3227) (data access 07.08.2025).
- Sougué M., Merz B., Sogbedji J.M., Zougmore F., 2023, Extreme rainfall in southern Burkina Faso, West Africa: trends and links to Atlantic Sea surface temperature, *Atmosphere*, 14 (2), DOI: 10.3390/atmos14020284.
- Sylla M.B., Giorgi F., Pal J.S., Gibba P., Kebe I., Nikiema M., 2015, Projected changes in the annual cycle of high-intensity precipitation events over West Africa for the late twenty-first century, *Journal of Climate*, 28 (16), 6475-6488, DOI: 10.1175/JCLI-D-14-00854.1.
- Täzen F., Diarra A., Kabore R.F., Ibrahim B., Bologo/Traoré M., Traoré K., Karambiri H., 2019, Trends in flood events and their relationship to extreme rainfall in an urban area of Sahelian West Africa: The case study of Ouagadougou, Burkina Faso, *Journal of Flood Risk Management*, 12, DOI: 10.1111/jfr3.12507
- Thomasson S.A., 2017, Improving forecast performance of LPG demand, Master's Thesis, University of Twente, 109 pp.
- Trepekli K., Friborg T., Allotey A.N., Möller-Jensen L., 2019, Influence of climate change on the future precipitation pattern in the region of Ghana: Climate change resilience in urban mobility, University of Copenhagen, 16 pp.
- Wiguna I.K.A.G., Utami N.L.P.A.C., Parwita W.G.S., Udayana I.P.A.E.D., Sudipa I.G.I., 2023, Rainfall forecasting using the Holt-Winters exponential smoothing method, *Jurnal Info Sains: Informatika dan Sains*, 13 (01), 15-23.
- Yaméogo J., 2024, Changes in the seasonal cycles of extreme temperatures in the Sudano-Sahelian domain in West Africa: a case study from Burkina Faso, *Meteorology Hydrology and Water Management*, 12 (2), DOI: 10.26491/mhwm/194451.
- Yaméogo J., 2025, Annual rainfall trends in the Burkina Faso Sahel: a comparative analysis between Mann–Kendall and innovative trend method (ITM), *Discover Applied Sciences*, 7, DOI: 10.1007/s42452-025-06675-1.
- Yaméogo J., Rouamba S., 2023a, Extreme temperature in Burkina Faso: decadal spatio-temporal changes between 1960 and 2019, *European Journal of Theoretical and Applied Sciences*, 1 (6), 441-450, DOI: 10.59324/ejtas.2023.1(6).43.
- Yaméogo J., Rouamba S., 2023b, Climatic disasters in Burkina Faso from 1960 to 2020: Occurrence, spatiotemporal dynamics and socio-environmental consequences, *African Journal on Land Policy & Geospatial Sciences*, 6 (5), 1022-1043.
- Yaméogo J., Sawadogo A., 2024, Consequences of precipitation variability and socio-economic activity on surface water in the Vranso water basin (Burkina Faso), *Bulletin of the Serbian Geographical Society*, 104 (1), 255-266, DOI: 10.2298/GSGD2401255Y.



- Yaméogo J., Yanogo I.P., Ndoutorlengar M., 2022, Approvisionnement en eau potable en milieu urbain dans les quartiers informels de la ville de Boromo (Burkina Faso): entre accommodements locaux, enjeux socioéconomiques et risques sanitaires, *Annales de Moundou. Série A: Annales de la Faculté des Lettres, Arts et Sciences Humaines*, 9 (1), 57-91.
- Yanogo I.P., Yaméogo J., 2023, Recent rainfall trends between 1990 and 2020: contrasting characteristics between two climate zones in Burkina Faso (West Africa), *Bulletin of the Serbian Geographical Society*, 103 (1), 87-106, DOI: 10.2298/GSGD2301087Y.
- Zhang X., Yang F., 2004, *RClimDex (1.0) User Manual*, Climate Research, Branch Environment, Canada, 23.

# Simulation of runoff under climate change in the tropical Ba River basin, Vietnam

Hang Thi Thanh Phan 

Institute of Earth Sciences, Vietnam

## Abstract

Tropical river basins exhibit complex hydrological dynamics and are increasingly susceptible to the impacts of climate change. However, there remains a lack of data and methodological frameworks to comprehensively assess runoff responses in these regions. This study proposes a framework for evaluating the impact of climate change on runoff in the Ba River basin. Long-term trends in temperature, rainfall, and discharge from 1981 to 2020 were analyzed. The SWAT model was applied to simulate future discharge under four climate change scenarios (SSP1-2.6, SSP2-4.5, SSP3-7.0, and SSP5-8.5) for the periods 2021-2040, 2041-2060, 2061-2080, and 2081-2100. Results indicate that annual discharge at the An Khe station (upper basin) is projected to decline by 30.2 to 39.0%, while the Cung Son station (lower basin) is expected to experience change ranging from -4.0% to +15.6%. During the flood season, discharge is projected to decrease at the An Khe station (-6.1 to -17.3%) but increase substantially at the Cung Son station (+32.0 to +57.9%). In contrast, low-flow season discharge is projected to decline sharply at both stations by 68.0 to 85.2% at the An Khe station and 86.7 to 98.6% at the Cung Son station. The anticipated reduction in low-flow-season discharge highlights critical risks for water security in tropical basins. These findings underscore the urgent need for improved management strategies and operational frameworks to ensure sustainable water use under future climate conditions.

## Keywords

Ba River basin, CMIP6, discharge, rainfall, SWAT, temperature.

Submitted 2 May 2025, revised 15 July 2025, accepted 28 August 2025

DOI: 10.26491/mhwm/209996

## 1. Introduction

According to the World Economic Forum's Global Risk Report of 2020 (WEF 2020), climate change is one of the most significant global challenges, both in terms of probability and impact. It profoundly disrupts the hydrological cycle, altering runoff patterns and influencing the frequency and intensity of extreme weather events (Esit, Yuce 2022; Tayara-Zobaida 2023). The acceleration of global warming exacerbates these effects, increasing risks globally. The average global temperature has risen by approximately 1.0°C compared to pre-industrial levels, with the period from 2015 to 2019 being the hottest years on record. This rise in temperature has significantly altered the frequency, duration, magnitude, and spatial distribution of extreme weather events. Moreover, a report by the World Meteorological Organization in 2021 (WMO 2021) revealed that, due to climate change, at least 3.6 billion people worldwide faced water scarcity each month in 2018. This number is expected to rise to 5 billion by 2050, highlighting the intensifying impact of climate change on global water resources. As a result, climate change presents significant challenges to sustainable water resource management worldwide. In Central Asia, including Kazakhstan, Uzbekistan, Kyrgyzstan, Turkmenistan, and Tajikistan, more than 93% of the land is arid. Since the 1970s, nearly half of the large lakes in this region have shrunk, and rivers are rapidly drying up, attributable to both climate change and human activities (Yue et al. 2021). In the Mediterranean

region, global warming is occurring at a faster rate than in other parts of the world, resulting in significant changes in temperature, precipitation, and other climatic variables (Lionello, Scarascia 2018). Australia, too, has experienced a 1.0°C increase in temperature and a 16% decrease in rainfall since the 1970s (Silberstein et al. 2012), leading to more intense heatwaves, severe bushfire weather, reduced rainfall, and prolonged droughts (Aryal et al. 2020).

Vietnam, in Southeast Asia's tropical monsoon zone, is highly exposed to the impacts of climate change (Schmidt-Thomé et al. 2014). Between 1958 and 2018, the annual temperature in the country rose 0.89°C (approximately 0.15°C per decade) (MONRE 2021). Rainfall patterns have become more variable, with northern Vietnam experiencing a decrease in rainfall (5-10% over 61 years), while southern Vietnam has seen an increase (5-15% over the same period) (MONRE 2021). Additionally, the fluctuations between high and low water volumes during different seasons create challenges for water usage and integrated water resources management in Vietnam's river basins. The impacts of climate change on water resources vary greatly across regions (Guo et al. 2014; Lobodzinskyi et al. 2023), making it essential to conduct location-specific assessments, especially in tropical regions, which are undergoing significant changes. The Ba River basin, one of the largest river basins in the Central Highlands and south-central coast of Vietnam, plays a vital role in regional agriculture, hydropower generation, and domestic water supply. However, this basin has been increasingly subjected to hydrometeorological extremes such as droughts and floods, which are expected to intensify under future climate scenarios.

Despite the growing number of studies on climate change impacts on water resources in Vietnam, significant research gaps remain, particularly for the Ba River basin. First, most previous studies have focused on major river systems such as the Red River (Duong 2016; Duong et al. 2016; Ha, Bastiaanssen 2023; Nguyen, Tran 2024) and Mekong River basins (Khoi, Thang 2017; Le et al. 2024; Sam, Khoi 2022), leaving medium-sized basins like the Ba River relatively understudied. Second, existing assessments often rely on historical data or outdated climate scenarios (e.g., RCPs), with limited application of updated CMIP6-based shared socioeconomic pathways (SSPs) for long-term projections. The CMIP6 (Eyring et al. 2016) project's global climate models (GCMs) are better at predicting the global energy balance (Wild 2020). Third, spatially explicit analyses of runoff changes within sub-basins or critical water-demand zones are scarce, limiting the understanding of local vulnerabilities. Additionally, little attention has been given to seasonal water shortages, especially during the dry season when competition for water use among agriculture, domestic supply, and hydropower becomes most intense. Uncertainty analysis, an essential component for validating climate-impact assessments, is often lacking or insufficiently addressed. Furthermore, there is a lack of integration between hydrological modeling outcomes and practical water management or adaptation strategies tailored to local contexts.

This study aims to address these gaps by developing a scientific framework for evaluating the impacts of climate change on runoff in the Ba River basin. Several previous studies have considered the development of a framework for assessing the impact of climate change on water resources (Hrour et al. 2023). Hydrological models are the main tools in this realm (Phan et al. 2010; Bekele et al. 2019; Kohnová et al.

2019; Khoi et al. 2021; Tariku et al. 2021; Gurung et al. 2022; Takele et al. 2022; Yang et al. 2022).

However, the scarcity of monitoring stations within a basin poses a significant challenge for water resources research, an issue commonly encountered in basins worldwide. Using a combination of observed data (1981-2020), projected data under four SSP scenarios (SSP1-2.6, SSP2-4.5, SSP3-7.0, and SSP5-8.5) for the periods 2021-2040, 2041-2060, 2061-2080, and 2081-2100, and an integrated modeling approach, this research analyzes both historical trends and future changes in runoff. The Mann-Kendall test is applied to detect trends in temperature, rainfall, and runoff data; the Soil and Water Assessment Tool (SWAT) is used to simulate runoff responses to climate variations. The outcomes of this study are expected to provide valuable insights for water resource planning and adaptation strategies in tropical river basins under changing climate conditions.

## **2. Methods and materials**

### **2.1. Study area**

The Ba River basin (Fig. 1), covering an area of 13,848 km<sup>2</sup>, was selected as the study area, with its upper part in the Central Highlands and its lower part in the south-central coastal region of Vietnam. The Ba River basin plays a vital role in the socio-economic development of the Central region, spanning three provinces: Gia Lai, Dak Lak, and Phu Yen, supporting a population of approximately two million people. The terrain ranges from 0 m above sea level (asl) in the eastern coastal plain to a maximum elevation of 1,983 m asl in the northern mountainous area, with an average basin elevation of 469 m asl. The Ba River originates from Ngoc Ro Peak (1,549 m asl) in the Truong Son Mountain range; the mainstem length is 374 kilometers. The river network density is approximately 0.22 km per km<sup>2</sup>.

The Ba River basin, located in the tropical climate zone, is monitored by four meteorological stations, An Khe, AyunPa, MDrak, and Tuy Hoa, and by two hydrological stations, An Khe and Cung Son, which collected data from 1981 to 2020. The characteristics of these stations are summarized in Table 1. The meteorological stations provide daily data on rainfall, temperature, humidity, wind speed, and solar radiation, while the hydrological stations record discharge and water levels within the basin.

The variability of climatic factors in tropical river basins is very complex, and the Ba River basin is a clear example. Descriptive statistics for 30 data series at 4 meteorological stations and 2 hydrological stations in the Ba River basin are presented in Table 2. The temperature in the Ba River basin varies widely across the basin. Normally, the temperature in the high mountainous area is lower than on the plains. During the period 1981-2020, the average annual temperatures at the An Khe, AyunPa, MDrak, and Tuy Hoa meteorological stations were 23.7°C, 25.5°C, 24.0°C, and 26.8°C, respectively. The difference between the maximum and minimum monthly temperatures in the basin ranges between 6 and 7°C. The maximum temperature in the basin is 41.3°C at the AyunPa station; the minimum is 9°C at the An Khe station.

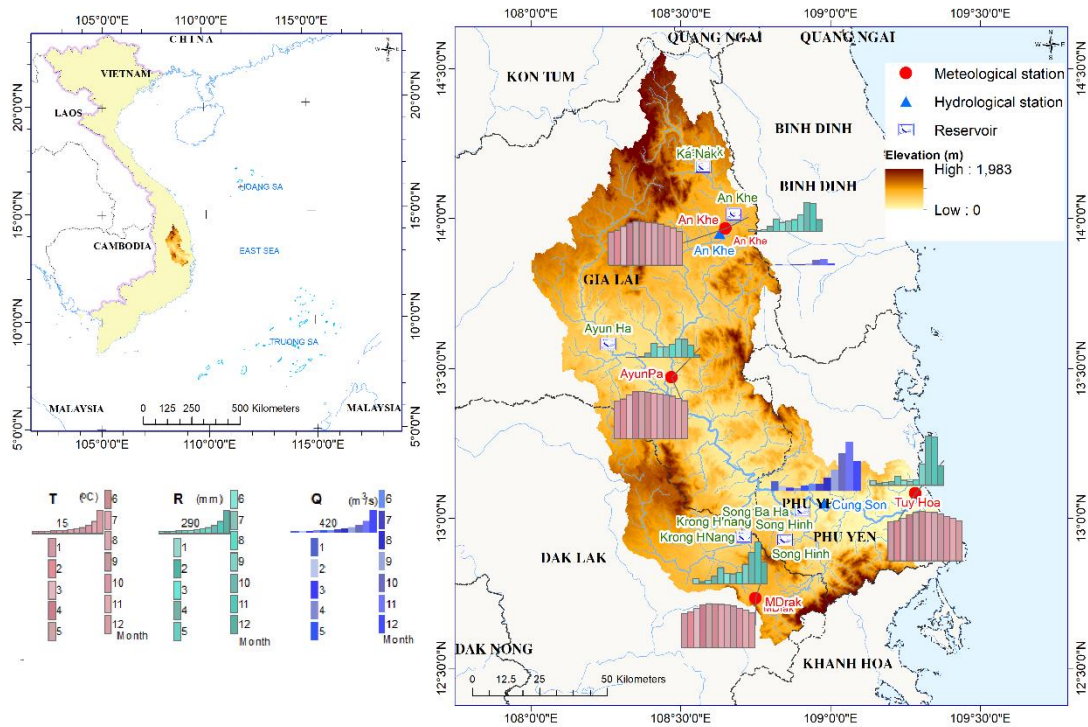


Fig. 1. Distribution of monthly temperature (T), rainfall (R) and discharge (Q) in the Ba River basin.

Table 1. Network of gauging stations in the Ba River basin.

No	Station	Longitude	Latitude	Elevation (m)	Observation period
Meteorological station					
1	An Khe	108.03°E	13.97°N	442.16	1981-2020
2	AyunPa	108.47°E	13.47°N	159.70	1981-2020
3	MDrak	108.75°E	12.73°N	419.03	1981-2020
4	Tuy Hoa	109.28°E	13.08°N	10.90	1981-2020
Hydrological station					
5	An Khe	108.65°E	13.95°N		1981-2020
6	Cung Son	108.98°E	13.04°N		1981-2020

Annual rainfall in the Ba River basin is also highly variable and complex in both spatial and temporal distribution, depending significantly on topography and atmospheric circulation. The average annual rainfall in the Ba River basin is spatially variable: 1638 mm at the An Khe station, 1249 mm at the AyunPa station, 2103 mm at the MDrak station, and 2052 mm at the Tuy Hoa station during the period 1981-2020. The rainy season accounts for approximately 90% of total annual rainfall (from May to December) in mountainous areas and 75-85% (from September to December) in coastal plains. Heavy rainfall events occur especially in October and November. During the dry season, rainfall accounts for only 10-25% of the annual total.

The average annual discharge was 28 m<sup>3</sup>/s at the An Khe station and 273.4 m<sup>3</sup>/s at the Cung Son station during the period 1981-2020. In the upstream area, the flood season lasts four months (from September to December) due to the influence of the southeastern monsoon. In the downstream area located on the eastern slope of the Truong Son Range, the flood season lasts three months (from October to December),

influenced by the northeastern monsoon circulation and associated weather disturbances. The flood season in the Ba River basin is typically short, but it contributes approximately 70% of the annual water volume. The highest flows occur in October in the upstream area and in December in the downstream area. The low-flow modulus of the Ba River basin is 9.2 l/s/km<sup>2</sup>. The low-flow season discharge of the Ba River basin is among the lowest in Vietnam. The month with the lowest discharge is typically April, during which discharge accounts for less than 2% of the total annual flow.

Table 2. Statistical results for observed data series at stations. TA = average annual temperature, TX = maximum temperature, TN = minimum temperature, RA = annual rainfall, RX = maximum 1-day rainfall, Qy = average annual discharge, Qf = discharge in flood season, Qd = discharge in low-flow season, Qx = maximum discharge, Qn = minimum discharge.

No	Station	Parameter	Minimum	Maximum	Mean	Std. deviation	Skewness	Kurtosis
Meteorological station								
1	An Khe	TA (°C)	22.98	26.09	23.80	0.64	1.78	4.56
		TX (°C)	34.90	40.00	36.59	1.17	0.81	0.55
		TN (°C)	9.00	15.50	12.63	1.51	−0.42	−0.15
		RA (mm)	684.90	3442.30	1638.42	530.53	0.00	4.56
		RX (mm)	46.40	260.10	139.69	56.48	0.47	−0.64
2	AyunPa	TA (°C)	25.20	27.20	25.96	0.53	0.63	−0.52
		TX (°C)	36.90	41.30	38.89	0.99	0.27	0.06
		TN (°C)	10.30	16.70	13.26	1.71	−0.11	−0.81
		RA (mm)	696.90	1765.00	1248.57	258.29	0.11	−0.45
		RX (mm)	50.00	211.60	109.71	38.06	1.10	1.45
3	MDrak	TA (°C)	23.26	24.88	23.96	0.44	0.40	−0.97
		TX (°C)	26.70	37.80	31.88	3.56	0.41	−1.35
		TN (°C)	11.80	16.90	13.85	1.19	0.17	−0.16
		RA (mm)	914.50	4224.80	2103.38	679.48	1.12	1.21
		RX (mm)	59.90	443.40	172.26	87.15	1.53	2.66
4	Tuy Hoa	TA (°C)	25.92	28.06	26.81	0.48	0.61	0.23
		TX (°C)	36.60	40.50	38.61	0.82	0.13	−0.04
		TN (°C)	2.20	19.70	17.09	2.68	−4.57	25.46
		RA (mm)	963.40	3360.00	2052.21	574.86	0.61	−0.32
		RX (mm)	91.20	628.90	231.63	134.86	1.50	1.74
Hydrological station								
5	An Khe	Qy (m³/s)	6.86	67.77	28.04	13.54	0.77	0.55
		Qf (m³/s)	5.09	181.90	58.76	41.90	1.06	0.67
		Qd (m³/s)	4.28	34.35	14.22	5.92	1.50	3.34
		Qx (m³/s)	106.00	3060.00	1156.30	751.31	0.75	0.27
		Qn (m³/s)	0.10	11.00	5.22	2.64	0.20	−0.15
6	Cung Son	Qy (m³/s)	107.39	477.04	273.43	94.04	0.33	−0.36
		Qf (m³/s)	124.20	1164.50	586.55	259.68	0.08	−0.76
		Qd (m³/s)	45.24	230.63	116.87	42.47	0.65	0.69
		Qx (m³/s)	559.00	20700.00	6206.43	4074.48	1.21	2.63
		Qn (m³/s)	1.40	80.00	20.04	17.30	1.44	2.78

Since 2001, six major hydroelectric reservoirs have operated within the Ba River basin (Fig. 1), with a total storage capacity of  $1455 \times 10^6 \text{ m}^3$ , approximately 17% of the average annual water volume recorded at the Cung Son station. Located upstream from this station, the reservoirs have a substantial influence on the flow regime. The average annual discharge at Cung Son declined from  $300 \text{ m}^3/\text{s}$  in 1981-2000 to  $247 \text{ m}^3/\text{s}$  in 2001-2020. These changes indicate that both climate change and hydropower activities have contributed to alterations in the flow regime of the basin. This study adopts the 1981-2000 period as the baseline to evaluate the impacts of climate change on runoff in the Ba River basin.

## 2.2. Homogeneity test of data series

Ensuring the homogeneity of temperature, rainfall, and discharge data series is a crucial step in hydrometeorological analysis. Tests such as Pettitt's, the standard normal homogeneity test (SNHT), Buishand range test, and the von Neumann test are widely applied to detect inhomogeneities or change-points in observed data series. Pettitt's test, a non-parametric method, can detect abrupt changes at any point in the series without assuming a normal distribution. The SNHT is particularly effective in identifying shifts in the mean that occur near the center of the series, which may result from changes in station location or instrumentation. The Buishand Range test evaluates changes in the mean by analyzing cumulative deviations from the overall mean, making it suitable for detecting step changes. The von Neumann test is used to assess randomness in the data, helping to identify inhomogeneities caused by irregular changes between consecutive observations. Applying these tests to rainfall or streamflow data enables researchers to verify and cross-check results, thereby increasing the reliability of homogeneity assessments. Early detection of inhomogeneities allows for correction or adjustment of the data, minimizing systematic errors. As a result, trend analysis, simulation, and projections based on the data become more accurate. These procedures are particularly important for evaluating the impacts of climate change on water resources. This research used the XLSAT tool in Excel to calculate Pettitt's test, SNHT, the Buishand range test, and the von Neumann test. To test the homogeneity of the observation data series, Pettitt's test, SNHT, the Buishand range test, and the von Neumann test at 5% significance level were calculated by XLSTAT. The homogeneity test results for 30 datasets are shown in Table 3. The results were classified into three categories, namely "useful," "doubtful," and "suspect," based on four homogeneity tests to select the homogeneous observed data series. The results of the Pettitt test, SNHT, Buishand test, and Von Neumann ratio test showed that 10, 11, 11, and 7 out of the 30 data sets, respectively, were identified as inhomogeneous.

The annual average temperature (TA) data showed inhomogeneity at AyunPa, MDrak, and Tuy Hoa stations. The maximum temperature (TX) data indicated inhomogeneity at MDrak station, while the minimum temperature (TN) data revealed inhomogeneity at An Khe and AyunPa stations. The annual rainfall (RA) data were homogeneous across all monitoring stations; however, the data on the maximum 1-day rainfall (RX) indicated inhomogeneity at AyunPa. The breakpoints detected by all tests tended to occur at various points throughout the study period.



Table 3. Homogeneity test results for observed data series at meteorological stations using different methods at 95% significance level. TA = average annual temperature, TX = maximum temperature, TN = minimum temperature, RA = annual rainfall, RX = maximum 1-day rainfall, Qy = average annual discharge, Qf = discharge in flood season, Qd = discharge in low-flow season, Qx = maximum discharge, Qn = minimum discharge.

No	Station	Parameter	p value				Result
			Pettitt	SNHT	Buishand	Von Neumann	
Meteorological station							
1	An Khe	TA	<b>0.001</b>	0.088	0.053	0.246	Useful
		TX	0.762	<b>0.039</b>	0.270	0.285	Useful
		TN	<b>0.008</b>	<b>0.002</b>	<b>0.003</b>	<b>0.019</b>	<b>Suspect</b>
		RA	0.080	0.077	<b>0.008</b>	0.105	Useful
		RX	0.487	0.233	0.204	0.311	Useful
2	AyunPa	TA	<b>&lt;0.0001</b>	<b>0.000</b>	<b>0.000</b>	<b>&lt;0.0001</b>	<b>Suspect</b>
		TX	0.869	0.099	0.277	0.676	Useful
		TN	<b>0.007</b>	<b>0.004</b>	<b>0.001</b>	0.056	<b>Suspect</b>
		RA	0.139	0.136	0.056	0.756	Useful
		RX	<b>0.027</b>	<b>0.041</b>	<b>0.011</b>	0.285	<b>Suspect</b>
3	MDrak	TA	<b>&lt;0.0001</b>	<b>&lt;0.0001</b>	<b>&lt;0.0001</b>	<b>&lt;0.0001</b>	<b>Suspect</b>
		TX	<b>&lt;0.0001</b>	<b>&lt;0.0001</b>	<b>&lt;0.0001</b>	<b>&lt;0.0001</b>	<b>Suspect</b>
		TN	0.241	0.095	0.056	0.574	Useful
		RA	0.516	0.418	0.238	0.156	Useful
		RX	0.885	0.759	0.654	0.431	Useful
4	Tuy Hoa	TA	<b>0.000</b>	<b>0.001</b>	<b>0.000</b>	<b>0.001</b>	<b>Suspect</b>
		TX	0.845	0.793	0.597	0.925	Useful
		TN	0.411	0.099	<b>0.040</b>	0.615	Useful
		RA	0.579	0.711	0.856	0.747	Useful
		RX	0.312	0.155	0.051	0.121	Useful
Hydrological station							
5	An Khe	Qy	0.254	<b>0.045</b>	0.160	0.052	Useful
		Qf	0.266	<b>0.006</b>	0.189	0.077	Useful
		Qd	0.571	0.593	0.533	<b>0.034</b>	Useful
		Qx	0.882	0.604	0.825	0.639	Useful
		Qn	<b>0.033</b>	<b>0.004</b>	<b>0.020</b>	0.065	<b>Suspect</b>
6	Cung Son	Qy	0.744	0.280	0.293	0.383	Useful
		Qf	0.953	0.250	0.434	0.778	Useful
		Qd	0.456	0.937	0.726	0.549	Useful
		Qx	0.891	0.822	0.556	0.334	Useful
		Qn	<b>&lt;0.0001</b>	<b>0.004</b>	<b>&lt;0.0001</b>	<b>0.001</b>	<b>Suspect</b>

The data on average annual discharge, flood season flow, dry season flow, and maximum discharge are all homogeneous. Meanwhile, the minimum discharge data show inhomogeneity at both An Khe and Cung Son stations. It can be seen that many hydrometeorological data series lack homogeneity, which creates difficulties in calculations and assessments. Several studies aimed at checking the homogeneity of hydrometeorological data series have yielded comparable results. For instance, a study of annual rainfall data in Turkey (Bickici Arıkan, Kahya 2019) from 1974 to 2014 identified 44 out of 160 stations as having

non-homogeneous data. Likewise, research on rainfall, temperature, and humidity in Nineveh Governorate (Iraq) (Elzeiny et al. 2019) during the 1990-2020 period also revealed non-homogeneity in some data series across the 8 monitoring stations analyzed.

### 2.3. Trend analysis using the Mann-Kendall test

The Mann-Kendall non-parametric statistical test (Kendall 1970), further developed by the U.S. Geological Survey (Helsel et al. 2006), has been widely used in climate and hydrological sciences to detect trends in time series data. In this study, the Mann-Kendall test was applied to identify trends in climatic and hydrological variables in the Ba River basin. Observed data from the period 1981 to 2020 were used in the analysis.

The data values are evaluated as an ordered time series where each data value is compared to all subsequent data values.  $a_1, a_2, \dots, a_n$  represent  $n$  data points where  $a_j$  represents the data point at time  $j$  and  $a_j$  and  $a_k$  are sequential data in series. The Mann-Kendall test statistic ( $S$ ) is identified using the following equation:

$$S = \sum_{k=1}^{n-1} \sum_{j=k+1}^n \text{sign}(a_j - a_k) \quad (1)$$

Where:

$$\begin{aligned} \text{sign}(a_j - a_k) &= 1 && \text{if } a_j - a_k > 0 \\ &= 0 && \text{if } a_j - a_k = 0 \\ &= -1 && \text{if } a_j - a_k < 0 \end{aligned}$$

$$Tau = \frac{S}{n(n-1)/2} \quad (2)$$

The variance of  $S$ ,  $VAR(S)$  is calculated by the following equation:

$$VAR(S) = \frac{1}{18} \left[ n(n-1)(2n+5) - \sum_{p=1}^g t_p(t_p-1)(2t_p+5) \right] \quad (3)$$

Where  $n$  is the number of data points,  $g$  is the number of tied groups, and  $t_p$  is the number of data points in the  $p^{\text{th}}$  group.

The normalized  $Z$  statistics value is used to test the trend, in which a negative value  $Z$  statistic indicates a decreasing trend, while a positive value  $Z$  statistic indicates an increasing trend. The following formula is used to calculate a normalized test statistic  $Z$ :

$$\begin{aligned}
&= \frac{S - 1}{[VAR(S)]^{1/2}} \quad \text{if } S > 0 \\
Z &= 0 \quad \text{if } S = 0 \\
&= \frac{S + 1}{[VAR(S)]^{1/2}} \quad \text{if } S < 0
\end{aligned} \tag{4}$$

#### 2.4. Bias correction using CMHyd

Cropland accounts for 45-50% of the Ba River basin (CCI 2017), which is why this study uses predicted data from the ACCESS-ESM1.5 model. ACCESS-ESM1.5 is Australia's version of a global climate model and one of 23 models participating in Phase 6 of the Coupled Model Intercomparison Project (CMIP6) collected from WorldClim2. It can be used for various climate application (ns, including estimating the individual and combined impacts of different factors on past, present, and future climate change (Ziehn et al. 2020). Moreover, ACCESS-ESM1.5's distinctiveness lies in its status as (to this researcher's knowledge) the only CMIP6 model with terrestrial phosphorus limitation (Ziehn et al. 2020). Studies have shown that climate model outputs often contain biases; therefore, it is strongly recommended to apply bias correction to GCMs and regional climate model (RCM) outputs before using them in hydrological models (Willkofer et al. 2018; Hrou et al. 2023). Climate model data for hydrologic modeling (CMhyd) is a Python-based tool that facilitates the use of global and regional climate data in hydrological simulations by applying both spatial and temporal bias correction techniques. In this study, monthly rainfall, as well as maximum and minimum temperature data, were extracted at a spatial resolution of 30 arc-seconds for the four meteorological stations. The data included both historical (1992-2001) observations and future climate projections under the SSP1-2.6, SSP2-4.5, SSP3-7.0, and SSP5-8.5 scenarios from the ACCESS-ESM1.5 model, using ArcGIS 10.5. These datasets were then bias corrected using the CMhyd tool. The CMhyd model was applied to correct biases in maximum and minimum temperature, as well as average monthly rainfall data. Previous studies have compared various bias correction techniques to determine the most suitable method (Hrou et al. 2023). In this study, both the linear and delta methods were tested. The delta method performed poorly for rainfall data at the Tuy Hoa station; therefore, the linear method was selected for bias correction in this analysis.

#### 2.5. Hydrological model

The SWAT model was used to evaluate the impact of climate change on the runoff in the study basin. The version used in this study was ArcSWAT 2012.10-5.24. The SWAT model requires data for meteorological (daily rainfall, humidity, temperature, wind speed, and solar radiation) and spatial (digital elevation model, land use, and soil maps) variables. It is common that a lack of meteorological and hydrological measurement networks, or only very recent measurements, has led to limited or absent data in many river basins, including in Vietnam. In this study, we use meteorological data from the four observation stations in the Ba River basin.

Spatial data were collected from various sources and configured to meet the requirements of the SWAT model. A digital elevation model (DEM) with a resolution of 30 m was collected from the ASTER Global Digital Elevation Map data source, which can be downloaded at no cost from <http://asterweb.jpl.nasa.gov/gdem.asp>, and extracted into the study basin (Fig. 1). The study also used a land-cover map with a resolution of 300 m from the Climate Change Initiative Land Cover team at the Université Catholique de Louvain (CCI 2017). The maps employ a legend based on the FAO/UNEP Land Cover Classification System to be compatible with previous products (Fig. 2a). This legend is converted to types of land-cover classes, which are similar to SWAT's classification. A soil map with scale 1:5,000,000, produced by the United Nations Food and Agriculture Organization (Fig. 2b), was used in this study (FAO 2003). The database used for this soil map in SWAT was taken from MWSWAT2012. To our knowledge, this is the first time that the ASTER-CCI-FAO spatial input dataset has been configured for a tropical basin in the SWAT model.

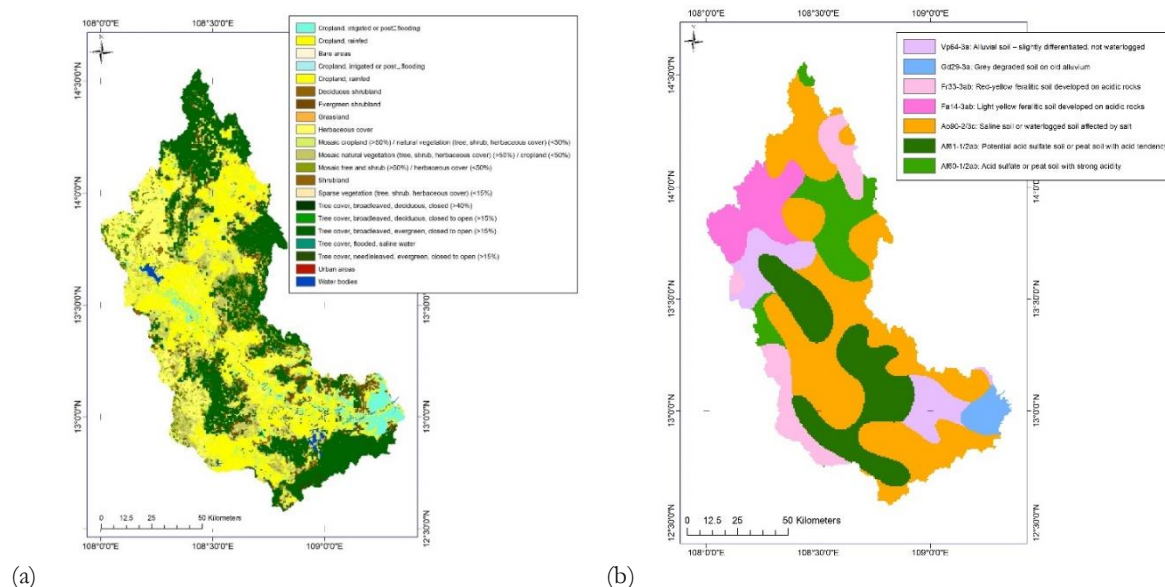


Fig. 2. Maps of land cover for 1998 (a) and soil classification (b) in the Ba River basin.

Direct measurement of evapotranspiration ( $ETo$ ) is often difficult, time-consuming, and costly. Consequently,  $ETo$  is commonly estimated using climatic variables such as humidity, temperature, wind speed, and solar radiation. In the SWAT model, various methods are employed for this estimation: The Hargreaves (HG) method, which is temperature-based; the Priestley-Taylor (P-T) method, which is radiation-based; and the Penman-Monteith (P-M) method, which combines various factors. In this study, we used meteorological data from the four stations An Khe, AyunPa, MDrak, and Tuy Hoa (Fig. 1) to estimate  $ETo$  using the Penman-Monteith method.

Because hydropower plants in the basin proliferated rapidly after 2001, to simulate the change in natural discharge, the study used monitoring data at the Cung Son station from 1992-2001. River discharge data from the period 1992-1996 were used to calibrate the model, data from 1997-2001 to validate it. Because

the reservoir system began operating in the Ba River basin in 2002, this study did not use data after 2002 for calibrating and validating the model.

## 2.6. Evaluation of the hydrological model performance

This study applied the SWAT-Calibration and Uncertainty Programs (SWAT-CUP) program with the SUFI2 (Sequential Uncertainty Fitting algorithm) uncertainty analysis procedure (Abbaspour 2015) for sensitivity/calibration analysis. The calculated indices were as follows:

Coefficient of determination ( $R^2$ ):

$$R^2 = \frac{\left[ \sum_{i=1}^n (Q_{obs}^i - \bar{Q}_{obs})(Q_{sim}^i - \bar{Q}_{sim}) \right]^2}{\sum_{i=1}^n (Q_{obs}^i - \bar{Q}_{obs})^2 \sum_{i=1}^n (Q_{sim}^i - \bar{Q}_{sim})^2} \quad (5)$$

Where  $n$  is the number of observations,  $Q_{obs}^i$  is the observation value,  $Q_{sim}^i$  is the simulation value, and  $\bar{Q}_{obs}$  is the average of observation values.

The Nash-Sutcliffe efficiency ( $NSE$ ), a normalized statistic, establishes how much residual variation there is in relation to the variance of the measured data (Nash, Sutcliffe 1970). An ideal match between the simulated and the observed data is indicated by  $NSE = 1$ . In contrast,  $NSE \leq 0$  indicates that the model's simulation is less accurate than the observed mean.

$$NSE = 1 - \left[ \sum_{i=1}^n (Q_{obs}^i - Q_{sim}^i)^2 \right] / \left[ \sum_{i=1}^n (Q_{obs}^i - \bar{Q}_{obs})^2 \right] \quad (6)$$

The  $PBIAS$  coefficient is expressed by Equation 3:

$$PBIAS = \sum_{i=1}^n (Q_{obs}^i - Q_{sim}^i) \times 100 / \sum_{i=1}^n Q_{obs}^i \quad (7)$$

$PBIAS = 0$  indicates a correct simulation of the model.  $PBIAS > 0$  indicates that the simulated value is lower than the actual value, whereas  $PBIAS < 0$  indicates that the simulated value is higher than the actual value (Gupta et al. 1999).

## 3. Results and discussion

### 3.1. Trend of temperature and rainfall in the tropical basin

Prior to trend determination, a Durbin-Watson test (Order = 1) was performed to assess the presence of autocorrelation. The results indicated that all 20 temperature and precipitation data series yielded  $p$ -values  $< 0.0001$ , confirming that the subsequent trend analysis would not be influenced by autocorrelation. To consider climate change in the basin, the study applied the Mann-Kendall test to calculate trends in temperature and rainfall parameters. The  $p$ -values of average annual and minimum temperature at An Khe station, average annual temperature at the AyunPa station, average annual and maximum temperature at the MDrak stations, and average annual temperature at the Tuy Hoa station were  $< 0.05$  (Tab. 4)m

indicating significant trends. The *Tau*, *S*, and *Z* values of the average annual, maximum, and minimum temperature at the four stations were  $> 0$  (Tab. 4). During 1981–2020, temperature either demonstrated a statistically significant increasing trend or showed no discernible trend. The annual average temperature showed an increasing trend at all four monitoring stations, with relatively small differences in the rate of increase. Specifically, the rates of increase in annual average temperature at An Khe, AyunPa, MDrak, and Tuy Hoa were 0.25°C, 0.35°C, 0.28°C, and 0.29°C per decade, respectively.

Table 4. Results of the Mann-Kendall test for trends. TA = average annual temperature, TX = maximum temperature, TN = minimum temperature, RA = annual rainfall, RX = maximum 1-day rainfall, *Tau* = Kendall's Tau, *S* = Mann-Kendall test statistic, *Z* = the normalized test statistic, *p* = probability.

No	Station	Parameter	<i>Tau</i>	<i>S</i>	<i>Z</i>	<i>p</i>	Result
1	An Khe	TA	0.424	331	3.845	0.0001	Increasing
		TX	0.072	56	0.641	<b>0.5213</b>	<b>No trend</b>
		TN	0.336	262	3.045	0.0023	Increasing
		RA	0.139	114	1.269	<b>0.2044</b>	<b>No trend</b>
		RX	0.144	112	1.293	<b>0.1959</b>	<b>No trend</b>
2	AyunPa	TA	0.572	446	5.201	0	Increasing
		TX	0.046	36	0.408	<b>0.683</b>	<b>No trend</b>
		TN	0.371	289	3.358	0.0008	Increasing
		RA	−0.185	−144	−1.666	<b>0.0957</b>	<b>No trend</b>
		RX	−0.21	−164	−1.899	<b>0.0575</b>	<b>No trend</b>
3	MDrak	TA	0.545	425	4.94	0	Increasing
		TX	0.438	342	3.977	0.0001	Increasing
		TN	0.186	145	1.68	<b>0.093</b>	<b>No trend</b>
		RA	0.149	116	1.34	<b>0.1803</b>	<b>No trend</b>
		RX	0.062	48	0.548	<b>0.584</b>	<b>No trend</b>
4	Tuy Hoa	TA	0.595	464	5.395	0	Increasing
		TX	0.121	94	1.086	<b>0.2773</b>	<b>No trend</b>
		TN	0.2	156	1.808	<b>0.0705</b>	<b>No trend</b>
		RA	−0.054	−42	−0.478	<b>0.6329</b>	<b>No trend</b>
		RX	−0.164	−128	−1.48	<b>0.139</b>	<b>No trend</b>

The calculated results of *Tau*, *S* and *Z* of the annual rainfall total and maximum 1-day rainfall at two stations, An Khe and MDrak, were  $> 0$  while those at the AyunPa and Tuy Hoa stations were  $< 0$ . However, all parameters also had a *p*-value  $> 0.05$ . The average annual and maximum 1-day rainfall in the Ba River basin did not have a significant trend. The results of the Mann-Kendall trend test and the homogeneity test identified a unique trend of increasing average annual temperature at An Khe station. The analysis of annual data showed that climate change in tropical river basins is very complex, and it is difficult to identify trends. A study on the lower Mekong River (Dang et al. 2020) also showed that during the period 1989–2017, rainfall exhibited complex fluctuations, and the impact of southern oscillation (ENSO) processes on rainfall was very strong. Analysis of precipitation records indicates a pronounced influence of large-scale climatic oscillations on rainfall distribution within the basin. During El Niño years, exemplified by 1997, annual precipitation was markedly below the multi-year climatological mean.

Specifically, in 1997, the mean annual rainfall at the An Khe, AyunPa, MDrak, and Tuy Hoa meteorological stations was 1100, 1271, 1270, and 1769 mm, respectively. In contrast, La Niña years, such as 1999, were associated with substantially above-average precipitation. In that year, total annual rainfall reached 1889.1 mm at An Khe, 1720.5 mm at AyunPa, 3259.8 mm at MDrak, and 2771.1 mm at Tuy Hoa, reflecting the strong positive phase of the El Niño-ENSO impact on regional hydrometeorological conditions. Therefore, based on the characteristics of water use in the Ba River basin, the study selected the period 1981-2000 as the baseline for comparative calculations.

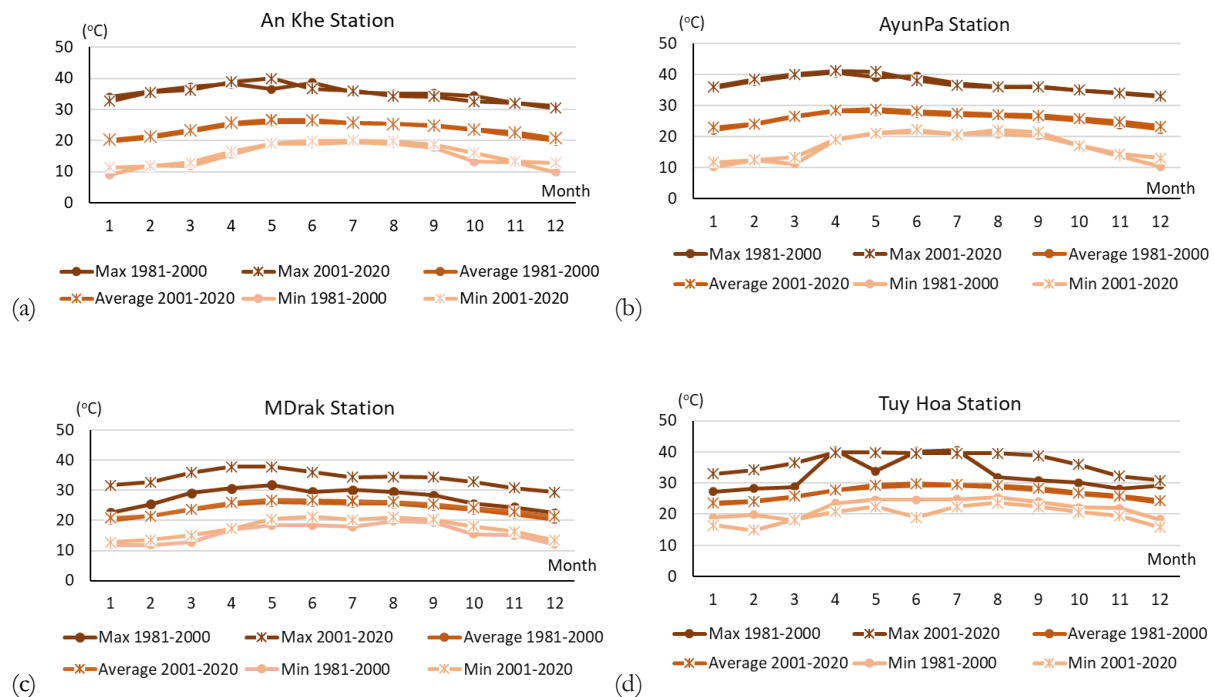


Fig. 3. Monthly average, maximum, and minimum air temperatures for the periods 1981-2000 and 2001-2020 at (a) the An Khe, (b) AyunPa, (c) MDrak and (d) Tuy Hoa stations.

The average monthly air temperatures at all meteorological stations during the period 2001-2020 were higher than those in the 1981-2000 baseline period (Fig. 3). The average annual temperatures during the baseline period were 23.5°C at the An Khe station, 25.6°C at the AyunPa station, 23.7°C at the MDrak station, and 26.6°C at the Tuy Hoa station. In comparison, during the period 2001-2020, these values increased to 23.9°C, 26.3°C, 24.4°C, and 27.1°C, respectively.

Rainfall also differed between the two periods, 1981-2000 and 2001-2020, across the meteorological stations. Monthly rainfall for both periods at the four stations is illustrated in Figure 4. During the baseline period 1981-2000, the average annual rainfall was 1509 mm at the An Khe station, 1349 mm at the AyunPa station, 2057 mm at the MDrak station, and 2149 mm at the Tuy Hoa station. For the period 2001-2020, these values were 1767, 1148, 2150, and 1955 mm, respectively. Comparing the two periods before and after 2000, rainfall tended to increase at stations situated in high-altitude areas (above 400 m asl), such as An Khe and MDrak, whereas it tended to decrease at stations located in lower-altitude areas



(below 160 m asl), such as AyunPa and Tuy Hoa. The duration of the rainy season varies across the basin. In the upper basin, it typically extends from May to December, contributing more than 90% of the annual rainfall. In contrast, the rainy season in the downstream areas lasts from September to December, accounting for less than 80% of the annual total. The concentration of high rainfall in just four months in the downstream region presents challenges for freshwater availability in tropical river basins in general, and particularly in the Ba River basin.

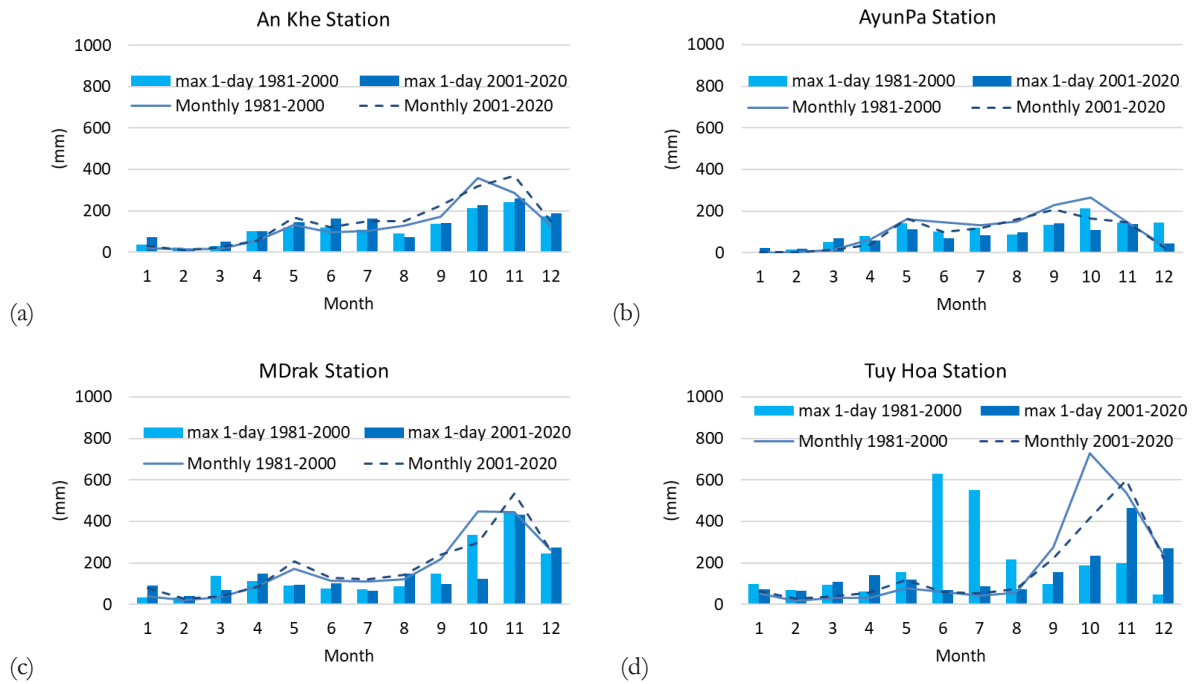


Fig. 4. Monthly average and maximum 1-day rainfall for 1981-2000 and 2001-2020 at (a) the An Khe, (b) AyunPa, (c) MDrak, and (d) Tuy Hoa stations.

### 3.2. Trend of runoff in the tropical basin

Before assessing discharge trends, a Durbin-Watson test (order = 1) was applied to detect potential autocorrelation. All 10 discharge time series produced  $p$ -values  $< 0.0001$ , thereby confirming that autocorrelation would not influence the subsequent trend analysis. To identify the runoff trend in the basin, the study applied the Mann-Kendall test to estimate trends in runoff parameters (Tab. 5). Values of  $Tau$ ,  $S$ , and  $Z$  of almost all parameters (except minimum discharge) at the An Khe station were  $< 0$  (Tab. 5). However, only the  $p$ -value of minimum discharge at the Cung Son station was  $< 0.05$ . Other parameters of runoff in the Ba River basin did not have significant trends. Based on the Mann-Kendall trend test and the homogeneity test, no trend was identified at any station in the Ba River basin. Similar to climatic factors, runoff data calculations show that runoff in tropical river basins is very complex, making it difficult to determine trends. In 1997, streamflow at hydrological stations within the Ba River basin reached exceptionally low levels, with values of  $19.65 \text{ m}^3/\text{s}$  at the An Khe station and  $201.3 \text{ m}^3/\text{s}$  at the Cung Son station. In contrast, in 1999, streamflow was considerably higher, measuring  $46.0 \text{ m}^3/\text{s}$  at An Khe and  $459.5 \text{ m}^3/\text{s}$  at Cung Son.

Table 5. Calculated results by the Mann-Kendall test.  $Q_y$  = average annual discharge,  $Q_f$  = discharge in flood season,  $Q_d$  = discharge in low-flow season,  $Q_x$  = maximum discharge,  $Q_n$  = minimum discharge,  $Tau$  = Kendall's Tau,  $S$  = Mann-Kendall test statistic,  $Z$  = the normalized test statistic, and  $p$  = probability.

No	Station	Parameter	$Tau$	$S$	$Z$	$p$	Result
1	An Khe	$Q_y$	-0.038	-30	-0.338	0.736	No trend
		$Q_f$	-0.131	-102	-1.177	0.239	No trend
		$Q_d$	-0.005	-4	-0.035	0.972	No trend
		$Q_x$	-0.182	-142	-1.643	0.100	No trend
		$Q_n$	0.154	120	1.387	0.166	No trend
2	Cung Son	$Q_y$	-0.115	-90	-1.037	0.300	No trend
		$Q_f$	-0.118	-92	-1.06	0.289	No trend
		$Q_d$	-0.074	-58	-0.664	0.507	No trend
		$Q_x$	-0.086	-67	-0.769	0.442	No trend
		$Q_n$	-0.496	-387	-4.498	0.000	Decreasing

Monthly, maximum, and minimum discharge values for 1981-2000 and 2001-2020 at two stations in the Ba River basin are illustrated in Figure 5. In contrast to the complex fluctuations in rainfall, runoff showed a decreasing trend between the two periods. Specifically, the observed discharge at the An Khe station declined by 13.8%, while that at the Cung Son station decreased by 17.6%.

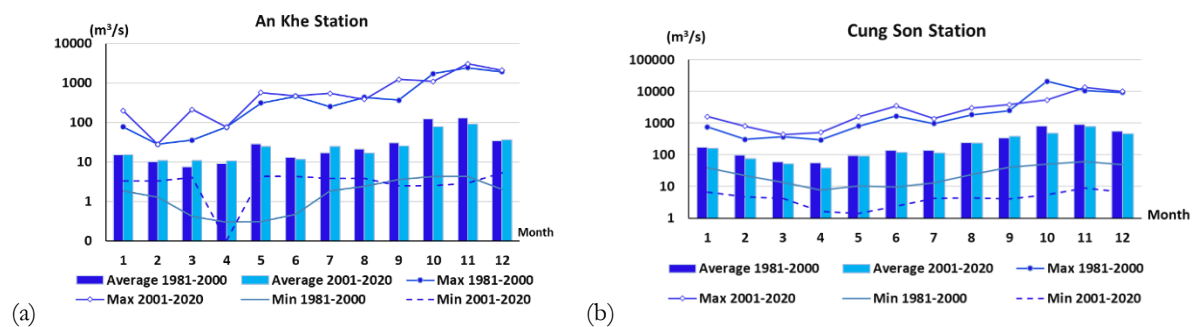


Fig. 5. Monthly average, maximum, and minimum discharges for 1981-2000 and 2001-2020 at (a) the An Khe and (b) Cung Son stations.

Between the two periods, 1981-2000 and 2001-2020, flood season water volume decreased by 20.7% at the An Khe station and 19.8% at the Cung Son station. In contrast, the water volume during the low-flow season increased by 2% at the An Khe station but decreased by 11.6% at the Cung Son station. At the An Khe station, the maximum discharge during 1981-2000 and 2001-2020 was 2440 m<sup>3</sup>/s and 3060 m<sup>3</sup>/s, respectively, while the minimum discharge was 0.295 m<sup>3</sup>/s and 0.1 m<sup>3</sup>/s. At the Cung Son station, the maximum discharge during 1981-2000 and 2001-2020 was 20,700 m<sup>3</sup>/s and 13,500 m<sup>3</sup>/s, respectively, while the minimum discharge was 7.73 m<sup>3</sup>/s and 1.41 m<sup>3</sup>/s. The distribution of water resources between the flood and low-flow seasons is greatly imbalanced in tropical river basins – a characteristic feature of these regions that also complicates water resource management. Therefore, it is essential to consider seasonal flow variations when planning and regulating water use in tropical river basins.

### 3.3. Climate change scenarios

Future climate data were extracted from the ACCESS-ESM1.5 model under four scenarios: SSP1-2.6 (sustainability), SSP2-4.5 (middle of the road), SSP3-7.0 (regional rivalry), and SSP5-8.5 (fossil-fueled development), corresponding to the time periods 2021-2040, 2041-2060, 2061-2080, and 2081-2100. The data were extracted at a high spatial resolution of 30 arc-seconds for the four meteorological stations in the Ba River basin using ArcGIS 10.5 software.

The extracted datasets included maximum and minimum temperatures as well as average monthly rainfall for each scenario and time period. For bias correction by CMHyd, historical climate data from the period 1992-2001 were also extracted and used as the reference baseline at the four meteorological stations.

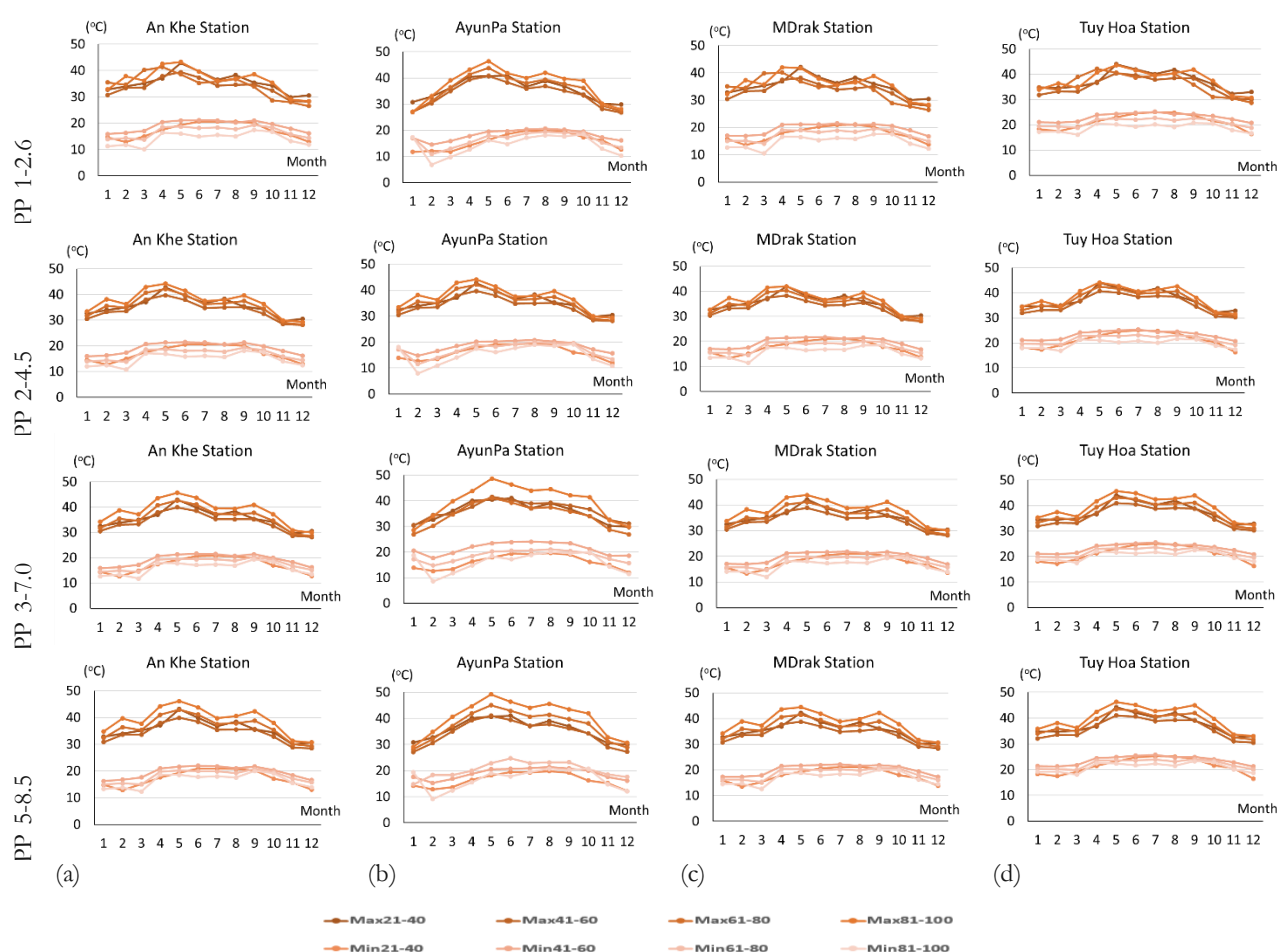


Fig. 6. Projected maximum and minimum temperatures for the periods 2021-2040, 2041-2060, 2061-2080 and 2081-2100 under the four scenarios of SSP1-2.6, 2-4.5, 3-7.0, and 5-8.5 at (a) the An Khe, (b) AyunPa, (c) MDrak, and (d) Tuy Hoa stations with bias correction.

The results after bias correction, illustrated in Figures 6 and 7, were used as input data for the SWAT model to simulate discharge in the Ba River basin. Changes in maximum and minimum temperatures and annual average rainfall during the periods 2021-2040, 2041-2060, 2061-2080, and 2081-2100 under the

SSP1-2.6, SSP2-4.5, SSP3-7.0, and SSP5-8.5 scenarios, in comparison with the baseline period 1981-2000, are presented in Table 6.

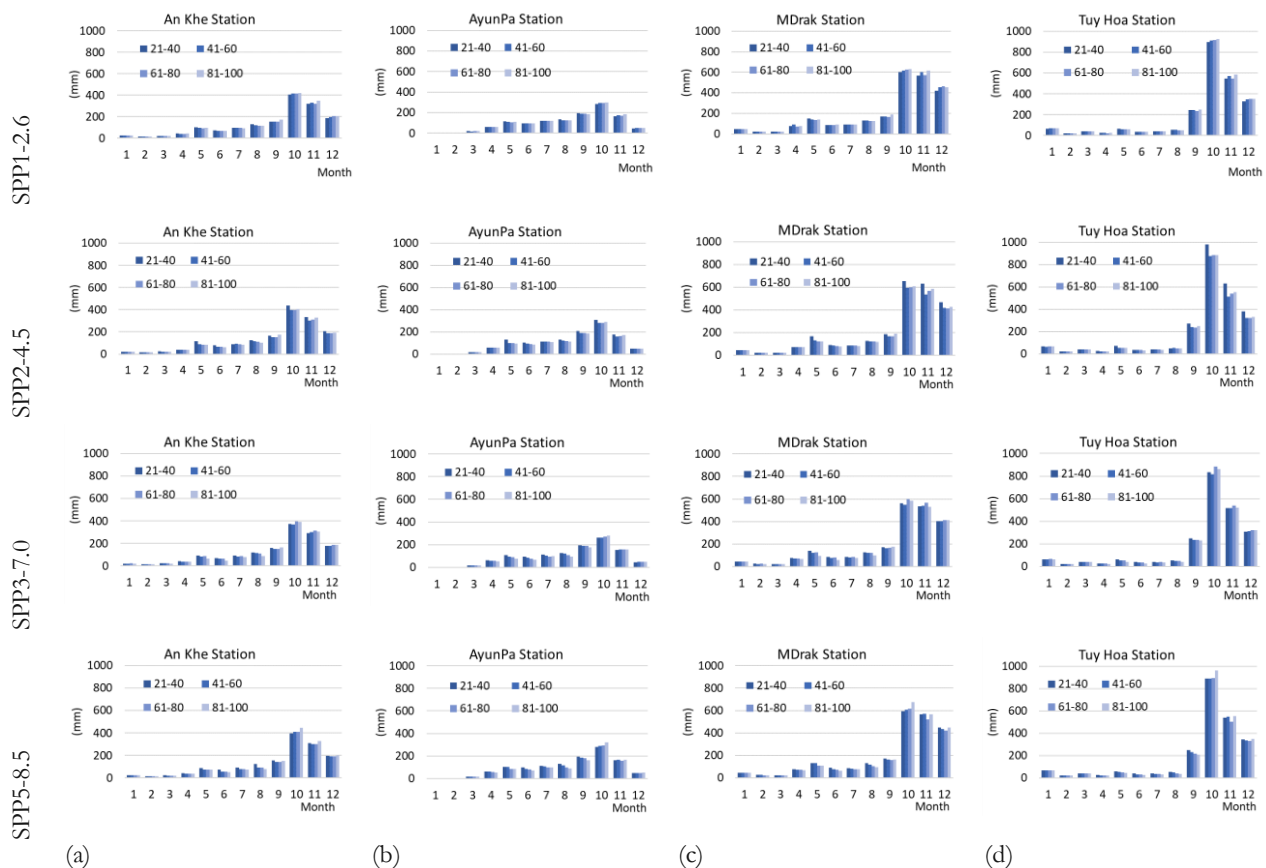


Fig. 7. Projected monthly rainfall for the periods 2021-2040, 2041-2060, 2061-2080, and 2081-2100 under the four scenarios of SSP1-2.6, 2-4.5, 3-7.0, and 5-8.5 at (a) the An Khe, (b) AyunPa, (c) MDrak, and (d) Tuy Hoa stations with bias correction.

Rainfall and temperature data were bias corrected to match the observed data during the reference period. The range of maximum temperature variation was from  $-6.5^{\circ}\text{C}$  to  $+6.0^{\circ}\text{C}$  without bias correction, and from  $-1.8^{\circ}\text{C}$  to  $+12.7^{\circ}\text{C}$  with bias correction. For minimum temperature, the range was from  $-4.3^{\circ}\text{C}$  to  $+14^{\circ}\text{C}$  without correction, and from  $-3.5^{\circ}\text{C}$  to  $+7.3^{\circ}\text{C}$  with correction. For rainfall, the range was from  $-43\%$  to  $+7.9\%$  without correction, and from  $-20.6\%$  to  $+25.2\%$  with correction. Linear scaling was applied for the bias correction. The results after bias correction show that the maximum temperature increased at all stations, except for the period 2021-2040 under the SSP2-4.5 scenario at the AyunPa station, and for the period 2041-2060 under the SSP1-2.6 and SSP5-8.5 scenarios at the Tuy Hoa station (Tab. 6). The minimum temperature in the four periods under the four climate change scenarios showed periods of both increase and decrease compared to the baseline period. Typically, high-emission scenarios (SSP3-7.0 and SSP5-8.5) exhibit higher maximum and minimum temperatures than low-emission scenarios (SSP1-2.6 and SSP2-4.5). The annual average rainfall increased at two stations in the upper basin and decreased at two stations in the lower basin during all four periods under the four climate change

scenarios. The high-emission scenario (SSP5-8.5) tended to show a smaller increase in rainfall compared to the low-emission scenario (SSP1-2.6).

Table 6. Changes in maximum and minimum temperature (°C) and annual average rainfall (%) compared to the period 1981-2000 with bias correction.

Station	Period	$\Delta T_{\max}$ (°C)				$\Delta T_{\min}$ (°C)				$\Delta$ Annual rainfall (%)			
		SSP 1-2.6	SSP 2-4.5	SSP 3-7.0	SSP 5-8.5	SSP 1-2.6	SSP 2-4.5	SSP 3-7.0	SSP 5-8.5	SSP 1-2.6	SSP 2-4.5	SSP 3-7.0	SSP 5-8.5
An Khe	2021-2040	+4.2	+4.1	+4.3	+4.5	+3.8	+6.9	+3.6	+3.8	+3.6	+9.4	<b>-2.2</b>	+1.6
	2041-2060	+0.7	+1.1	+1.3	+1.3	+6.9	+6.9	+6.9	+7.2	+4.7	<b>-0.4</b>	<b>-4.4</b>	<b>-4.4</b>
	2061-2080	+2.8	+3.5	+4.0	+4.3	+4.7	+4.8	+5.5	+5.9	+3.9	<b>-0.6</b>	<b>-0.6</b>	<b>-4.4</b>
	2081-2100	+4.6	+5.6	+7.0	+7.5	+1.1	+1.7	+2.8	+3.3	+7.5	+1.7	<b>-6.2</b>	<b>-0.5</b>
AyunPa	2021-2040	+0.1	<b>-0.1</b>	+0.3	+0.3	+1.5	+1.6	+1.6	+1.8	<b>-7.4</b>	<b>-2.8</b>	<b>-11.9</b>	<b>-9.7</b>
	2041-2060	+0.1	+0.1	+0.8	+4.4	+4.2	+4.5	+7.3	+4.9	<b>-7.1</b>	<b>-11.6</b>	<b>-15.3</b>	<b>-11.8</b>
	2061-2080	+3.1	+3.2	+0.4	+4.4	+0.5	+1.2	+4.5	+4.4	<b>-8.1</b>	<b>-11.9</b>	<b>-17.5</b>	<b>-16.9</b>
	2081-2100	+5.7	+6.0	+8.0	+8.5	<b>-3.5</b>	<b>-2.3</b>	<b>-1.7</b>	<b>-1.2</b>	<b>-6.6</b>	<b>-12.5</b>	<b>-20.6</b>	<b>-16.4</b>
MDrak	2021-2040	+10.4	+10.3	+10.5	+10.5	+1.7	+1.6	+1.5	+1.7	+16.1	+25.2	+10.3	+15.5
	2041-2060	+6.5	+6.6	+7.1	+9.3	+5.0	+5.1	+5.1	+5.4	+20.3	+11.7	+7.2	+13.7
	2061-2080	+8.4	+8.6	+9.4	+9.8	+2.3	+2.8	+2.9	+3.4	+18.3	+12.6	+12.6	+8.5
	2081-2100	+10.3	+10.3	+12.2	+12.7	-1.3	-0.4	+0.2	+0.8	+21.9	+15.3	+6.3	+14.1
Tuy Hoa	2021-2040	+3.4	+3.3	+3.4	+3.6	<b>-1.5</b>	<b>-1.6</b>	<b>-1.6</b>	<b>-1.4</b>	+10.6	+21.9	+4.7	+9.9
	2041-2060	<b>-0.2</b>	+0.1	+0.3	<b>-1.8</b>	+2.9	+2.9	+3.0	+3.3	+12.8	+6.2	+2.3	+8.2
	2061-2080	+1.6	+1.9	+2.5	+3.8	+0.9	+1.3	+1.6	+2.0	+11.8	+7.5	+7.5	+4.4
	2081-2100	+3.0	+3.6	+5.1	+5.6	<b>-1.8</b>	<b>-1.1</b>	<b>-0.4</b>	+0.1	+14.9	+9.0	+2.8	+9.9

### 3.4. Impact of climate change on runoff

Based on the results extracted from the ACCESS-ESM1.5 model, this study applied the SWAT model to simulate the monthly water discharge. The calibration results for the period 1992-1996 at the Cung Son station showed  $R^2$ ,  $NSE$  and  $PBIAS$  indices of 0.90, 0.90, and  $-0.8\%$ , respectively. The validation results for the period 1997-2001 at the Cung Son station showed  $R^2$ ,  $NSE$  and  $PBIAS$  indices of 0.89, 0.88, and  $2.6\%$ , respectively. To assess the sensitivities of the parameters, the SUFI-2 method from SWAT-CUP was applied, resulting in the identification of the seven most sensitive parameters. A total of 1000 simulations was performed to optimize the model outputs. A list of the sensitive parameters is provided in Table 7. The uncertainty in the simulation results may stem from the sparse distribution of meteorological stations within the basin, with only four stations covering an area of  $13,848 \text{ km}^2$ .

Moreover, these stations are positioned at locations that do not adequately represent the geographical characteristics of the basin. The average elevation of the basin is 469 m asl (ranging from 0 to 1983 m asl). The stations were located lower than the average basin elevation. However, the calibration and validation results indicated that the SWAT model could effectively simulate flow in the Ba River basin. The SWAT model has been used successfully for hydrological assessments of water resource management, even in cases of data scarcity, such as in the Brahmaputra River basin (Dutta, Sarma 2021).

Table 7. List of sensitive parameters used for model calibration.

Parameters	Fitted_ Value	Min_ Value	Max_ Value	<i>p</i> value
CN2 – SCS runoff curve number	0.23	–20	20	0
ALPHA_BF – Baseflow alpha factor (day)	0.479	0	1	0.0366
GW_DELAY – Groundwater delay (days)	277.485	30	450	<b>0.006</b>
GWQMN – Threshold depth of water in the shallow aquifer required for return flow to occur (mm)	471.15	0	5000	<b>0</b>
SOL_AWC – Available water capacity of the soil layer	1.004	1	2.5	<b>0.0001</b>
CH_N2 – Manning's "n" value for the main channel	0.123318	0.01	0.3	<b>0.0103</b>
CH_K1 – Effective hydraulic conductivity in tributary channel alluvium	18.375	0	300	<b>0.0079</b>

These findings further underscore the potential of the SWAT model in tropical basin contexts, despite data limitations. Since the model does not include water exploitation in the basin, the simulated discharge represents natural flow. This study is the first to use a spatial dataset for the SWAT model, comprising DEM data from the ASTER's web, land cover data from the CCI program, and a soil map from the FAO. The calibration and validation results indicate that these data inputs are suitable for use in SWAT models for tropical river basins. Therefore, this spatial dataset can support investigations for integrated water resource management in river basins that lack sufficient data for calculating water resource allocation. To assess the effects of climate change on runoff in the basin, this study considered the existing hydropower stations in the basin during the period 2001-2020. The predicted monthly discharge values for the periods 2021-2040, 2041-2060, 2061-2080, and 2081-2100 under the four scenarios (SSP1-2.6, SSP2-4.5, SSP3-7.0, and SSP5-8.5) are shown in Figure 8. The changes in annual, low-flow season, and flood-season discharges for these periods, compared to the baseline period of 1981-2000, are shown in Table 8. Using the baseline period of 1981-2000, this study calculated and compared surface runoff changes at hydrological stations under climate change scenarios. The predicted annual discharge at the An Khe station decreased by 30.2% to 39.0%, the low-flow season discharge decreased by 68.0% to 85.2%, and the flood-season discharge decreased by 6.1% to 17.3% compared to the baseline period. At the Cung Son station, the predicted annual discharge varied between –4.0% and +15.6% from baseline, with a tendency for flood-season discharge to increase by 32.0% to 57.9%, and low-flow season discharge to decrease by 86.7% to 98.6% compared to the baseline period.

The predicted discharge in the lower basin exhibited more complex variation than the upper basin. This study found that both annual and seasonal discharge trends tended to decrease in the upper area, while in the lower basin, the flood season showed an increasing trend, and the low-flow season showed a decreasing trend compared to the baseline period. By the end of the 21<sup>st</sup> century (2081-2100), discharge in both the upper and lower areas is predicted to decrease during the low-flow season, indicating that tropical river basins, like the Ba River basin, may face significant risks of water shortages during the low-flow season by the century's end. The impacts of climate change will significantly affect future water resource allocation in such regions.

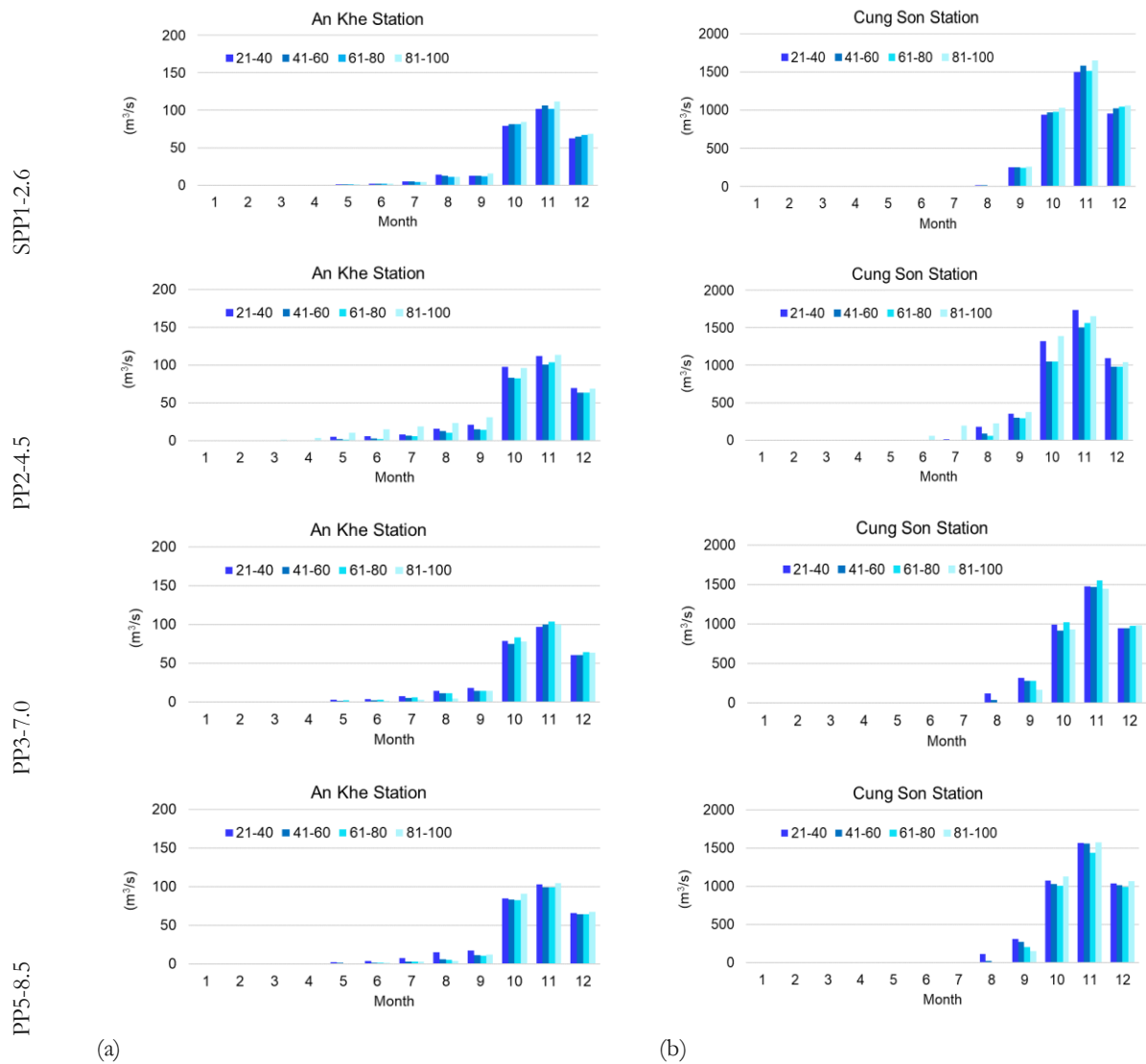


Fig. 8. Projected monthly discharge for the periods 2021-2040, 2041-2060, 2061-2080, and 2081-2100 under the four scenarios of SSP1-2.6, 2-4.5, 3-7.0, and 5-8.5 at (a) the An Khe and (b) the Cung Son stations.

Table 8. Changes in annual, flood-season, and low-flow season discharges (%) compared to the period 1981-2000.

Station	Period	$\Delta$ Annual discharge (%)				$\Delta$ Flood-season discharge (%)				$\Delta$ Low-flow discharge (%)			
		SSP	SSP	SSP	SSP	SSP	SSP	SSP	SSP	SSP	SSP	SSP	SSP
		1-2.6	2-4.5	3-7.0	5-8.5	1-2.6	2-4.5	3-7.0	5-8.5	1-2.6	2-4.5	3-7.0	5-8.5
An Khe	2021-2040	-35.8	-30.2	-34.7	-30.6	-14.2	-6.1	-16.9	-10.5	-76.2	-75.2	-68.0	-68.1
	2041-2060	-34.1	-39.0	-37.7	-37.5	-10.9	-17.3	-17.0	-12.8	-77.5	-79.6	-76.4	-83.8
	2061-2080	-35.1	-38.7	-33.7	-38.2	-11.7	-16.1	-11.6	-13.2	-78.9	-81.0	-75.0	-84.8
	2081-2100	-30.9	-35.4	-38.8	-34.3	-6.6	-11.5	-14.9	-7.1	-76.4	-80.1	-83.5	-85.2
Cung Son	2021-2040	+2.2	+15.6	+7.3	+14.7	+40.0	+57.9	+43.1	+53.4	-97.0	-95.4	-86.7	-86.9
	2041-2060	+7.4	-4.0	+1.7	+8.6	+47.0	+32.0	+38.6	+48.4	-96.6	-98.6	-94.9	-95.9
	2061-2080	+5.6	-2.6	+6.9	+1.6	+45.2	+34.0	+46.8	+39.7	-98.3	-98.6	-97.6	-98.4
	2081-2100	+11.7	+1.7	-1.4	+9.4	+53.5	+39.9	+35.6	+50.5	-98.1	-98.6	-98.5	-98.4

Several studies have examined the impacts of climate change on river flow in various watersheds globally; however, research on the effects of climate change specifically during low-flow seasons remains limited. In

the Meuse Basin in Northwest Europe, for instance, climate change is projected to reduce discharge during the low-flow season (de Wit et al. 2007). As discussed earlier, the low-flow season in tropical river basins typically lasts twice as long as the flood season, yet the water volume during this period accounts for less than half of the flood season's discharge. If the water volume during the low-flow season continues to decrease, it will present numerous challenges for water use within the basin. Under high-emission scenarios, by the end of the 21<sup>st</sup> century, the volume of water in the low-flow season is expected to decrease even further. This suggests that meteorological and hydrological factors are not only highly variable seasonally but also fluctuate significantly over time. The irregular distribution of rainfall and runoff presents considerable challenges for water resource management in tropical river basins. The results from this study provided a scientific basis for developing water use plans in order of priority for tropical river basins.

#### **4. Conclusions**

The research results indicate that climatic factors, such as temperature and rainfall, along with runoff in tropical river basins, exhibit complex variations. Ten out of 30 hydrometeorological data series for the period 1981-2020 were found to be heterogeneous. An increasing trend was identified only in the annual average temperature data series for all four meteorological stations. Projected variations in maximum and minimum temperatures were found to be complex, with predicted annual rainfall decreasing in the upper basin and increasing in the lower basin toward the end of the century under SSP climate change scenarios.

The spatial dataset, including DEM (ASTER30), land cover (CCI), soil (FAO), and data from four meteorological stations, was constructed for the SWAT model. The calibration and validation results confirmed that the SWAT model and the input dataset construction methods are suitable for tropical river basins. The study also successfully integrated the land cover map (CCI) and the soil map (FAO) into the SWAT model using appropriate conversion methods. The results indicate a projected decrease in discharge during the low-flow season, signaling a worsening of water shortages in the Ba River Basin. These findings are particularly significant, as the observed trends suggest a future decline in surface water resources during the dry season in an area already experiencing water stress, underscoring the urgent need for a robust adaptation strategy supported by reliable drought monitoring and forecasting systems. This study has developed a framework for evaluating climate change impacts on water resources in tropical basins with sparse observational data. Although the results are valuable, the accuracy of the simulations could be improved with a denser observational network. The study relied on projections from a single GCM; future research should explore multi-model ensembles to enhance the robustness of climate change impact assessments in tropical river basins.

#### **Acknowledgments**

This study was supported by the Vietnam Academy of Science and Technology under the grant number KHCBTD.01/24-25.



## References

- Abbaspour K., 2015, SWAT-CUP: SWAT Calibration and Uncertainty Programs – A User Manual, Swiss Federal Institute of Aquatic Science and Technology, Eawag, Dübendorf, Switzerland. Integrated Assessment, and Modeling (SIAM): Dübendorf, Switzerland.
- Aryal S.K., Silberstein R.P., Fu G., Hodgson G., Charles S.P., McFarlane D., 2020, Understanding spatio-temporal rainfall-runoff changes in a semi-arid region, *Hydrological Processes*, 34 (11), 2510-2530, DOI: 10.1002/hyp.13744.
- Bekele D., Alamirew T., Kebede A., Zeleke G., Melesse A.M., 2019, Modeling climate change impact on the hydrology of Keleta watershed in the Awash River basin, Ethiopia, *Environmental Modeling and Assessment*, 24 (1), 95-107, DOI: 10.1007/s10666-018-9619-1.
- Bickici Arian B., Kahya E., 2019, Homogeneity revisited: analysis of updated precipitation series in Turkey, *Theoretical and Applied Climatology*, 135 (1), 211-220, DOI: 10.1007/s00704-018-2368-x.
- CCI, 2017, Land Cover CCO. Product User Guide, Version 2.0, UCL-Geomatics: London, UK.
- Dang V.H., Tran D.D., Cham D.D., Hang P.T.T., Nguyen H.T., Truong H.V., Tran P.H., Duong M.B., Nguyen N.T., Le K.V., Pham T.B.T., Nguyen A.H., 2020, Assessment of rainfall distributions and characteristics in coastal provinces of the Vietnamese Mekong Delta under climate change and ENSO processes, *Water*, 12 (6), DOI: 10.3390/w12061555.
- de Wit M.J.M., van den Hurk B., Warmerdam P.M.M., Torfs P.J.J.F., Roulin E., van Deursen W.P.A., 2007, Impact of climate change on low-flows in the river Meuse, *Climatic Change*, 82 (3), 351-372, DOI: 10.1007/s10584-006-9195-2.
- Duong P.C., 2016, Assessment of climate change impact on river flow regimes to support decision-making in water resources management in the Red River Delta, Vietnam – A case study of Nhue-Day River Basin. *Salween and Red Rivers: Sharing Knowledge*, 1001.
- Duong P.C., Nauditt A., Phong N.T., 2016, Assessment of climate change impact on river flow regimes in the Red River Delta, Vietnam – a case study of the Nhue-Day River Basin, *Journal of Natural Resources and Development*, 6, 81-91, DOI: 10.5027/JNRD.V6I0.09.
- Dutta P., Sarma A.K., 2021, Hydrological modeling as a tool for water resources management of the data-scarce Brahmaputra basin, *Journal of Water and Climate Change*, 12 (1), 152-165, DOI: 10.2166/wcc.2020.186.
- Elzeiny R., Khadr M., Zahran S., Rashwan E., 2019, Homogeneity analysis of rainfall series in the upper Blue Nile River basin, Ethiopia. *Journal of Engineering Research*, 3 (3), 46-53.
- Esit M., Yuce M.I., 2022, Comprehensive evaluation of trend analysis of extreme drought events in the Ceyhan River Basin, Turkey, *Meteorology Hydrology and Water Management*, 11 (1), 22-43, DOI: 10.26491/mhwm/154573.
- Eyring V., Bony S., Meehl G.A., Senior C.A., Stevens B., Stouffer R.J., Taylor K.E., 2016, Overview of the Coupled Model Intercomparison Project Phase 6 (CMIP6) experimental design and organization, *Geoscientific Model Development*, 9 (5), 1937-1958, DOI: 10.5194/gmd-9-1937-2016.
- FAO, 2003, Digital soil map of the world and derived soil properties, available online at <https://www.fao.org/soils-portal/data-hub/soil-maps-and-databases/faounesco-soil-map-of-the-world/en/> (data access 01.09.2025).
- WEF, 2020, The Global Risks Report 2020, World Economic Forum, available online at <https://www.weforum.org/publications/the-global-risks-report-2020/> (data access 01.09.2025).
- Guo Y., Li Z., Amo-Boateng M., Deng P., Huang P., 2014, Quantitative assessment of the impact of climate variability and human activities on runoff changes for the upper reaches of Weihe River, *Stochastic Environmental Research and Risk Assessment*, 28 (2), 333-346, DOI: 10.1007/s00477-013-0752-8.
- Gupta H.V., Sorooshian S., Yapo P.O., 1999, Status of automatic calibration for hydrologic models: Comparison with multilevel expert calibration, *Journal of Hydrologic Engineering*, 4 (2), 135-143, DOI: 10.1061/(ASCE)1084-0699(1999)4:2(135).
- Gurung P., Dhungana S., Kyaw Kyaw A., Bharati L., 2022, Hydrologic characterization of the Upper Ayeyarwaddy River Basin and the impact of climate change, *Journal of Water and Climate Change*, 13 (7), 2577-2596, DOI: 10.2166/wcc.2022.407.
- Ha L.T., Bastiaanssen W.G., 2023, Determination of spatially-distributed Hydrological Ecosystem Services (HESS) in the Red River Delta using a calibrated SWAT model, *Sustainability*, 15 (7), DOI: 10.3390/su15076247.

- Helsel D.R., Mueller D.K., Slack J.R., 2006, Computer program for the Kendall family of trend tests, Scientific Investigations Report 2005-5275, DOI: 10.3133/sir20055275.
- Hrour Y., Fovet O., Lacombe G., Rousseau-Gueutin P., Sebari K., Pichelin P., Thomas Z., 2023, A framework to assess future water-resource under climate change in northern Morocco using hydro-climatic modelling and water-withdrawal scenarios, *Journal of Hydrology: Regional Studies*, 48, DOI: 10.1016/j.ejrh.2023.101465.
- Kendall M.G., 1970, Rank Correlation Methods, Griffin, 202 pp.
- Khoi D.N., Nguyen V.T., Sam T.T., Mai N.T.H., Vuong N.D., Cuong H.V., 2021, Assessment of climate change impact on water availability in the upper Dong Nai River Basin, Vietnam, *Journal of Water and Climate Change*, 12 (8), 3851-3864, DOI: 10.2166/wcc.2021.255.
- Khoi D.N., Thang L.V., 2017, Climate change impacts on streamflow and non-point source pollutant loads in the 3S Rivers of the Mekong Basin, *Water and Environment Journal*, 31 (3), 401-409, DOI: 10.1111/wej.12256.
- Kohnová S., Rončák P., Hlavčová K., Szolgay J., Rutkowska A., 2019, Future impacts of land use and climate change on extreme runoff values in selected catchments of Slovakia, *Meteorology Hydrology and Water Management. Research and Operational Applications*, 7 (1), 47-55, DOI: 10.26491/mhwm/97254.
- Le X.-H., Kim Y., Van Binh D., Jung S., Nguyen D.H., Lee G., 2024, Improving rainfall-runoff modeling in the Mekong River basin using bias-corrected satellite precipitation products by convolutional neural networks, *Journal of Hydrology*, 630, DOI: 10.1016/j.jhydrol.2024.130762.
- Lionello P., Scarascia L., 2018, The relation between climate change in the Mediterranean region and global warming, *Regional Environmental Change*, 18 (5), 1481-1493, DOI: 10.1007/s10113-018-1290-1.
- Lobodzinskyi O., Vasylenko Y., Koshkina O., Nabyvanets Y., 2023, Assessing the impact of climate change on discharge in the Horyn River basin by analyzing precipitation and temperature data, *Meteorology Hydrology and Water Management*, 11 (1), 93-106, DOI: 10.26491/mhwm/163286.
- MONRE, 2021, Climate Change, Sea Level Rise. Scenarios for Vietnam, Ministry of Natural Resources and Environment, Ha Noi.
- Nash J.E., Sutcliffe J.V., 1970, River flow forecasting through conceptual models part I – A discussion of principles, *Journal of Hydrology*, 10 (3), 282-290, DOI: 10.1016/0022-1694(70)90255-6.
- Nguyen Q.H., Tran V.N., 2024, Temporal changes in water and sediment discharges: Impacts of climate change and human activities in the Red River basin (1958-2021) with projections up to 2100, *Water*, 16 (8), DOI: 10.3390/w16081155.
- Phan T.T.H., Sunada K., Oishi S., Sakamoto Y., 2010, River discharge in the Kone River basin (Central Vietnam) under climate change by applying the BTOPMC distributed hydrological model, *Journal of Water and Climate Change*, 1 (4), 269-279, DOI: 10.2166/wcc.2010.046.
- Sam T.T., Khoi D.N., 2022, The responses of river discharge and sediment load to historical land-use/land-cover change in the Mekong River Basin, *Environmental Monitoring and Assessment*, 194 (10), DOI: 10.1007/s10661-022-10400-5.
- Schmidt-Thomé P., Nguyen T.H., Pham T.L., Jarva J., Nuottimäki K., 2014, Climate change in Vietnam, [in:] *Climate Change Adaptation Measures in Vietnam: Development and Implementation*, P. Schmidt-Thomé, T.H. Nguyen, T.L. Pham, J. Jarva, K. Nuottimäki (eds.), Springer, 7-15, DOI: 10.1007/978-3-319-12346-2\_2.
- Silberstein R., Aryal S., Durrant J., Pearcey M., Braccia M., Charles S., Boniecka L., Hodgson G., Bari M., Viney N., 2012, Climate change and runoff in south-western Australia, *Journal of Hydrology*, 475, 441-455, DOI: 10.1016/j.jhydrol.2012.02.009.
- Takele G.S., Gebrie G.S., Gebremariam A.G., Engida A.N., 2022, Future climate change and impacts on water resources in the Upper Blue Nile basin, *Journal of Water and Climate Change*, 13 (2), 908-925, DOI: 10.2166/wcc.2021.235.
- Tariku T.B., Gan T.Y., Li J., Qin X., 2021, Impact of climate change on hydrology and hydrologic extremes of Upper Blue Nile River Basin, *Journal of Water Resources Planning and Management*, 147 (2), DOI: 10.1061/(ASCE)WR.1943-5452.000132.
- Tayara-Zobaida E., 2023, Hydrologic drought characteristics of selected basins in various climate zones of Lebanon, *Meteorology Hydrology and Water Management*, 11 (2), 28-51, DOI: 10.26491/mhwm/174194.
- Wild M., 2020, The global energy balance as represented in CMIP6 climate models, *Climate Dynamics*, 55 (3), 553-577, DOI: 10.1007/s00382-020-05282-7.

- Willkofer F., Schmid F.-J., Komischke H., Korck J., Braun M., Ludwig R., 2018, The impact of bias correcting regional climate model results on hydrological indicators for Bavarian catchments, *Journal of Hydrology: Regional Studies*, 19, 25-41, DOI: 10.1016/j.ejrh.2018.06.010.
- WMO, 2021, 2021 State of Climate Services: Water, World Meteorological Organization, available online at <https://wmo.int/publication-series/2021-state-of-climate-services-water> (data access 01.09.2025).
- Yang K., Chen T., Ao T., Zhang X., Zhou L., Gao D., 2022, Response of runoff in the upper reaches of the Minjiang River to climate change, *Journal of Water and Climate Change*, 13 (1), 260-273, DOI: 10.2166/wcc.2021.038.
- Yue Y., Yan D., Yue Q., Ji G., Wang Z., 2021, Future changes in precipitation and temperature over the Yangtze River Basin in China based on CMIP6 GCMs, *Atmospheric Research*, 264, DOI: 10.1016/j.atmosres.2021.105828.
- Ziehn T., Chamberlain M.A., Law R.M., Lenton A., Bodman R.W., Dix M., Stevens L., Wang Y.-P., Srbinovsky J., 2020, The Australian earth system model: ACCESS-ESM1.5, *Journal of Southern Hemisphere Earth Systems Science*, 70 (1), 193-214, DOI: 10.1071/ES19035.